NiCo-Oxide-Based Anodes for Water Splitting and Wastewater Treatment Applications

by

Emmanuel Onyekachi Nwanebu

A thesis submitted to McGill University in partial fulfillment of the requirements of the degree of Doctor of Philosophy

at

Department of Chemical Engineering
McGill University
Montréal, Québec, Canada

November 2020

I dedicate this thesis to God Almighty who, through HIS grace and love, brought me forth through my beautiful, lovely and virtuous mother, Uche Philomena Nkechinyere. The woman who inspired me to aspire for the highest level of academic excellence. Mummy, your dedication and strive to improve on your educational training knew no bounds. Even in your penultimate year with us, you were still gearing to embark on another advanced learning program. I promised to succeed for us. Thank God for the grace to accomplish my promise.

ABSTRACT

In order to meet the growing need for ample sustainable energy supply for the future generations, it is envisioned that the world energy economy should be less dependent on the environmentally-unfriendly fossil fuel energy. Hydrogen, as an energy carrier, has gained enormous interest. However, the commercialisation of a sustainable futuristic hydrogen economy achievable *via* water electrolysis is largely setback by the slow kinetics of the anodic oxygen evolution reaction (OER) in the water-splitting process. Therefore, the intrinsic nature of the anode material is a key determinant in the potential viability of the hydrogen economy. Also, electrochemical anode materials of relatively larger oxygen evolution overpotential may serve as efficient electrode materials in the electrocatalytic degradation of organic pollutants in wastewater treatment technologies.

This Ph.D. project presents a comprehensive systemic study on the development of novel, low-cost nickel-cobalt-based oxide anodes that could be utilized both in the production of hydrogen and as energy-efficient electrodes for the anodic oxidation of recalcitrant organic contaminants in wastewater systems. Hence, the main focus of this PhD thesis was to fabricate and characterize low-cost, durable Ni-Co-oxide electrocatalysts that are capable of achieving (i) high electroactive performance towards the OER, and (ii) highly effective and energy-efficient electrochemical oxidation of organic pollutants in wastewater treatment schemes.

Surface characterization techniques were employed to study the surface behavior and nature of the fabricated Ni-Co-oxide based anode materials. Scanning electron microscopy (SEM) and energy dispersive X-ray spectroscopy (EDX) were deployed to investigate the surface structural morphologies and chemical compositions of the oxide films. X-ray diffraction (XRD) was utilized to determine the different oxide phases as well as the crystallinity and porosity of the coating surfaces. Further, X-ray photoelectron spectroscopy (XPS) was employed to determine the atomic composition of the topmost layer of the oxide films and to substantiate the various oxide phases in the anode material. Also, electrochemical testing procedures such as linear sweep voltammetry (LSV), chronopotentiometry, cyclic voltammetry (CV), electrochemical impedance spectroscopy (EIS) were utilized to characterize the extrinsic and intrinsic electrocatalytic OER activity and long-term durability of the synthesized oxides. Lastly, UV/Vis spectrophotometry was employed to monitor the destruction of a model organic pollutant over time.

First, the results on the influence of Ni-Co-oxide composition on its electrocatalytic activity in the oxygen evolution reaction during electrolysis in adverse acidic conditions were presented. The surface roughness of the oxide film was found to be composition dependent and comprised crystalline NiO, Co_3O_4 and CoO. The OER electrocatalytic activity of the oxide surfaces was found to be greatly dependent on their Ni-to-Co ratio. The electrochemical characterization of these surfaces revealed that $Ni_{0.4}Co_{0.6}$-oxide exhibited the highest intrinsic activity. The OER activity of this oxide was inferior to the state-of-the art IrO_2 anode; however, it demonstrated the potential to serve as a building block to develop better active, long-term stable anodes.

As a result, studies on the improvement of the OER activity of the composition-optimized $Ni_{0.4}Co_{0.6}$-oxide in the oxygen evolution reaction were conducted in acidic and alkaline media. It was shown that the incorporation of small amounts (up to.10 at.%) of Ir into the $Ni_{0.4}Co_{0.6}$-oxide matrix resulted in the substantial improvement of the intrinsic electrocatalytic activity of the anode. The enhancement in the OER activity was attributed to the modulation of the electronic structure of the catalyst and to the reduction in its band gap energy relative to $Ni_{0.4}Co_{0.6}$-oxide and pure Ir-oxide. The fabricated novel $(Ni_{0.4}Co_{0.6})_{0.9}Ir_{0.10}$-oxide anode was found to be stable and more active than the current state-of-the-art Ir-oxide OER anode in the acidic electrolyser, while also offering a significantly higher electrocatalytic activity than current nickel anodes employed in alkaline electrolyser.

Furthermore, the influence of fabrication temperature on the electrocatalytic properties of Ni-Co-Ir-oxide and Ni-Co-Ru-oxide in the oxygen evolution reaction was studied in the alkaline medium. It was found that the intrinsic OER electrocatalytic activity of the oxides depended on the material’s calcination temperature, reaching a maximum at 300°C. The enhancement in OER electroactivity was attributed to the intrinsic synergistic interaction among the oxides’ electroactive species, primarily due to the modification of their electronic structures and in part due to the increase in their hydroxide content and oxygen vacancies. The specific OER performance of both oxides was found to be either close to, or better than the state-of-the-art Ir-oxide and Ru-oxide anodes, despite having only one-tenth of the content of the noble metals.

Finally, $Ni_{0.6}Co_{0.4}$-oxide, which was discovered to have the largest OER overpotential (i.e. lowest intrinsic OER activity) of all the tested Ni-Co-oxide compositions, was utilized as an electrochemical anode in the degradation of a common organic wastewater pollutant, methylene blue (MB) dye. The $Ni_{0.6}Co_{0.4}$-oxide proved to be an effective anode material for the complete oxidation of the organic pollutant. It was found that the rate of the degradation (oxidation) process was significantly improved in the presence of chloride ions in the electrolyte, which was attributed to the *in situ* electrochemical formation of active chlorine species. The anode material was found to be electrochemically stable over a 50-hour period of MB degradation.

RÉSUMÉ

Afin de répondre au besoin croissant d'un approvisionnement suffisant en énergie durable pour les générations futures, il est envisagé que l’économie mondiale de l’énergie soit moins dépendante de l’énergie fossile peu respectueuse de l’environnement. L’hydrogène, en tant que vecteur d’énergie, a suscité un vif intérêt. Cependant, la commercialisation d’une économie futuriste durable de l’hydrogène réalisable par électrolyse de l’eau est largement contrecarrée par la cinétique lente de la réaction d’évolution de l’oxygène anodique (OER) dans le processus de craquage de l'eau. Par conséquent, la nature intrinsèque du matériau d’anode est un déterminant clé de la viabilité potentielle de l’économie de l’hydrogène. De plus, les matériaux d'anode électrochimique d'un surpotentiel d’évolution de l’oxygène relativement plus grand peuvent servir de matériaux électrodes efficaces dans la dégradation électrocatalytique des polluants organiques dans les technologies de traitement des eaux usées.

Ce projet de doctorat présente une étude compréhensive sur le développement de nouvelles anodes d'oxyde à base de nickel-cobalt peu coûteuses qui pourraient être utilisées à la fois dans la production d'hydrogène et comme électrodes écoénergétiques pour l'oxydation anodique de contaminants organiques récalcitrants dans les systèmes d'eaux usées. Par conséquent, l’objectif principal de cette thèse était de fabriquer et de caractériser des électrocatalyseurs au Ni-Co-oxyde durables et peu coûteux qui sont capables d’atteindre (i) des performances électroactives élevées vers l'OER, et (ii) une oxydation électrochimique hautement efficace et éconergétique des polluants organiques dans les systèmes de traitement des eaux usées.

Des techniques de caractérisation de surface ont été utilisées pour étudier le comportement de surface et la nature des matériaux d'anode fabriqués à base de Ni-Co-oxyde. La microscopie électronique à balayage (MEB) et la spectroscopie de rayons X à dispersion d'énergie (EDS) ont été déployées pour étudier les morphologies structurales de surface et les compositions chimiques des films d'oxyde. La diffraction de rayons X (XRD) a été utilisée pour déterminer les différentes phases d’oxyde ainsi que la cristallinité et la porosité des surfaces de revêtement. De plus, la spectroscopie de photoélectrons (XPS) a été utilisée pour déterminer la composition atomique de la couche la plus haute des films d’oxyde et pour corroborer les différentes phases d’oxyde dans le matériau d’anode. En outre, les procédures d’essais électrochimiques tels que la polarisation linéaire de Tafel (LTP), la chronopotentiométrie, la voltamétrie cyclique (CV), et la spectroscopie

d’impédance électrochimique (EIS) ont été utilisées pour caractériser l'activité OER électrocatalytique extrinsèque et intrinsèque et la durabilité à long terme des oxydes synthétisés. Enfin, la spectrophotométrie UV / Vis a été utilisée pour suivre la destruction d'un polluant organique modèle au fil du temps.

D'abord, les résultats sur l'influence de la composition du Ni-Co-oxyde sur son activité électrocatalytique dans la réaction de dégagement d'oxygène pendant l'électrolyse dans des conditions acides défavorables ont été présentés. On a trouvé que la rugosité de surface du film d'oxyde dépendait de la composition et comprenait des phases cristallines de NiO, Co_3O_4 et CoO. L'activité électrocatalytique OER des surfaces d’oxyde s’est avérée fortement dépendante de leur rapport Ni / Co. La caractérisation électrochimique de ces surfaces a révélé que le $Ni_{0.4}Co_{0.6}$-oxyde présentait la plus forte activité intrinsèque. L’activité OER de cet oxyde était inférieure à l’anode IrO_2 de pointe; cependant, elle a démontré le potentiel de servir de base pour développer des anodes plus actives et stables à long terme.

En conséquence, des études sur l’amélioration de l’activité OER de la composition optimisée $Ni_{0.4}Co_{0.6}$-oxyde dans la réaction d’évolution de l’oxygène ont été menées dans des milieux acides et alcalins. On a été montré que l’incorporation de petites quantités d’iridium (jusqu’à 0,10 %) dans la matrice de $Ni_{0.4}Co_{0.6}$-oxyde a entraîné une amélioration substantielle de l’activité électrocatalytique intrinsèque de l’anode. L’amélioration de l’activité OER a été attribuée à la modulation de la structure électronique du catalyseur et à la réduction de sa bande d'énergie interdite par rapport à $Ni_{0.4}Co_{0.6}$-oxyde et IrO_2. La nouvelle anode fabriquée « $(Ni_{0.4}Co_{0.6})_{0.9}Ir_{0.10}$-oxyde » s'est avérée stable et plus active que l’anode OER Ir-oxyde de pointe actuelle dans l'électrolyseur acide, tout en offrant une activité électrocatalytique plus élevée que les anodes de nickel actuelles utilisées dans l'électrolyseur alcalin.

En outre, l’influence de la température de fabrication sur les propriétés électrocatalytiques de Ni-Co-Ir-oxyde et Ni-Co-Ru-oxyde dans la réaction d’évolution de l’oxygène a été étudiée dans le milieu alcalin. On a découvert que l’activité électrocatalytique intrinsèque des OER des oxydes dépendait de la température de calcination du matériau, atteignant un maximum à 300°C. L’amélioration de l’électroactivité OER a été attribuée à l’interaction synergique intrinsèque entre les espèces électroactives des oxydes, principalement en raison de la modification de leurs structures électroniques et en partie en raison de l'augmentation de leur teneur en hydroxyde et des lacunes d'oxygène. La performance OER spécifique des deux oxydes s'est avérée proche ou supérieure à celle des anodes IrO_2 et RuO_2 de pointe, même si elles ne contenaient qu'un dixième des métaux nobles.

Enfin, le $Ni_{0.6}Co_{0.4}$-oxyde, dont on a découvert qu'il avait la plus grande surpotentielle de OER (ou la plus faible activité intrinsèque de OER) de toutes les compositions de Ni-Co-oxyde testées, a été utilisé comme anode électrochimique dans la dégradation d'un polluant organique commun des eaux usées, le bleu de méthylène (MB). Le $Ni_{0.6}Co_{0.4}$-oxyde s'est avéré être un matériau d'anode efficace pour l'oxydation complète du polluant organique. On a été constaté que le taux de dégradation (oxydation) du procédé a été significativement amélioré en présence d'ions chlorure dans l'électrolyte, ce qui a été attribué à la formation électrochimique in situ d'espèces de chlore actif. Le matériau d'anode s'est avéré être électrochimiquement durable sur une période de 50 heures de dégradation du MB.

TABLE OF CONTENTS

LIST OF FIGURES

LIST OF TABLES

ACKNOWLEDGEMENTS

It is with great joy and happiness that I express my gratitude to everyone who has helped make the successful completion of this research project a pleasant reality. The journey was challenging, demanding, and sometimes appeared to be unpredictable and unattainable. Nevertheless, you were there for me, and I am very grateful. First, I would like to recognize the immense contribution of Prof. Sasha Omanovic for his supervisory role on this project. It is hard to imagine how this thesis project could have been completed without you. I appreciate your encouragement to keep pushing the bounds when the going was tough, especially for your patience and understanding for such an extended period after the birth of my daughter, Sinachi.

I would like to thank my darling wife, whose persistent presence during this doctorate program helped bolster its success. In this period, we became colleagues, friends, life partners, and parents. I am exceedingly grateful to you, *asa nne*. Thank you for being my go-to person when I needed advice and problem-solving strategy to adopt in order to surmount the apparent roadblocks that showed up during this Ph.D. project. When the writing was difficult and seemingly unending, you were there to steady the ship and offer your editorial skills. To my spousal parents, I say thank you for your trust and prayers that have inspired this joyous feat. Also, I would like to acknowledge the rest of my family back home for their love and support.

Thanks to all my colleagues, both past and present, with whom I shared the Electrochemistry and Corrosion laboratory and engaged in several critical reasoning and deliberations on different subject matters: Saloumeh, Abraham, Deepak, Mahmoud, Elmira, Ahmad, Ipsita, Logan, Xingge, Kanghoon, Hao, Zhuoya, Rihab, Amir, Vincent, and Raed.

It was my pleasure working with Yusong Zao, Raed Gharbi, Dara Shogbanmu, Nathalie Abou Harb, and Xiacheng Liu. These undergraduate students were instrumental in helping me achieve some of the targets of this research project. I greatly appreciate the time and effort they invested in the accomplishment of the sub-projects.

My special appreciation goes to Frank Caporuscio, who made my work in the lab less stressful. It was practically impossible to solve certain technical issues and make progress in this Ph.D. program without your assistance either directly or indirectly. Frank, you are a great man.

God bless you. Thank you to the rest of the Departmental staff with whom I interfaced with such as Andrew, Ranjan, Gerald, Roberto, Lou, Lisa, Louis, Anna, and Kevin.

I am enormously indebted to the Nigerian Petroleum Technology Development Fund (PTDF), Natural Sciences and Engineering Research Council of Canada (NSERC), and the McGill Engineering Doctoral Award (MEDA) for funding this project. I would also like to appreciate my wife and my supervisor for their financial assistance during the final year of my program.

Finally, I would like to thank all my cheerleaders like Sarah, Ibukun, and everyone else that was associated with the success story of this Ph.D. project in one way or the other. You all rock!

CONTRIBUTIONS OF AUTHORS

This Ph.D. thesis is presented in a manuscript-based style and consists of four articles. The first two articles have been published in peer-reviewed scientific journals, the third article has been submitted for publication, and the last one is being prepared for submission. The contribution of the authors to each of the manuscript are presented as follows:

Chapter 3: The influence of Ni_xCo_{1-x}-oxide composition on its electrocatalytic activity in the oxygen evolution reaction

In this chapter, a range of different Ni-Co-oxide compositions were prepared by thermal decomposition technique on button-shaped titanium substrates and these binary oxides were evaluated as oxygen evolution reaction electrocatalyst in acidic water electrolysis. The resulting article was published in the *Materials Chemistry and Physics* journal and is cited as following:

> E. O. Nwanebu and S. Omanovic, "The influence of NixCo1-x-oxide composition on its electrocatalytic activity in the oxygen evolution reaction," *Materials Chemistry and Physics,* vol. 228, pp. 80-88, 2019.

The work was conceived, planned, conducted, analyzed and written by Emmanuel Nwanebu (the Ph.D. candidate). Prof. Sasha Omanovic supervised the work, assisted in the interpretation and discussion of the results and reviewed the article.

Chapter 4: The influence of Ir content in $(Ni_{0.4}Co_{0.6})_{1-x}Ir_x$-oxide anodes on their electrocatalytic activity in oxygen evolution by acidic and alkaline water electrolysis

This chapter presents an article that has been published in the *Journal of Electroanalytical Chemistry*. The article is cited as follows:

> E. O. Nwanebu, Y. Yao, and S. Omanovic, "The Influence of Ir Content in $(Ni_{0.4}Co_{0.6})_{1-x}Ir_x$-oxide Anodes on their Electrocatalytic Activity in Oxygen Evolution by Acidic and Alkaline Water Electrolysis," *Journal of Electroanalytical Chemistry,* p. 114122, 2020.

The project was conceptualized, planned, performed, analyzed and written by Emmanuel Nwanebu (the Ph.D. candidate). The preliminary investigation on the OER performance of the Ni-Co-Ir-oxide in the acidic medium was conducted by Yusong Yao, (a McGill University undergraduate student engaged at the time in a summer project in the Electrochemistry and Corrosion lab). The work was supervised, reviewed and edited by Prof. Sasha Omanovic.

Chapter 5: The Effect of Calcination Temperature on the Electrocatalytic Activity of Ni-Co-Ir-oxide and Ni-Co-Ru-oxide Anodes in the Oxygen Evolution Reaction in Alkaline Medium

The results presented in this chapter have been submitted for publication in the *Solid State Sciences* journal . The citation of the article is thus:

> E. O. Nwanebu, N. Abou Harb, R. Gharbi, and S. Omanovic, "The Effect of Calcination Temperature on the Electrocatalytic Activity of Ni-Co-Ir-oxide and Ni-Co-Ru-oxide Anodes in the Oxygen Evolution Reaction in Alkaline Medium," 2020.

The contributions of the authors are as follows: Emmanuel Nwanebu conceptualised the idea of investigating the possible influence of calcination temperature on the OER activity of Ni-Co-Ir/Ru-oxide, designed the experiments, synthesized the samples, performed the experiments, analyzed the empirical results, and wrote the manuscript. Natalie Abou Harb (a summer student at McGill University on exchange from the Lebanese University) investigated and validated the electrochemical characterisation experiments involving the Ni-Co-Ru-oxide samples and helped review the manuscript. Raed Gharbi (at the time, a McGill University undergraduate student) conducted the initial electrochemical measurement on Ni-Co-Ru-oxide as part of his undergraduate summer project. Prof. Sasha Omanovic provided supervisory guidance and helped in the interpretation and discussion of the data and reviewed the manuscript.

Chapter 6: Electrochemical Degradation of Methylene Blue using Novel Ni-Co-oxide Anode

Results that are presented in this chapter are contained in an article that is in preparation for submission to a peer-reviewed scientific journal. The citation for the article is:

> E. O. Nwanebu, X. Liu, and S. Omanovic, "Electrochemical Degradation of Methylene Blue using Novel Ni-Co-oxide Anode," 2020.

The contributions of each author are as follows: Emmanuel Nwanebu (the Ph.D. candidate) designed the experiments, prepared the samples, performed the experiments, analyzed the experimental data, and wrote the manuscript. Xiaocheng Liu (at the time, a non-thesis MEng Chemical Engineering student) was involved in the investigation of the influence of chloride ion concentration on the degradation rate of the organic pollutant by Ni-Co-oxide anode. Prof. Sasha Omanovic was responsible for the supervision of the work, interpretation and discussion of the data and the review of the manuscript.

Chapter 1 Introduction

1.1 Preface

Alternative renewable energy research is currently at the forefront of futuristic energy solution drive to address the World's overreliance on fossil fuel sources that are not only limited in supply but are inimical to the environment. Researchers are assiduously working to find long-lasting answers to effectively address the issue of overdependence on hydrocarbon energy. However, the World, as we know it today, cannot function effectively without fossil fuel energy supply. This is because sustainable alternative energy sources are scarcely available. For example, most motorists are heavily dependent on gasoline-powered vehicles to get by their daily lives. Also, it is common knowledge that exhaust fumes from vehicular transports and industrial processes are the major sources of greenhouse gases like CO_2 that are continuously released into our atmospheric environment.

The real-time data from NASA's Goddard Institute for Space Studies (GISS) [1] showed that at the end of 2019, the observed CO_2 emission level has risen by ca. 33% since 1950. Consequently, the global surface temperature relative to the 1951 – 1980 average temperatures has increased by ca. 1°C. Moreover, this increasing level of atmospheric CO_2 is known to be mainly responsible for the prevalent global rise in sea level. As a result, in the past 70 years, the global sea level has risen by ca.140 mm primarily due to CO_2 emission as reported by NASA/GISS data [1]. Therefore, given the environmental risks such as climate change, a key global energy challenge initiative is to develop environmentally-clean and sufficiently available energy – i.e., CO_2 emission-free. Interestingly, electrolytic hydrogen production as an alternative source of energy generation is touted as the solution to meeting the above stated Mondial energy needs, especially for future vehicular fuel requirement.

Hydrogen is considered as a future clean energy carrier suitable for transition from the current hydrocarbon economy [2]. This is because it is a recyclable substance with practically unlimited supply and possesses criteria that make it the best alternative energy source [3-6]. Recently, there has been a vast interest in hydrogen production technology. Hydrogen can be produced by hydrocarbon reforming, ammonia cracking, or electrolysis of water. In the electrolytic process, water (H_2O) is split directly into hydrogen (H_2) and oxygen (O_2) by means of electricity

[7, 8]. However, water electrolysis as a means of producing hydrogen is not yet cost-competitive in comparison to commercial natural gas reforming or industrial ammonia decomposition and separation processes, since it requires a substantial initial investment and has high operational cost due to high energy consumption. As a result, only 4% of the World hydrogen production is obtained through water electrolysis [9]. Nevertheless, water electrolysis is considered the cleanest way to produce large volumes of hydrogen when the required electricity is derived from renewable energy sources [8]. In addition, surplus of electrical energy could conveniently be stored in the form of hydrogen.

In practice, the efficiency of water electrolysis is mostly limited by large anodic overpotential of the oxygen evolution reaction (OER) [10]. Thus, it is important to find the optimal oxygen-evolving electrocatalyst (anode) to minimize the resulting energy losses. Over the past fifty years, considerable research effort has been devoted to the design, synthesis, and characterization of anode materials, to achieve useful OER rate at the lowest possible overpotential, to optimize the overall efficiency of the electrolytic process [11].

An adequate OER electrocatalyst is one that is characterized by low overpotential, large active surface area, physical and electrochemical stability (including corrosion stability), selectivity, low cost, ease of use, and good electrical conductivity [12]. As such, the state-of-the-art anode materials are oxides of the noble transition metals such as iridium, ruthenium, and platinum. These metals exhibit good corrosion resistance in certain aggressive environments and show high catalytic activity towards OER through their ability to generate high current per unit area of external surface [13-16]. However, they are not economically viable on a commercial scale since they are both expensive and geographically limited in supply. To counter this economic challenge imposed due to the scarcity of these precious metals, a lot of research is currently ongoing in the development of low-cost, readily available electrocatalysts with good electrochemical activity and stability towards the OER. Hence, this Ph.D. thesis focuses on the development of inexpensive, stable anode materials for the efficient evolution of oxygen without the need to sacrifice electrocatalytic performance.

Previous researches have shown nickel to be a low-cost non-noble transition metal OER catalyst with high intrinsic electrocatalytic activity and long-term stability, especially in alkaline medium [17-19]. This relatively inexpensive metal, when alloyed with other transition metals like iron, manganese, or cobalt exhibited even higher electrocatalytic activity towards OER as a result of modified *d*-shell electronic configuration [17, 20]. In addition, nickel alloys can manifest surface morphological alterations leading to increased electroactive surface area and advantageous surface roughness. However, pure Ni and its alloys lack long-term stability and activity required to serve as excellent electrocatalysts in an acidic environment. For example, they are not suitable for use in polymer electrolyte membrane (PEM) electrolysers as a result of their poor corrosion resistance at low pH. On the contrary, their oxides have been reported to exhibit better stability [21, 22] while offering sufficient performance.

Research works on metal oxide electrodes, particularly those of transition metals, have shown good performance in the oxygen evolution reaction [11, 17, 23]. These oxide electrodes have also attracted attention in other relevant electrocatalytic reactions such as cathodic hydrogen evolution [20, 24, 25], and oxygen reduction [22, 26, 27]. However, the reported research on oxygen evolution at stable metal oxide anodes is limited. Hence, more effort needs to be devoted to develop more stable anodes. Indeed, stability is the main reason for industrial success of dimensionally stable anodes (DSA), that are formed by coating a metal oxide on a (usually) titanium substrate that are utilized for water oxidation. Their stability success story is attributed to three main factors, namely: the formation of surface products, mechanical strength, and electronic conductivity [22]. DSAs are said to have infinite life (ideally) within a certain electrode potential limit. Therefore, the achievements in the development of DSAs show that by synergistically mixing metal oxides, stability can be maximized by lifting the limit of surface oxidation potential [22, 28].

Taking a cue from the above-given information on metal oxides, the primary goal of this Ph.D. project was to develop and study novel low-cost NiCo-based mixed metal oxide (MMO) materials *via* a systematic approach to investigate the influence of compositional Ni/Co ratio and the significant impact of calcination temperature on the thermally-prepared oxide materials. The optimized MMO should offer high OER electrocatalytic activity and excellent electrochemical and structural stability, within operable surface oxidation potential, for industrial applicability in both acidic and alkaline environments.

Moreover, mixed metal oxides that are not good for OER potentially have the added advantage of serving as low-cost anodes in the oxidative treatment of wastewater. Therefore, an additional objective of this Ph.D. thesis was to investigate the applicability of synthesized Ni/Co-oxide anodes that performed poorly in the OER as potentially good anodes for the degradation of recalcitrant organic contaminants in wastewater treatment applications. Hence, the anodic oxidation of methylene blue on NiCo-oxide surface was studied.

1.2 Objectives

There is an overwhelming urgent need to develop more sustainable sources of fuel to meet global growing energy demands. And as such, there has been increased research in renewable alternative energy sources in which hydrogen (as an energy vector) production is strongly and largely considered. The primary objective of this Ph.D. thesis project was to develop NiCo-oxide-based MMO anodes aimed at enhancing the efficiency of the electrolytic production of hydrogen, achieved through significant improvement of the electrocatalytic activity of the OER and long-term stability performance of the developed OER anodes. The metal components of the base anode materials (Ni and Co) were selected due to their low-cost, availability, ease of use, and favourable research results on the pure components, while the addition of small amounts of Ir and Ru to NiCo-oxide to form three-metal-oxide MMOs was based on the premise of exceptional OER catalytic activity of Ir and Ru, and the hypothesis that these new MMOs would offer higher electrocatalytic activity than pure state-of-the-art Ir-oxide and Ru-oxide. The main goal of the project was accomplished through the following specific objectives:

- Optimization of a facile method of fabricating thermally-prepared MMO on a flat titanium substrate for easy electrochemical testing.
- Investigation of various physicochemical properties (chemical composition, wettability, surface morphology, crystalline structure) of the MMO coatings and their electronic and morphological properties on the resulting electrochemical properties as it relates to their OER electrocatalytic activity.
- Evaluation of the electrochemical stability of the MMO anodes in the OER.

Furthermore, the additional objective of the Ph.D. thesis involved the fabrication of electrochemically-active MMO anode for the treatment of a wastewater system. This was achieved through the following specific objectives:

- Evaluation of the least-effective (poorly-performing) OER NiCo-oxide electrocatalyst composition as a possible anode for the electrochemical treatment (destruction) of methylene blue dye in an aqueous environment.
- Improvement of the electrochemical degradation process kinetics by formation of chlorine active species as additional oxidants.

1.3 Thesis organization

This thesis is prepared in a manuscript-based style in accordance with the guidelines and regulations stipulated by the McGill University Graduate and Postdoctoral Studies (GPS) so as to fulfill the requirements for a doctorate degree. Each of the eight chapters are written coherently so the reader can follow the aim of the research work, the development of the objectives, reported results, corresponding discussions and the achieved outcome of the research.

Chapter 1 contains the introductory part of the thesis. It outlines the consequences of overdependence on fossil fuel as the primary source of energy and the importance of developing an alternative renewable energy vector, hydrogen. The objectives of this thesis are also presented in this chapter to elucidate the relevance and contribution of the novel MMO anodes towards the actualization of a futuristic hydrogen economy and the possible application of these anodes in the wastewater treatment technologies. In chapter 2, the theoretical background and relative concepts in electrochemistry that are utilized for the development of these new anode materials for the advancement of the future energy carrier and their use in wastewater application are explained.

The next four chapters are written in a manuscript-based format as scientific papers either published, or currently going through a review process, or prepared for submission to peer-reviewed journals to address the objectives of this Ph.D. research. The systematic development of NiCo-oxide anodes and the influence of its Ni/Co ratio on the OER electrocatalytic activity in a harsh acidic environment are discussed in chapter 3. Chapter 4 presents the significant improvement in the intrinsic OER electrocatalytic activity and stability of NiCo-oxide anodes by adding a small amount of Ir. The resulting Ni-Co-Ir could effectively replace the current state-of-the-art IrO_2 electrode. In Chapter 5, the effect of calcination temperature on the OER electrocatalytic activity of the thermally-formed Ni-Co-Ir/Ru-oxides in an alkaline condition is studied. Chapter 6 addresses the use of high OER overpotential Ni-Co-oxide anode in the electrochemical oxidative removal of methylene blue towards wastewater purification.

Chapter 7 sums up the thesis in such a way to delineate the key conclusions of the study. Finally, Chapter 8 highlights the original fundamental scientific contributions of the thesis and recommends future research work that could be done.

Chapter 2 Background and Literature Review

This section presents background information and essential scientific concepts associated with the development of efficient oxygen evolution reaction electrocatalyst. Also, the current state-of-the-art research on OER anodes for hydrogen production technology and its use in wastewater treatment applications are discussed.

2.1 Hydrogen economy

The hydrogen economy entails the utilization of hydrogen as a low carbon energy fuel for heating, transportation fuel, and energy storage. The rationale behind the development of this concept is to limit the usage of fossil fuels and minimize global warming since hydrogen is seen as a potential alternative fuel source (vector). It can be combusted to produce heat or reacted with oxygen in a fuel cell to generate electricity with clean water as the only by-product. Another equally important factor is the fact that hydrogen is the simplest and lightest earth-abundant non-toxic molecule known [29, 30]. Also, H_2 has the highest specific energy content (142 kJ/g) when compared to other energy vectors and fuels other than nuclear energy. These properties indeed make hydrogen a promising alternative secondary source of energy. It must be noted that hydrogen is not a primary energy source, but an *energy carrier (vector)* because it is not found in naturally-occurring reservoirs. Thus, it has to be extracted from other molecules like water, ammonia and most often hydrocarbons.

For the world economy to utilize hydrogen as the major energy carrier, the volume of hydrogen produced has to be enormously increased. The current production of hydrogen is not enough compared to what is required to create a hydrogen economy, which is an energy system whereby hydrogen is used to deliver energy (see Figure 2.1).

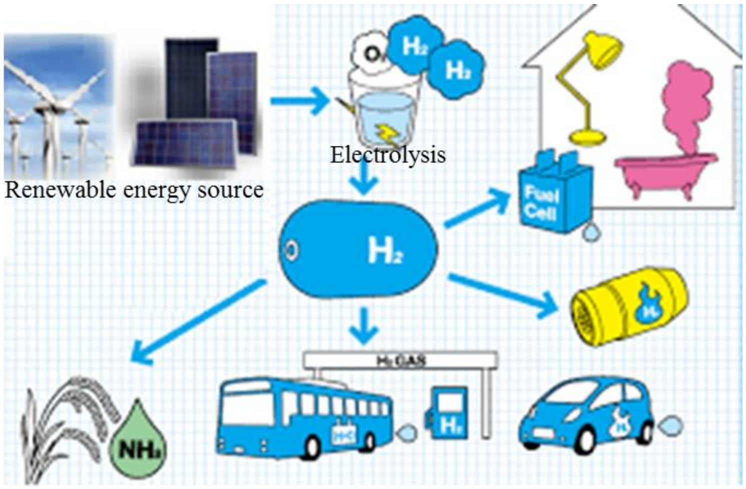

Figure 2.1: Schematic representation of the hydrogen economy (Angstrom Advance Inc.)

In 1977, the Hydrogen Implementing Agreement (HIA) was established to harness this system [31], and for over four decades now, the World's attention has been focused on developing ways of producing this promising green fuel. Countries and companies alike have already made huge capital investments on the futuristic hydrogen economy. For instance, Honda and Toyota have started selling hydrogen-fuel-cell-powered vehicles, and there are increasing numbers of hydrogen-refueling stations being built in Europe, Japan and the USA. Furthermore, portable hydrogen-fuel-cell-powered battery chargers for small-scale consumer appliances, such as laptop computers and cellular phones, are already in the market. Nevertheless, there is still a long way to go before the broad-scale commercialization of the hydrogen technology. Notwithstanding, the global initiatives and commitments from car manufacturers, for example, are significant as the World makes in-road towards an economy driven by hydrogen energy.

The major demerit of the future hydrogen-based energy system is in the high cost of producing hydrogen. However, when the life cycle assessment of the environmental impact of the present-day hydrocarbon system is made, it can be seen that hydrogen becomes a viable alternative as an environmentally-friendly energy source[32]. Therefore, reducing costs while paying close attention to environmental and safety concerns is the most pressing task currently addressed by research and development programs on hydrogen energy. One of the key findings today shows that the technology faces a difficult challenge in terms of improving the energy efficiency of the employed hydrogen production method. This is because the current method of generating hydrogen of which ca. 96% [9] are sourced from fossil fuels, is not close to a 90 % efficiency [33, 34].

2.1.1 Hydrogen Production Technology

The methods of producing hydrogen are well-known. Although hydrogen is majorly generated by steam reforming of natural gas (methane), there are three other main hydrogen production methods, namely: partial oxidation of hydrocarbons, coal gasification and water electrolysis [30, 33, 35]. These industrial methods will be briefly explained in the following sections.

2.1.1.1 Steam Reforming of Natural Gas

This process involves the heating of natural gas in the temperature range of 700 – 1100°C in the presence of steam and a nickel catalyst resulting in an exothermic reaction that breaks up the gas (methane) molecules into carbon monoxide and hydrogen. The produced CO is typically passed over an oxide layer catalyst (at about 300 – 400°C), thereby undergoing an endothermic water gas shift reaction in which more hydrogen is generated. The overall process is ca. 80% efficient [33, 34]. The typical simplified reactions are given below:

$$CH_4 + H_2O \leftrightarrow CO + 3\,H_2 \qquad 2.1$$

$$CO + H_2O \leftrightarrow CO_2 + H_2 \qquad 2.2$$

Although hydrogen produced from natural gas is currently the cheapest, the problem with the steam reforming process is that its main by-product is CO_2, a greenhouse gas. From equations (2.1) and (2.2), it implies that 5.5 kg of stoichiometric CO_2 is emitted per kg of hydrogen produced, which has a deleterious effect on our environment and the climate including, global warming. In addition, this process is not sustainable over a long term as CH_4 deposits are limited.

2.1.1.2 Partial Oxidation of Hydrocarbons

Here, a fuel-air or fuel-oxygen mixture is burnt in a partial oxidation reactor leading to the formation of hydrogen-rich syngas. The process could be either a thermal partial oxidation or catalytic partial oxidation as given in the general equation (2.3).

$$C_aH_b + 1/_2\,O_2 \rightarrow a\,CO + b/_2\,H_2 \qquad 2.3$$

In the catalytic oxidation, the presence of CO is even more undesirable since CO can easily poison the catalyst. Although CO can be removed by the water shift reaction as in the steam reforming method, the CO_2 by-product is inimical to the environment. Another disadvantage of the partial oxidation method is that it involves a higher investment cost with accompanying overall process efficiency [35].

2.1.1.3 Gasification of Coal

Hydrogen is produced by coal gasification when steam and a requisite amount of gases are utilized to break molecular bonds in coal, thereby forming gaseous mixture of hydrogen and carbon monoxide. Producing hydrogen via coal gasification is quite advantageous because the gaseous by-products from the gasification process can serve as fuel to generate electricity [34]. Hence, gasification is an attractive option for the production of hydrogen. On the other hand, coal gasification leads to the emission of a large amount of CO_2 that is environmentally unfriendly. Furthermore, the yield of this hydrogen production method is relatively low, and the coal deposits are limited, making this process also unsustainable over a longer period.

2.1.1.4 Electrolysis of Water

In water electrolysis, direct current is used to split water into component oxygen and hydrogen gases. Interestingly, the produced high-purity hydrogen could be both sustainable and environmentally friendly when renewable energy sources like solar/hydro/wind are employed as the primary energy source in the water-splitting process. In view of this, water electrolysis is considered the most environmentally viable option for the production of hydrogen. However, this process lacks a competitive advantage over the other main methods of hydrogen production outlined above because of its high-cost with regards to both the input energy demands and the current electrode materials utilized. Consequently, there are a good number of research and development programs driven towards making the process more cost-competitive.

This Ph.D. thesis primarily presents results on the studies of the water splitting, more specifically on the oxygen evolution reaction (OER) electrocatalysis in alkaline and acidic media, with the aim of contributing to the actualization of commercial-scale production of hydrogen by water electrolysis.

2.1.2 Hydrogen Storage

For the realization of the hydrogen economy, it is relevant to consider ways of storing the produced hydrogen for easy access and utilization in the future. Consequently, several methods of hydrogen storage have been researched, raging from high-pressure storage tanks to conversion of hydrogen to hydrides that regenerates H_2 when needed. It should be noted that high-pressure-stored hydrogen is a convenient source of fuel required for transportation. Also, stored hydrogen can be used as a grid energy power bank for intermittent energy sources such as wind and solar power to compensate for extended period of fluctuations in these renewable energy sources in times of seasonal variations. Furthermore, small amounts of hydrogen can be stored in pressurized vessels at 100 ~ 300 bar or liquefied at 20.3K (-253°C) for easy transportation and retail consumption [36].

On the other hand, large amounts of hydrogen can be stored in artificial underground salt caverns of up to 500,000 m^3 at 200 bar, corresponding to a storage capacity of 100 GWh electricity [37]. One might wonder why such a huge storage volume is required to generate similar energy output in comparison to smaller volumes requirements of its hydrocarbon counterparts? The reason lies in the fact that though molecular hydrogen has very high energy density, however as a gas at ambient conditions, it has a very low energy density by volume. As a result, pure hydrogen gas has to be stored in an energy-dense form to provide sufficient driving range when used as onboard vehicle fuel, for example.

Subsequently, there is intense research into other less voluminous storage options such as chemical hydride or other hydrogen-containing compounds like ammonia. Hydrogen can react with specific materials to yield hydrogen storage materials for easy transportation and then decompose at the point of use under favorable temperature and pressure conditions to regenerate hydrogen gas. Metal hydrides have proven to be an attractive alternative for hydrogen storage systems because of their beneficial properties, such as high volumetric and gravimetric density. Nonetheless, more research is needed in order to meet the United States Department of Energy’s requirements for storage capacity, kinetics, cost, and release temperature [36, 38]. Another approach involves the employment of lighter low-cost materials (relative to hydrides) such as activated carbon or nano-based carbon materials. Carbon-based materials can adsorb molecular hydrogen by way of electrochemical storage [39, 40] that can offer good reversibility, fast kinetics, and high capacities [41]. The latter method is expected to advance research into hydrogen storage focused on storing hydrogen as a lightweight, compact energy carrier, especially for mobile applications.

2.1.3 Hydrogen Conversion to Energy

The development of affordable material systems for the efficient conversion of hydrogen energy to electrical/heat energy is equally essential for the implementation of the low-carbon economy. Hydrogen can be re-electrified in the fuel cells with moderate efficiencies, or by combustion in combined cycle gas power plants [37]. The hydrogen fuel cells (HFCs) are expected to play a pivotal role in the futuristic hydrogen economy, and they are already primarily being used as backup power for commercial and residential buildings and in areas of remote access. Coincidentally, the emergence of proton exchange membrane HFCs (the most researched fuel cell) has led to the development of a variety of hydrogen energy applications ranging from small portable electronic devices to cars and to medium-sized stationary power generators [42].

Although hydrogen fuel cells are electrochemical devices with superior theoretical combined efficiency over the heat engine (83% in comparison to 35 – 45% for internal combustion engines (ICE) [43]), according to the World Energy Council, however, they are still more expensive to produce than the ICE. This is mainly due to the costly noble metals like platinum used at the electrodes and the polymer electrolyte / proton-exchange membrane (PEM). Besides, the purity requirement of the hydrogen utilized in fuel cells, at current technology, is needed to be close to 100% pure to minimize the poisoning of the electrocatalyst. Hence, the foregoing issues associated with the HFCs make a strong case for the development of low-cost and effective electrode materials for the efficient production of extra-pure hydrogen by water electrolysis. Water-splitting, when combined with water/solar/hydro energy, is the most realistic method of producing pristinely clean hydrogen with zero-emission of greenhouse gasses, including CO (which is produced in large quantities when hydrogen is produced from hydrocarbons or coal) that poisons the platinum anode in a fuel cell.

2.2. Water Electrolysis and Oxygen Evolution Reaction

Electrolysis of water is an efficient method of producing high-quality hydrogen that can serve as the energy carrier of the future [30]. However, the tremendous benefit of utilizing electrolytic hydrogen as a clean, abundant fuel can only be realized if the water-splitting process is coupled with renewable energy sources like wind, hydro, or solar. The water-splitting process depicted in Figure 2.2 involves the evolution of hydrogen as well as oxygen. Recently, liquid oxygen was utilized as the fuel oxidant of a Space X rocket ship, the first human-crewed commercial flight, to space. Therefore, electrolysis could have a pivotal role to play not only in the production of future energy carrier like hydrogen, but also in the generation of liquid oxygen to propel spaceships to Mars.

There are three main electrolysers for the large-scale production of hydrogen: solid oxide, alkaline and acidic (the latter also known as polymer-electrolyte membrane (PEM)) electrolyser cells. The solid oxide electrolysers operate at temperatures ca. 800°C and are consequently termed high-temperature electrolysis. PEM electrolysers which in recent times are increasingly being used for commercial applications typically operate below 100°C. However, the commercial alkaline electrolysers which typically operate between 80 to 90°C are most commonly used because they have a competitive advantage over the PEM cells as their electrodes are usually non-precious metals. Hence, the alkaline cells are cheaper and easier to fabricate, leading to relatively substantial cost savings [44].

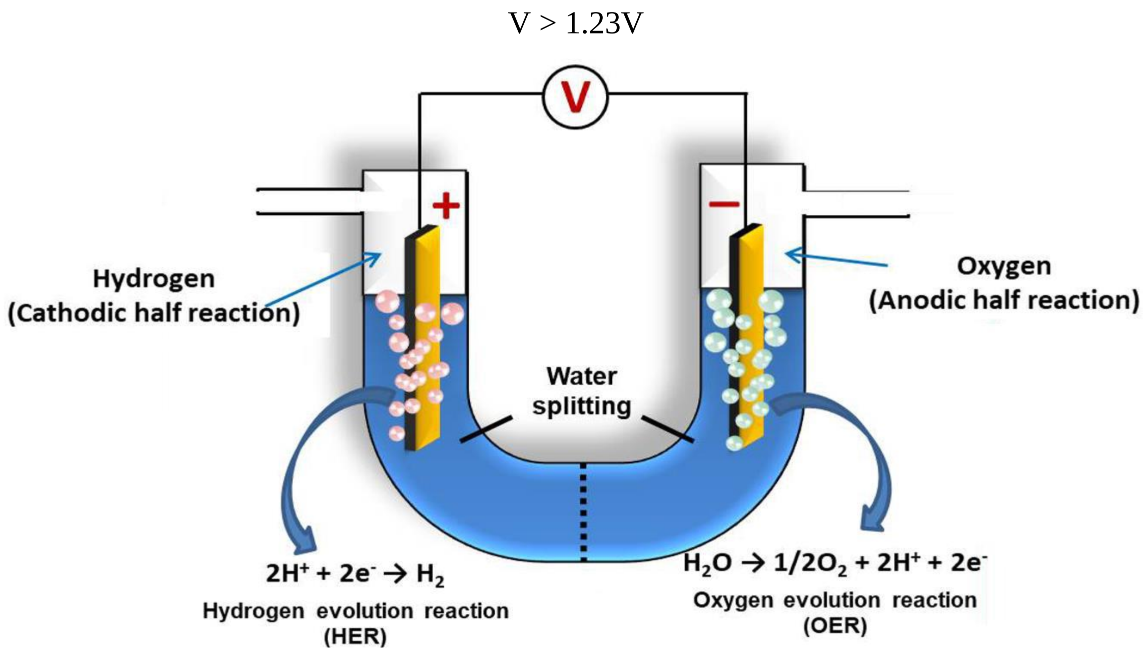

Figure 2.2: Electrochemical cell for splitting of water with electricity to generate hydrogen and oxygen [45].

The core of an electrolyser is an electrochemical cell that contains an aqueous electrolyte solution and two electrodes connected to an external power supply. At a specific potential difference, which should be, under standard conditions, larger than the water-splitting equilibrium potential (1.23 V vs. RHE), the electrodes begin to produce oxygen gas at the positively-biased electrode (anode) and hydrogen gas at the negatively-biased electrode (cathode). The volume of gases produced per unit time is directly related to the current that passes through the electrochemical cell, according to Faraday's law of electrolysis.

In alkaline electrolyte, the corresponding simplified partial electrode reactions are:

Anode:

$$4OH^-_{(aq)} \leftrightarrow 2H_2O_{(l)} + O_{2(g)} + 4e^- \tag{2.4a}$$

and

Cathode:

$$4H_2O_{(aq)} + 4e^- \leftrightarrow 2H_{2(g)} + 4OH^-_{(aq)} \tag{2.4b}$$

whereas, in an acidic environment, the reactions are:

Anode:

$$2H_2O_{(aq)} \leftrightarrow O_{2(g)} + 4H^+ + 4e^- \qquad (2.5a)$$

and

Cathode:

$$4H^+_{(aq)} + 4e^- \leftrightarrow 2H_{2(g)} \qquad (2.5b)$$

The overall reaction in both cases is then:

$$2H_2O_{(l)} \leftrightarrow O_{2(g)} + 2H_{2(g)} \qquad (2.6)$$

When current i (A), is supplied by a direct current power source and passed through the electrodes/electrolyte system (Figure 2.2), water is split into H_2 and O_2 once the cell potential is greater than the reversible water electrolysis potential (1.23V vs. RHE, at standard conditions). The consumption of electric power is proportional to $\Delta V \times i$, where ΔV (in volts) is the voltage (potential difference) applied to the cell, and i is the current flowing through the cell, as mentioned above. For a given i, it is necessary to minimize ΔV. Note that ΔV consists of several components [22]:

$$\Delta V = \Delta E + \Delta \eta + \Delta V_\Omega + \Delta V_t \qquad (2.7)$$

where ΔE is the thermodynamic (equilibrium) potential difference for the electrode reactions; $\Delta \eta$ is the sum of the overpotentials (activation overpotential at the two electrodes under kinetic limitations, and the concentration overpotential due to the mass transport of the gaseous products away from the anode and cathode surfaces) [8, 22]; ΔV_Ω the ohmic drop (iR) due to the inter-electrode gap of the connected electrodes; ΔV_t is the so-called ‘stability’, i.e. the drift of ΔV with time due to degradation of the electrode performance. For fresh electrodes $\Delta V_t = 0$ [22]. All the parameters in Eq. (2.7) are in volts.

The activation overpotential increases with rising current density and can be lowered by using precious metal electrodes of significant electrocatalytic action, such as platinum, ruthenium, and iridium. In practice, the iR drop may be ca. 0.25V [8]. Nevertheless, the effect of the iR drop can be negligible when a high concentration of electrolyte is used, or when a PEM-type cell is employed due to the high conductivity of the hydrogen ion in the acidic medium. Furthermore, it is best to keep overpotential $\Delta\eta$ as low as possible in order to maximize cell efficiency and to minimize the production of heat. On the other hand, if the overpotential (which is primarily dependent on the OER kinetics) is decreased, the electrode reactions slow down. Thus, there is a need for a trade-off. Nonetheless, one popular way in the literature to increase current without necessarily increasing the overpotential is to accentuate the area of contact between the electrodes and the electrolyte [8, 46].

This Ph.D. thesis focuses on the oxygen evolution reaction side of the water-splitting process. This is the more 'problematic' reaction in the electrolytic production of hydrogen. Anodes are typically beset by the significantly large OER overpotential and stability issues, especially in acidic (aggressive) PEM cells. Therefore, comprehending and enhancing the oxygen evolution reaction is an enormous research challenge in hydrogen energy science and technology.

The OER may appear to be a simple reaction, however, it does not proceed in one reaction step. The detailed OER reaction mechanism is, in fact, quite complex. This is because the OER mechanism is sensitive to the structure of electrode surface; different materials or one material with different facets can exhibit various reaction mechanisms [47, 48]. However, the generally accepted overall reaction pathways for the OER involves four discrete electron-transfer steps [48-51] involving the formation of OER intermediates M–OH, M–O, and M–OOH associated with the potential determining step (PDS). However, the alternative mechanistic pathway has been proposed as shown in Table 2.1 which is useful in describing the OER mechanism without altering the PDS [52, 53].

Table 2.1: Overall reaction mechanism for the OER in acidic and alkaline solutions. M represents one electrocatalytic active site on the electrode surface [52, 54].

Overall reaction (condition)	**Reaction pathway**	**Tafel slope (mV/dec)**
(Acidic solution) $2H_2O \rightarrow O_2 + 4H^+ + 4e^-$	$M + H_2O \rightarrow M–OH + H^+ + e^-$	120
	$M–OH \rightarrow M–O + H^+ + e^-$	40
	$2M–O \rightarrow 2M + O_2$	30
	$M + H_2O \rightarrow M\text{-}OH_{ads} + H^+ + e^-$	60
	$M\text{-}OH_{ads} \rightarrow M\text{-}OH$	60
(Alkaline solution) $4OH^- \rightarrow O_2 + 2H_2O + 4e^-$	$M + OH^- \rightarrow M–OH + e^-$	120
	$M–OH + OH^- \rightarrow M–O + H_2O + e^-$	40
	$M–O + OH^- \rightarrow M–OOH + e^-$	60
	$M–OOH + OH^- \rightarrow M–OO^- + H_2O$	30
	$M–OO^- \rightarrow M + O_2 + e^-$	15

This universally-accepted mechanisms [51, 52, 55], predicts the difference between the adsorption free energy states of two intermediates ($\Delta G^{O}_{M\text{-}O} - \Delta G^{O}_{M\text{-}OH}$) as a unique descriptor for the catalytic activity of several different metal oxide materials towards OER. The material surfaces that bind oxygen too weakly, give intermediates that cannot easily react, and the potential is limited by the oxidation of M–OH. Whereas for surfaces that bind oxygen too strongly, the potential is limited by the formation of M–OOH species and their intermediate states and the adsorbed products are quite stable [51]. The optimum case, is therefore, an intermediate binding strength, such as is found in transition metal oxides of RuO_2, Co_3O_4, NiO, PtO_2, $SrCoO_3$, $LaNiO_3$ just to name a few [56] as this gives a good balance between the reaction free energy steps of M–OH oxidation and M–OOH formation [51]. This will be further explained in the proceeding section.

Another factor that is expected to influence the OER mechanism is the density of state of the electron at the Fermi level and the degree of overlapping between the orbitals of the active site and the adsorbed species on the anode surfaces that determines the rate of electron transfer [57]. The active sites, which are typically the transition metal cations at anode surface, are expected to electrocatalytically decrease the activation energy of the rate-determining step in the oxygen evolution reaction [57].

The Tafel slope is equally an important empirical parameter that helps with the determination of the mechanistic pathway of the oxygen evolution reaction. Figure 2.3 shows a typical Tafel graph, in the oxygen evolution region, which is a semi-log plot of the anodic current density (mA/cm^2) versus the overpotential, η (volt).

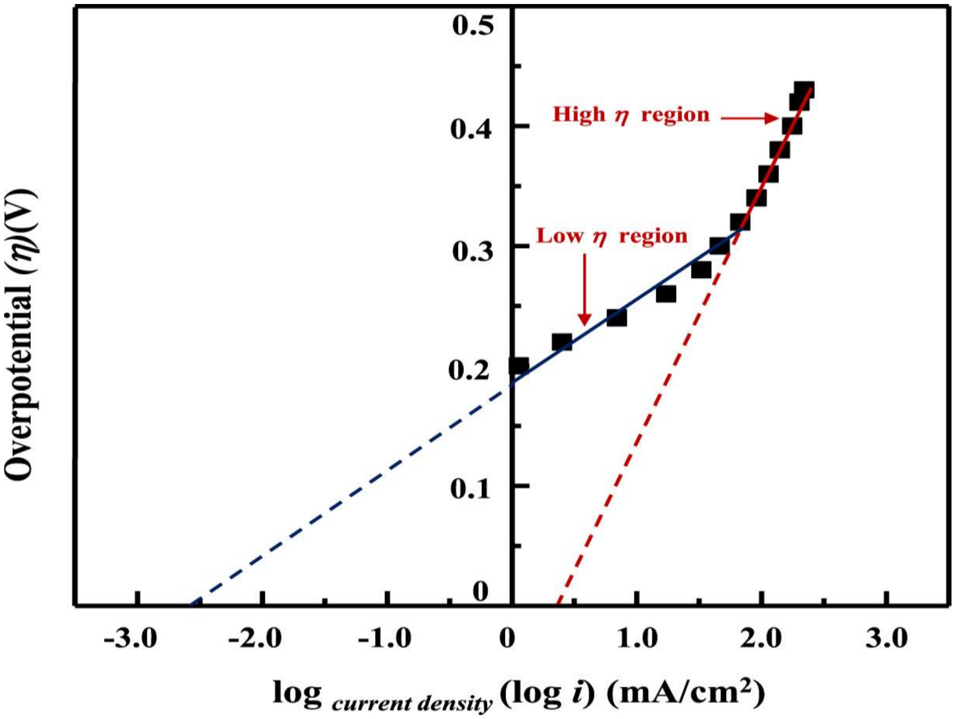

Figure 2.3: Tafel plot for the oxygen evolution reaction (OER) over the Pd-80 at% Ni electrode in 30 wt% KOH electrolyte at 298 K [58].

By analyzing the above presented Tafel plot around the low-overpotential linear region, the Tafel slope *b* (mV/dec) can be directly obtained as the slope of the curve in Figure 2.3. The linear section of the graph is described by Eq.(2.8):

$$b = \frac{2.303\mathrm{RT}}{\alpha \mathrm{nF}} \tag{2.8}$$

where R is the molar gas constant (8.314 J/mol/K)., T is the temperature (K), F is the Faraday constant (96,486.3 C/mol), *n* is the number of electrons participating in the oxygen evolution rate determining step, and α which can easily be evaluated from Eq.(2.8), represents the electron transfer coefficient that is related to the energy input required to lower the activation barrier for the anodic reaction[59]. Typically, larger values of α, which range from 0 to 1, are more desirable. Conversely, a smaller b value indicates that a small increase in overpotential leads to a larger increase in current density. Therefore, the best electrocatalysts should have a low Tafel slope and high exchange current density (intercept on the current density axis, extrapolated from the linear Tafel region to overpotential of zero). In addition, as stated above, the observed Tafel slope is descriptive of which step in Table 2.1 is rate determining [52, 54]. Hence, b can be useful in identifying the possible OER rate determining step.

2.3. Electrocatalysis of the Oxygen Evolution Reaction

Electrocatalysis is simply a catalytic process at the electrode surface. Therefore, an electrocatalyst speeds up the rate of an electrochemical reaction without undergoing self-degradation. These effects can be primary or secondary [60]. The interactions of reactants, products and/or intermediates with the electrode surface are referred to as the primary effects. In the primary effects, bonds are made and broken with a direct effect on the activation energy of the rate-determining step [22]. On the other hand, secondary effects are related only to the diverse structure of electrical double layer. Electrocatalytic studies are aimed at identifying the primary variable which influences electrochemical reaction rate. Fundamentally, overpotential $\Delta\eta$ is the term which most directly measures electrocatalysis [22]. Consequently, the reduction in $\Delta\eta$ implies improvement in electrocatalytic activity for a given material.

Two key factors determine the electrocatalytic activity of an electrode material: electronic/surface-energy (intrinsic) and geometric (extrinsic) factors. The intrinsic characteristics, which depend on the microstructure and chemical composition of the material, influence the surface-intermediate bond strength and electron-transfer rate, while the extrinsic quality relates specifically to the apparent surface area of the material and is not directly relate to its electrocatalytic properties since it does no influence on the activation energy of the reaction [22]. In as much as it is pertinent to study the intrinsic quality of catalyst materials for better catalyst design, it should be noted that for practical applications, the catalysts' extrinsic property is paramount as this influences the effective overall performance of the material.

The oxygen evolution reaction is generally catalyzed by highly active but expensive noble metals like iridium and ruthenium, to counter the slow-kinetics associated with OER due to large anodic overpotential. However, the comparatively high-cost and shortage of these precious materials precludes their availability for commercial usage in wide-spread hydrogen energy production. As a result, many research works on the development of novel low-cost electrocatalysts of high catalytic activity and long-term stability are ongoing, to facilitate the actualization of commercially-available clean hydrogen energy.

2.3.1. Metal Oxide Electrocatalysts and the Volcano plot

Recently, OER electrocatalysts of transition metal oxides have been studied in comparison to their pure metal counterparts because the oxides of these metals are considered to be more stable [17, 61-65]. Also, in an attempt to improve both stability and activity of anode materials, novel nanomaterial alloys, based on low precious metal oxide content and high inexpensive transition metal oxides, have been explored as alternatives to precious (noble) electrocatalysts for OER [66-68]. The choice of metal oxides to select and synergistically combine, is made easier by considering the so-called *Volcano plot.* This plot (Figure 2.4) correlates the intrinsic surface adsorption properties and electronic structure of an electrocatalyst with its catalytic activity. The correlation successfully explains the observed trend in the catalytic activity for different surfaces and provides a guide for the development of catalysts with substantial catalytic activity [48, 51, 56].

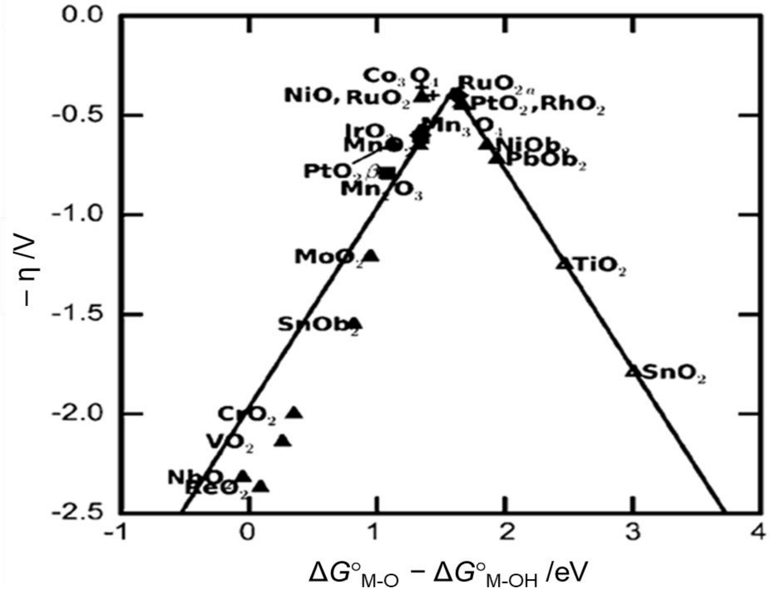

Figure 2.4: Activity Volcano plot for selected metal oxides towards OER [51]

Since the OER overpotential is a key parameter in determining the activity of anodic oxygen evolving catalyst, Man *et al* [51] calculated the theoretical overpotential of a wide range of oxide surfaces by applying standard density functional theory in combination with the computational standard hydrogen electrode model. The resulting theoretical overpotential values showed good agreement with empirical data from the literature. Thus, having elucidated the origin of the OER overpotential, the authors were able to introduce the difference in adsorption free energy of M–O and M–OH ($\Delta G^{\circ}_{M\text{-}O} - \Delta G^{\circ}_{M\text{-}OH}$) as a unique descriptor for the oxygen evolution activity that gave rise to the activity volcano plot (Figure 2.4). The curve suggests a fundamental limitation on the maximum oxygen evolution activity of planar oxide catalysts. Consequently, oxide surfaces with intermediate binding energies are most desirable in comparison to those at the two extreme ($\Delta G^{\circ}_{M\text{-}O} - \Delta G^{\circ}_{M\text{-}OH}$) values since they correspond to the lowest overpotential.

2.3.2. Requirements for OER Electrocatalysts

A high-quality electrocatalyst material must primarily possess high electrocatalytic activity and electrochemical stability. Also, it should have a large specific surface area (m^2/m^3 or m^2/g) as this increases the number of active sites. Particularly, this yields beneficial cost-savings especially when noble metal-based catalysts are employed. Furthermore, high electrical conductivity is also required to minimize the ohmic drop (iR) in the material [69].

In addition to the aforementioned requirements is the catalyst current selectivity. The latter is vital to the development of advanced OER electrocatalyst materials. For example, certain catalysts might oxidize water via 2 e^- transfer rather than 4 e^- transfer, leading to the production of peroxide species instead of oxygen. Subsequently, the catalyst current selectivity can be determined by differentiating and measuring the anodic current that contributes to oxygen evolution. Fortunately, certain known techniques such as the rotating ring-disk electrode [56] and *in situ* mass spectroscopy [70] can be used to monitor the different contributions.

Furthermore, wettability of electrodes is another prevalent factor that can influence the catalytic performance of an electrocatalyst. When oxygen is formed at the electrodes during electrolysis, the gas bubbles remain attached to the electrode surfaces until they have grown to some size. However, these bubbles can detach more easily if the surfaces are more hydrophilic because the electrolyte can flow easily over the surface and replace evolving gas bubbles, thereby freeing the catalyst surface area and improving the catalyst utilization [56, 71].

Also, the raw materials involved in the development of the electrocatalyst should be environmentally safe. In addition to this, the materials have to be readily available and inexpensive enough for an economical large-scale production [69]. Nevertheless, corrosion stability is a mandatory requirement for OER catalysts. During water-splitting operation, the anodic side experiences severe oxidative conditions. For example, in PEM units, the anode is exposed to an acidic environment. Therefore, the electrode material should be able to withstand the corrosive environment associated with the PEM units.

2.4. Development of Active OER Anodes

The oxygen evolution reaction is the foremost and most important reaction in the water electrolysis process as it is the prerequisite for hydrogen generation *via* water splitting. However, it poses a major obstacle to the development of sustainable large-scale hydrogen production technology due to the large anodic overpotentials of known anode materials deployed, thereby resulting in the slow-kinetics of the OER. As a result, a number of metals and alloys have been tested as electrocatalysts to optimize the kinetics of the OER [48, 52]. This sub-section gives a brief description on the work that has been done in the development of active oxygen evolving electrocatalyst as it relates to the advancement of the electrolytic production of hydrogen towards the actualization of the hydrogen economy.

2.4.1. Pure Metal Electrocatalysts

A quality OER electrocatalyst must possess characteristics such as low overpotential, large active specific surface area, physical and electrochemical stability, low cost, ease of use, and good electrical conductivity. Therefore, from the onset, researchers sought to develop materials that are capable of meeting these properties. The initial studies on the development of active oxygen-evolving catalysts in the water electrolysis process were done majorly on pure metal electrodes in acidic solution. Iridium and ruthenium were found to be the best oxygen-evolving electrocatalysts [72, 73] as most of the other metals underwent anodic corrosion (dissolution) [73].

However, for these active metal OER electrocatalysts, their metal oxide properties were observed to be the dominant factor affecting their electrocatalytic activities [73]. This is due to the oxide layer that forms on the surface of the pure metal in the potential region where oxygen is evolved. Subsequently, the oxide layer on the metal typically affects the reaction mechanism and ultimately the OER electrocatalysis. As a result, researchers tend to favor the use of metal oxides in their studies rather than pure metal electrodes.

2.4.2. Metal Oxides (MO)

Generally, metal oxides are used as OER anodes in comparison to their pure metal counterparts because they are believed to be more stable (most naturally occurring metals are present in ores as oxides, in their most thermodynamically-stable state). Among the many metal oxides investigated, transition metal oxides have shown to be excellent OER active electrocatalysts with good electrochemical stability in acidic and basic conditions. Recently published studies have shown that these transition metal oxide materials have been utilized in a number of other electrochemistry-based applications, besides water electrolysis, such as: material corrosion protection, electrodes for organic synthesis and wastewater treatment (which will be presented in the later section) [74-77].

Also, MO have been studied for their electrocatalytic activity for the hydrogen evolution and oxygen reduction reactions. However, not much literature has been published on the study of OER on metal oxide surfaces [11, 17, 23, 78-80]. The main reason for the insufficient literature on MO as anode materials for OER is attributed to MO semiconducting nature which makes them less attractive [81]. However, metal oxides can behave as good conductors depending on the potential window of investigation.

Notwithstanding the foregoing, an electrode system of metal oxide surface typically provides improved electrocatalytic activities, long-term service life, and optimum operating voltages for specific applications [82], thereby improving the surface and electrochemical properties of the system. Moreover, certain anode metal oxides like IrO_2 have shown to be stable across all pH, therefore making them potentially promising materials for the oxygen evolution reaction. In the literature, a number of metal oxides have been reported as suitable anodes for OER such as IrO_2 [83], RuO_2 [84], PtOx [85], Co_3O_4 [86], NiO [87], FeOx [88], MnOx [89], just to name a few. However, in most cases, the costly noble metal oxides are used because of their superior electrocatalytic OER activity.

2.4.3. Transition Metal Oxide Anodes

The precious metal oxides of ruthenium oxide and iridium oxide are considered as the benchmark for the OER electrocatalysts because they exhibit high activity in a wide range of pH values. Subsequently, IrO_2 and RuO_2 based nanomaterials with high surface area-to-mass ratio have been researched a lot [66, 90-92]. However, not only does their high cost and scarcity limit their usage for commercial applications in electrochemical energy devices, but these state-of-the-art anode materials are also beset with corrosion stability issues. For example, RuO_2 has significant high initial electrocatalytic OER activity in acidic environment but it deteriorates after a short while, thereby making it not suitable for PEM electrolysers [93]. On the other hand, IrO_2 is less active and stable in an alkaline medium.

In an attempt to address the challenges posed due to their high cost and scarcity, non-noble earth abundant metal oxides are actively studied as a possible cost-efficient replacement solution. Non-precious transition metal oxides that contain Mn, Fe, Co, Ni, Zn or the mixed oxides of these have been reported as suitable alternative electrocatalyst materials for water electrolysis [94]. Moreover, these low-cost earth-abundant transition metal oxides whose OER activities are not optimum also suffer fouling and have long-term stability issues.

2.4.4. Mixed Metal Oxides (MMO)

To improve the electrocatalytic performance and stability of metal oxide anodes, researchers have tried to investigate the effect of mixed (multi-) metal oxide films towards the oxygen evolution reaction. Through this approach, earth-abundant catalysts like MnO_2 that are generally not stable enough in acidic environment were stabilized by doping their near-surface oxide layers with Ti [95], for example. In another case, it was reported that fluorine-doped Cu-Mn mixed oxide constituted a stable OER electrocatalyst under harsh acidic condition. The improved stability was attributed to the introduction of the fluorine anions with a high oxidation potential that stabilized the OER catalyst [96]. In another study using Ni-Fe binary oxide, remarkable improvement in electrocatalytic performance coupled with outstanding stability was noted [97, 98] partly due to iron incorporation into the Ni-oxide. Further, a ternary mixed oxide of $Sn_{0.5}Ru_{0.25}Ir_{0.25}O_2$ characterized under an accelerated stress test showed significantly improved electrochemical stability (although with slightly decreased initial activity relative to the reference IrO_2). The improved stability was associated with the formation of a thermodynamically metastable phase of rutile Sn-Ir-Ru-oxide structure resulting from the incorporation of Sn into the binary Ir-Ru oxide mix [93].

2.5. Ni-Co-based Mixed Metal Oxides (MMO)

Although ruthenium, iridium, and platinum oxide catalysts have shown high activities for the OER (see Figure 2.4), their scarcity, high cost, and instability in acidic environments, in the case of ruthenium and platinum, limit these noble metal oxide anodes usage in commercial applications for hydrogen generation. PtO_2 is sensitive to poisoning due to the deposition of trace-metals from the electrolyte onto the PtO_2 surface at open circuit [99, 100]. Although, it has been demonstrated that poisoning by foreign ions is negligible on IrO_2 [101] and RuO_2 surfaces [102], iridium oxide is not highly active in the alkaline medium [103] while ruthenium oxide exhibits stability issues in acids [100]. In order to overcome these highlighted significant barriers without sacrificing catalytic performance, numerous research efforts are dedicated to reducing their consumption or replacing them with other materials [104].

Several studies have been done to investigate materials with lower overpotential for the oxygen evolution reactions [20, 22, 24, 25, 99, 105-110]. Particularly, Ni, Fe, or Co alloys are all good candidates for lowering the overpotential of the OER [109]. Nickel is a very attractive metal for hydrogen production by water electrolysis as it is relatively electrocatalytically active, cheap, and largely abundant [111]. In Figure 2.4, NiO can be found up the Volcano curve, and it is competitive with the best catalysts (the expensive noble metals). For this reason, Ni is an acceptable and interesting alternative anode material [112] together with its transition metal alloys such as Co. Although NiO is stable in the alkaline environment, this material cannot be used in the PEM electrolysers due to its poor stability at low pH [113]. On the other hand, Co-oxide is a stable electrode in the acidic environment with a relatively good OER electrocatalytic performance.

Hence, the objective is to increase the electrocatalytic activity and stability of Ni in the OER by alloying Ni with other metal oxides, including Co. This is expected to modify the electronic structure of the material, thus, significantly improving the OER performance [106, 114]. For example, the incorporation of cobalt oxide has shown to boost mass current density of RuO_2 [115]. More recently, Halck *et al.* [116] demonstrated that the incorporation of Co or Ni into

RuO_2 structure significantly improved the OER activity of the material by activating the proton donor-acceptor functionality on the inactive surface sites of a conventional RuO_2.

Cheng *et al.* [117] showed that the formation of NiO nanosheets array on carbon cloth (NiO NA/CC) exhibited an OER overpotential of 422 mV to drive a current density of 10 mA/cm^2. This result was ascribed to the high synergistic effect between Ni and neighboring heteroatoms leading to better surface adsorption properties and subsequently to the observed enhancement in the electrocatalytic properties of the material [45]. Similarly, Ng *et al.* [82] examined the combined effects of cerium dopant and gold substrate on the OER activity of electrodeposited NiO_x film. They found that the as-synthesized $NiCeO_x$–Au catalyst demonstrated high OER activity in alkaline solution. In another study, Koza et al. [86] electrodeposited Co_3O_4 film on a gold substrate and tested it in 1M KOH: the catalyst exhibited an overpotential of 400 mV at a current density of 10 mA/cm^2. Nickolov et al. [118] also found that the OER activity on a binary oxide, $Li_xCo_{3-x}O_4$, increased significantly relative to pure Co_3O_4.

Therefore, the fundamental basis of this thesis is to conduct a systematic study to establish the possible OER synergistic compositional relationship between Ni and Co in the mixed-metal oxide using predominantly a harsh acidic environment as the test medium. The best composition would serve as a basis to develop active cost-effective alternative replacement to expensive state-of-the-art pure IrO_2.

2.6. Electrochemical Wastewater Treatment Anodes

The utilization of metal oxides as electrochemical anodes in the treatment of organic contaminants in wastewater treatment systems have become popular in recent years [119-123]. This is accentuated by the high operational costs associated with conventional treatment methods applied in sewage plants such as biological, physical and chemical processes, as well as the possibility of forming toxic sludge that requires further treatment *via* the latter method [119, 124]. Moreover, the conventional methods are typically ineffective for the removal of recalcitrant organic pollutants due to the high biochemical stability, relatively high molecular weight, and the presence of aromatic rings in organic pollutants [119]. Hence, there is a drive to develop efficient treatment technologies for the effective removal of these contaminants and their potentially hazardous transformation products [125].

Thus, electrochemical oxidation has gained relevance as a potential alternative to conventional methods due to its environmental compatibility, ease of installation and use, its modularity, small foot-print, and effectiveness for breaking down high molecular weight pollutants such as dye effluents [119-121]. It has also been demonstrated that the electrochemical oxidation technology can provide clean water for both domestic and industrial consumptions [120]. Although this technology was reported as far back as the nineteenth century, it was not until recently that it gained practical application [120, 126].

Electrochemical oxidation of wastewater is an environmentally-friendly process that consists of two different mechanistic actions. Namely, the direct oxidation of contaminants on the surface of the electrocatalyst, and the indirect oxidation of the pollutants in the electrolyte by reactive species such as hydroxyl radical (OH•), atomic oxygen (O), hydrogen peroxide (H_2O_2), and ozone (O_3) [119, 120, 127] generated during the water oxidation process. If the electrolyte contains chloride ions, the reactive species could also be hypochlorous acid (HClO), hypochlorite ion (ClO^-), and evolved-chlorine gas. Thus, wastewater electrochemical oxidation is considered a heterogeneous advanced oxidation process (hAOP) because when the electrocatalyst anode surface (solid phase) is polarized, it generates radicals that act as powerful oxidizing agents that subsequently degrade the pollutants present in the electrolyte (aqueous phase), and transform them to less and even non-toxic products [127].

2.6.1 Direct Oxidation

The direct oxidation of wastewater contaminants by electrocatalysts consists of two key steps, namely, the diffusion of pollutants from the bulk solution to the anode surface and the subsequent oxidation of the pollutants at the anode surface. Hence, the overall efficiency of the electrochemical oxidation is dependent on the relationship between mass transport of the contaminant and electron transfer at the electrocatalyst surface, which is a function of the electrode activity [121]. The anodic oxidation of the organic pollutants could either be partial oxidation to less toxic transformation products that could require further treatment, or the complete mineralization of the organic materials into inorganic compounds such as water and carbon dioxide [121]. In a very simplified way, the process can schematically be presented as:

$$R + A \leftrightarrow A\text{-}R_{ads} \tag{2.9}$$

$$A\text{-}R_{ads} \rightarrow A + R' \text{ (or } H_2O + CO_2\text{)} + xe^{-} \tag{2.10}$$

where R is the pollutant molecule, A is the anode surface, and R’ is the oxidized pollutant molecule.

2.6.2 Indirect Oxidation

In general, the indirect electrochemical oxidation entails the electrogeneration of a powerful oxidizing agent(s) at the surface of the anode that subsequently degrades the organic contaminants in the bulk electrolyte solution. In a very simplified way, the process can schematically be presented as:

$$A + H_2O \rightarrow (A\text{-}OH\cdot) + H^{+} + e^{-} \tag{2.11}$$

$$R + (A\text{-}OH\cdot) \rightarrow A + R' \text{ (or } H_2O + CO_2\text{)} \tag{2.12}$$

where the first step involves the anodic formation of hydroxyl radicals (OH·), which then oxidize the pollutant molecule, R, in the second step.

Some of the typically generated oxidants are hydroxyl radicals, hydrogen peroxide, ozone, and sometimes peroxodisulfuric acid ($H_2S_2O_8$) [121]. Also, the employment of metal catalytic mediators (such as Fe^{2+}, Co^{3+}) as in Fenton-like oxidation reaction in acidic solutions to generate hydroxyl radicals that are capable of detoxifying several organic pollutants constitutes another form of indirect oxidation of wastewater. However, the use of metal ions can lead to the production of sludge that may be more toxic than the original effluent resulting in further costly treatment [121, 124]. Instead of these problematic catalytic mediators, it is much more convenient to utilize active chlorine species as oxidants. In any case, chloride ions are practically present in a number of wastewater systems originating from daily nutritional salt consumption habits. The dissolved chloride ions can be easily oxidized to gaseous chlorine, hypochlorous acid or hypochlorite ions, which then oxidize the pollutant molecules [121, 124].

2.7. Selection of Efficient Wastewater Treatment MMO Anode

The high overall efficiency of electrochemical oxidation of contaminants in a wastewater setup using metal oxide anodes has been ascribed to the synergistic effect of the combined direct and indirect oxidation of the organic pollutants on the electrode surface [120]. Consequently, the selection of the appropriate anode material is of high importance for the electrocatalytic oxidation process as it affects not just the overall efficiency of the process, but equally its selectivity [120-122]. It is reported in the literature that the oxidation of organics and the oxygen evolution are competitive reactions during water electrolysis on the surface of the anode [121, 128, 129]. As a result, materials with low OER overpotentials are typically of high electroactivity towards the oxygen evolution reaction, and thus they are not suitable as wastewater treatment anodes. In contrast, high OER overpotential anodes are better suited for the oxidation of organics because they exhibit minimal selective oxygen evolution reaction [129]. Previous research works have studied the suitability of high OER overpotential anodes such as boron-doped diamond (BDD) [123], TiO_2 [130], PbO_2 [131], SnO_2 [132], SnO_2-Sb_2O_3/PbO_2 [74] as effective electrochemical anode materials for treatment of organic pollutants in wastewater systems.

In this Ph.D. research work, the mixed metal oxide anode that showed the highest OER overpotential during the MMO screening process (i.e. the poorest OER electrocatalytic activity) was tested as a potential anode in the electrochemical oxidation of wastewater. Methylene blue, a common wastewater contaminant, was employed in the wastewater treatment process.

Chapter 3 - The influence of Ni_xCo_{1-x}-oxide composition on its electrocatalytic activity in the oxygen evolution reaction

Emmanuel Onyekachi Nwanebu* and Sasha Omanovic

Department of Chemical Engineering, McGill University, 3610 University St., Montreal,
Quebec, H3A 0C5, Canada

*corresponding author: emmanuel.nwanebu@mail.mcgill.ca

3.1. Preface

As already stated, one of the aims of this PhD project was to investigate the possibility of using mixed bimetal NiCo-oxides as potential OER electrocatalysts in an acidic environment. The main goal of this part of the research project was to investigate the influence of Ni/Co ratio in the oxide on the resulting OER electrocatalytic performance. To do this, various Ni_xCo_{1-x}-oxide anodes were produced and then characterized in terms of their physicochemical, surface and structural properties. The work has been published as a peer-reviewed manuscript, and the corresponding reference is: E. O. Nwanebu and S. Omanovic, "The influence of Ni_xCo_{1-x}-oxide composition on its electrocatalytic activity in the oxygen evolution reaction," *Materials Chemistry and Physics,* vol. 228, pp. 80-88, 2019.

Highlights

- Ni_xCo_{1-x}-oxides are good potential candidates for anodes in acidic water electrolysers.
- $Ni_{0.4}Co_{0.6}$-oxide exhibits the highest extrinsic and intrinsic electrocatalytic activity in acid.
- The variation in electroactivity was related to the anode intrinsic, rather than extrinsic properties.
- Ni_xCo_{1-x}-oxides are potential economic substitute for Ir-oxide.

Abstract

The influence of Ni_xCo_{1-x}-oxide composition ($0 \leq x \leq 1$) on the material's electrocatalytic activity in the oxygen evolution reaction (OER) was studied in the acidic medium. The electroactive oxide was formed by thermal decomposition of corresponding metal salt solutions on a titanium substrate. The surface of Ni_xCo_{1-x}-oxide coatings was found to be composed of crystalline NiO, Co_3O_4 and CoO, and the surface morphology/roughness was found to be composition-dependant. The electrocatalytic activity of the oxides in the OER was determined to be highly dependent on their relative metal ratio in the oxide, with $Ni_{0.4}Co_{0.6}$-oxide offering the highest intrinsic activity and good stability. Although still inferior to state-of-the-art IrO_2, $Ni_{0.4}Co_{0.6}$-oxide was deemed as a potentially good replacement anode material in the acidic medium due to its significantly lower cost.

Keywords

Hydrogen; Oxygen evolution; Water electrolysis; Metal oxides; NiCo-oxide

3.2. Introduction

One of the major global challenges is to secure sufficient energy that is environmentally clean since traditional energy sources like fossil fuels are not only diminishing constantly but also continue to constitute an environmental hazard. Hydrogen production as an alternative source of energy storage has been touted as the solution to meeting clean energy need. Hydrogen is recyclable and practically unlimited in supply, and it is considered as a future clean energy carrier in the transition from the existing hydrocarbon economy [2, 4, 5]. Indeed, the commercialization of hydrogen "fuel" technology is already being exploited by, for example, auto-industry giants like Toyota, Honda and Hyundai in the manufacture of hydrogen fuel-cell consumer cars. Nevertheless, about 95 % of currently-produced hydrogen is obtained from the environmentally-unfriendly and unsustainable hydrogen reforming process, and the rest is produced mainly by water electrolysis – by splitting water directly into hydrogen and oxygen gas by means of electricity.

Water electrolysis is considered to be the cleanest way to produce hydrogen when the required electricity is derived from renewable energy sources [8]. Unfortunately, this method is presently not cost-effective in comparison to methods used to produce hydrogen from fossil fuels. This is largely due to energy efficiency losses in the water-splitting process for hydrogen production [133]. In practice, the efficiency of water electrolysis is largely limited by the slow kinetics of the oxygen evolution reaction (OER), requiring large anodic overpotential [10, 133]. In addition, the durability of water electrolyser anodes is lower than that of cathodes. Hence, further research to address these drawbacks is required [11].

A good electro-catalyst for the OER should have characteristics such as low overpotential, large active specific surface area, physical and electrochemical stability (including the corrosion stability), selectivity, low cost, ease of use, and good electrical conductivity [12]. Among the most electrocatalytically-active OER anode materials are expensive noble metal oxides like Ru- and Ir-oxides, which are considered state-of-the-art OER electrocatalysts. The latter is currently used as an anode material in a polymer-electrolyte-membrane (PEM) water electrolysers [134]. Nevertheless, these precious oxides are very expensive. Hence, there is a need to develop relatively cheap and stable anode materials with high activity towards OER. Some transition metals have been identified as good candidates that could meet these needs [135-137].

Nickel, an inexpensive non-noble transition metal, together with its transition metal alloys (including Fe, Co, Mn) have shown high intrinsic electrocatalytic activity towards OER because of a modified *d*-shell electronic configuration [17, 20, 107, 138]. However, these materials lack long-term stability, especially when used in the PEM water electrolyser. On the other hand, their metal oxides have gained reputation as stable electrodes in certain applications [21, 22] with desirable performance. For example, photochemically prepared amorphous NiCoFe-oxides displayed excellent OER performance in an alkaline medium. In another case, low-cost Co-based spinel and perovskite structures such as Co_3O_4 and $(Ln_{0.5}Ba_{0.5})CoO_{3-\delta}$ (Ln = Pr, Sm, Gd and Ho) have shown to be alternative, stable, efficient OER electrocatalysts [69, 139]. Likewise, Mn-oxide modified surfaces [23, 26] have demonstrated satisfactory OER activity in both acidic and basic media. In the literature, there have also been claims of certain metal-oxide anodes that were quite stable across the entire pH scale [41, 69, 140]. Moreover, reduced and Ag-doped Co_3O_4 nano-based materials have shown enhanced OER activity and good stability in basic [141] and acidic media [142].

This work reports results on the investigation of the applicability of low-cost mixed metal oxides (MMO) of nickel and cobalt, produced by thermal decomposition on a titanium substrate, as OER anodes in the acidic environment. The aim of the work was not to produce a long-term stable anode, but rather to *investigate the influence of relative oxide composition on the resulting OER electrocatalytic activity*, *i.e.* to do initial screening of Ni_xCo_{1-x}-oxide compositions as possible candidates for water electrolyser anode materials, and set the ground for further research and possible development of these electrodes. Although there are a few recent works on Ni/Co-based OER electrocatalyst [75, 142], to the best of the authors' knowledge, no systematic work on the influence of Ni/Co ratio in a metal oxide on the resulting electrocatalytic activity for the OER in an acidic medium has been reported in the literature.

3.3. Experimental Procedure[1]

3.3.1. Electrode preparation

Ni_xCo_{1-x}-oxide (x = 0, 0.2, 0.25, 0.3, 0.4, 0.43, 0.5, 0.6, 0.7, 0.75, 0.8, 1) and Ir-oxide coatings were formed on titanium coin-shaped substrates (Grade 2, 99% pure, McMaster Carr) employing a thermal decomposition method. Stock 0.5 M solutions of nickel, cobalt and iridium salts were prepared by dissolving $NiCl_2 \cdot 6H_2O$ (ReagentPlus, 100%, Sigma Aldrich), $Co(NO_3)_2 \cdot 6H_2O$ (Pure, 99%, ACROS Organics), and $IrCl_3 \cdot 3H_2O$ (53 to 56% (Ir), ACROS Organics) in a 50vol.% isopropanol (Fisher) and 50vol.% water mixture. All solutions were prepared using deionized water (resistivity: 18.2 MΩ cm). For each coating composition, the precursor solution was prepared by mixing the appropriate amounts of the corresponding stock solutions.

The titanium substrates were coins of 1.21 cm in diameter and 0.2 cm in thickness. These coins were pretreated before the deposition of coatings: they were wet-polished using 600-grit SiC sandpaper, then rinsed thoroughly and sonicated for 30 min in deionized water to remove polishing residues, after which they were etched in boiling solution of hydrochloric acid (33wt.%, Fisher) and deionized water (1:1, v/v) for 30 min. Finally, the substrates were thoroughly rinsed with deionized water and dried with argon gas.

The metal precursor solutions were applied evenly on the pretreated sides of titanium substrates by brushing. The prepared samples were first placed in an oven at 383 K for 5 min in order to vaporize the solvent and then annealed at 773 K in a furnace for 15 min. These samples were then removed from the furnace and allowed to cool in air for 10 minutes before the subsequent coating layers were applied. The coating application procedure was repeated another

---

[1] All the measurements were done in multiplets and the presented data are the average values plus the corresponding errors.

five times to form a six-layered coating on the titanium substrates. Lastly, the samples were annealed in the furnace at 773 K under air for one hour to complete the formation of Ni_xCo_{1-x}-oxides [143].

3.3.2. Coating Characterization

All electrochemical measurements were done in a three-electrode / two-compartment cell employing a computer-controlled combination potentiostat/galvanostat/frequency response analyzer (Autolab PGSTAT30, Metrohm, NL) using NOVA software package (v. 2.1; Metrohm, NL). Ni_xCo_{1-x}-oxide samples were used as a working electrode. These samples were mounted in a special holder which exposed a total geometric surface area of 0.43 cm^2 of the coated side to the electrolyte. Graphite electrode (cathode) was used as a counter electrode and it was separated from the working electrode compartment by a glass frit (Ace Glass, Inc., USA), which precluded hydrogen evolved at the cathode from coming in contact with the anode and interfering with the oxygen evolution reaction. All potentials were measured versus the Ag/AgCl (Fisher Scientific, product no. 1362053, sat.KCl) reference electrode.

The electrochemical surface area (EASA) of as-synthesized electrode coatings was determined by cyclic voltammetry (CV) measurements recorded in 1 mM hexaammineruthenium(III) chloride (98%, Sigma Aldrich) in 0.1 M KNO_3 (≥99%, Sigma Aldrich) as a redox probe[2]. This solution was deoxygenated by purging with argon (99.998wt% pure, MEGS Specialty Gases Inc., Canada) for 40 min before the start of experiments. At the end of the purging process, the deoxygenated solution was left unperturbed during the CV measurement in order to ensure that the redox species were transported by diffusion only. A detailed description of this EASA determination procedure can be found in the literature [144-146].

Investigation of the electrocatalytic activity of the produced anodes was done in 0.5 M H_2SO_4 (made from 95wt% H_2SO_4, Fisher Scientific) at 296 ± 2 K. This solution was purged by argon before (for 40 min) and throughout the electrochemical measurements. The electrocatalytic activity of the oxides was investigated by linear polarization measurements recorded in a potential window between 0.7 V to 1.5 V at 1 mV/s scan rate.

---

[2] See the detailed description for the EASA determination procedure in appendix 3.6

The surface roughness of coating samples was studied employing the DektakXT surface profiler from Bruker, using a diamond tip of equivalent stylus force of 6 mg. The surface roughness (Ra) data was extracted by Bruker's Vision64 software. Furthermore, the surface morphologies and surface chemical compositions of the coatings were studied by scanning electron microscopy (SEM) and energy-dispersive X-ray spectroscopy (EDX), respectively, using a Hitachi SU3500 scanning electron microscope. The crystalline structure of the oxides was analyzed by X-ray diffraction (XRD) performed using a Bruker Discover D8-2D diffractometer with a 0.5 mm dia. collimated Cu Kα (1.54 A) radiation at room temperature in a standard q–2θ mode. X-ray photoelectron spectroscopy (XPS) measurements were performed using a ThermoScientific K-Alpha spectrometer equipped with an Ar ion gun. The X-ray non-monochromatic source was Al Kα (1486.6 eV photon energy, 400 µm spot size). The XPS spectra were recorded to reveal the chemical compositions of the as-synthesized metal oxides. These spectra were analysed using ThermoScientific Avantage 5.932 software.

The energy band-gaps of coating compositions were measured by photoluminescence spectroscopy utilizing a 266-nm excitation laser and a UV/Vis spectrometry (ThermoScientific Evolution 300) using green light to generate diffused reflectance.

3.4. Results and Discussion

3.4.1. Scanning electron microscopy (SEM)

The SEM images depicting the surface microstructures of the as-synthesized Ni_xCo_{1-x}-oxide and reference Ir-oxide (control) coatings are shown in Figure 3.1. The surface morphology of the samples resembles features similar to those of thermally-formed metal-oxide coatings [77]. The control Ir-oxide coating (Figure 3.1(A)) appears to be the most compact coating at the scale presented, while the Ni-oxide coating (Figure 3.1(B)) displays a dual morphology characterized by larger agglomerates and smaller <1 μm size particles. However, with the addition of Co to the Ni-oxide coating (Figs. 1(C-H), the morphology of the coating changes significantly, adopting a sponge-like structure and yielding micro-pores, which remained present even on the pure Co-oxide (Figure 3.1(I)). However, the latter coating is also characterized by micron-sized particles buried deeper into the coating pores. Figures 3.2(A and B) show the distribution of Ni and Co on $Ni_{0.4}Co_{0.6}$-oxide surface, evidencing that both metals are uniformly distributed on the surface, rendering the surface uniform from the chemical point of view. Figures 3.2(C and D) show that the morphology of this surface did not change significantly after 7h of electrolysis at 10 mA/cm^2 (and the inset to Figure 3.5 evidences high stability of this electrode surface).

EDX analysis was performed to determine the actual metal surface composition of coatings, and the results are presented in Table 3.1.

Table 3.1: Relative percentage atomic composition of Ni in Ni_xCo_{1-x}-oxide coatings. Nominal values refer to the Ni content in the metal precursor solution while EDX values represent the measured surface composition of Ni in the coatings.

Nominal Compositions of Ni (%)	**Actual composition**
	EDX
80	80.3 ± 0.3
70	69.6 ± 0.2
60	60.8 ± 0.8
50	52.1 ± 0.5
43	43.1 ± 0.3
40	39.5 ± 0.4
30	30.0 ± 0.4
20	18.2 ± 0.4

The data show a very good agreement between the true average metal surface composition of coatings and the nominal composition. Further in the text, the nominal composition values will be used to denote the coatings.

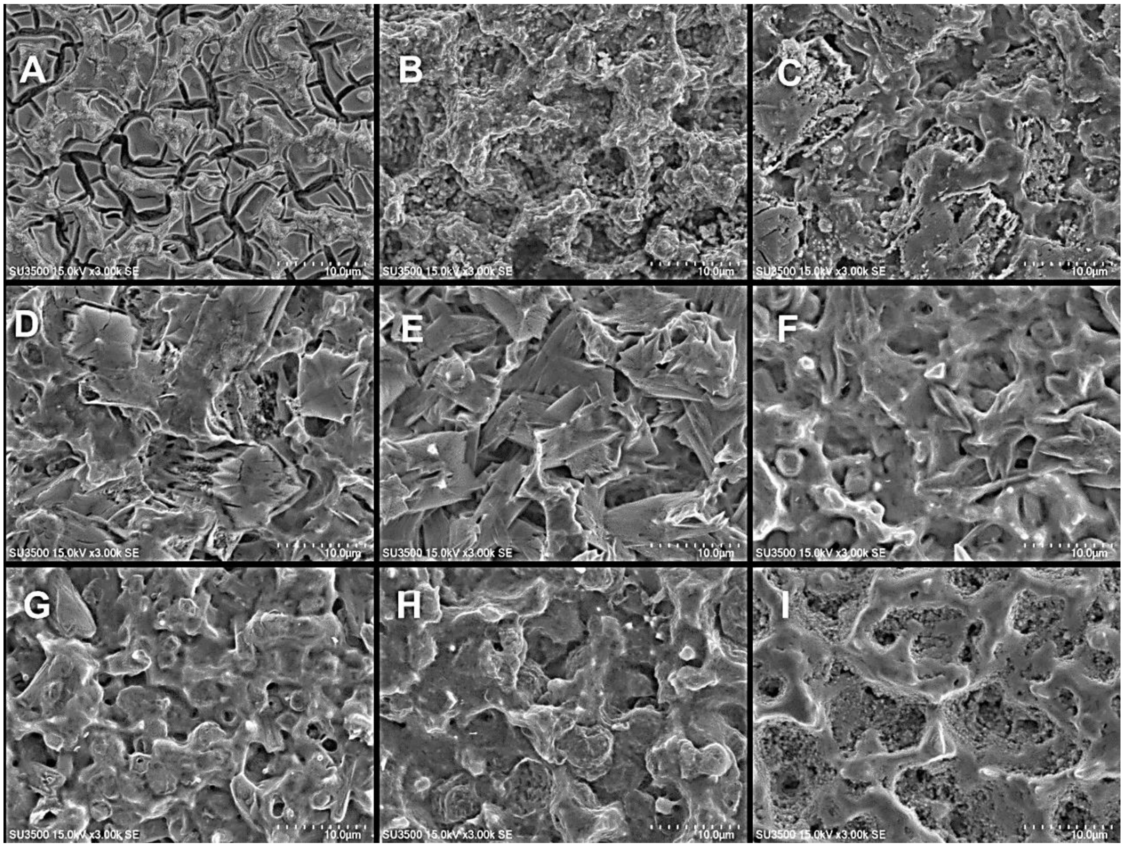

Figure 3.1: SEM images showing surface morphology of: (A) Ir-oxide; (B) Ni-oxide; (C) $Ni_{0.8}Co_{0.2}$-oxide; (D) $Ni_{0.7}Co_{0.3}$-oxide; (E) $Ni_{0.6}Co_{0.4}$-oxide; (F) $Ni_{0.4}Co_{0.6}$-oxide; (G) $Ni_{0.3}Co_{0.7}$-oxide; (H) $Ni_{0.2}Co_{0.8}$-oxide; (I) Co-oxide coating.

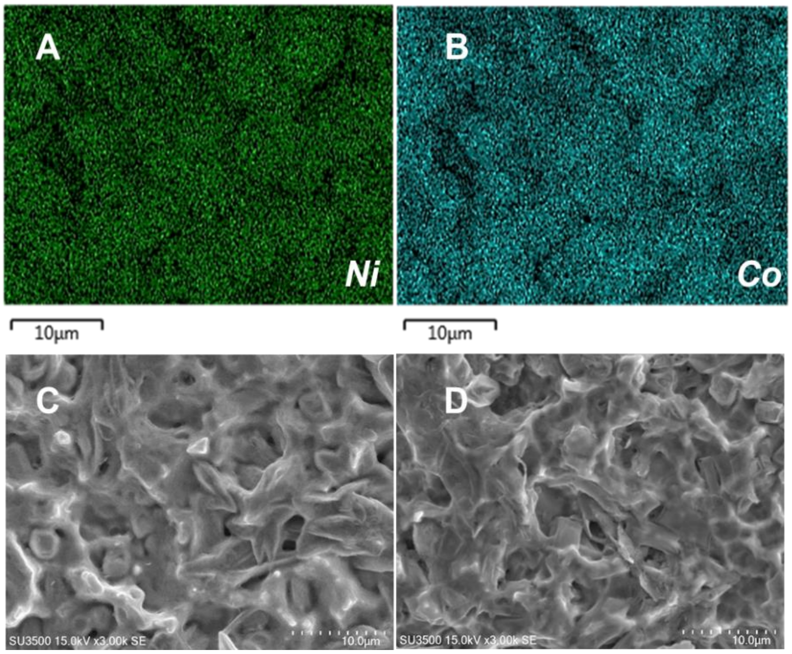

Figure 3.2: Distribution of (A) Ni and (B) Co on the $Ni_{0.4}Co_{0.6}$-oxide surface and its morphology (C) before and (D) after 7 h of electrolysis at 10 mA/cm^2.

3.4.2. X-ray diffraction

The X-ray diffraction measurements reveal the successful formation of desired metal oxide samples and their relatively high degree of crystallinity (Figure 3.3). Common to all of the metal-oxide samples are the distinct diffraction peaks at 34.9°, 39.9°, 62.8°, 76.1° and 77.2°, attributed to metallic titanium (JCPDS, 44-1294) [77, 147] originating from the Ti substrate. This is a consequence of the coating preparation procedure whereby some Ti from the substrate dissolved into the surface-applied precursor solution layer during the first coating layer application and the annealing process. Due to the high oxygen affinity of Ti, which is greater than that of Ni and Co, it diffused towards the outer coating surface, where it was detected by XRD and EDX [148]. However, the top-most oxide surface layer did not contain Ti, as evidenced by the XPS results discussed in the next section. Diffraction peaks at 27.2° and 44.3° indicate rutile TiO_2 of corresponding (110) & (210) planes while peaks at 62.75° and 70.5° indexed to the (118) & (220) reflection of anatase TiO_2 (JCPDS no.: 88-1175 and 84-1286) [149] are seen. Further analysis of the XRD spectra showed that Ni_xCo_{1-x}-oxide samples with Ni content above 60% and 40% displayed peaks at 37.1° and 43.4°, respectively, indexed to (111) and (200) planes of rock salt structure NiO (JCPDS no. 78-0643) [150, 151]. The diffraction pattern of Ni_xCo_{1-x}-oxide samples with the Co content above 50% exhibited characteristic peaks of spinel Co_3O_4 at 18.9°, 31.2°, 36.7°, 44.5°, and 65.3° (JCPDS no. 42-1467) [152] and rock salt CoO at 36.5° and 58.9° (JCPDF 75-0533) [153]. Interestingly, the lattice fringes of the as-synthesized Ni_xCo_{1-x}-oxides (for $0 \leq x \leq 0.4$) can be assigned to $NiCo_2O_4$ spinel (JCPDF 73-1702) [154] which is similar to the Co_3O_4. This is reasonable as more of the trivalent Co^{3+} is available compared to the divalent Co^{2+} at the annealing temperature (773 K) [155]. However, for $0.5 \geq x < 1$ the fringes displayed a rock salt structure since the metal oxide coating was predominantly NiO because less of the trivalent Co^{3+} is available during the oxidative annealing process. Only pure Ni-oxide coating reveals the presence of metallic Ni at 51.8° (JCPDS no. 4-0835) [144, 156]. At 28.7° for the pure Ir-oxide sample, there is a peak indexed to the (110) reflection of rutile IrO_2 (JCPDS no. 15-870) [91].

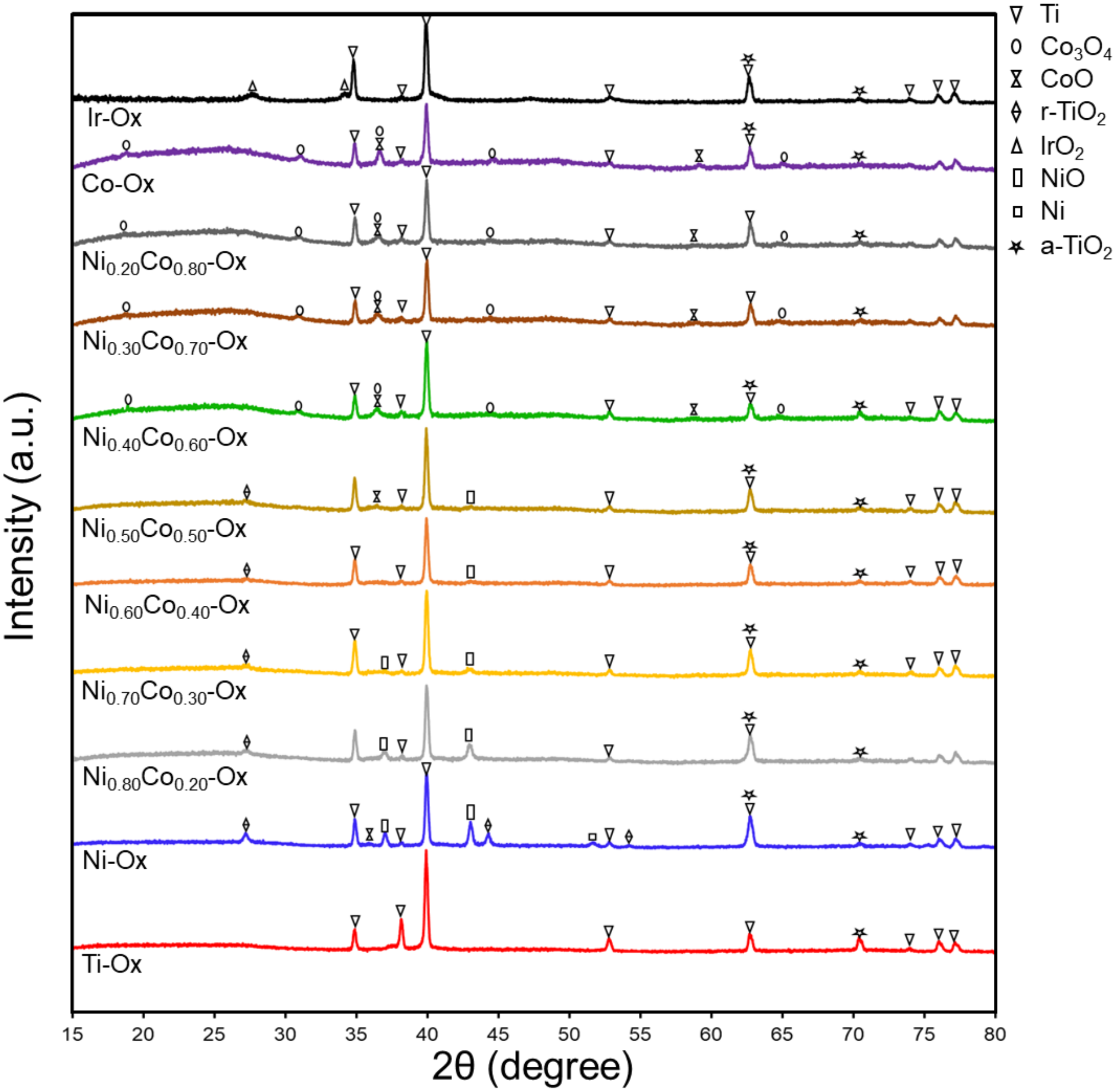

Figure 3.3: X-ray diffraction (XRD) patterns of Ni_xCo_{1-x}-oxide coatings deposited on Ti substrate. Result for reference Ir-oxide sample is presented for comparison.

3.4.3. X-ray photoelectron spectroscopy (XPS)

To further determine the chemical surface composition of the as-synthesized metal oxides, XPS analysis was performed on $Ni_{0.8}Co_{0.2}$-oxide and $Ni_{0.4}Co_{0.6}$-oxide (one of the least and the most OER active binary oxide composition, respectively – see Figure 3.6). The surface of each sample was examined at three different locations to ensure the reliability of results. A general survey[3] scan was first made, followed by recording high-resolution binding energy spectra for C 1s, O 1s, Ni 2p, Ti 2p and Co 2p regions. The binding energy spectra of samples were referenced to the C 1s peak of adventitious carbon at 284.8 eV [157, 158]. As expected, no spectrum was recorded for Ti[4] as the XPS rays penetrate only up to 10 nm below the surface, unlike in EDX and XRD where Ti was detected (the depth of penetration in EDX and XRD is significantly larger). Figure 3.4(A) reveals a typical doublet of Ni 2p peaks [159]. On the $Ni_{0.8}Co_{0.2}$-oxide surface, the Ni $2p_{3/2}$ doublet photoelectron peaks are visible at 853.8 and 855.4 eV and a satellite peak at 861.0 eV. Ni $2p_{1/2}$ doublet photoelectron peaks at 871.3 and 873.1 eV and a satellite peak at 879.1 eV are also visible on the spectrum. On the $Ni_{0.4}Co_{0.6}$-oxide surface, Ni $2p_{3/2}$ doublet peaks at 853.7 and 855.3 eV and a satellite peak at 861.0 eV are shown, together with Ni $2p_{1/2}$ doublet peaks at 871.2 and 872.9 eV and a satellite peak at 879.3 eV. This confirms the formation of NiO on the $Ni_{0.4}Co_{0.6}$-oxide and $Ni_{0.8}Co_{0.2}$-oxide surfaces [159-161], which cannot be seen from XRD results due to the poorer detection limit of XRD relative to XPS.

The XPS spectra for $Ni_{0.8}Co_{0.2}$-oxide in the Co 2p region (Figure 3.4(B)) show binding energies of Co $2p_{3/2}$ and Co $2p_{1/2}$ at 779.7 and 794.9 eV respectively, corresponding to the spectra of Co 2p electrons in rock salt Co^{2+}, while binding energy values of Co $2p_{3/2}$ and $2p_{1/2}$ at 781.2 and 796.5 eV for the Co^{3+} spinel are also visible [162, 163]. Apart from the main peaks, there were observable satellite peaks at 785.5 and 803.6 eV for Co^{2+} and a lone satellite peak at 789.1 eV for Co^{3+} [161, 164]. Similar peaks were also recorded for $Ni_{0.4}Co_{0.6}$-oxide, Figure 3.4(B). Consequently, the XPS spectra of cobalt revealed that the ratio of CoO to Co_3O_4 in the outermost layer of $Ni_{0.8}Co_{0.2}$-oxide is 1:2 while the ratio is 7:13 in $Ni_{0.4}Co_{0.6}$-oxide which is close to the former. Therefore, the observed trend in activity (see Figure 3.6) with varying Ni_xCo_{1-x}-oxide composition is not due to the variation of CoO:Co_3O_4 ratio in each composition. Furthermore, both Co oxides are known to have similar OER performance in acid [165]. The XRD spectra in Figure 3.3 did not reveal appreciable Co-oxides peaks in the $Ni_{0.8}Co_{0.2}$-oxide. This is due to the poorer sensitivity of XRD relative to XPS. The spectra in Figure 3.4(B) evidence that Co_3O_4 is the predominant cobalt oxide on the topmost surface of the two thermally-formed binary oxide coatings [155].

---

[3] The survey scan is shown in figure 3.9(A) in Appendix 3.6.

[4] See Figure 3.9 (B) in Appendix 3.6.

Figure 3.4(C) shows that by etching (depth-profiling) the surface of $Ni_{0.4}Co_{0.6}$-oxide (best-performing OER electrocatalyst), the $CoO:Co_3O_4$ ratio increased up to a maximum (3:2), and CoO became the predominant chemical state of Co beneath the outermost oxide surface layer [45]. This could possibly be explained by the lack of oxygen below the coating surface during the annealing process, thus hindering the oxidation of cobalt to the higher oxidation state. The Ni depth profile (inset to Figure 3.4(C)) remained relatively constant, demonstrating only a slight relative increase, while the Co profile depicts the $CoO:Co_3O_4$ ratio change.

In Figure 3.4(D), the O 1s spectra for $Ni_{0.4}Co_{0.6}$-oxide is presented (the other surface had a similar result). The high-resolution binding energy spectra can be deconvoluted into two components. The deconvoluted peak at 529.6 ± 0.2 eV represents oxygen in a crystal lattice (O^{2-}), while the peak at 530.8 ± 0.3 eV represents oxygen in hydroxyl group (OH) [161]. Therefore, Figure 3.4(D) shows that oxygen is prevalent at the top-most surface of the metal oxide coatings predominantly as oxygen in crystal lattice. Hence, the coating compounds are metal oxides and metal hydroxides existing in a ratio of 4:1.

XPS analysis of $Ni_{0.8}Co_{0.2}$-oxide and $Ni_{0.4}Co_{0.6}$-oxide samples also confirmed that the top-most surface compositions of the two coatings, $Ni_{0.74}Co_{0.26}$-oxide and $Ni_{0.34}Co_{0.66}$-oxide respectively, are very similar to their nominal compositions, which is corroborated by the EDX results (Table 3.1). The slight discrepancy between the XPS and EDX data is a common occurrence due to the difference in beam-penetration depth and has been reported in literature [77].

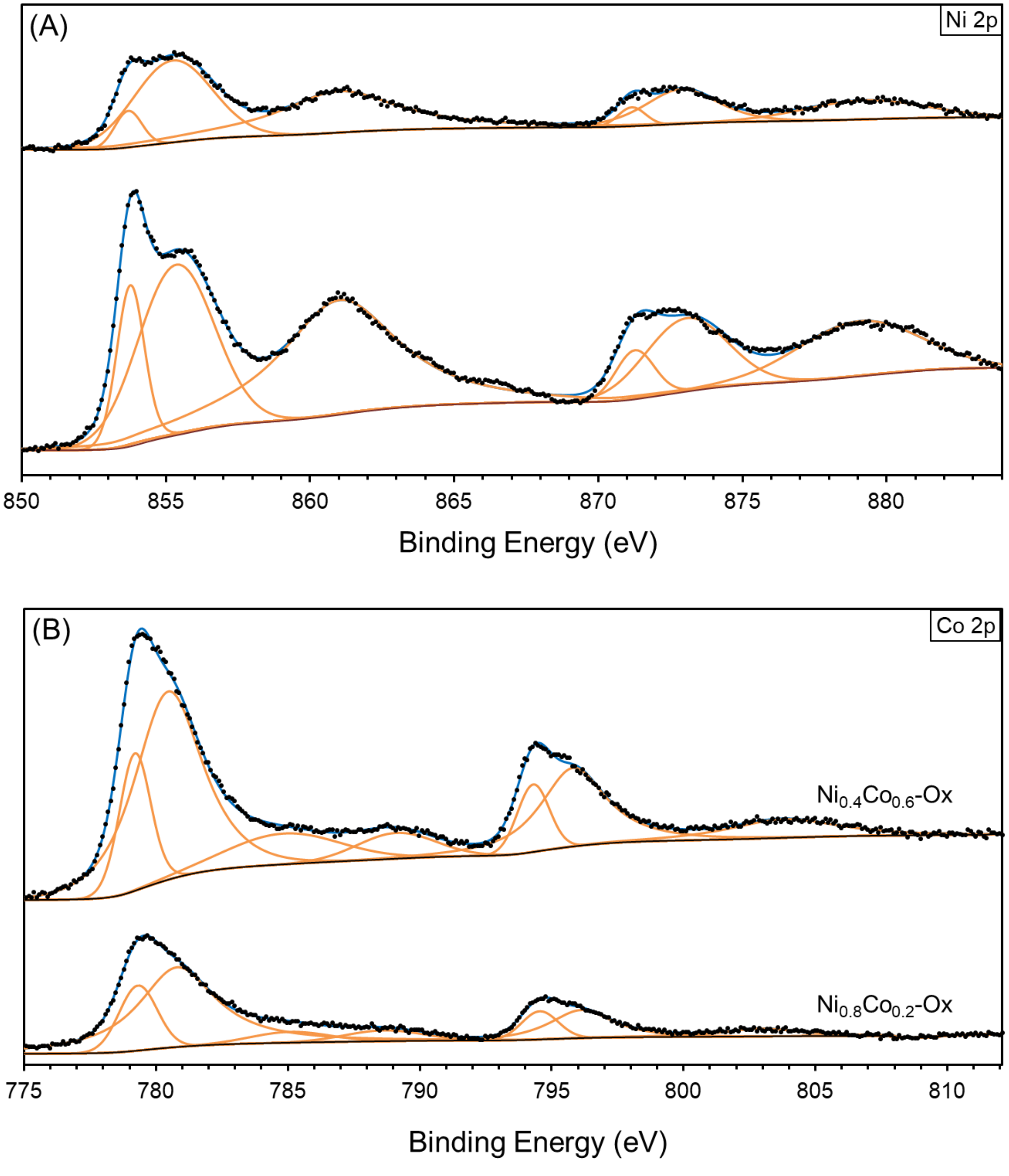
(A)
Ni 2p
850
855
860
865
870
875
880
Binding Energy (eV)
(B)
Co 2p
$Ni_{0.4}Co_{0.6}$-Ox
$Ni_{0.8}Co_{0.2}$-Ox
775
780
785
790
795
800
805
810
Binding Energy (eV)

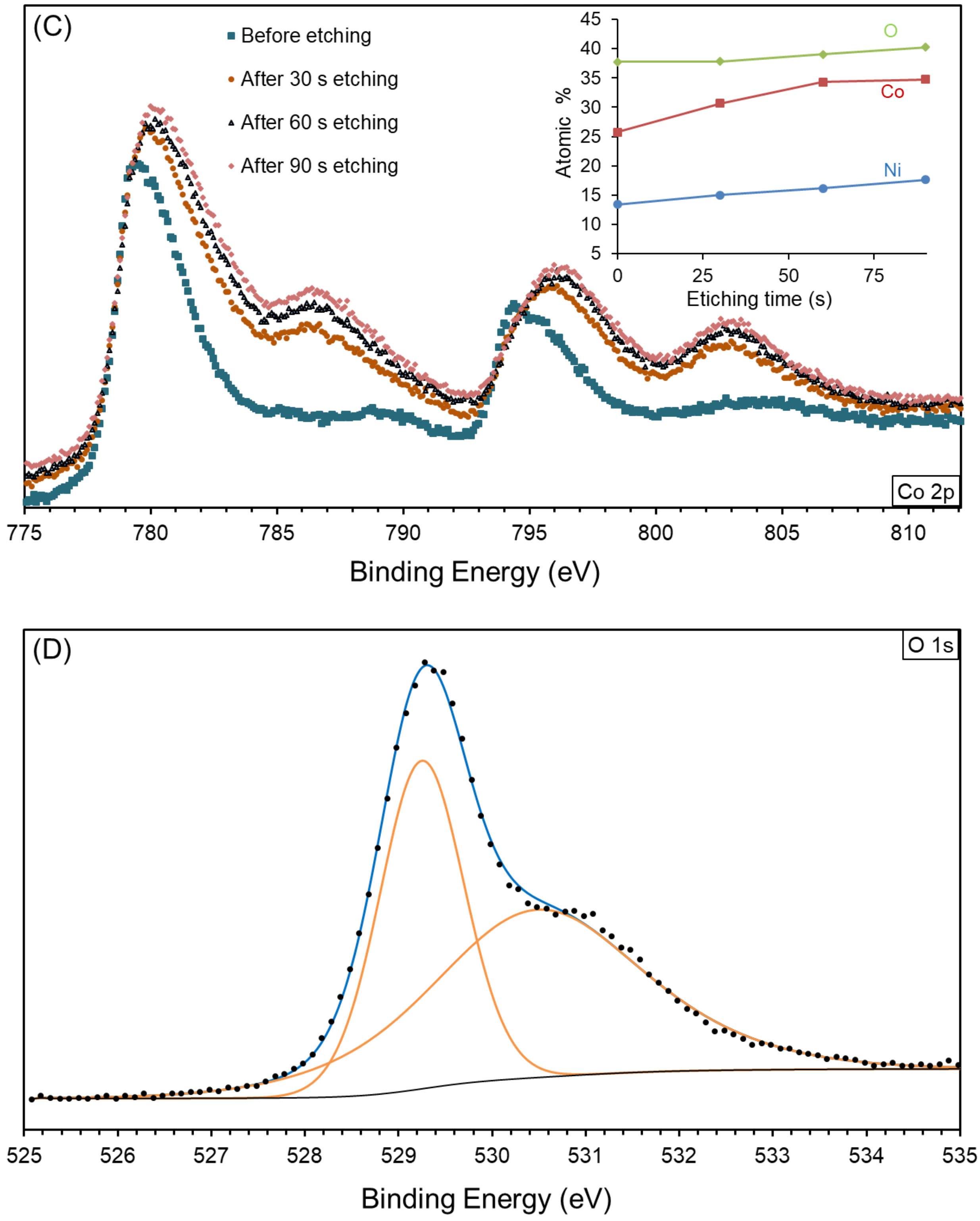

Figure 3.4: XPS spectra of Ni_xCo_{1-x}-oxide samples of (A) Ni 2p and (B) Co 2p, and of (C) Co 2p in $Ni_{0.4}Co_{0.6}$-oxide recorded at different depths after etching. The inset in (C) shows the corresponding atomic % profile for Ni, Co and O. (D) represents the O 1s XPS spectrum.

3.4.4. Surface roughness and area determination

As seen in Figure 3.1, the surfaces of the mixed metal oxide coatings are porous and rough to a certain extent, indicating that the surface roughness factor is greater than one. However, for electrochemical applications, it is crucial to determine the "electrochemically-active surface area" (EASA), rather than the total surface area. In this work, the EASA was determined by cyclic voltammetry employing the well-established hexaammineruthenium III/II chloride reversible redox reaction [144, 145], and the results are presented in Table 3.2. Although the SEM images in Figure 3.1 show that the coatings are rough, the EASA values obtained are rather low (smaller than the geometric area of the electrodes), indicating that only part of the total surface is electrochemically active (or electronically conductive). Nevertheless, the determination of EASA in this work is important for the comparison of intrinsic electrocatalytic activity of the coatings, which will be discussed further in the text.

In addition to determining EASA values, surface proliferometry was done and the corresponding surface roughness (Ra) values are presented in Table 3.2. Excluding the Ni-oxide coating, the trend in the Ra and EASA values is very similar validating both sets of measurements (the Ra/EASA ratio is 1.6 ± 0.1, yielding only a 6.5% relative deviation from the average). The deviation of Ni-oxide from the trend (much smaller EASA) might be due to poor electrochemical activity [166] and low stability [113] of pure nickel oxide in acid.

Table 3.2: The data show a very good agreement between the true average metal surface composition of coatings and the nominal composition. Further in the text, the nominal composition values will be used to denote the coatings.

Nominal composition (mol%)	**Electrochemically-active surface area (cm^2)**	**Surface Roughness, Ra (µm)**
Ir-Ox	0.373 ± 0.005	0.56 ± 0.02
Ni-Ox	0.131 ± 0.003	0.43 ± 0.01
$Ni_{0.70}Co_{0.30}$-Ox	0.218 ± 0.001	0.39 ± 0.04
$Ni_{0.60}Co_{0.40}$-Ox	0.272 ± 0.008	0.44 ± 0.02
$Ni_{0.50}Co_{0.50}$-Ox	0.280 ± 0.014	0.45 ± 0.02
$Ni_{0.40}Co_{0.60}$-Ox	0.313 ± 0.005	0.47 ± 0.01
$Ni_{0.30}Co_{0.70}$-Ox	0.351 ± 0.003	0.53 ± 0.04

3.4.5. Electrocatalytic activity in OER

To study the electrocatalytic activity of the as-synthesized Ni_xCo_{1-x}-oxide coatings in the oxygen evolution reaction (OER), slow-scan linear polarization (Tafel) measurements were performed on the binary oxides and on Ir-oxide anode as the control sample (this electrode is the state-of-the-art OER material in PEM-type water electrolysers). The Ir-oxide surface showed comparable activity to those reported in the literature [78, 91, 167, 168]. The insert in Figure 3.5 shows that the variation of potential during electrolysis at 10 mA/cm^2 on the surface of $Ni_{0.4}Co_{0.6}$-oxide anode is indicative of good stability of the anode; the potential remained constant during the measurement at 1.624 ± 0.009 V vs. Ag/AgCl. This corresponds to OER overpotential of 559 ± 9 mV. Charles et al. [169] investigated OER activity in 1M H_2SO_4 on a range of mono- and binary-metal oxides, among which $NiCoO_x$ (the actual composition was not specified) offered OER overpotential, at the beginning of electrolysis, close to what we measured for our electrode; however, after two hours of electrolysis, the overpotential increased to above 900 mV. Similarly, in the work of Abidat et al. [170], the $NiCo_2O_{4-\delta}$ electrode tested in 0.1 M KOH offered OER overpotential of 422 mV, but at a lower current density (1 mA/cm^2); assuming the behaviour of the electrode is characterized by a constant Tafel slope calculated from the plot (78.8 mV/dec), extrapolation to 10 mA/cm^2 gives overpotential of ca. 500 mV, which is close to the value in the inset to Figure 3.5.

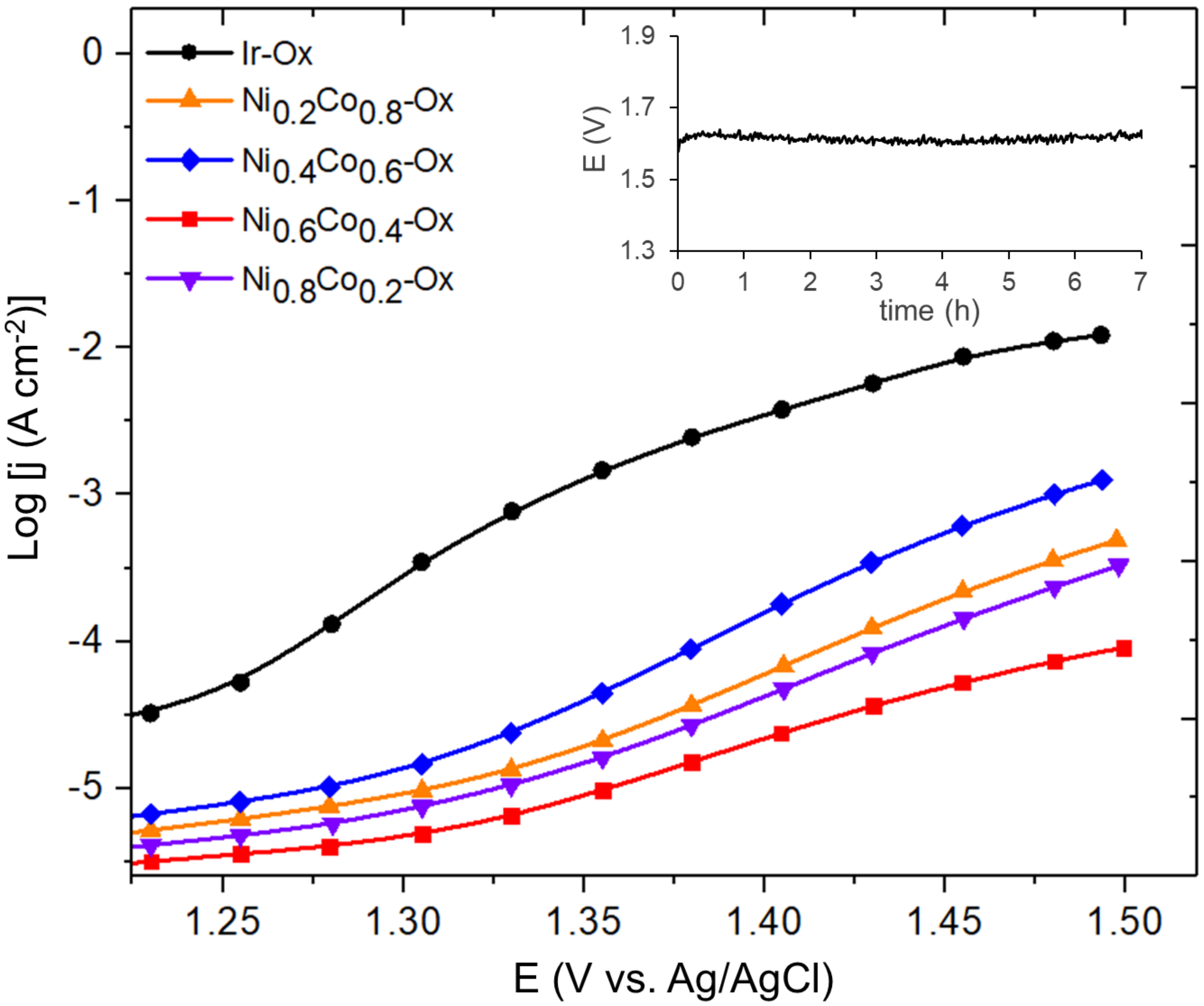

Figure 3.5: Tafel polarization curves recorded on selected Ni_xCo_{1-x}-oxide and Ir-oxide coatings in 0.5 M H_2SO_4. Sweep rate: 1 mV/s. The inset shows a variation in potential during 7 h of electrolysis at 10 mA/cm^2 on $Ni_{0.4}Co_{0.6}$-oxide catalyst.

From the curves in Figure 3.5 (and the associate replicates), a set of OER kinetic parameters were determined and presented in Table 3.3 [52, 59].

Table 3.3: Tafel slope and electron-transfer-coefficient values for the OER obtained from the Tafel curves in Figure 3.5.

Sample	***b_a*** **(mV/dec)**	***α*_a**
IrOx	59.8 ± 1.2	0.982 ± 0.020
$Ni_{0.8}Co_{0.2}Ox$	109.0 ± 0.2	0.539 ± 0.001
$Ni_{0.7}Co_{0.3}Ox$	181.8 ± 6.6	0.323 ± 0.012
$Ni_{0.6}Co_{0.4}Ox$	124.7 ± 0.1	0.471 ± 0.001
$Ni_{0.55}Co_{0.45}Ox$	85.4 ± 1.4	0.688 ± 0.011
$Ni_{0.5}Co_{0.5}Ox$	90.6 ± 0.5	0.649 ± 0.004
$Ni_{0.4}Co_{0.6}Ox$	81.0 ± 0.4	0.725 ± 0.003
$Ni_{0.3}Co_{0.7}Ox$	75.1 ± 0.7	0.783 ± 0.008
$Ni_{0.2}Co_{0.8}Ox$	97.9 ± 4.5	0.601 ± 0.028
CoOx	204.3 ± 0.9	0.288 ± 0.001

The OER is a complex reaction and various possible mechanistic pathways have been proposed [52, 56, 90, 171-176]. In an acidic medium, the steps listed below are proposed [90, 176]. The reaction is initiated by the adsorption of hydroxyl species on the catalyst surface, M:

$$\mathrm{M + H_2O \rightarrow M\text{-}OH_{ads} + H^+ + }e^- \tag{3.1}$$

which is characterized by a Tafel slope of 120 mV / dec. The second step can go through two possible paths; the “electrochemical oxide path”:

$$\mathrm{M\text{-}OH_{ads} \rightarrow M\text{-}O_{ads} + H^+ + }e^- \tag{3.2}$$

or the “oxide path”

$$\mathrm{2M\text{-}OH_{ads} \rightarrow M\text{-}O_{ads} + M + H_2O} \tag{3.3}$$

characterized by a Tafel slope of 40 mV / dec (for Step (3.3), the value can slightly differ).

The last step involves the formation of O_2:

$$\mathrm{2M\text{-}O_{ads} \rightarrow O_2 + 2M} \tag{3.4}$$

yielding a Tafel slope value of 30 mV / dec.

The data in Table 3.3 show that the values of b_a range from ca. 60 to 204 mV/dec for different compositions of the oxides. For pure Ir-oxide (control), a value of ca. 60 mV / dec was obtained, which is similar to the values reported in the literature [167, 176]. Slightly higher values are obtained on the binary NiCo-oxide surfaces with Ni content ranging from 30 to 55%; for these compositions, the deviation of the Tafel slope from 60 mV/dec might be due to the occurrence of parallel surface process (*i.e.* oxidation of metal constituents to a higher oxidative state). It has been shown in literature that a Tafel slope of 60 mV/dec is obtained when a slow step in the OER is the formation of M-OH$_{ads}$ according to the following path [176]:

$$M + H_2O \rightarrow M\text{-}OH^*_{ads} + H^+ + e^- \qquad (3.5)$$

$$M\text{-}OH^*_{ads} \rightarrow M\text{-}OH_{ads} \qquad (3.6)$$

where the two adsorbed species have the same chemical structure but their energy states are different due to the difference in bond strength with the catalyst [176]. Hence, the results in Table 3.3 indicate that path (3.5 – 3.6) in the OER is *rds* on pure Ir-oxide and on NiCo-oxides with Ni content ranging from 30 to 55%. On the other hand, for NiCo-oxide surfaces containing 20, 60 and 80% of Ni, the Tafel slope values are closer to the value that indicates that path (3.1) is *rds*. The high Tafel slope values on $Ni_{0.7}Co_{0.3}$-oxide and pure Co-oxide are indicative of additional contributions arising from surface processes. Contrary to Tafel slope values, a larger value of the electron transfer coefficient, α_a, is desirable since this value is related to the amount of energy input, *i.e.* overpotential needed to lower the activation barrier for the anodic reaction [59, 177]. This value normally ranges from 0 to 1. Table 3.3 shows that $Ni_{0.3}Co_{0.7}$-oxide has the highest transfer coefficient value among all the NiCo-oxide compositions investigated.

Although the kinetic parameters in Table 3.3 are useful in extracting the OER kinetic data, for practical purposes it is more convenient to compare the behaviour OER electrodes in terms of the rate of oxygen evolution at a constant (specific) overpotential. For this purpose, current density values recorded at electrode potential of 1.5 V for various electrode compositions (excluding the Ir-oxide) are presented in Figure 3.6 as blue bars. The trend is similar to that seen in the electron transfer coefficient and the inverse of Tafel slope presented in Table 3.3. Namely, as the fraction of cobalt in the coating increases, the corresponding OER electrocatalytic activity also increases, reaching a maximum for the $Ni_{0.4}Co_{0.6}$-oxide. With a further increase in cobalt fraction in the coating, the OER electrocatalytic activity of the electrode decreases.

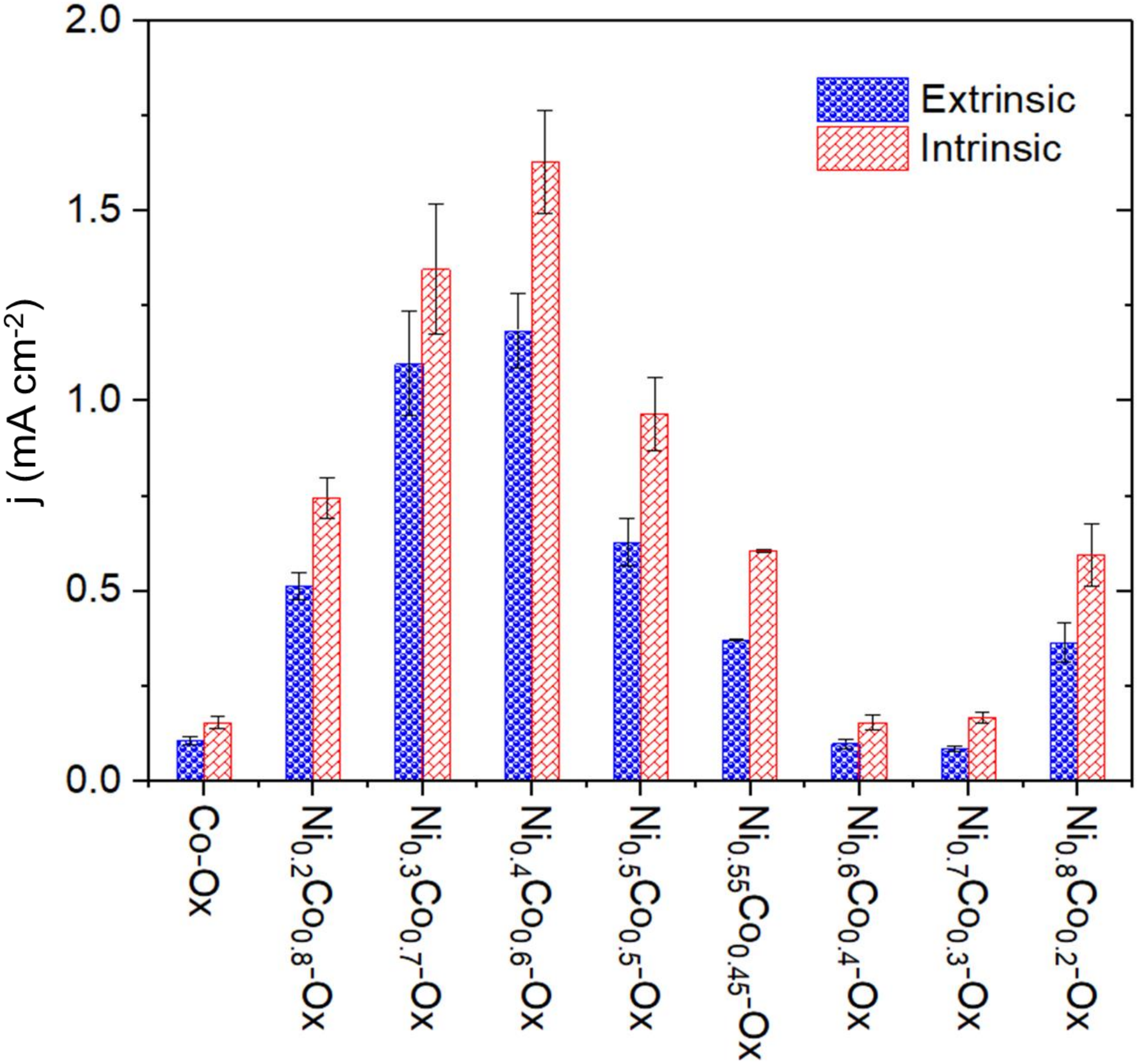

Figure 3.6: Relative extrinsic and intrinsic electrocatalytic activity of Ni_xCo_{1-x}-oxides in OER measured at 1.5 V vs. Ag/AgCl (corrected for iR-drop[5]) in 0.5 M H_2SO_4, obtained from Tafel measurements.

The aforementioned trend may be explained by the stabilization of cobalt active centres with the addition of Ni [170]. This leads to the improved electrocatalytic performance in the OER up to the optimum $Ni_{0.4}Co_{0.6}$-oxide composition, after which the electrocatalytic activity decreased with further increase of Ni, particularly since NiO is known to possess poor electrochemical activity in acid [166]. This intrinsically leads to a decrease in the number of OER-active sites on

---

[5] The iR-drop was determined by electrochemical impedance spectroscopy

the surface. Another explanation can be related to semiconducting properties of the oxides, *i.e.* to the narrowing of band gap and consequential improvement of electrocatalytic activity [17, 20, 178, 179]. In order to see if this could, at least partially, explain the origin of the trend in Figure 3.6, the direct band gap values for the investigated compositions were determined (see Figure 3.7). The values obtained are similar to literature values [180]. The minimum is indeed obtained for the $Ni_{0.4}Co_{0.6}$-oxide electrode, which shows the highest OER activity (Figure 3.6). Nevertheless, it should be noted that a number of other parameters may be responsible for the trend in Figure 3.6 (surface-charge distribution, distribution of Ni and Co on the surface and their various oxides, electronic structure, to name a few).

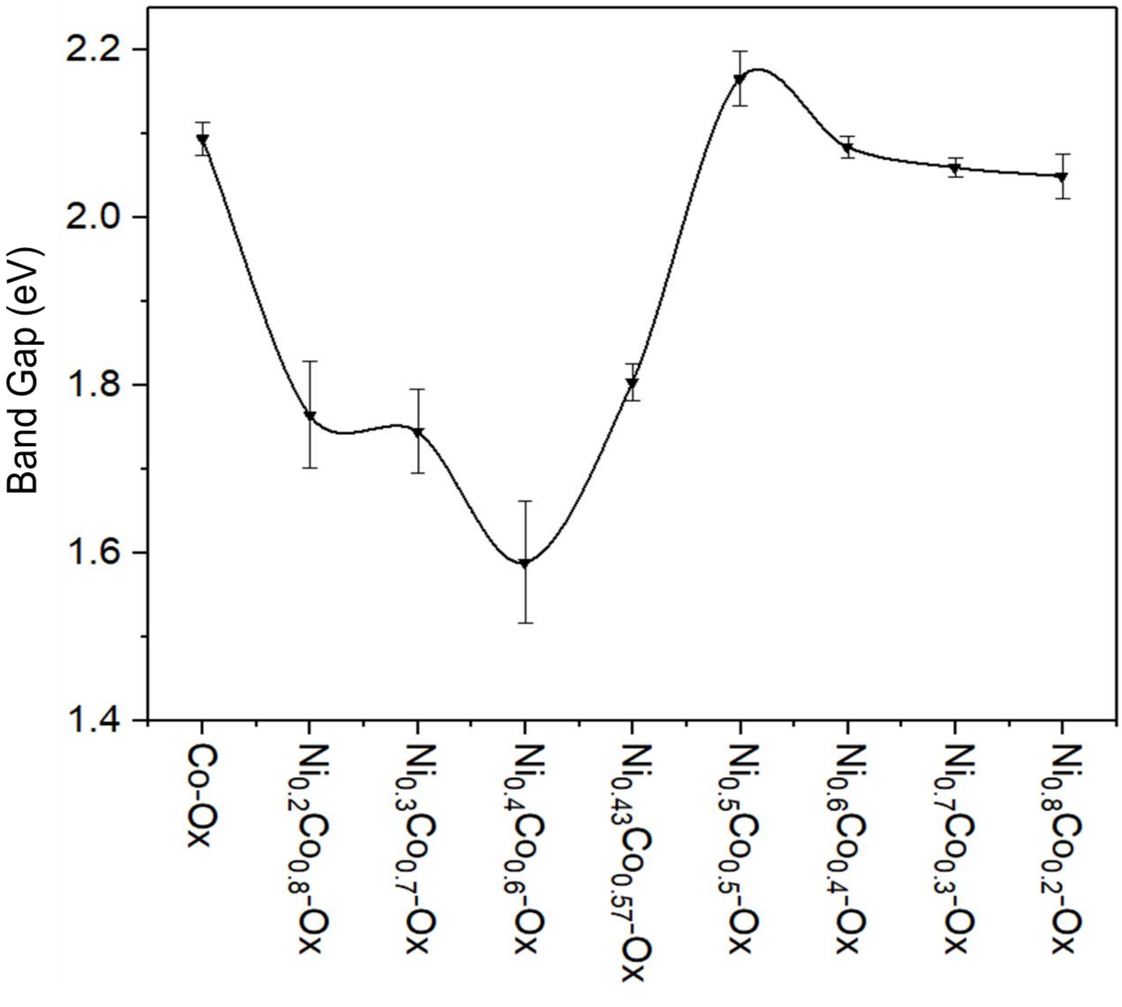

Figure 3.7: Variation of band-gap of as-synthesized metal oxides with composition.

It is also known that the metal-oxide coating thickness can influence its electrocatalytic activity. The thickness of coatings produced in this work was determined and it was noted that all the coatings are of a very similar thickness (3 ± 0.3 μm by EDX and 3.1 ± 0.3 μm by surface profiling), thus excluding the coating thickness as the origin of the trend in Figure 3.6.

However, it should be noted that the electrocatalytic activity of $Ni_{0.4}Co_{0.6}$-oxide is still inferior to the Ir-oxide benchmark, by ca. one order of magnitude (Figure 3.5). Nevertheless, in practical applications, this would be compensated by increasing the electroactive area, *i.e.* by increasing the loading of $Ni_{0.4}Co_{0.6}$-oxide. Employing this approach, significant savings would be achieved, considering the difference in cost of Ni+Co to Ir (ca. 1:4000) [181].

The blue bars in Figure 3.6 show the 'extrinsic' OER electrocatalytic activity of the materials investigated, which could be influenced by both the intrinsic activity of the material and by the surface-area effect. In order to eliminate the latter and investigate the intrinsic activity of the electrodes, current density values were normalized with respect to the EASA values from Table 3.2 and are presented as red bars in Figure 3.6. Comparing the trend in the intrinsic to the extrinsic behaviour, it can be seen that there is no significant difference between the two; the $Ni_{0.4}Co_{0.6}$-oxide electrode still shows the highest electrocatalytic activity, and it could be deemed that this composition (along with the $Ni_{0.3}Co_{0.7}$-oxide electrode, whose activity is not statistically different from that of $Ni_{0.4}Co_{0.6}$-oxide) represents the best intrinsically-electroactive Ni/Co-oxide-based anode investigated here, for OER in the acidic medium.

Given the complexity of the electrode compositions investigated (bi-component materials, different oxides and surface morphologies), neither the origin of the trend seen in Figure 3.6, nor that of the improved OER electrocatalytic activity of most of the binary Ni/Co-oxide composition relative to pure Co-oxide (which is known to be a good OER electrocatalyst) can be fully and reliably explained by the results gathered/presented. As discussed above, the semiconducting properties of the investigated oxides could, at least to a certain extent, be responsible for the trend observed [17, 20, 178, 179]. Likewise, it could be as a result of the effect of Ni on cobalt active centres [170]. Another alternative explanation could be that mixing transition metal oxides with opposite reactivity can lead to improved catalytic performance [182-184]. In addition, the spillover process has been used to highlight the synergistic interaction of transition metal alloys which is also taken to be the same for their corresponding oxides.

3.5. Conclusion

Ni_xCo_{1-x}-oxide coatings were successfully produced on flat titanium substrates by thermal decomposition of metal precursor solutions and their electrocatalytic performance towards oxygen evolution in acidic media was studied in order to obtain initial information to be used for further possible development of Ni_xCo_{1-x}-oxide-based anodes for PEM water electrolysers.

SEM results showed that the surface morphology of the coatings was composition-dependent. Likewise, the true electrochemically active surface area and surface roughness of the oxide coatings were dependent on their chemical composition, but not to a large extent. XRD and XPS analysis confirmed that Ni_xCo_{1-x}-oxide coatings contained NiO, Co_3O_4 and CoO on their surfaces.

Electrochemical measurements showed that the relative electrocatalytic activity of the Ni_xCo_{1-x}-oxide coatings was related predominantly to the coatings' intrinsic electrocatalytic properties, rather than to the extrinsic (surface area) effects.

Although the current state-of-the-art anode, Ir-oxide, offers one order of magnitude better electrocatalytic activity in the OER, this can conveniently be compensated (and even exceeded) by a larger loading of the best binary composition, $Ni_{0.4}Co_{0.6}$-oxide, while still lowering the anode cost.

Acknowledgement: This paper was supported by the Nigerian Petroleum Technology Development Fund (PTDF), Natural Sciences and Engineering Research Council of Canada (NSERC), and the McGill Engineering Doctoral Award (MEDA).

3.6. Appendix A. Supplementary material

This section contains the supplemental information to the article in this chapter. Namely, it describes the procedure used to determine the electrochemically active surface area (EASA) of the metal-oxide coatings. The procedure is based on determining the reduction current of the hexaammineruthenium III/II (HexRu(III)|HexRu(II)) chloride couple:

$$[Ru(NH_3)_6]^{3+} + e^- \leftrightarrow [Ru(NH_3)_6]^{2+} \tag{3.7}$$

which showcases a reasonably reversible cyclic voltammetric (CV) response (see Figure 3.8(A)) [145]. Consequently, cathodic peak current I_p is extracted from CV curve recorded on oxide surfaces in the range of scan rates (ν = 5, 10, 20, 30, 40, 50, 100, 200, 300 mV/s) in a 0.1 M KNO_3 (purity 99wt.%, Fisher Scientific, Canada) electrolyte containing 1 mM HexRu(III) chloride (purity 98wt.%, Sigma-Aldrich, USA). The slope of I_p vs $\nu^{1/2}$ shown in Figure 3.8(B) is employed in the Randles-Sevcik equation to obtain the EASA:

$$A = \frac{\mathrm{slope} \times (RT)^{\frac{1}{2}}}{(0.4463) \times (Fn)^{\frac{3}{2}} \times D^{\frac{1}{2}} \times C} \tag{3.8}$$

In the above equation, n represents the number of electrons in the half equation (one in this case), ‘A’ gives the electroactive surface area (cm^2), D is the diffusion coefficient of the hexaammineruthenium(III) cation in 0.1 M KNO3 electrolyte (8.03×10^{-6} cm^2/s) [145], C is the concentration of the analyte in mol/dm^3, F is the Faraday constant (96,486.3 C/mol) and R is the molar gas constant (8.314 J/mol/K).

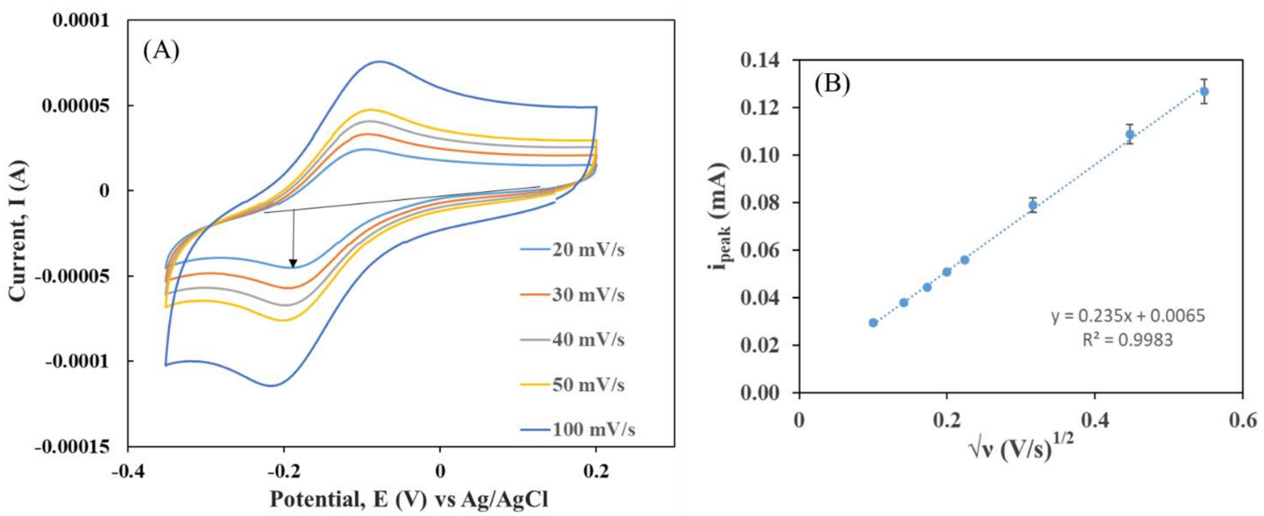

Figure 3.8: Typical cyclic voltammograms recorded on NiCo-oxide at given scan rates, ν in 1 mM hexaammineruthenium(III) chloride in 0.1 M KNO_3 electrolyte to determine (A) cathodic peak current, Ip and (B) the slope of Ip vs square-root of the scan rate.

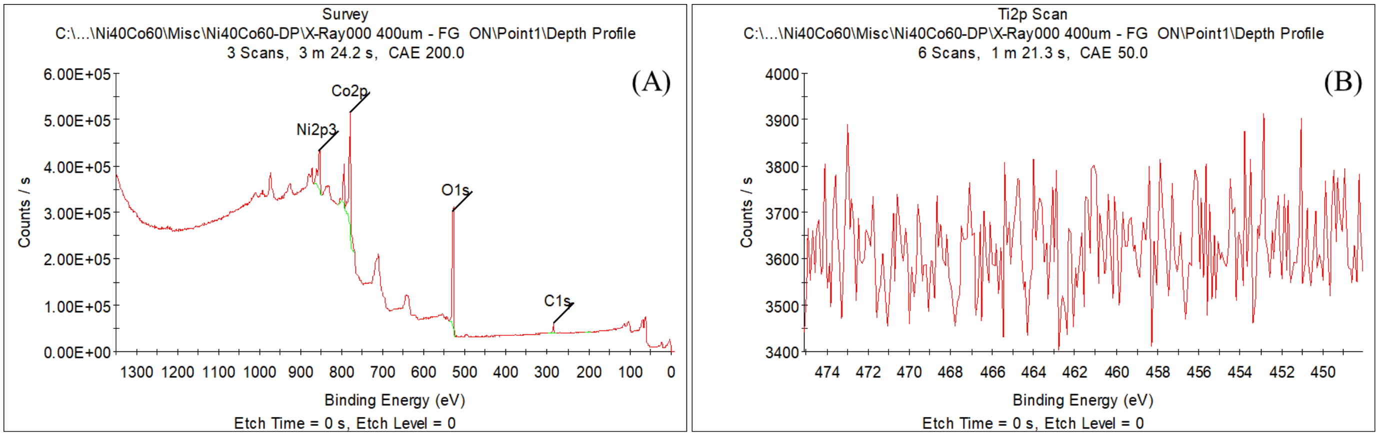

Figure 3.9: The XPS survey scan on Ni0.4Co0.6-oxide and (B) High resolution spectra in the Ti 2p region demonstrating the absence of Ti.

Chapter 4 - The Influence of Ir Content in $(Ni_{0.4}Co_{0.6})_{1-x}Ir_x$-oxide Anodes on their Electrocatalytic Activity in Oxygen Evolution by Acidic and Alkaline Water Electrolysis

Emmanuel Onyekachi Nwanebu*, Yusong Yao and Sasha Omanovic

Department of Chemical Engineering, McGill University, 3610 University St., Montreal, Quebec, H3A 0C5, Canada

*corresponding author: emmanuel.nwanebu@mail.mcgill.ca

4.1. Preface

The results on the impact of the relative Ni to Co ratio on the OER electrocatalytic activity of NiCo-oxide in an acidic medium was presented and discussed in the preceding chapter. It was found that the relative electrocatalytic activity of the Ni_xCo_{1-x}-oxide coatings was intrinsic in nature, and the best binary composition is $Ni_{0.4}Co_{0.6}$-oxide. Though this NiCo-oxide composition was inferior to the state-of-the-art IrO_2 anode by one order of magnitude, it could, however, serve as a base to develop alternative effective OER electrocatalysts. Therefore, it was hypothesized that at this best intrinsic composition, it was possible to further improve its specific OER performance of NiCo-oxide by incorporating a small amount of a highly electroactive precious metal such as Ir into the binary oxide base.

In this present chapter, results on the influence of Ir content on the OER electrocatalytic performance of $Ni_{0.4}Co_{0.6}$-oxide are reported. It will be shown that the OER electroactivity of Ni-Co-Ir-oxide of 10 at.% Ir significantly surpassed that of the $Ni_{0.4}Co_{0.6}$-oxide base and the state-of-art IrO_2 anode. Therefore, the enhancement in OER activity was attributed to the intrinsic synergistic interactions among the constituent oxides which led to the modification of the electronic structure of the catalyst and a reduction in its band gap energy relative to both $Ni_{0.4}Co_{0.6}$-oxide and Ir-oxide.

The work has been published as a peer-reviewed manuscript, and the corresponding reference is: E. O. Nwanebu, Y. Yao, and S. Omanovic, "The Influence of Ir Content in $(Ni_{0.4}Co_{0.6})_{1-x}Ir_x$-oxide Anodes on their Electrocatalytic Activity in Oxygen Evolution by Acidic and Alkaline Water Electrolysis," *Journal of Electroanalytical Chemistry,* p. 114122, 2020.

Highlights

- Addition of Ir to NiCo-Ox increases its electrocatalytic activity towards OER.
- Activity of $(Ni_{0.4}Co_{0.6})_{0.9}Ir_{0.1}$-Ox surpasses that of pure state-of-the-art Ir-Ox.
- Enhancement in electrocatalytic activity of NiCoIr-Ox is of an intrinsic nature

Abstract

Hydrogen is envisaged as the future energy fuel vector. Unfortunately, one of the most environmentally-viable hydrogen production option, water electrolysis (when coupled with solar/wind/hydro electrical energy) is still not energy efficient, as it requires expensive electrocatalytically-active noble metal anodes. The authors recently identified $Ni_{0.4}Co_{0.6}$-oxide as good alternative anode-material candidate, nevertheless, the electrocatalytic activity of this anode needs further augmentation. Therefore, with the aim of improving the anode's activity towards oxygen evolution in both the acidic and alkaline media, the influence of addition of small amounts (≤10%) of Ir to $Ni_{0.4}Co_{0.6}$-oxide was studied. The investigation showed that the incorporation of Ir into the $Ni_{0.4}Co_{0.6}$-oxide matrix yielded a synergetic effect, resulting in a significant improvement of the anode's intrinsic electrocatalytic activity relative to both $Ni_{0.4}Co_{0.6}$-oxide and pure Ir-oxide. This was ascribed to the change in the electronic structure of the catalyst and to the reduction in band gap energy relative to $Ni_{0.4}Co_{0.6}$-oxide and Ir-oxide. The as-made $(Ni_{0.4}Co_{0.6})_{0.9}Ir_{0.10}$-oxide composition was found to be stable and significantly more active than the current state-of-the-art IrO_2 PEM oxygen-evolution anode, while also offering a considerably higher electrocatalytic activity than nickel anodes used in alkaline electrolysers.

Keywords: Hydrogen; Oxygen evolution; Water electrolysis; Anodes; Nickel-Cobalt-Iridium-oxides

4.2. Introduction

The world needs sustainable energy sources that are environmentally friendly. Currently, the global energy demand is met with traditional unsustainable fossil fuel sources, resulting in global warming and a consequent mondial surface temperature rise. Hydrogen is seen as a viable practical alternative energy vector especially since it is recyclable and vastly abundant in the universe. However, hydrogen does not exist in its pure state in nature and it is typically found in combination with other elements such as carbon in hydrocarbons and oxygen in water. Consequently, hydrogen is chiefly generated by an environmentally-unfriendly hydrocarbon reforming process (ca. 95%) and much less by the cleaner water-splitting process otherwise known as water electrolysis (ca. 5%), in which electricity is applied to split water into oxygen and hydrogen gases [185].

When the applied electrical current is derived from renewable energy sources, the water-splitting process becomes the cleanest method of producing hydrogen. However, this process is not yet cost-competitive. This is, in part, because the wide-spread commercialization of sustainable hydrogen production technology *via* water electrolysis is hindered by the slow kinetics of the anode oxygen evolution reaction (OER). In addition, when hydrogen production is performed in acidic polymer electrolyte membrane (PEM) electrolysers, expensive noble metal anodes (usually made of iridium) need to be used due to stability issues. While inexpensive nickel metal anodes may be used as a substitute in a milder alkaline environment, nevertheless, their long-term stability and electrocatalytic activity are still not satisfactory [110].

However, metal oxides of non-noble transition metals of Co, Fe, Mn and Ni [18, 19, 95, 110, 185] have been identified as possible cost-effective substitutes. Nonetheless, the monometallic oxides of these elements are beset with activity and stability issues [95, 151, 185]. Reports in the literature show that the mixed-metal oxides of the aforementioned metals with Ir or Ru [63, 66, 79, 186-193] and more recently mixed NiCo-oxide [185] showed improved intrinsic catalytic OER performance due to their transition metal ions ability to act and stabilize active centres [170, 185, 194]. In another case, Ti was found to stabilize earth-abundant MnO_2 in acid [95].

Our previous study reported results on the investigation of the activity of Ni_xCo_{1-x}-oxide electrodes in the OER, and $Ni_{0.4}Co_{0.6}$-oxide was identified as the most-active composition [185]. Further, IrO_2 has been considered as the current state-of-the-art OER electrocatalyst in the acidic PEM environment [92], but this anode is rather expensive. Taking into account these two facts, the hypothesis of the authors was that the intrinsic activity of the $Ni_{0.4}Co_{0.6}$-oxide can be substantially increased by incorporating a small amount of Ir (up to 10at.% relative to the total metal content) into the oxide structure. Consequently, this investigation entails the systematic work on the influence of Ir incorporation into the $Ni_{0.4}Co_{0.6}$-oxide matrix on the resulting OER electrocatalytic activity in acid and, to the best of the authors' knowledge, for the first time in the alkaline medium. The observed enhancement of the activity of the trimetal oxide anode is attributed to the modification of the material’s electronic structure. It should be noted that the current study is of a predominantly fundamental nature. Therefore, the aim was to investigate the intrinsic properties of the produced materials rather than to produce extrinsically exceptionally-good OER electrocatalyst of high specific surface area (e.g. nanostructured surfaces). Thus, the electrodes were prepared as two-dimensional surfaces, instead of nano-structured three-dimensional surfaces.

4.3. Materials and methods[6]

4.3.1. Anode material preparation

Anode coatings were formed on titanium button-shaped substrates (Grade 2, 99% pure, McMaster Carr) by thermal salt decomposition procedure. 0.5M precursor salt solutions of nickel, cobalt and iridium were made by dissolving $NiCl_2 \cdot 6H_2O$ (ReagentPlus, 100%, Sigma Aldrich), $Co(NO_3)_2 \cdot 6H_2O$ (Pure, 99%, ACROS Organics), and $IrCl_3 \cdot 3H_2O$ (53 to 56% (Ir), ACROS Organics) respectively in a 1:1 volume mixture of isopropanol (Fisher) and nanopure water of resistivity 18.2 MΩ cm. The required coating compositions were made by incorporating a predetermined quantity of Ir precursor solution into a 40:60 at.% Ni/Co metal-based solution and the resulting coating solutions were sonicated for 10 min; the as-produced coatings had compositions that can be presented as $(Ni_{0.4}Co_{0.6})_{1-x}Ir_x$-oxide [185].

Titanium substrates of diameter 1.21 cm and thickness 0.2 cm were prepared using the same procedure as in our previous work [185]. A flat Ni (99.9% pure) plate that underwent a similar polishing, sonicating and drying preparation procedure, but without etching, was used as a control anode in the alkaline electrolyte solution.

The pretreated substrates were evenly sprayed with coating solutions using a clean standard paintbrush. These wet-painted substrates were then dried in an oven at 383 K for 5 min followed by 15 min calcination at 773 K in a furnace. The calcined samples were air-cooled for 10 min and

---

[6] All the measurements were preformed in triplicates or more, and the presented results are the average values with corresponding standard errors.

further five layers of coatings were applied in the same manner. Finally, the six-layered coated samples were calcined for 1 h at 773 K to form $(Ni_{0.4}Co_{0.6})_{1-x}Ir_x$ -oxides [185]. The backsides of the coated samples were dry-polished using 600-grit SiC sandpaper to provide consistent electrical contact throughout the different coating compositions.

4.3.2. Surface characterization

The surface morphology and surface elemental composition of the anode materials were investigated by scanning electron microscopy (SEM) and energy-dispersive X-ray spectroscopy (EDX) techniques, with the aid of Hitachi SU3500 scanning electron microscope.

The crystalline structure of the different oxide phases was analyzed by X-ray diffraction (XRD) employing a Bruker Discover D8-2D diffractometer with a 0.5 mm dia. Collimated Cu Kα (1.54 Å) radiation at room temperature in a standard q–2θ mode [185].

Also, X-ray photoelectron spectroscopy (XPS) measurements were done using a ThermoScientific K-Alpha spectrometer. The X-ray non-monochromatic source was Al Kα (1486.6 eV photon energy, 400 µm spot size). In order to ensure the reliability of results, XPS spectra were recorded on each sample at three different locations to determine the metal atomic surface compositions of these as-produced metal oxide anode materials. ThermoScientific Avantage 5.932 software was used to analyze the resulting XPS spectra [185].

Furthermore, the anode coating thickness was determined with the aid of a DektakXT stylus (Bruker, USA) surface profilometer, which corroborated the coating thickness analysis performed by EDX line scan measurements of the side cross-section of coated samples.

Finally, the band-gap energies of the best performing coating composition, $(Ni_{0.4}Co_{0.6})_{0.9}Ir_{0.10}$-oxide, and the reference control samples were obtained by photoluminescence spectroscopy employing a 266-nm excitation laser coupled with a UV/Vis spectrometer (ThermoScientific Evolution 300) that generated diffused reflectance by green light [185].

4.3.3. Electrochemical Characterization

Electrochemical characterization of the anode materials was performed in a three-electrode/two-compartment electrochemical cell setup employing an Autolab potentiostat/galvanostat/frequency response analyzer (PGSTAT30/FRA2, Metrohm, NL) controlled by NOVA software package (v. 2.1.2; Metrohm, NL). The cell configuration comprised the Ni-Co-Ir-oxide working electrode (WE) coatings with a 0.43 cm^2 geometric area exposed to the electrolyte, a graphite counter electrode (CE) separated from the WE compartment by a glass frit (Ace Glass, Inc., USA), and an Ag/AgCl (Fisher Scientific, product no. 1362053, sat. KCl) reference electrode (RE) [185]. In control experiments, a flat Ni plate (purity, 99.9%) was used as the working electrode.

The electrocatalytic activity and stability of the anode materials in acidic and alkaline media were studied in 0.5 M H_2SO_4 of pH = 0.4 (made from 95 wt% H_2SO_4, Fisher Scientific) and in 1 M NaOH of pH = 13.4 (made from 99 wt% NaOH crystals, Sigma-Aldrich) respectively by employing linear Tafel polarization and chronopotentiometry techniques. The electrochemically-active surface area (EASA) of as-made materials was investigated by cyclic voltammetric (CV) measurements recorded at different scan rates in 1 mM hexaammineruthenium(III) chloride (98%, Sigma Aldrich) redox probe dissolved in 0.1 M KNO_3 (≥99%, Sigma Aldrich) supporting solution. A detailed description of the EASA determination procedure can be found in the literature [145, 146, 185]

All solutions used were deoxygenated by a 40 min argon (99.998% pure, MEGS Specialty Gases Inc., Canada) purge before the start of each experiment. For EASA determination alone, the deoxygenated solution was left unperturbed in order to ensure that the redox species were transported particularly by diffusion, during measurement. All the electrochemical measurements were performed at 295 ± 2 K, and the potentials quoted in this text were corrected for the *iR*-drop measured by electrochemical impedance spectroscopy [185].

4.4. Results and Discussion

4.4.1. Scanning electron microscopy

The surface morphology of as-produced $(Ni_{0.4}Co_{0.6})_{1-x}Ir_x$-oxide coatings was characterized by SEM analysis while the coating surface composition was evaluated by EDX elemental mapping. The SEM images shown in Figures 4.1(A-F) depict a fairly homogeneous morphological distribution of Ni-Co-Ir-oxide coatings with a few agglomerated clusters. The micrographs are typical of Ni_xCo_{1-x}-oxide and Ir-oxide deposited on Ti substrate by thermal decomposition [77, 185]. The SEM images highlight the existence of granular networks which is the consequence of the interaction of the $Ni_{0.4}Co_{0.6}$-oxide and Ir-oxide in the coatings. It is noted that as the Ir content increased from 2% to 6%, there is a greater formation of hexagonal granular particles that became more compact and flattened at 10% Ir content. The morphology of the as-synthesized $(Ni_{0.4}Co_{0.6})_{1-x}Ir_x$-oxide is dominated by the microsurface structure of $Ni_{0.4}Co_{0.6}$-oxide, while the pure Ir-oxide coating (Figure 4.1(F)) displays a completely different morphology, characterized by a cracked-mud pattern typical for pure Ir-oxide coatings.

The EDX elemental mapping of the $(Ni_{0.4}Co_{0.6})_{0.9}Ir_{0.10}$-oxide coating (Figures 4.2(A-D)) show the uniform dispersion of Ni, Co, and Ir in the coating. The thickness of coatings was determined by EDX line scan analysis of the side view cross-section of the coated samples by measuring the Ni/Co/Ir distribution profile in the coating top-layer. The coating thickness was 3 ± 0.3 μm. A very close value was obtained by using a surface proliferometer (3.1 ± 0.3 μm). Furthermore, the EDX data presented in Table 1 shows a very good agreement between the actual average surface composition of coatings and their nominal composition. However, for clarity, the nominal composition value is used throughout the text to denote the coating's composition.

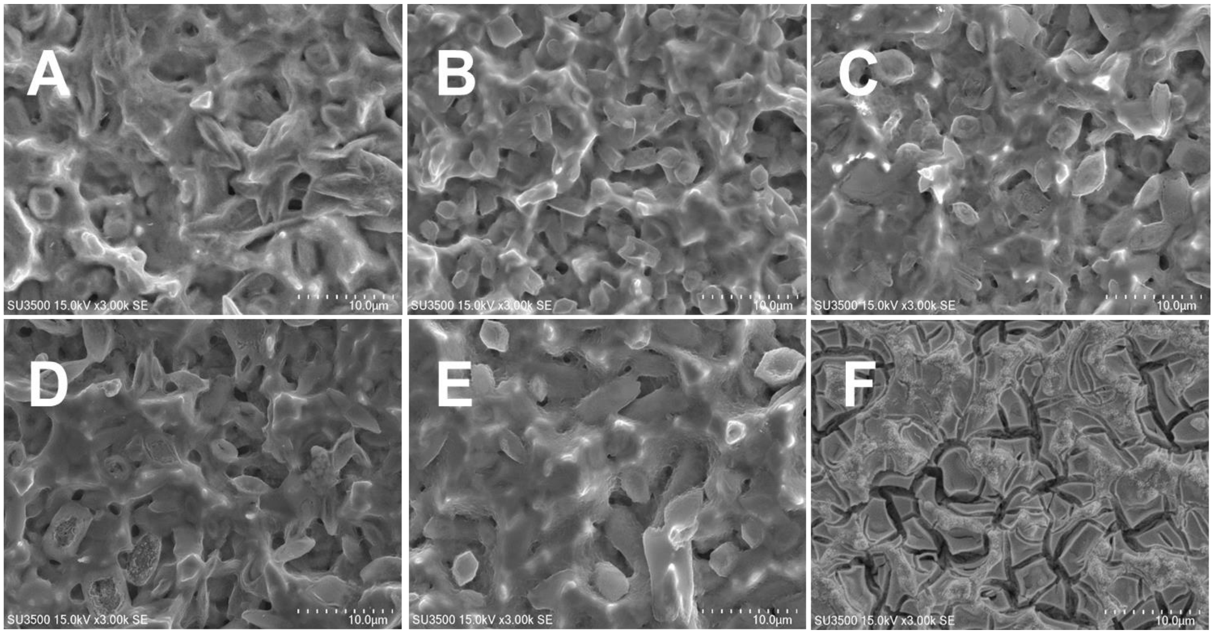

Figure 4.1: Scanning electron micrographs of: (A) $Ni_{0.4}Co_{0.6}$-oxide; (B) $(Ni_{0.4}Co_{0.6})_{0.98}Ir_{0.02}$-oxide; (C) $(Ni_{0.4}Co_{0.6})_{0.96}Ir_{0.04}$-oxide; (D) $(Ni_{0.4}Co_{0.6})_{0.94}Ir_{0.06}$-oxide; (E) $(Ni_{0.4}Co_{0.6})_{0.90}Ir_{0.10}$-oxide; (F) Ir-oxide coating.

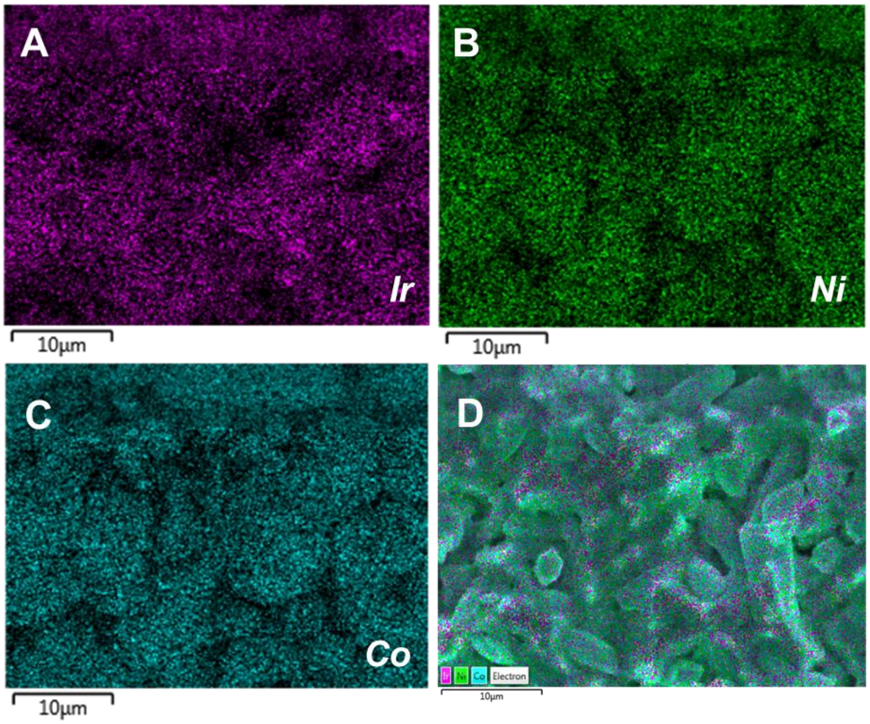

Figure 4.2: Morphological distribution of (A) Ir, (B) Ni, (C) Co, and (D) Ir/Ni/Co on the as-synthesized $(Ni_{0.4}Co_{0.6})_{0.90}Ir_{0.10}$-oxide surface.

Table 4.1: Relative atomic ratio of Ir, Co and Ni in $(Ni_{0.4}Co_{0.6})_{1-x}Ir_x$-oxide coatings (excluding the contribution of oxygen). EDX and XPS values represent the measured surface composition of Ir, Co and Ni in the respective coatings employing the two corresponding surface-analysis techniques.

Nominal composition	**Actual composition**	
	EDX	**XPS**
$Ni_{0.4}Co_{0.6}$-Ox	$Ni_{0.40}Co_{0.60}$-Ox	$Ni_{0.34}Co_{0.66}$-Ox
$(Ni_{0.4}Co_{0.6})_{0.98}Ir_{0.02}$-Ox	$(Ni_{0.42}Co_{0.58})_{0.98}Ir_{0.02}$-Ox	$(Ni_{0.37}Co_{0.63})_{0.98}Ir_{0.02}$-Ox
$(Ni_{0.4}Co_{0.6})_{0.96}Ir_{0.04}$-Ox	$(Ni_{0.41}Co_{0.59})_{0.96}Ir_{0.04}$-Ox	$(Ni_{0.37}Co_{0.63})_{0.96}Ir_{0.04}$-Ox
$(Ni_{0.4}Co_{0.6})_{0.94}Ir_{0.06}$-Ox	$(Ni_{0.40}Co_{0.60})_{0.94}Ir_{0.06}$-Ox	$(Ni_{0.38}Co_{0.62})_{0.95}Ir_{0.05}$-Ox
$(Ni_{0.4}Co_{0.6})_{0.90}Ir_{0.10}$-Ox	$(Ni_{0.39}Co_{0.61})_{0.90}Ir_{0.10}$-Ox	$(Ni_{0.38}Co_{0.62})_{0.91}Ir_{0.09}$-Ox
Ir-Ox	Ir-Ox	Ir-Ox

4.4.2. X-ray diffraction

The X-ray diffraction profiles of $Ni_{0.4}Co_{0.6}$-oxide, $(Ni_{0.4}Co_{0.6})_{0.90}Ir_{0.10}$-oxide and pure Ir-oxide coatings that show the different crystalline phases in the aforementioned oxides are presented in Figure 4.3. Common to the three diffractograms are the characteristic diffraction peaks at 2θ values of 35.0°, 38.4°, 40.2°, 53.0°, 62.9°, 74.2°, 76.2°, and 77.4° associated with the metallic Ti (JCPDS, 44-1294) which is due to the underlying Ti substrate [77, 185]. These peaks are visible because the depth analysis of the X-ray penetration is at least twice more than the thickness of the oxide coatings.

Similarly, the diffractograms exhibit strong peaks at 62.8° and 70.6° indexed to (118) and (220) reflections of anatase TiO_2 (JCPDS, 84-1286), and a diffraction peak at 27.5° ascribed to rutile TiO_2 (110) reflection plane (JCPDS, 88-1175) [149], with the exception of pure Ir-oxide where this peak was not apparent. The formation of TiO_2 could be a consequence of the relative affinity of Ti for oxygen compared to Ni, Co & Ir and its consequent diffusion towards the oxygen-rich outer surface where it is oxidized [148, 185].

Further analysis of the crystalline phases in Ir-oxide reveal strong diffraction peaks at 28.0°, 34.4°, and 41.1° attributed to the rutile IrO_2 (110), (101), and (200) crystal reflection planes (JCPDS, 15-870) [91]. However, in the case of $(Ni_{0.4}Co_{0.6})_{0.90}Ir_{0.10}$-oxide, the overlapping of reflections centred at 28.0° and 27.5° due to rutile IrO_2 (110) and TiO_2 (110) respectively, resulted in the broadening of the diffraction peaks in this low 2θ-angle region. This behaviour is typical of overlapping rutile-type oxide phases with strong reflections, as only weak close reflections can be separated [195]. Furthermore, the XRD pattern of pure Ir-oxide shows the presence of a weak-intensity peak at 47.6° corresponding to metallic Ir (200) reflection plane. Moreover, this peak was absent in $(Ni_{0.4}Co_{0.6})_{0.90}Ir_{0.10}$-oxide coatings. This implies that virtually all of the applied Ir precursor coating solution was oxidized under the employed calcination condition.

Diffraction peaks at 37.1° and 43.4° indexed to (111) and (200) reflection planes of face-centred cubic rock-salt NiO (JCPDS, 78-0643) [48, 185] are visible on the two spectra containing nickel. The XRD spectra of all the trimetal $(Ni_{0.4}Co_{0.6})_{1-x}Ir_x$-oxide coatings have revealed the existence of six distinct peaks at 18.9°, 31.1°, 36.7°, 44.6°, 59.2°, and 64.9° assigned to (111), (220), (311)), (400), (511), and (440) reflection planes of spinel Co_3O_4 (JCPDS, 42-1467) [152] and a peak at 36.5° of rock salt CoO (111) phase (JCPDS, 75-0533) [27] (note that for the purpose of presentation, the diffractograms of $(Ni_{0.4}Co_{0.6})_{0.90}Ir_{0.10}$-oxide alone is shown in Figure 4.3; the remaining Ni-Co-Ir-oxides have similar XRD profile but with less peak intensity at 28.0°). Furthermore, the presence of NiO (111) reflection at 37.1° which appears as a discernible shoulder at Co_3O_4 (311) and CoO (111) phase reflections suggests that a single mixed oxide phase could be present instead of a discrete phase mixtures of Ni and Co oxides in the $Ni_{0.4}Co_{0.6}$-oxide [151]. Upon incorporation of Ir into the $Ni_{0.4}Co_{0.6}$-oxide structure, the peaks at 36.7°, 44.6°, 59.2°, and 64.9° shifted to lower values, which is expected due to the change in the unit crystal structure as a result of the incorporation of a larger-size species, iridium [196]. Finally, it is noted that the addition of Ir into the $Ni_{0.4}Co_{0.6}$-oxide matrix resulted in the broadening of strong diffraction peaks of the as-made trimetal oxides. This suggests that the crystallite sizes of oxide phases decreased with increasing Ir content. Consequently, this might, to a certain extent, explain the improvement of coating materials intrinsic electrocatalytic activity, as discussed further in the text.

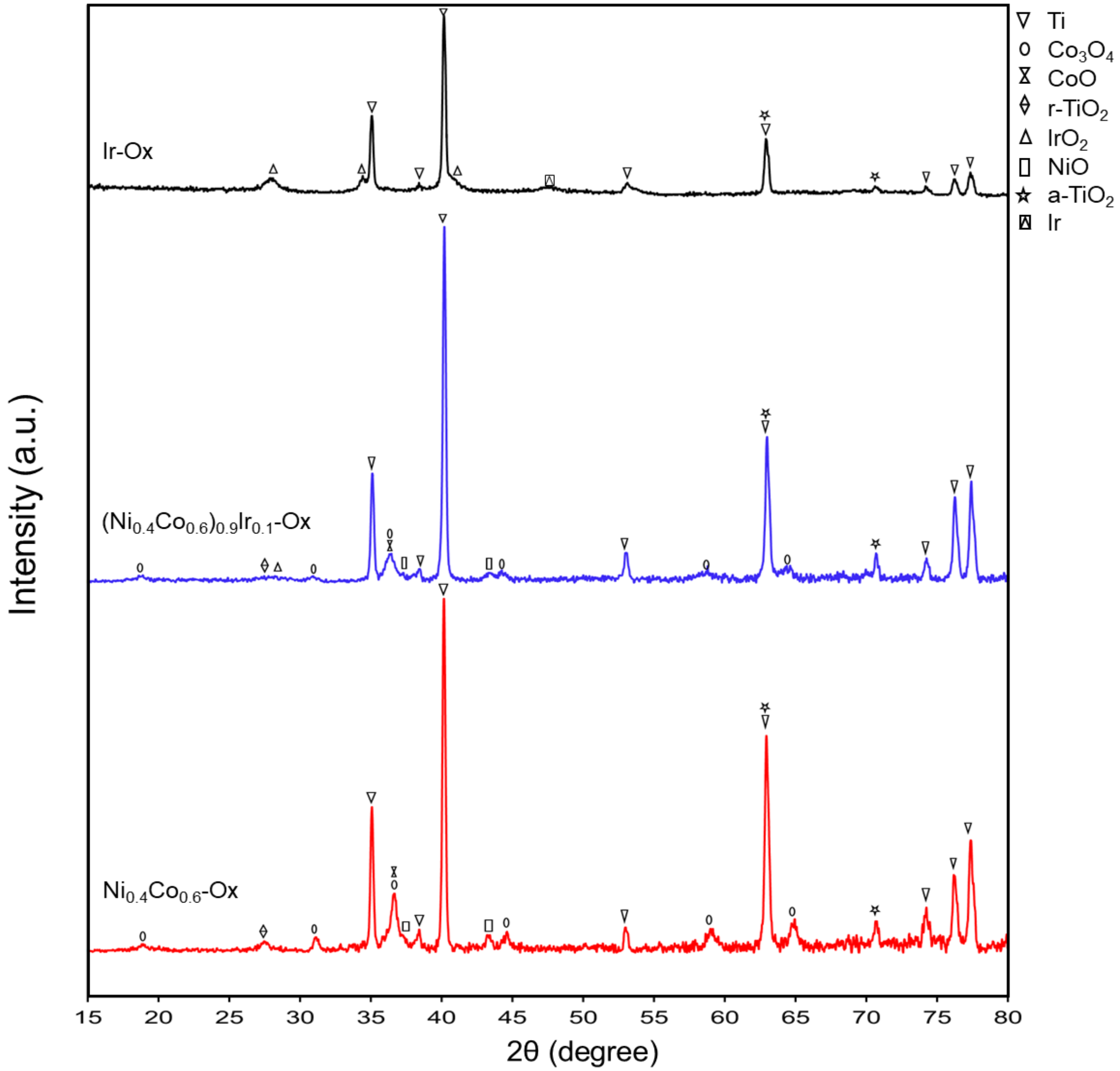

Figure 4.3: Diffraction patterns of $(Ni_{0.4}Co_{0.6})_{1-x}Ir_x$-oxide coatings deposited on Ti substrate.

4.4.3. X-ray photoelectron spectroscopy

The chemical state of the top-most species of the as-synthesized $(Ni_{0.4}Co_{0.6})_{1-x}Ir_x$-oxide was further investigated by X-ray photoelectron spectroscopy and the resulting deconvolution spectra are shown in Figure 4.4. The XPS survey scan revealed strong binding energy peaks of O 1s, Ni 2p, Co 2p, Ir 4f and a detectable quantity of C 1s of adventitious carbon. Hence, for convenience, the spectra of all high-resolution scans of detected chemical species are charge corrected to C 1s (C-C peak of adventitious carbon) set at 284.8 eV [161]. The data from the XPS survey analysis of the topmost layer of the coating surface (< 10nm) is presented in Table 4.1, and these data corroborate the results obtained by EDX analysis.

Figure 4.4(A) showcases the multiplet splitting and satellite structure of the Ni 2p envelope. The high-resolution scan of $(Ni_{0.4}Co_{0.6})_{0.90}Ir_{0.10}$-oxide reveals Ni $2p_{3/2}$ doublet photoelectron peaks at 853.7 and 855.4 eV and a satellite peak at 860.9 eV [161]. The higher binding energy Ni $2p_{1/2}$ area shows multiplet-split peaks at 871.4 and 872.9 eV and a satellite peak at 879.3 eV due to shake processes [160]. Similar results were obtained on other $(Ni_{0.4}Co_{0.6})_{1-x}Ir_x$-oxide compositions (not shown), and also on $Ni_{0.4}Co_{0.6}$-oxide reported in our previous work [185]. The binding energy separation between the Ni $2p_{3/2}$ and Ni $2p_{1/2}$ satellite peaks gives a split spin-orbit value of 18.3 eV associated with stoichiometric NiO [197]. This confirms the presence of NiO in all relevant coatings.

The surface-sensitive XPS high-resolution analysis on $(Ni_{0.4}Co_{0.6})_{0.90}Ir_{0.10}$-oxide in the Co 2p region shows a mixture of core-level and satellite features due to Co^{2+} and Co^{3+} (see Figure 4.4(B)). The core-level Co 2p spectrum section (Co $2p_{3/2}$ and Co $2p_{1/2}$) has main peaks at 779.6 and 796.3 eV attributed to Co 2p electrons in rock salt Co^{2+}, while binding energy values of 780.9 and 794.7 eV centred at Co $2p_{3/2}$ and Co $2p_{1/2}$ primary peak positions correspond to the spinel Co^{3+} [163]. It is also possible to distinguish Co oxidation states via the satellite features of the Co 2p spectrum. Co^{2+} has observable Co $2p_{3/2}$ and Co $2p_{1/2}$ satellite peaks at 785.1 and 802.6 eV [141], whereas Co^{3+} has Co $2p_{3/2}$ and Co $2p_{1/2}$ satellite peaks at 789.1 and 805.0 eV [185]. The overall outlook of the Co 2p XPS profile is resemblance of a typical X-ray photoelectron spectrum ascribed to Co_3O_4. This suggests that Co_3O_4 is present in the top-oxide (outer-most) layer of the $(Ni_{0.4}Co_{0.6})_{0.90}Ir_{0.10}$-oxide coating (the same was obtained for other $(Ni_{0.4}Co_{0.6})_{1-x}Ir_x$-oxide coating compositions). However, a closer look at the profile indicates that the known broad satellite peak feature of Co_3O_4 around binding energy of 786 – 789.5 eV [162] is further stretched towards the lower binding energy. Hence, the presence of additional Co-oxide species can be elicited. Interestingly, the deconvolution fitting lines of the peaks are perfectly analogous to typical Co_3O_4 and CoO spectra, thereby confirming that both types of cobalt oxides were formed on the surface of the as-prepared oxide coatings. The surface CoO:Co_3O_4 ratio in all the $(Ni_{0.4}Co_{0.6})_{1-x}Ir_x$-oxide coatings was found to be ca. 1:1. Therefore, the observed trend in electrocatalytic activity discussed later in the text (see Figure 4.6) is not due to the variation of $CoO:Co_3O_4$ ratio in each composition [185].

Figure 4.4(C) shows the photoelectron spectra of Ir 4f region. The high-resolution scan for pure Ir-oxide indicates an asymmetrical peak profile characteristic of rutile type IrO_2 [198]. The Ir 4f core-level has primary peaks centred at 61.8 and 64.8 eV for $4f_{7/2}$ and $4f_{5/2}$ peak positions respectively with a split spin-orbit value of 3 eV [67]. These peaks correspond to the Ir^{4+} oxidation state. In addition to this main spin-orbit doublet, two broader peaks observed at 62.9 and 66.1 eV are visible; these are considered to be due to the final-state screening effect by virtue of intermediate species (probably Ir^{3+} oxidation state of IrOOH [67, 90]). In the $(Ni_{0.4}Co_{0.6})_{0.90}Ir_{0.10}$-oxide (Figure 4.4(C)), the $4f_{7/2}$ peak position shifted to a higher binding energy, from 61.8 to 62.2 eV, and the $4f_{5/2}$ peak from 64.8 to 65.8 eV, while the peak positions due to the intermediates are centred at 59.9 and 68.5 eV. This modification in the electronic structure results in the spread-out of the electron cloud. It can further be seen in Figure 4.4(C) that the $4f_{7/2}$ and $4f_{5/2}$ peaks for $(Ni_{0.4}Co_{0.6})_{0.90}Ir_{0.10}$-oxide are broader and more asymmetric in comparison to those of pure Ir-Ox, indicating a difference in the local surrounding Ir atoms and enhancement in the metallic character of $(Ni_{0.4}Co_{0.6})_{0.90}Ir_{0.10}$-oxide [199]. All the $(Ni_{0.4}Co_{0.6})_{1-x}Ir_x$-oxide coatings had similar Ir 4f spectra, but with slight shifts in the peak positions.

For further understanding of the surface characteristics of the as-made oxides, the high-resolution O 1s spectra are analyzed. Figure 4.4(D) shows the core-level peaks in the O 1s envelope. In pure Ir-oxide, the O 1s spectrum has photoelectron peaks located at 529.8, 530.8, and 532.4 eV attributed to oxygen in the crystal lattice, hydroxyl group and adsorbed oxygen, respectively. Meanwhile, in the trimetal $(Ni_{0.4}Co_{0.6})_{1-x}Ir_x$-oxides, the aforementioned peaks are centred at 529.4, 530.9 and 532.4 eV, respectively [195]. Therefore the presence of the binding energy peak at ca. 532.4 eV, due to surface adsorbed oxygen, can be said to emanate from the IrO_2 in the trimetal oxide mixture since this peak was absent in the O 1s spectrum of pure $Ni_{0.4}Co_{0.6}$-oxide [185]. Further, upon the incorporation of Ir into the $Ni_{0.4}Co_{0.6}$-oxide structure, the peak related to the oxygen in the crystal lattice shifted to a higher energy by ca. 0.2 eV (from 529.2 to 529.4 eV), suggesting a slight polarization of metal-oxygen shared electrons away from the oxygen atom [200]. Finally, the ratio of (O^{2-}):(OH):$(O^{-})_{ads}$ is calculated as ca. 8:7:5 and 4:3:1 in the pure

Ir-oxide and in all the investigated trimetal $(Ni_{0.4}Co_{0.6})_{1-x}Ir_x$-oxides, respectively. Therefore, there is twice as much adsorbed oxygen in the former oxide than in the latter oxides.

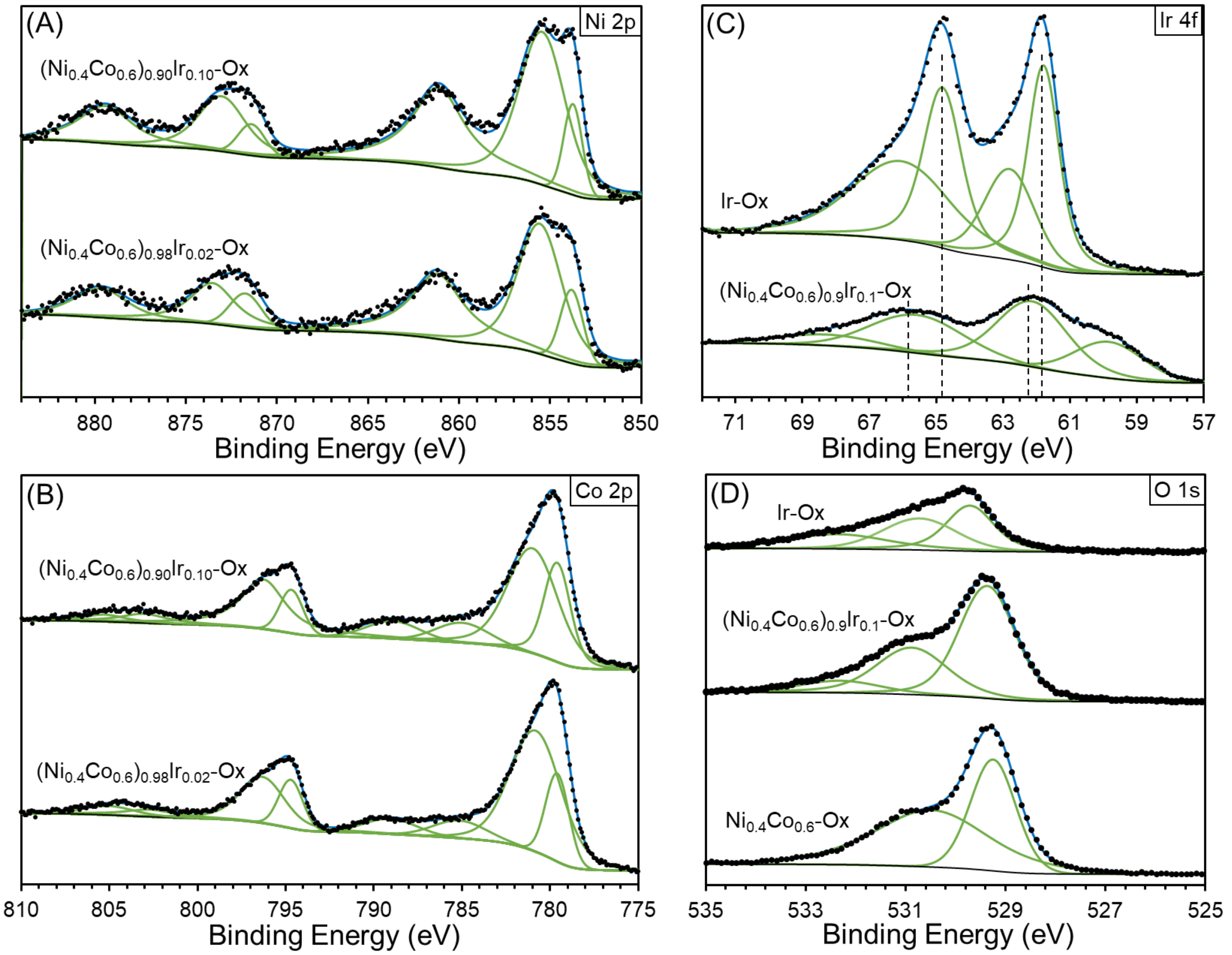

Figure 4.4: XPS spectra of $(Ni_{0.4}Co_{0.6})_{1-x}Ir_x$-oxide samples of (A) Ni 2p (B) Co 2p (C) Ir 4f and of (D) O 1s.

4.4.4. OER Electrocatalytic activity

In order to investigate the electrocatalytic activity of $(Ni_{0.4}Co_{0.6})_{1-x}Ir_x$-oxide coatings towards OER in the acidic and alkaline electrolyte, linear sweep voltammetric (LSV) measurements were recorded in 0.5 M H_2SO_4 and 1 M NaOH, respectively. The corresponding Tafel polarization curves, corrected for *iR*-drop, are presented in Figure 4.5 (the equivalent LSV curves are shown in Figure 4.9 of the supporting information). Pure Ir-oxide is presented as the control sample in the acidic medium (IrO_2 is considered to be the state-of-the-art OER electrocatalyst in the acidic medium), while in addition, pure Ni is presented as the control anode in the alkaline medium (also, Ni is the current state-of-the-art OER anode in this medium).

Taking into account that the ordinate is on the logarithmic scale, the Figures 4.5(A and B) demonstrate that the composition of the electrodes has a marked influence on the electrocatalytic activity of the coatings, in both electrolytes. In general, as the content of Ir in the oxide increases, the current at a fixed overpotential also increases. The curves could be divided into two regions, the linear Tafel region at low/mid overpotentials, and the 'plateau' region at higher overpotentials.

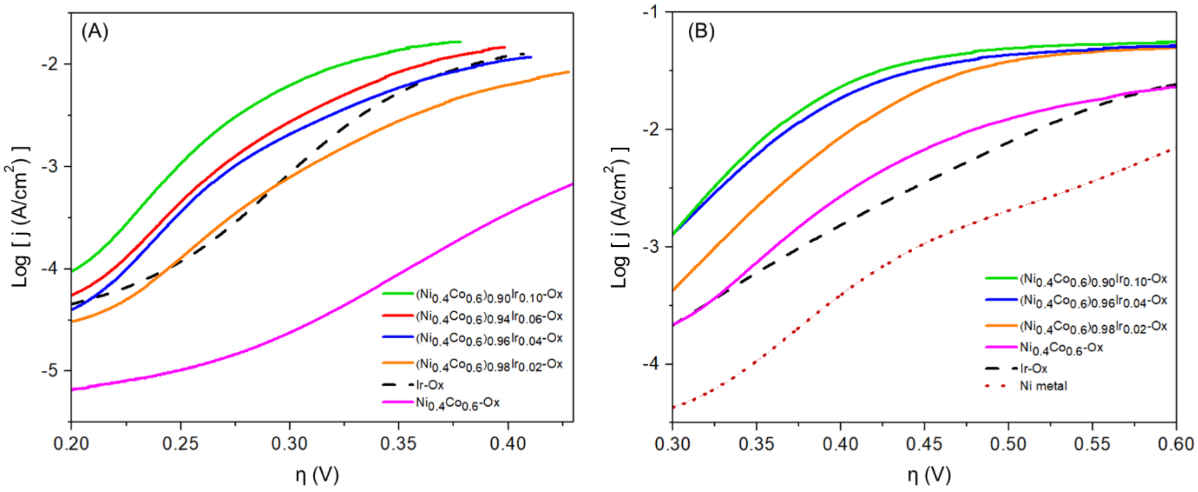

Figure 4.5: Tafel polarization curves recorded on (Ni$_{0.4}$Co$_{0.6}$)$_{1-x}$Ir$_x$-oxide samples in (a) 0.5 M H_2SO_4 and (b) 1M NaOH, including Ni control. Sweep rate: 1 mV/s.

At higher overpotentials, the curves start to level off into a plateau, and this effect was more pronounced in the basic medium. This could be due to decrease in surface area of the electrode in contact with the electrolyte as bigger oxygen bubbles are formed, which are harder to detach from the anode surface, thereby decreasing the effective surface area of the anode. However, at lower overpotentials, the curves exhibit the typical linear Tafelian behaviour. The Tafel slope values extracted from these linear sections are presented in Table 4.2.

Table 4.2: Tafel slope values for the OER obtained from the Tafel curves in Figure 4.5.

Sample	Tafel slope (mV/dec) Acid	Base
$Ni_{0.40}Co_{0.60}$-Ox	81.0 ± 0.4	80.8 ± 0.8
$(Ni_{0.4}Co_{0.6})_{0.98}Ir_{0.02}$-Ox	58.8 ± 1.2	73.5 ± 5.1
$(Ni_{0.4}Co_{0.6})_{0.96}Ir_{0.04}$-Ox	45.5 ± 1.5	67.4 ± 5.4
$(Ni_{0.4}Co_{0.6})_{0.94}Ir_{0.06}$-Ox	46.7 ± 1.2	64.3 ± 0.7
$(Ni_{0.4}Co_{0.6})_{0.90}Ir_{0.10}$-Ox	43.6 ± 0.9	62.1 ± 2.7
Ir-Ox	59.8 ± 1.2	108.8 ± 4.2
Ni metal	-	85.2 ± 3.8

It has been demonstrated in the literature that Tafel slope is an important kinetic parameter observed in OER electrocatalytic measurement and it is given by a rate-determining step (*rds*) within the pertaining OER reaction mechanism [79, 201].

In the 0.5 M H_2SO_4 solution, this slope decreases from ca. 81 to 44 mV/dec, as the Ir content in the $(Ni_{0.4}Co_{0.6})_{1-x}Ir_x$-oxide surfaces increases, indicating an improvement in electrocatalytic activity in comparison to the binary $Ni_{0.4}Co_{0.6}$-oxide and IrO_2. These values are close to those reported for other Ir-based oxides [68, 176, 185]. Hence, for $(Ni_{0.4}Co_{0.6})_{1-x}Ir_x$-oxide coatings with $0< x<0.04$ and for pure Ir-oxide, with Tafel slope around and slightly different from 60 mV/dec, the rate-determining step in the mechanistic pathway for the OER is the formation step of $M\text{-}OH_{ads}$, as shown in previous work [185]. On the other hand, for $0.04\geq x\leq 0.1$, the Tafel slope values are suggestive that the oxide path is the *rds* [90, 185].

In another case, the Tafel slopes derived from the LSV measurements in 1M NaOH electrolyte ranged from ca. 62 to 109 mV/dec, decreasing with increase in Ir content in $(Ni_{0.4}Co_{0.6})_{1-x}Ir_x$-oxide, from 81 to 62 mV/dec. The result in Table 4.2 affirms that pure Ir-oxide tends to have a high OER Tafel slope value in alkaline solution [92, 202] in comparison to acidic solution [176]. On the other hand, the Tafel slopes for all $(Ni_{0.4}Co_{0.6})_{1-x}Ir_x$-oxide coatings are around 65 mV/dec, and that of $Ni_{0.4}Co_{0.6}$-oxide is 81 mV/dec, suggesting that the OER might be following the same mechanism on these surfaces.

However, it must be noted that literature has suggested that a *rds* cannot be determined solely on the basis of Tafel slope, since different *rds* in different reaction mechanisms can yield similar Tafel slope values [79].

In order to more clearly compare the electrocatalytic behaviour of the anodes presented in Figures 4.5(A and B), the current density at three selected overpotentials is presented as a function of electrode composition, Figure 4.6. As it can be seen, the behaviour is linear in the acidic electrolyte; with an increase in Ir content in the oxide, the corresponding OER current increases linearly at all three overpotential values. This indicates that the OER activity of the $(Ni_{0.4}Co_{0.6})_{1-x}Ir_x$-oxides in the acidic medium is directly proportional to the amount of Ir in the oxide in this composition range; however, it should be noted that the reference 100% Ir-oxide yielded OER activity that is only slightly higher than that of $(Ni_{0.4}Co_{0.6})_{0.98}Ir_{0.02}$-oxide, but significantly lower than that of $(Ni_{0.4}Co_{0.6})_{0.9}Ir_{0.1}$-oxide. This suggests that there is synergy in the OER activity of $(Ni_{0.4}Co_{0.6})_{1-x}Ir_x$-oxides due to the mutual actions of Ir-oxide and $Ni_{0.4}Co_{0.6}$-oxide. Furthermore, the fact that the activity of pure $Ni_{0.4}Co_{0.6}$-oxide (0% Ir) is significantly lower than $(Ni_{0.4}Co_{0.6})_{0.98}Ir_{0.02}$-oxide activity (Figure 4.5(A)) further justifies the previous statement.

The same conclusions presented above can also be applied for the performance of $(Ni_{0.4}Co_{0.6})_{1-x}Ir_x$-oxides in the alkaline electrolyte (Figure 4.6(B)); however, the increase in OER activity with Ir content is not linear. Nevertheless, the existence of synergy in the $(Ni_{0.4}Co_{0.6})_{1-x}Ir_x$-oxides is also, here, quite clearly evident. In addition, one can see that the $(Ni_{0.4}Co_{0.6})_{1-x}Ir_x$-oxide anodes yield much higher OER activity not only in comparison to pure Ir-oxide, but also with respect to the state-of-the-art anode commonly used in commercial alkaline electrolysers - nickel.

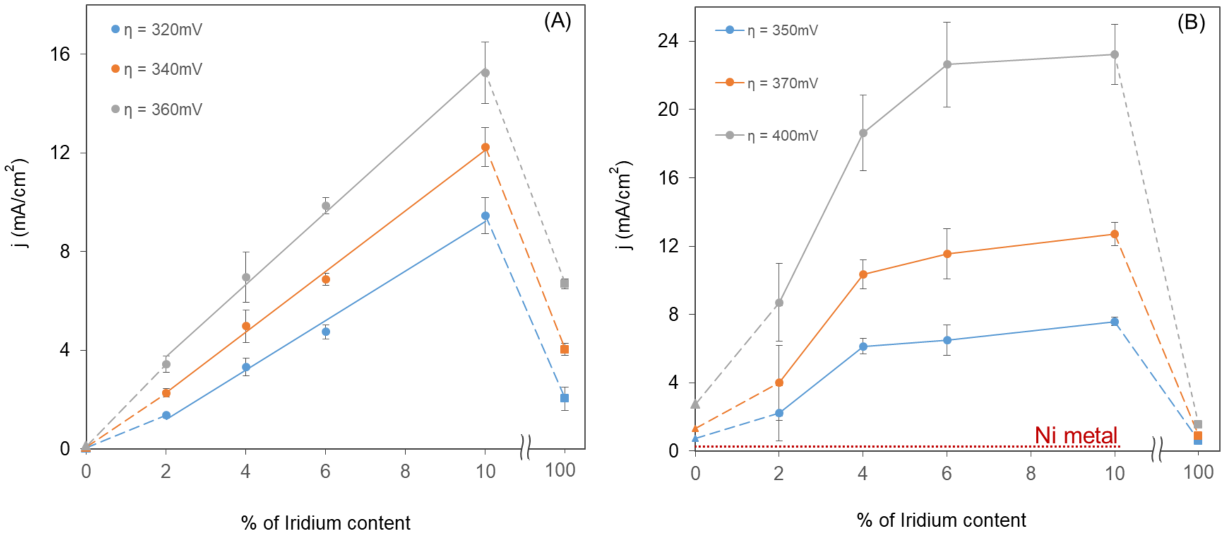

Figure 4.6: Variation of oxygen evolution current density at fixed overpotential, as a function of Ir content in the $(Ni_{0.4}Co_{0.6})_{1-x}Ir_x$-oxide in (A) 0.5 M H_2SO_4 and in (B) 1M NaOH. Note that the dashed horizontal line in (B) represents the OER current recorded on nickel at an overpotential of 400 mV.

As seen in Figure 4.6, the $(Ni_{0.4}Co_{0.6})_{1-x}Ir_x$-oxide with only 10 at.% Ir offers a significantly higher OER activity than the corresponding state-of-the-art control samples – pure IrO_2 and metallic Ni. This is also true when comparing the performance of $(Ni_{0.4}Co_{0.6})_{1-x}Ir_x$-oxides to the performance of IrO_2 and Ni anodes studied by other groups, in the corresponding electrolytes [44, 202, 203]. Moreover, the $(Ni_{0.4}Co_{0.6})_{0.9}Ir_{0.1}$-oxide anode yields an OER overpotential of 320 mV at 10 mA/cm^2 in H_2SO_4, which is lower than values reported for some other metal-oxide anodes with even higher Ir content, such as 330 mV for $Ir_{0.7}Co_{0.3}O_x$ [204], 335 mV for $Ir_{0.7}Ni_{0.3}O_{2-y}$ [205], 365 mV for $Bi_2Ir_2O_7$ [206], and 394 mV for RuIrCoOx [207].

Although for practical purpose, it is useful to compare catalytic activities based on geometric surface area, the main goal of this work was to investigate the *intrinsic* effect of Ir addition to $Ni_{0.4}Co_{0.6}$-oxide on the resulting performance of the material in the OER. In order to do this, the effect of surface area needs to be subtracted from the overall performance of the anode materials. For this purpose, the electrochemically-active surface area (EASA) of all the electrodes was determined by employing the well-established hexaammineruthenium III/II chloride reversible redox probe [145, 185], and the obtained EASA values are presented in Table 4.3.

Table 4.3: The electrochemically-active surface area (EASA) obtained from cyclic voltammetry data. The geometric area of electrolyte-exposed electrodes is 0.43 cm^2.

Sample	EASA (cm^2)	Ref
$Ni_{0.4}Co_{0.6}$-Ox	0.313 ± 0.005	[1]
$(Ni_{0.4}Co_{0.6})_{0.98}Ir_{0.02}$-Ox	0.354 ± 0.013	This work
$(Ni_{0.4}Co_{0.6})_{0.96}Ir_{0.04}$-Ox	0.338 ± 0.008	This work
$(Ni_{0.4}Co_{0.6})_{0.94}Ir_{0.06}$-Ox	0.348 ± 0.003	This work
$(Ni_{0.4}Co_{0.6})_{0.90}Ir_{0.10}$-Ox	0.362 ± 0.004	This work
Ir-Ox	0.373 ± 0.005	[1]

Considering the SEM images in Figures 4.1(A – F), which show that the electrode surfaces are rather rough, it can be deduced from Table 4.3 that part of the total geometric surface (0.43 cm^2) is not electrochemically active. The possible explanations for part of the surface being electrochemically inactive could be due to the lack of accessibility of the electrolyte to the entire coating surface as a result of coating pore size distribution and also because parts of the surface are electrically non-conducting. Further, except for 2% Ir, the dependence of EASA on Ir content is highly linear ($R^2 = 0.9987$). Taking the values in Table 4.3 into account, the data from Figure 4.6 were normalized with respect to the EASA and the corresponding trends (Figure 4.10 – supplementary data) are very similar to the trends for the extrinsic behaviour of the coatings shown in Figure 4.6. Hence, the observed differences in OER performance are of intrinsic nature. Therefore, these results evidence that $(Ni_{0.4}Co_{0.6})_{0,9}Ir_{0.1}$-oxide is the best anode material investigated in this work, showing a much higher intrinsic OER electrocatalytic activity in the acidic and alkaline medium than the current state-of-the-art, IrO_2 and Ni, respectively. Notably, this material has an analogous activity to some of the best OER electrocatalyst reported in the literature [63, 66, 79, 186, 192, 193].

One possible explanation for the observable improvement in the OER activity of the $Ni_{0.4}Co_{0.6}$-oxide coating by incorporating iridium into its structure may be related to the synergistic interaction among the three metals in the oxide, as already mentioned before, leading to the modification of the f-shell electronic structure of Ir, as shown by the XPS result (Figure 4.4(C)). Consequently, Ir not only increases the number of active sites [192] but also stabilizes the Co active sites in the base material. A further contribution to the increased OER activity of

$(Ni_{0.4}Co_{0.6})_{0.90}Ir_{0.10}$-oxide could come from the narrowing of the band gap [185]. As shown in Table 4.4, the band gap in $(Ni_{0.4}Co_{0.6})_{0.9}Ir_{0.1}$-oxide is narrower than those of $Ni_{0.4}Co_{0.6}$-oxide [180, 185] and IrO_2 [208], which is also related to the change in the electronic structure of the materials (Figure 4.4) and has been discussed in detail by Ryang et al. [209].

Table 4.4: Measured energy band gap of Ni, Co, Ni-Co and Ni-Co-Ir oxide coatings.

Sample	Band gap (eV)	Ref
Ni-Ox	2.15 ± 0.01	This work
Co-Ox	2.09 ± 0.02	[1]
$Ni_{0.4}Co_{0.6}$-Ox	1.59 ± 0.07	[1]
$(Ni_{0.4}Co_{0.6})_{0.90}Ir_{0.10}$-Ox	1.46 ± 0.03	This work
Ir-Ox	2.38 ± 0.21	This work

The observed difference in intrinsic electrocatalytic activity could also be related to the contribution of “adsorbed oxygen” on the ternary oxide, which emanates from the iridium oxide as shown in Figure 4.4(D). This adsorbed nonstoichiometric near-surface oxygen can cause partial polarization of cobalt [208] from Co^{2+} to Co^{3+} leading to oxygen vacancies known to influence OER activity [141, 164]. Moreover, the high-resolution O 1s spectra of the $(Ni_{0.4}Co_{0.6})_{1-x}Ir_x$-oxides indicate that the surfaces exist partly in a hydrous state. The increased presence of hydroxide surface species, evident from the O^{2-}:OH ratio change from 4:1 in the $Ni_{0.4}Co_{0.6}$-oxide [185] to 4:3 in the $(Ni_{0.4}Co_{0.6})_{1-x}Ir_x$-oxides may significantly contribute to the enhancement in OER activity [198].

4.4.5. Electrocatalytic stability in OER

The OER electrocatalytic stability of a catalyst is as important as its activity since an active anode is expected to function over a long-term service period. Therefore, the stability of the best performing electrocatalyst, $(Ni_{0.4}Co_{0.6})_{0.9}Ir_{0.1}$-oxide, was investigated in 0.5 M H_2SO_4 and in 1 M NaOH *via* chronopotentiometric measurements at a current density of 10 mA cm^{-2} over a period of 24 h The results depicted in Figure 4.7 show that the electrocatalyst is stable over the investigation time span. However, it can be observed that, initially, the overpotential slightly increased and later stabilised. This minor increase in overpotential can be attributed to the decrease in the available surface area of the electrode due to the blockage of narrow pores by produced oxygen bubbles. This was verified by performing subsequent experiments using the same electrodes after the 24 h of electrolysis and after shaking off (detaching) oxygen bubbles; the recorded curves were superimposed onto the curves from the preceding experiments.

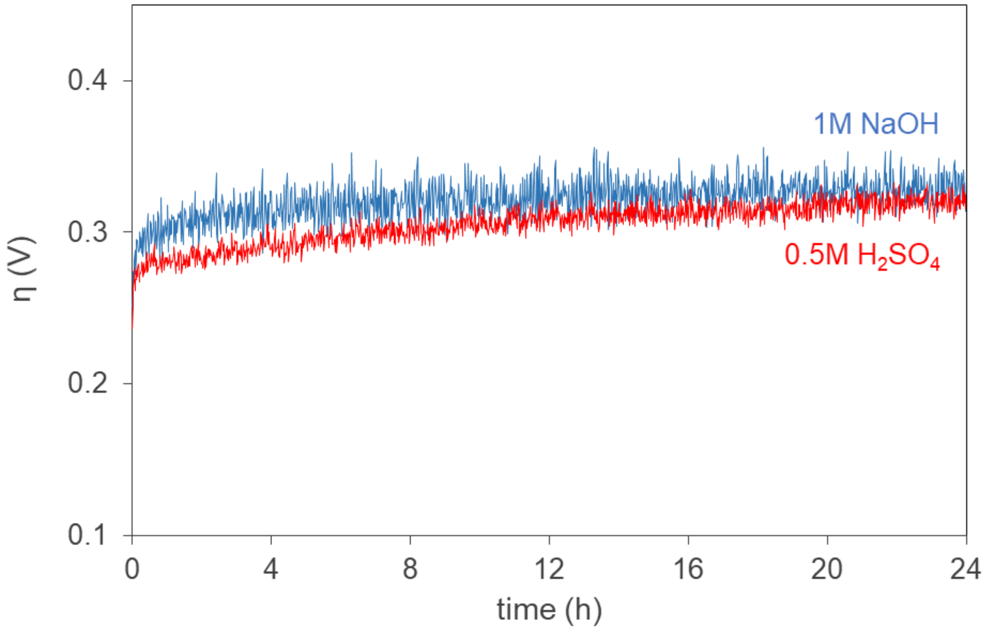

Figure 4.7: Long-term stability test measured galvanostatically at 10 mA / cm^2 on $(Ni_{0.4}Co_{0.6})_{0.9}Ir_{0.10}$-oxide electrode in 0.5M H_2SO_4 and 1M NaOH.

The above-stated observations were corroborated by the SEM images presented in Figure 4.8, which shows that the morphology of the catalyst, after the long-term electrolysis, did not change significantly in comparison to that of the freshly-prepared surface (Figure 4.1(E)).

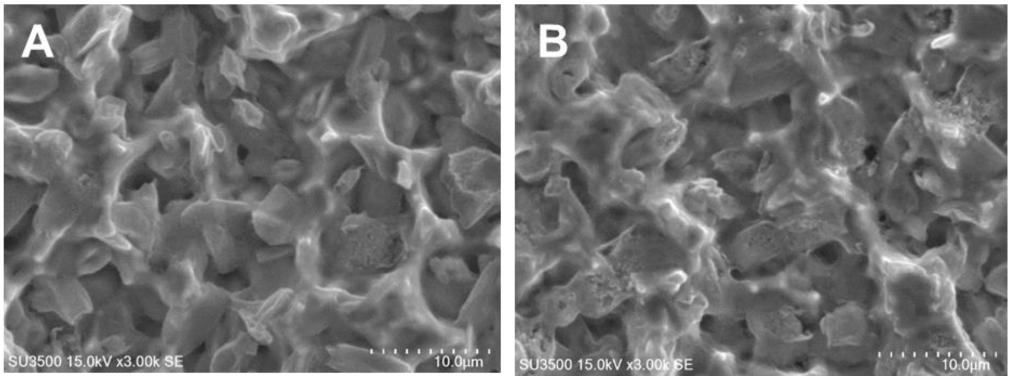

Figure 4.8: The SEM images of $(Ni_{0.4}Co_{0.6})_{0.90}Ir_{0.10}$-oxide surface after 24 h of electrolysis at 10 mA / cm^2 in (A) 0.5 M H_2SO_4 and (B) 1M NaOH.

Further, at the end of the electrolysis experiment, Tafel polarization curves were recorded on the sample using fresh electrolytes and then compared with those recorded initially on the freshly-prepared electrode, prior to the start of the electrolysis so as to study possible changes in its activity. The activity before and after the 24-hour electrolysis was the same, also evidencing the good stability of the surface.

4.5. Conclusion

Addition of small amount of Ir to $Ni_{0.4}Co_{0.6}$-oxide increases its electrocatalytic activity towards OER, yielding an efficient material that could be a cost-effective replacement for the expensive current state-of-the-art IrO_2 anodes in acidic water electrolysis. The electrochemical tests in this study revealed rising trend in electrocatalytic performance of $(Ni_{0.4}Co_{0.6})_{1-x}Ir_x$-oxide coatings with Ir content, dominated by the intrinsic electrocatalytic properties of the material. The $(Ni_{0.4}Co_{0.6})_{0.90}Ir_{0.10}$-oxide composition was found to be significantly more active than IrO_2, while also offering a considerably higher OER electrocatalytic activity than Ni anodes used in alkaline electrolysers.

Results from SEM imaging show that the granular-type morphology of the as-synthesized coatings is composition-dependent, while the EDX and XPS characterization of the coating surface confirmed that the actual composition of the top layer of the coating is very close to its targeted (nominal) composition and the distribution of Ni, Co and Ir in the top layer of the coating is uniform. The XRD analysis confirmed the crystalline nature of the coatings.

The XPS analysis elicits evidence of a synergistic relationship among crystalline IrO_2, Co_3O_4, CoO and NiO in the ternary mixed metal oxide coatings which resulted in the modification of the Ir f-shell electronic configuration that correlates with increased catalytic activity.

Acknowledgement: The authors are highly indebted to the Nigerian Petroleum Technology Development Fund (PTDF), Natural Sciences and Engineering Research Council of Canada (NSERC), and the McGill Engineering Doctoral Award (MEDA) for their immense financial support.

4.6. Appendix A. Supplementary material

This section contains the supplemental file to the manuscript.

Oxygen evolution current density versus applied voltage on the $(Ni_{0.4}Co_{0.6})_{1-x}Ir_x$-oxide in (A) 0.5 M H_2SO_4 and in (B) 1M NaOH

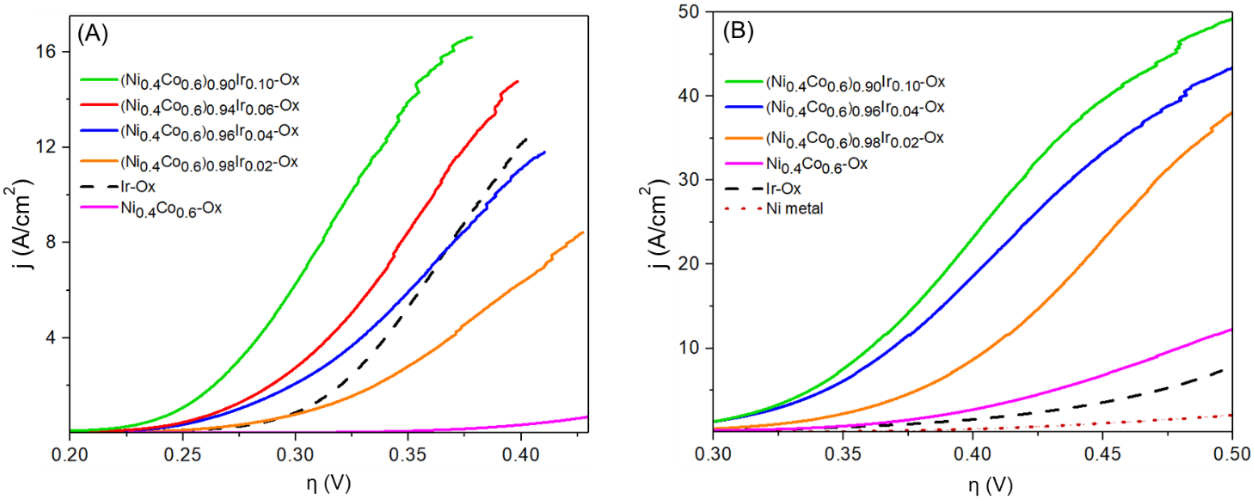

Figure 4.9: LSV curves recorded on $(Ni_{0.4}Co_{0.6})_{1-x}Ir_x$-oxide samples in (A) 0.5 M H_2SO_4 and (B) 1M NaOH, including Ni control. Sweep rate: 1 mV/s.

Variation of oxygen evolution current density at fixed overpotential, as a function of Ir content in the $(Ni_{0.4}Co_{0.6})_{1-x}Ir_x$-oxide in (A) 0.5 M H_2SO_4 and in (B) 1M NaOH based on the electrochemically-active surface area

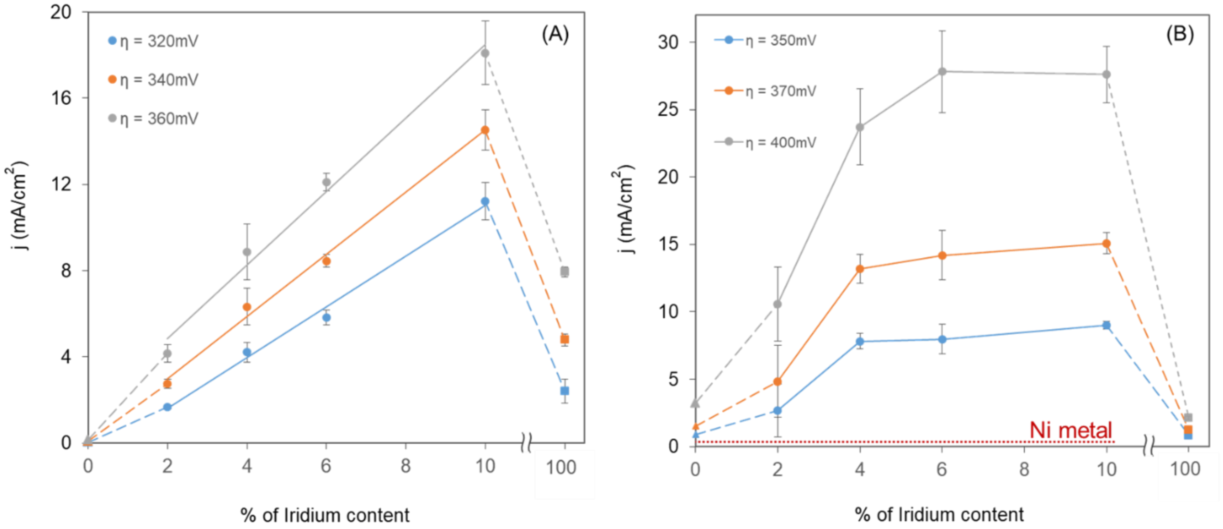

Figure 4.10: Results from Figure 4.6 normalized with respect to the electrochemically-active surface area (EASA).

Chapter 5 - The Effect of Calcination Temperature on the Electrocatalytic Activity of Ni-Co-Ir-oxide and Ni-Co-Ru-oxide Anodes in the Oxygen Evolution Reaction in Alkaline Medium

Emmanuel Onyekachi Nwanebu*, Nathalie Abou Harb, Raed Gharbi and Sasha Omanovic

Department of Chemical Engineering, McGill University, 3610 University St., Montreal,
Quebec, H3A 0C5, Canada

*corresponding author: emmanuel.nwanebu@mail.mcgill.ca

5.1. Preface

The previous chapter presented results on the influence of Ir content on the electrocatalytic properties of $Ni_{0.4}Co_{0.6}$-oxide in the oxygen evolution reaction. It was demonstrated that the OER activity of the binary oxide was significantly enhanced with the addition of 10 at.%Ir, surpassing the state-of-the-art IrO_2 in the acidic electrolyser and the Ni anodes typically used in the alkaline electrolysers while maintaining good durability. It was found that the oxygen evolution current density (activity) at fixed overpotentials increased linearly with Ir content (≤10%) in the acidic medium. Though the same linear variation was not observed in the alkaline solution, nevertheless, the improvement in activity was likewise significant.

In light of the above-stated outcomes and with a view of developing low-cost, active and stable OER anodes, it was hypothesized that $Ni_{0.4}Co_{0.6}$-oxide could have similar beneficial intrinsic synergistic interaction with a low content of incorporated Ru especially since RuO_2, the best known OER catalyst in the alkaline medium, is scarce and expensive. Furthermore, it has been shown in the literature that the charge storage capacity of Ir- and Ru-oxides may vary as a function of fabrication (calcination) temperature. This prompted us to investigate whether the same would influence the kinetics of the OER on these surfaces.

This chapter presents the results on the effect of fabrication (calcination/annealing) temperature on the OER electrocatalytic performance of the thermally-prepared NiCoRu- and NiCoIr-oxides. It will be shown that the fabrication temperature had a profound effect on the OER electroactivity of the trimetal oxides. The improvement in specific OER activity was associated with the modification of the electronic structure and to the increase in hydroxide content and oxygen vacancies in the oxides.

The work has been submitted for publication to a peer-reviewed journal, and the corresponding reference is: E. O. Nwanebu, N. Abou Harb, R. Gharbi, and S. Omanovic, "The Effect of Calcination Temperature on the Electrocatalytic Activity of Ni-Co-Ir-oxide and Ni-Co-Ru-oxide Anodes in the Oxygen Evolution Reaction in Alkaline Medium ," submitted to the *Solid State Sciences* journal .

.

Highlights

- Calcination temperature influences the electrocatalytic activity of NiCoRu/Ir-oxides
- Maximum electrocatalytic activity in oxygen evolution is achieved at 300°C
- NiCoRu/Ir(300^{o}C)-oxides performed better or close to pure Ir- and Ru-oxide
- There exists synergy between NiCo-oxide and Ir/Ru when used as oxygen anodes

Abstract

The influence of calcination temperature on the electrocatalytic properties of thermally-prepared $(Ni_{0.4}Co_{0.6})_{0.90}Ir_{0.10}$-oxide and $(Ni_{0.4}Co_{0.6})_{0.90}Ru_{0.10}$-oxide in the oxygen evolution reaction (OER) was investigated in an alkaline medium. It was shown that by lowering the calcination temperature, the OER activity of the two materials increased significantly, yielding a maximum at 300^{o}C. The increase in electrocatalytic activity of the oxides was related to the change in intrinsic properties of the anodes, predominantly to the modification of the electronic structure and to the increase in hydroxide content. Despite the relatively low content of the two noble metals in the synthesised oxides, $(Ni_{0.4}Co_{0.6})_{0.90}Ir_{0.10}$-oxide was found to significantly outperform the current state-of-the-art OER electrocatalyst, pure Ir-oxide, while the electrocatalytic activity of $(Ni_{0.4}Co_{0.6})_{0.90}Ru_{0.10}$-oxide was measured to be much higher than that of the $Ni_{0.4}Co_{0.6}$-oxide base, thus demonstrating the synergistic action of Ni/Co/Ir and Ni/Co/Ru in their oxides. These results suggest that the fabrication of the trimetal oxides at the appropriate temperature can be an approach for augmenting the OER performance of the anode materials.

Keywords: Hydrogen; Oxygen; Alkaline water electrolysis; Anodes; Metal Oxides; Temperature; Nickel; Cobalt; Iridium; Ruthenium

5.2. Introduction

The demand for clean energy continues to be one of the most pressing needs of our society today. As the population of the world continues to rise, there is an equivalent increase in energy demand to meet its ever-evolving economic, social and technological development. Hence, meeting this growing global energy demand in an environmentally-responsible fashion is very important for the future of our planet. Currently, fossil fuels serve as the primary source of energy. However, this resource is limited in supply, and its persistent usage is damaging to the environment. In the past few decades, the aforementioned environmental impact of fossil fuel usage has become more pronounced due to increased demand for energy. Hence, it is paramount to develop alternative sustainable energy sources. One promising alternative energy solution that has gained massive interest over the past few years is the use of hydrogen as an energy carrier [210]. Hydrogen has very high specific (mass-based) energy density, yet an engine (internal combustion engine or fuel cell) that uses pure hydrogen produces just water. The National Aeronautics and Space Administration (NASA) [211] has been using liquid hydrogen as rocket fuel for decades, to propel space shuttles and other rockets into the orbit. Further, other commercial applications for hydrogen include fuel cell vehicles (FCV) such as passenger cars and buses which have been running for several years now, around the world [212, 213].

As of today, most commercially-produced hydrogen emanates from fossil fuel sources primarily via steam reforming process [34, 214]. This is due to the fact that the technology is cost-effective since it requires lower fixed and operating costs. However, it does not address the adverse effects of fossil fuel use. In a future energy scenario based on renewable sources, an environmentally-friendly way of producing hydrogen is best achieved through water-splitting. Water electrolysis, when coupled with other sustainable external energy sources like solar and wind, produces hydrogen that can be deployed as a simple non-toxic way of storing, transporting and availing energy.

Nevertheless, the main obstacle facing hydrogen production from water electrolysis is the energy efficiency limitation of the technology. The energy inefficiency is mostly due to the large overpotential requirement of its anodic oxygen evolution reactions (OER), in comparison to the cathodic hydrogen evolution reaction (HER) [215, 216]. Thus, to optimise the overall water-splitting process, considerable research efforts have been devoted, over the years, to the synthesis and characterisation of efficient anode materials to achieve useful OER rates. In addition to having a low overpotential, a commercially-viable anode should possess a large specific surface area, good electrical conductivity, electrochemical and corrosion stability, low cost, and safe handling [57, 169, 217].

At practical OER current densities, the lowest known overpotentials are attributed to the expensive platinum, ruthenium, and iridium oxide anodes [57, 218]. However, besides being very expensive, these noble metal oxides suffer from poor chemical stability, especially in acidic media [219, 220]. In order to maximise their performance and minimise cost, previous research works [220] have focused on creating mixed metal oxides (MMO) composed of precious metal oxides of faster OER kinetics and other cheaper metal oxides of sufficient OER electrocatalytic activity such as tin [93], tantalum [221] manganese [222] just to name a few, resulting in MMOs with improved stability due to the combined effects of the metals acting synergistically together. Another approach widely employed entails the engineering of nano-based materials with immensely large specific catalytically-active surface area for enhanced extrinsic properties of the metal oxide anodes [64, 65, 91]. Moreover, other studies worked on varying the temperature under which the oxides are formed [69, 223-225]. Interestingly, the investigated materials had better electrocatalytic activities when thermally-prepared at lower temperatures but showed more inferior electrochemical stability.

Moreover, the high cost and scarcity of the precious metals make their commercial utilisation impractical. This has motivated an extensive search for earth-abundant electrocatalysts with particular emphasis on the various oxides of first-row transition metals, such as nickel [82, 117, 226] and cobalt [86, 118]. These non-noble metals have relatively low cost and long-term corrosion resistance in alkaline solution, making them attractive, alternative OER anode materials. In fact, various research studies carried out in several laboratories, including ours, found that Ni-Co mixed metal oxides offer comparable performance to that of noble metals [185, 227, 228]. Furthermore, the Ni anode is considered the state-of-the-art catalyst in the alkaline electrolyser. In a previous study investigating the electrocatalytic activity of low-cost mixed metal oxides of nickel and cobalt, it was found that $Ni_{0.4}Co_{0.6}$-oxide exhibited the highest activity and reasonable stability of all the prepared binary oxides of various Ni/Co ratios, in a harsh acidic medium [185]. Hence, the aforementioned material served as reference material in the current work.

5.3. Experimental Procedure[7]

5.3.1. Electrode Synthesis

The coatings of $(Ni_{0.4}Co_{0.6})_{1-x}Ru_x$-oxide and $(Ni_{0.4}Co_{0.6})_{1-x}Ir_x$-oxide were formed on titanium coins (Grade 2, 99 % pure, McMaster Carr) through a thermal decomposition method. The titanium substrates of diameter and thickness 1.21 and 0.2 cm, respectively, were first pretreated by wet-polishing using 600-grit SiC grinding paper. Afterwards, they were rinsed in nanopure water (resistivity: 18.2 MΩ cm) and sonicated in ethanol for 30 min to dislodge polishing residues. The samples were then etched in a boiling equivolume mixture of HCl and nanopure water for 30 min and dried with argon gas (purity 99.998 wt.%, MEGS Specialty Gases Inc., Canada) [185].

The coating materials were prepared from a 0.5M precursor salt solutions of nickel, cobalt, ruthenium and iridium made by dissolving $NiCl_2 \cdot 6H_2O$ (ReagentPlus, 100%, Sigma Aldrich), $Co(NO_3)_2 \cdot 6H_2O$ (99% pure, ACROS Organics), $RuCl_3 \cdot 3H_2O$ (≤100%, Sigma Aldrich), and $IrCl_3 \cdot 3H_2O$ (purity 53-56% Ir, Fisher Scientific Acros), respectively, in an equivolume mixture of isopropanol (Fisher Scientific) and nanopure water. Desired coating compositions were made by mixing the corresponding stock solutions, and the resulting 2 mL coating solutions were sonicated for 10 min in an ice bath to obtain homogeneous intact solutions [185].

Each precursor solution was applied evenly on the pretreated surface of the titanium substrate with a standard paintbrush. The coated substrate was then placed in an oven at 110 °C for 5 min to vaporize the solvent and then calcinated for 15 min at the predetermined temperature in a furnace to obtain the first oxide layer. The calcinated sample was left to cool to ambient temperature. Afterwards, further five oxide layers were applied in a similar fashion. After applying the last layer, the coating was calcined (annealed) for one hour to produce a coating material. In order to investigate the effect of annealing temperature on the catalytic performance of the coatings, the requisite samples were prepared at the following temperatures: 250°C, 300°C, 400°C, 500°C and 700°C.

---

[7] The measurements were done in multiplets and the presented data are the average values including the corresponding standard errors.

5.3.2. Surface Characterization

A scanning electron microscope (Hitachi SU3500) was used to study the surface morphology of the oxide coatings while their surface chemical compositions were determined through energy-dispersive X-ray spectroscopy (EDX).

Further, a Bruker Discover D8-2D diffractometer with a collimated Cu Kα radiation source ($\lambda = 1.5406$ Å, 40kV, 40mA) was used to characterize the crystalline structure of the various oxide phases via grazing incidence X-ray diffraction (GIXRD). The instrument was operated in a step scanning mode with step size of 0.005° 2θ. The monochromatic X-ray beam grazed the surfaces at a fixed, low glancing angle, $\alpha = 2°$.

X-ray photoelectron spectroscopy (XPS) was used to determine the surface chemical composition and state of the oxides by using a K-Alpha X-ray photoelectron spectrometer (Thermo Fisher Scientific, USA) of Al Kα radiation source (1486.6 eV photon energy, 400 μm spot size).

Finally, a goniometer model OCA 15EC high precision device equipped with a CCD camera (Data Physics, USA) was employed to record the contact angle of the surfaces using the SCA 20 software.

5.3.3. Electrochemical Characterization

Electrochemical tests were carried out in a three-electrode system at the ambient room temperature (296 ± 2 K) in a 1M NaOH (99wt% purity, Fisher Scientific) of $\mathrm{pH} = 13.4$ as electrolyte solution, to study the electrochemical behaviour of the anode materials. Polarization curves for anodes' OER activity were recorded via linear sweep voltammetry (LSV), whereas chronopotentiometric measurements were done to investigate the stability of the coatings in the argon-saturated solution. The electrochemical cell setup comprised the fabricated metal-oxide electrode coatings as the working electrodes (geometric surface area $= 0.43$ cm^2), a graphite counter electrode, which was separated from the main cell electrolyte compartment using a glass frit (Ace Glass, Inc., USA) to prevent hydrogen evolved on it from reaching the anode (working electrode), and of a standard Ag/AgCl (Fisher Scientific, product no. 1362053, sat. KCl) reference electrode. The ohmic resistance between the reference and working electrodes was determined by electrochemical impedance spectroscopy, which was used to correct the polarisation curves for the *iR*-drop.

The electrochemically-active surface area (EASA) of the produced metal oxides was determined by employing the method developed by Trasatti, which is based on the evaluation of double-layer capacitance *via* cyclic voltammetry (CV) [229, 230]. These CVs were recorded in 0.17M Na_2HPO_4 (100wt% purity, Fisher Scientific). All electrochemical tests were performed using Autolab potentiostat/galvanostat analyser (PGSTAT30, Metrohm, NL) controlled by NOVA software (version 2.1.3; Metrohm, NL).

5.4. Results and Discussion

5.4.1. Surface Characterization

The SEM micrographs of the $(Ni_{0.4}Co_{0.6})_{0.90}Ru_{0.10}$-oxide and $(Ni_{0.4}Co_{0.6})_{0.90}Ir_{0.10}$-oxide coatings presented in Figures 5.1(A-J) reveal the surface morphology and structure of the tri-metal oxide surfaces produced at different calcination temperatures. It is noted that relatively homogeneous porous morphologies characterise all the coatings. At 250°C (Figure 5.1(A)), $(Ni_{0.4}Co_{0.6})_{0.9}Ru_{0.10}$-oxide displayed granular agglomerates of particles buried into the coating's porous network. The porous structure, composed of granular particles, became more evident with an increase in temperature, resulting in the formation of larger particles (Figures 5.1(B-E)). This is because the oxide particles gradually agglomerated with an increase in calcination temperature, thereby resulting in particle sintering and an increase in particle size [223]. However, it must be noted that the surface formed at 300°C is largely compact. This less-porous network appears to be dictated by the $Ni_{0.4}Co_{0.6}$-oxide since Figure 5.7(E) reveals a compact fibrous network of $Ni_{0.4}Co_{0.6}$-oxide synthesized at 300°C relative to a much more extensive granular network of particles at 500°C. In addition, Figure 5.1(E) reveals that the surface, formed at 700°C, displays an agglomerated feature of melted particles. This explains the very low electrochemical activity of $(Ni_{0.4}Co_{0.6})_{0.90}Ru_{0.10}$-oxide film at this condition discussed later in the manuscript.

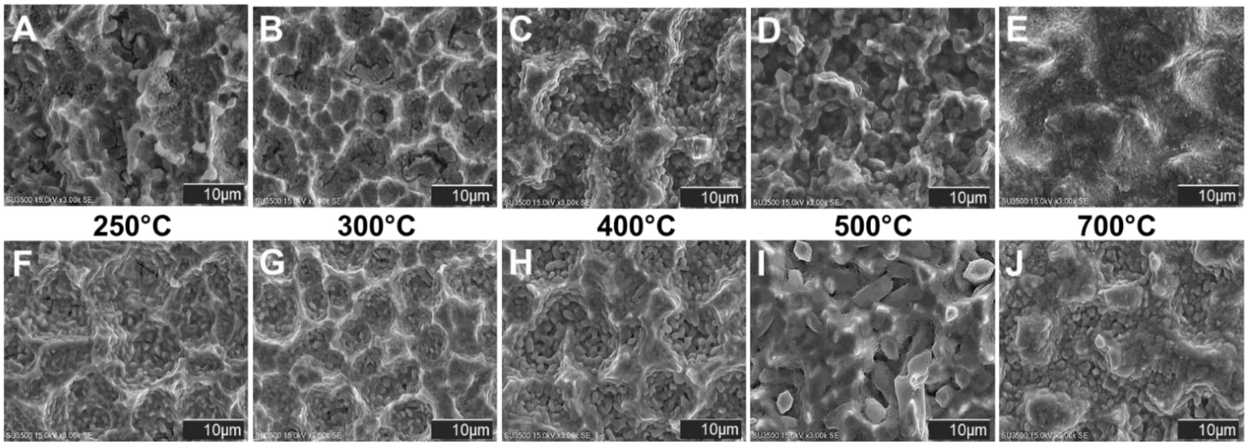

Figure 5.1: SEM images of: (A-E) $(Ni_{0.4}Co_{0.6})_{0.90}Ru_{0.10}$-oxide and (F-J) $(Ni_{0.4}Co_{0.6})_{0.90}Ir_{0.10}$-oxide annealed at temperatures between 250°C and 700°C.

The development of the surface microstructure with temperature for the $(Ni_{0.4}Co_{0.6})_{0.9}Ir_{0.10}$-oxide (Figure 5.1(F-J)) is similar to that of the $(Ni_{0.4}Co_{0.6})_{0.90}Ru_{0.10}$-oxide, with the exception of the surfaces annealed at 700°C. Furthermore, for $(Ni_{0.4}Co_{0.6})_{0.9}Ir_{0.10}$-oxide, the film surface is observed to showcase less deep pores as the size of the granular particles increased with a rise in temperature.

The elemental composition of the coatings was evaluated via EDX elemental mapping analysis. The surfaces revealed uniform dispersion of the corresponding elements (the $(Ni_{0.4}Co_{0.6})_{0.90}Ru_{0.10}$-oxide surface calcined at 300°C is presented for illustration purpose in Figures 5.8(A-C)). Nonetheless, the surface is impacted by the Ti substrate (Figure 5.8(D)), as Ti diffused to the outer surface due to its strong affinity for oxygen [185] and the porous nature of the surface. Consequently, some part of the oxide surface are expected to be less electrochemically active in OER due to the semiconductive TiO_2 areas [231]. The EDX data depicted in Table 5.1 were obtained by analyzing at least five different locations on each material surface. The table shows a good agreement between the empirical results and the nominal coating compositions. The thickness of the oxide layers synthesised at the different temperatures was determined as ca. 3.2 ± 0.5 μm.

Table 5.1: Relative percentage atomic composition of Ni, Co and Ru/Ir in $(Ni_{0.4}Co_{0.6})_{0.9}Ru_{0.10}$-oxide and $(Ni_{0.4}Co_{0.6})_{0.9}Ir_{0.10}$-oxide at varying calcination temperatures, recorded by EDX analysis. The average standard deviation of the data was ca. 0.3%.

Temp (°C)	$(Ni_{0.4}Co_{0.6})_{0.9}Ru_{0.10}$-oxide			$(Ni_{0.4}Co_{0.6})_{0.9}Ir_{0.10}$-oxide		
	% Ni	% Co	% Ru	% Ni	% Co	% Ir
250	32.9	57.6	9.5	31.9	58.3	9.7
300	30.6	59.1	10.2	30.5	59.1	10.4
400	37.1	54.9	8.0	39.1	50.6	10.3
500	37.9	52.7	9.5	35.3	54.8	9.9
700	32.0	59.5	8.5	31.1	59.1	9.8

5.4.2. X-ray Diffraction

The X-ray diffraction patterns of $(Ni_{0.4}Co_{0.6})_{0.90}Ru_{0.10}$-oxide and $(Ni_{0.4}Co_{0.6})_{0.90}Ir_{0.10}$-oxide calcined at different temperatures are depicted in Figure 5.2. The GIXRD technique was employed in order to minimize the typical strong intensity contribution of the underlying Ti metal substrate, due to the depth of penetration of the X-ray [231]. However, the diffraction features at the 2θ values of 35.0° and 40.2° are still present, indicating the presence of Ti, which might be due to the porosity of the oxide films and diffusion of Ti to the outside region of the film [185]. It is observed that the intensity of the 40.2° Ti peak decreased with increasing calcination temperature, which could be due to the decrease in coating porosity, which is in agreement with the SEM results in (Figures 5.1(A-J)).

To further substantiate the degree of oxide coating porosity and its influence on the level of detectable Ti in the outer oxide layer, $(Ni_{0.4}Co_{0.6})_{0.90}Ru_{0.10}$-oxide calcined at 700°C was investigated by both conventional XRD and GIXRD (Figure 5.9(A)); the disappearance of the strong intensity peak of Ti metal at 35.0° and 40.2° in the GIXRD profile is clearly evident, whereas the Ti peaks are much palpable in the conventional XRD, indicating that Ti is much less present in the outer oxide layer. In addition, the superimposed peaks due to Ir-oxide, Co-oxide and Ni-oxide in the 2θ ranges of 35 – 37° and 52 – 56° [185, 231] foretells the emergence of single-composite well-mixed coating layers. On the other hand, the distinct RuO_2 (Figure 5.9(A)) and IrO_2 (Figure 5.2(B)) phases centred around 2θ value of 28° are evident for oxides formed at 700°C, unlike at other temperatures.

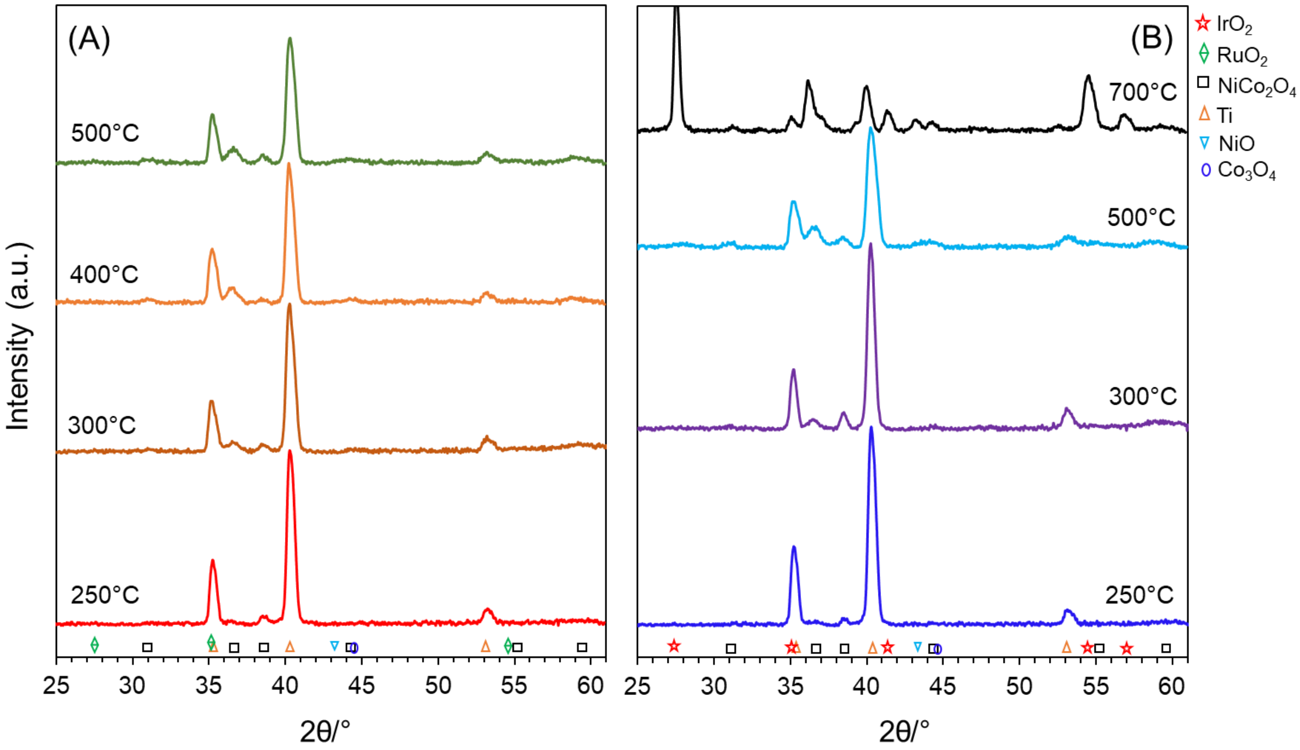

Figure 5.2: Diffraction patterns of: A) $(Ni_{0.4}Co_{0.6})_{0.90}Ru_{0.10}$-oxide and B) $(Ni_{0.4}Co_{0.6})_{0.90}Ir_{0.10}$-oxide coatings deposited on Ti by thermal decomposition at different calcination temperatures.

The XRD analysis of the metal-oxides coatings revealed crystallographic peaks at 31.0°, 36.6°, 38.2°, 44.3°, 55.4°, and 58.9°, with indices of (220), (311), (322), (400), (422), and (511) that are ascribed to a spinel-type nickel-cobalt oxide, $NiCo_2O_4$ (JCPDS, 20-0781) [232, 233] associated with the diffraction peaks of a mixed oxide film composed of Co_3O_4, CoO, and NiO [185, 231]. The stoichiometric conformation of the single mixed oxide phase of $NiCo_2O_4$ in the synthesized coatings was verified by the relative atomic ratio analysis via XPS (Table 5.3), which affirms the average Co to Ni ratio in the coatings as ca. 2, and this is also corroborated by the EDX elemental analysis (Table 5.1).

Furthermore, the spinel $NiCo_2O_4$ oxide phase displayed increasing crystallinity with calcination temperature [231] as highlighted by the strongest crystallographic peak centred at the (311) reflection, thereby suggesting a corresponding increase in the crystallite size (Figure 5.9(B)). To further explore this, the mean particle size of the oxide coatings formed at different calcination temperatures was determined from the (311) facet of $NiCo_2O_4$ using the *Scherrer's* formula [234]. The results in Table 5.2 corroborate the prior deductions from the SEM images, Figures 5.1(A-J).

The average crystallite size increases linearly with calcination temperature, for both oxides. This augmentation in crystallite size with annealing temperature may partly explain the improvement in OER performance of the catalysts with lowering synthesis temperature, as presented later (increase in the surface energy and the number of active sites with a decrease in crystallite size). A similar outcome was observed for pure RuO_2 synthesized at 500°C and 300°C Figure 5.9(A). The noticeable broadening and shift of RuO_2 peaks at 28°, 35°, and 54.2° (ICDD, 43-1027) [203] ascribed to the (110), (101), and (211) reflection planes to higher 2θ values of 28.2°, 35.3°, and 54.4° are the consequence of lattice contraction due to the lowering of the oxide calcination temperature. This can further explain the reduction in particle size and attenuation of crystallinity of the Ni-Co-Ru-oxide. Similar results were observed for $Ni_{0.4}Co_{0.6}$-oxide and Ir-oxide prepared at these temperatures.

Table 5.2: The average crystallite size of $(Ni_{0.4}Co_{0.6})_{0.9}Ru_{0.10}$-oxide and $(Ni_{0.4}Co_{0.6})_{0.9}Ir_{0.10}$-oxide determined at different calcination temperatures.

Temp (°C)	Mean crystallite size, *d* (nm)	
	$(Ni_{0.4}Co_{0.6})_{0.9}Ru_{0.10}$-oxide	$(Ni_{0.4}Co_{0.6})_{0.9}Ir_{0.10}$-oxide
250	12.4	11.8
300	15.8	13.8
400	19.3	18.8
500	20.4	21.7
700	28.9	29.5

5.4.3. X-ray photoelectron spectroscopy

X-ray photoelectron spectroscopy was conducted on the surface of each synthesized oxide layer at three different spots. This study revealed the top-surface atomic metal compositions of the materials. Table 5.3 shows the relative atomic percentage of the component elements on both oxide layers. The presented results are in good agreement with the nominal Ni:Co:Ru and Ni:Co:Ir composition of 36:54:10 in $(Ni_{0.4}Co_{0.6})_{0.9}Ru_{0.10}$-oxide and $(Ni_{0.4}Co_{0.6})_{0.9}Ir_{0.10}$-oxide. These results are also corroborated by the EDX data shown in Table 5.1.

Table 5.3: Relative percentage atomic composition of Ni, Co, and Ru/Ir in $(Ni_{0.4}Co_{0.6})_{0.9}Ru_{0.10}$- and $(Ni_{0.4}Co_{0.6})_{0.9}Ir_{0.10}$-oxides annealed at different temperatures, obtained by X-ray photoelectron spectroscopic measurements. The average standard deviation of the data was ca. 0.2%.

Temp (°C)	$(Ni_{0.4}Co_{0.6})_{0.9}Ru_{0.10}$-oxide			$(Ni_{0.4}Co_{0.6})_{0.9}Ir_{0.10}$-oxide		
	% Ni	% Co	% Ru	% Ni	% Co	% Ir
250	33.3	57.1	9.6	34.8	55.1	10.2
300	30.8	59.2	9.9	30.7	59.7	9.6
400	34.1	55.9	10.0	32.8	58.1	9.1
500	36.2	54.1	9.7	34.6	56.2	9.3
700	30.7	59.6	9.6	30.6	59.4	10.0

The X-ray photoelectron spectra characteristics of O-1s, Ni-2p, Co-2p, Ir-4f and Ru-3d core level peaks of $(Ni_{0.4}Co_{0.6})_{0.9}Ru_{0.10}$- and $(Ni_{0.4}Co_{0.6})_{0.9}Ir_{0.10}$-oxide samples are shown in Figures (5.3 and 5.4) [90, 231]. The deconvoluted spectra of the corresponding samples calcined at 300°C are presented as an example. The obtained XPS profiles were charge-corrected to C 1s (C-C peak of adventitious carbon) set at 284.8 eV [231].

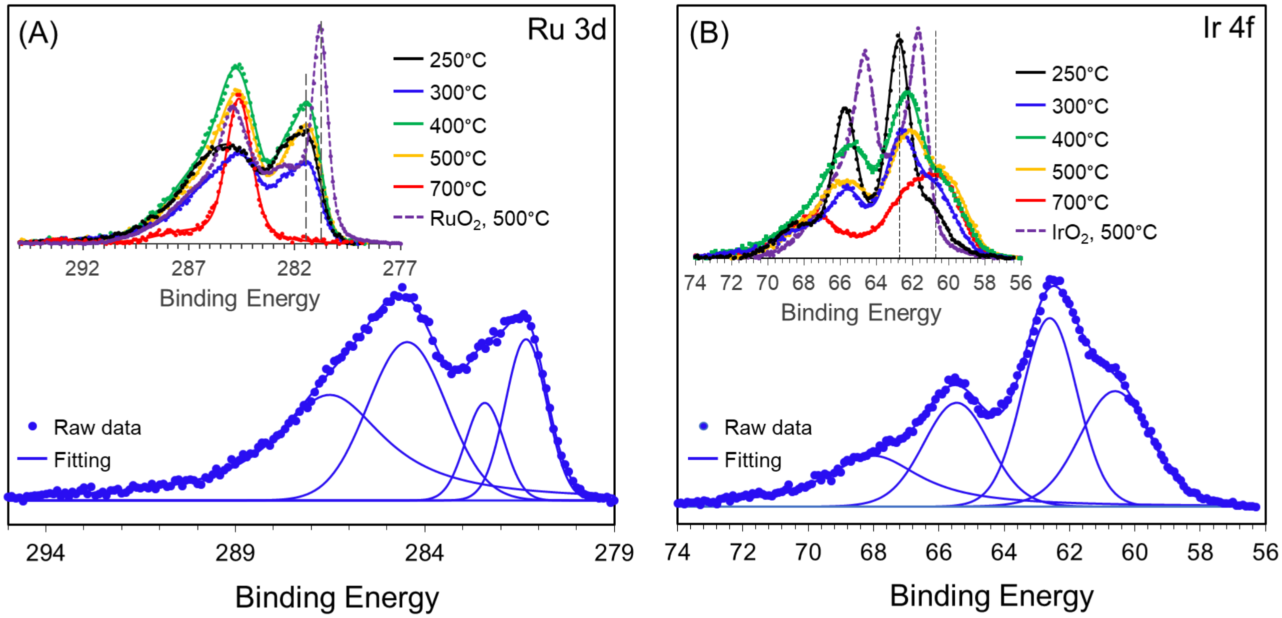

Figure 5.3: XPS profile of as-made (A) $(Ni_{0.4}Co_{0.6})_{0.9}Ru_{0.10}$-oxide in the Ru 3d region and (B) $(Ni_{0.4}Co_{0.6})_{0.9}Ir_{0.10}$-oxide in the Ir 4f region, annealed on Ti substrates at 250 – 300°C range of temperature.

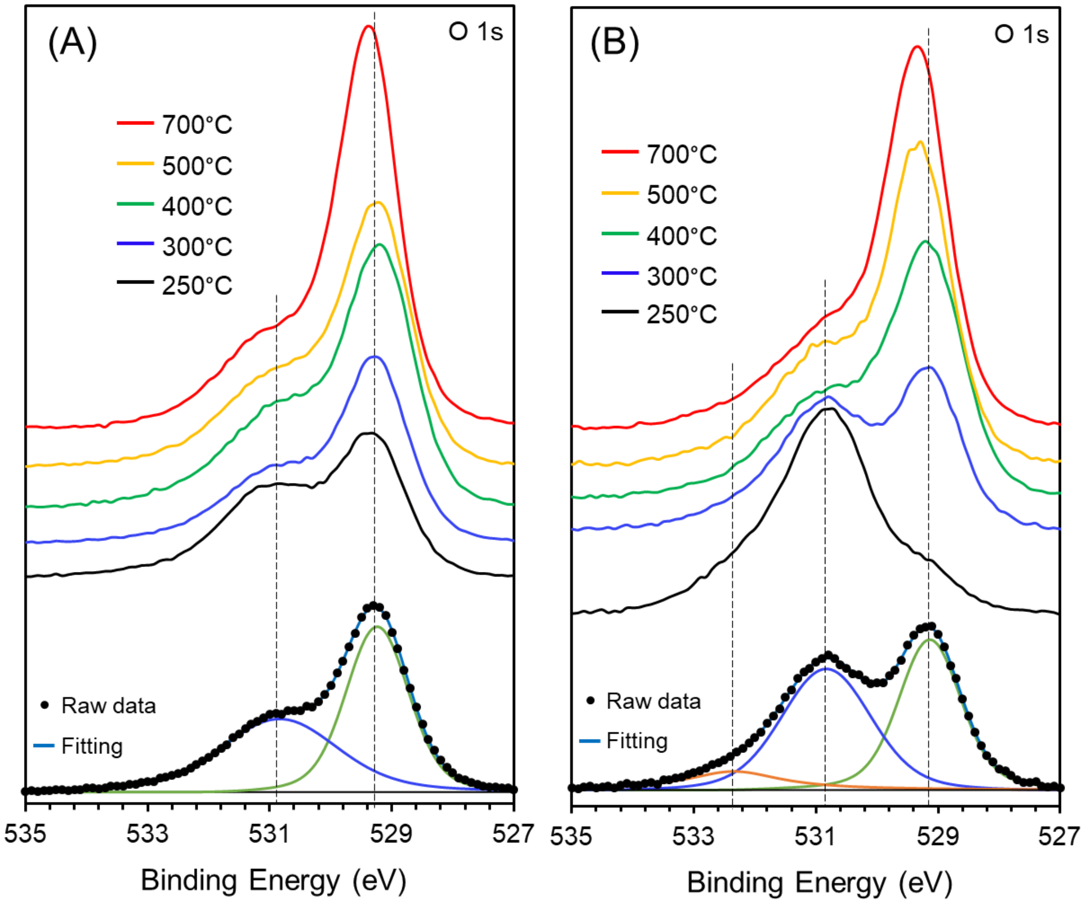

Figure 5.4: XPS spectra of (A) $(Ni_{0.4}Co_{0.6})_{0.90}Ru_{0.10}$-oxide and (B) $(Ni_{0.4}Co_{0.6})_{0.90}Ir_{0.10}$-oxide as a function of calcination temperature showing the binding energies of the deconvoluted O1s peaks of the samples annealed at 300°C.

Figure 5.3(A) showcases the doublet splitting in the Ru-3d spectrum of $(Ni_{0.4}Co_{0.6})_{0.9}Ru_{0.10}$-oxide sample, fabricated at 300°C. The photoelectron peaks centred at around 281.5eV and 284.7 eV are attributed to the Ru $3d_{5/2}$ and Ru $3d_{3/2}$ spin-orbit components of a hydrated RuO_2, respectively [90, 235, 236]. The asymmetric Ru-3d spectrum can be deconvoluted into two core level peaks at 281.3 eV and 284.5 eV and satellite peaks at 282.4 eV and 286.5 eV. The satellite peaks are attributed to the final-state screening effect [90] due to intermediate species associated with hydroxyl groups or oxygen vacancies [231, 237]. Further, it is observed that the $3d_{5/2}$ peak position of pure Ru-oxide centred at 280.8 eV shifted to higher binding energy by ca. 0.5 eV with the addition of $Ni_{0.4}Co_{0.6}$-oxide (see Figure 5.3(A) inset). However, unlike in the pure Ru-oxide, the $3d_{3/2}$ spin-orbit doublet of $(Ni_{0.4}Co_{0.6})_{0.9}Ru_{0.10}$-oxide compound is of a stronger intensity than the $3d_{5/2}$ spin-orbit doublet, except at 250°C. The fractional intensity of the doublets

($3d_{3/2}$:$3d_{5/2}$) decreased with the fabrication temperature of $(Ni_{0.4}Co_{0.6})_{0.9}Ru_{0.10}$-oxide. This evidences a modification of the Ru-3d electronic structure as the satellite peaks (shown in the inset to Figure 5.3(A)) became broader, shifting slightly to higher binding energy [236]. This implies that the variation in annealing temperature influenced the spin-orbit interactions of the electrons in and around the Ru-3d shell.

The XPS spectra on the main plot in Figure 5.3(B) depicts the Ir-4f core level of $(Ni_{0.4}Co_{0.6})_{0.9}Ir_{0.10}$-oxide annealed at 300°C. The typical Ir 4f doublet photoelectron peaks ascribed to the primary $4f_{7/2}$ and $4f_{5/2}$ spin-orbit components are visible at binding energies of 62.5 eV and 65.5 eV, respectively. The split spin-orbit value of 3 eV, which is in agreement with the literature [67, 231] confirms the presence of rutile IrO_2 in the coating. The high-resolution Ir-4f XPS response is deconvoluted into two main peaks at 62.6 and 65.5 eV that correspond to the Ir^{4+} oxidation state, and two broad peaks at 60.6 eV and 68.0 eV that are a consequence of the final-state screening effect by intermediate species [67, 90]. The inset in Figure 5.3(B) is the fitted empirical XPS profile of the same compound calcined at other temperatures, with pure Ir-oxide fabricated at 500°C as a reference. The binding energy for $(Ni_{0.4}Co_{0.6})_{0.9}Ir_{0.10}$-oxide centred around the dominant $4f_{7/2}$ peak is close to the 61.8 eV of pure IrO_2. Nevertheless, a more detailed examination of these peaks (Figure 5.3(B) inset) reveals a slight shift to higher binding energies with decreasing calcination temperature of $(Ni_{0.4}Co_{0.6})_{0.9}Ir_{0.10}$-oxide. Hence, the decrease in calcination temperature resulted in the reduced occupation of the low binding energy of state with a corresponding modulation of the Ir-4f electronic structure.

Further, the high-resolution O-1s spectra of $(Ni_{0.4}Co_{0.6})_{0.90}Ru_{0.10}$-oxide prepared at different temperatures are presented in Figure 5.4(A). Each XPS envelop was fitted by two deconvoluted O1s peaks. The fitted experimental and the deconvoluted spectra of the sample annealed at 300°C is shown as an example. The two peaks centred on the binding energy lines 529.2 eV and 530.8 eV represent oxide species attributed to oxygen in the crystal lattice (O^{2-}) and a hydroxyl group (OH^{-}) [236]. From Figure 5.4(A), it is evident that with decreasing annealing temperature, the relative proportion of OH^{-} increases, indicating a higher content of hydrated oxide at lower calcination temperatures. The quantitative analysis of the fraction, (O^{2-}):(OH^{-}) yielded a rise in OH^{-} content by ca. 77% within the investigated temperature range.

Figure 5.4(B) shows the variation in O-1s spectra of $(Ni_{0.4}Co_{0.6})_{0.90}Ir_{0.10}$-oxide sample with calcination temperature. The shown XPS responses indicate the existence of three oxygen species ascribed to (O^{2-}), (OH^{-}) and surface-adsorbed oxygen (O^{-}) [185]. The binding energy lines (529.1 eV, 530.8 eV, and 532.3 eV) of the respective oxygen species resulting from the O-1s response of the sample annealed at 300°C are shown in Figure 5.4(B), for illustration. As was in the case of $(Ni_{0.4}Co_{0.6})_{0.90}Ru_{0.10}$-oxide, the amount of OH^{-} in the $(Ni_{0.4}Co_{0.6})_{0.90}Ir_{0.10}$-oxide increased with lowering calcination temperature. Thus, the increase in hydroxide oxygen with decreasing calcination temperature presumably avails the Ir/Ru-Ni-Co-oxides with more oxygen vacancies [195, 237]. It has been shown in the literature [193, 238] that the increase in oxygen vacancies leads to improved electronic conductivity of the electroactive species in mixed metal oxides, thereby resulting in the augmentation of the OER kinetics of the composite oxides. This was confirmed by the OER activity data (Figure 5.5) presented in a later section of this report.

In order to elucidate the influence of decreasing annealing temperature on the hydroxide content of the electroactive species, the O1s spectra of the pure oxides were evaluated (see Figure 5.10). Note that the O1s spectra of Ru-oxide and Ir-oxide are deconvoluted into (O^{2-}), (OH^{-}), and (O^{-}), whereas that of $Ni_{0.4}Co_{0.6}$-oxide consists of two oxygen species (O^{2-}, OH^{-}); consequently, it can be elicited that the O1s response of Ni-Co-Ru-oxide is predominantly influenced by $Ni_{0.4}Co_{0.6}$-oxide whereas the response of Ni-Co-Ir-oxide sample is dominated by the response from the electroactive Ir-oxide [185]. In addition, it was found that the OH^{-} proportion in Ru-oxide, Ir-oxide, and $Ni_{0.4}Co_{0.6}$-oxide materials increased by 5%, 77%, and 19%, respectively, for a decrease in calcination temperature from 500°C to 300°C. This may suggest a corresponding improvement in the OER electrocatalytic activity of the pure oxides (see Figure 5.13). In addition, the significant increase in the hydroxide oxygen of Ir-oxide may partly explain why the specific OER activity of $(Ni_{0.4}Co_{0.6})_{0.90}Ir_{0.10}$-oxide is ca. 20 folds more than that of $Ni_{0.4}Co_{0.6}$-oxide at the lower fabrication temperature of 300°C, as discussed later in the text.

The high-resolution Co-2p and Ni-2p responses were found in the range of 779 – 805 eV and 853 – 879 eV respectively, and were statistically the same on all surfaces as described in a previous work [231]. Consequently, these results confirm the presence of the familiar CoO, Co_3O_4 and NiO chemical species in the calcination temperature-influenced $(Ni_{0.4}Co_{0.6})_{0.9}Ru_{0.10}$-oxide, $(Ni_{0.4}Co_{0.6})_{0.9}Ir_{0.10}$-oxide and $Ni_{0.4}Co_{0.6}$-oxide samples.

5.4.4. Wettability measurement

Wettability test was carried out to investigate the interfacial interaction between the prepared Ru/Ir-based ternary oxide surfaces and the electrolyte solution. This was done by measuring the contact angle on the surface of each $(Ni_{0.4}Co_{0.6})_{0.90}Ru_{0.10}$-oxide and $(Ni_{0.4}Co_{0.6})_{0.90}Ir_{0.10}$-oxide coatings. Table 5.4 presents the average values of the recorded contact angles. The values for the $(Ni_{0.4}Co_{0.6})_{0.9}Ir_{0.10}$-oxides are lower than those for the $(Ni_{0.4}Co_{0.6})_{0.9}Ru_{0.10}$-oxide, implying the better wettability of the former oxide surface. However, it can be seen that the contact angles for both oxides decrease with lowering annealing temperatures.

Table 5.4: The average contact angle of $(Ni_{0.4}Co_{0.6})_{0.9}Ru_{0.10}$-oxide and $(Ni_{0.4}Co_{0.6})_{0.9}Ir_{0.10}$-oxide coatings calcined at different temperature.

Temp (°C)	Average contact angle (θ)	
	$(Ni_{0.4}Co_{0.6})_{0.9}Ru_{0.10}$-oxide	$(Ni_{0.4}Co_{0.6})_{0.9}Ir_{0.10}$-oxide
250	75.2 ± 3.0	20.1 ± 0.1
300	81.6 ± 2.9	59.5 ± 0.9
400	90.1 ± 2.5	65.3 ± 0.4
500	95.4 ± 1.6	70.5 ± 3.7
700	98.5 ± 2.1	83.7 ± 1.1

This can be explained by the increasing proportion of hydroxide present in the oxide coatings, consequently increasing the cohesive force of attraction between the surface and the water droplet [239]. This intrinsic characteristic of the oxide is important in order to allow for better interaction with the aqueous electrolyte, thereby contributing to the improvement of the electrocatalytic properties of the surface towards oxygen evolution.

5.4.5. Electrochemical characterization

The electrocatalytic activity of the synthesized coatings towards OER was measured by linear sweep voltammetry (LSV) in 1 M NaOH (pH = 13.4). Figure 5.5 presents the *iR*-drop-corrected LSV curves that illustrate the electrocatalytic performance of $(Ni_{0.4}Co_{0.6})_{0.90}Ru_{0.10}$-oxide and $(Ni_{0.4}Co_{0.6})_{0.90}Ir_{0.10}$-oxide samples as a function of calcination temperature. The equivalent Tafel plots are shown in Figure 5.11, and the corresponding Tafel slopes obtained from the linear Tafel regions of these plots are presented in Table 5.5. It is observed from Figure 5.5 that both oxides, when synthesized at 700°C, exhibited an insignificant OER response (red curves).

However, the OER current density within the OER regions increased significantly as the calcination temperature of the oxides decreased from 700°C to 300°C, but at 250°C (black curves) the performance again decreased. This decrease could be explained by the fact that the oxides annealed at 250°C were unstable, as they were observed to degrade slightly after each linear polarisation measurement, whereas the oxide surfaces annealed between 300°C and 700°C remained intact.

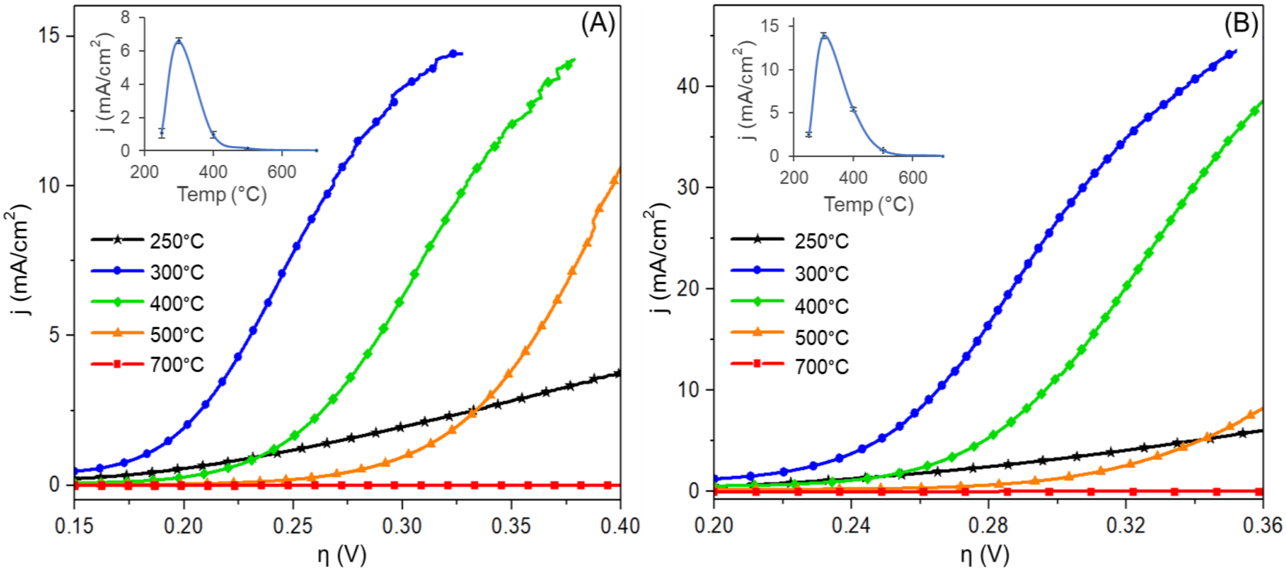

Figure 5.5: LSV curves recorded on (A) $(Ni_{0.4}Co_{0.6})_{0.90}Ru_{0.10}$-oxide and (B) $(Ni_{0.4}Co_{0.6})_{0.90}Ir_{0.10}$-oxide samples fabricated at different calcination temperatures. The curves were recorded in 1M NaOH. Sweep rate: 1 mV/s. The insets in (A) and (B) show the variation of OER current density with calcination temperature of $(Ni_{0.4}Co_{0.6})_{0.90}Ru_{0.10}$-oxide and $(Ni_{0.4}Co_{0.6})_{0.90}Ir_{0.10}$-oxide, determined at a fixed overpotential of 240 mV and 280 mV, respectively.

Table 5.5: The Tafel slope data for the formed oxides, and their corresponding electrochemically-active surface area (EASA). Geometric surface area of the electrodes = 0.43 cm^2.

Temp (°C)	$(Ni_{0.4}Co_{0.6})_{0.9}Ru_{0.10}$-oxide		$(Ni_{0.4}Co_{0.6})_{0.9}Ir_{0.10}$-oxide	
	Tafel slope (mV/dec)	EASA /cm^2	Tafel slope (mV/dec)	EASA /cm^2
250	117.8 ± 1.6	45.5 ± 3.1	114.2 ± 2.9	44.6 ± 2.4
300	65.3 ± 3.6	48.3 ± 1.4	58.8 ± 0.3	44.9 ± 2.2
400	65.6 ± 0.5	48.1 ± 0.7	57.1 ± 0.2	49.3 ± 3.8
500	71.3 ± 0.5	47.4 ± 0.5	62.1 ± 2.7	48.6 ± 1.4
700	483.9 ± 17.4	0.58 ± 0.19	599.2 ± 8.4	0.44 ± 0.05

The variation in OER electrocatalytic activity with temperature is more clearly illustrated in the insets to Figure 5.5, which show the variation in OER current density at fixed overpotential for the respective $(Ni_{0.4}Co_{0.6})_{0.90}Ru_{0.10}$-oxide and $(Ni_{0.4}Co_{0.6})_{0.90}Ir_{0.10}$-oxide samples as a function of their calcination temperature. The data show that the oxides produced at 300^{o}C yield a significantly higher OER electrocatalytic activity, with a ca. 45 and ca. 20 folds increase, respectively, in comparison to when the same samples were fabricated at 500°C. Common to all the oxides is the observed plateauing in current density at higher overpotential, which is clearly shown by the corresponding Tafel curves in Figure 5.11. This behaviour can be explained by the reduction in surface area of the anode in contact with the electrolyte as oxygen bubbles, which are more difficult to detach are formed, thereby decreasing the effective surface area of the anode [185].

Figures 5.5(A and B) also show that at a current density of 10 mA/cm^2 and calcination temperature of 300°C (most active surfaces), $(Ni_{0.4}Co_{0.6})_{0.90}Ru_{0.10}$-oxide and $(Ni_{0.4}Co_{0.6})_{0.90}Ir_{0.10}$-oxide yielded OER overpotential of 268±2 mV and 265±3 mV, respectively. These values are lower (better) than OER overpotentials recorded in electrolytes of similar or higher conductivity on some excellent OER anodes of a higher content of expensive noble metals [91, 204, 227, 240-243]. Further, the overpotential values displayed by both oxides are statistically the same; however, $(Ni_{0.4}Co_{0.6})_{0.90}Ir_{0.10}$-oxide showcases a better OER kinetics than $(Ni_{0.4}Co_{0.6})_{0.90}Ru_{0.10}$-oxide, as evidenced by its relatively lower Tafel slope values at each fabrication temperature, except at 700°C (see Table 5.5); note that a lower Tafel slope value is desirable as this indicates that a smaller change in overpotential is required to increase the OER current density.

It has been shown in the literature that the Tafel slope is a kinetic parameter that can potentially be used to elucidate the OER mechanism [231]. In an alkaline medium, several OER mechanistic pathways have been proposed [52, 172, 244, 245]. However, the Bockris electrochemical oxide reaction pathway is generally accepted. The first step of this mechanistic scheme involves the discharge of hydroxide ions at the active catalyst surface, M resulting in the formation of adsorbed hydroxide intermediate species:

$$M + OH^{-} \rightarrow M\text{–}OH + e^{-} \tag{5.1}$$

characterized by a Tafel slope of 120 mV/dec. The next path is the reaction between the litigated hydroxide intermediate and hydroxide ions in the bulk solution *via* a proton-coupled electron transfer step:

$$M\text{–}OH + OH^- \rightarrow M\text{–}O + H_2O + e^- \tag{5.2}$$

The theoretical Tafel slope of this step is dependent on the M-OH fractional coverage, and the slope ranges from 40 to 120 mV/dec for a transition from low to high M–OH surface coverage [52, 245].

The final step is a reaction that involves the formation of oxygen:

$$2M\text{–}O \rightarrow O_2 + 2M \tag{5.3}$$

which is theorized to have a very low Tafel slope value of 15 mV/dec. The above three steps are based on the assumption that the slow electron-transfer determines the overall kinetics of the OER. However, the step described by Eq.(5.2) can also proceed through two sub-steps, which first involves a chemical reaction:

$$M\text{–}OH + OH^- \rightarrow M\text{–}O^- + H_2O \tag{5.4}$$

followed by an electron-transfer step:

$$M\text{–}O^- \rightarrow M\text{–}O + e^- \tag{5.5}$$

termed as the "Krasil' shchikov's Path"[52]. If the step in Eq.(5.4) is *rds*, the corresponding Tafel slope would be 60 mV/dec, while the step in Eq.(5.5) is characterized by a Tafel slope of 40 mV/dec.

The higher Tafel slope values of the oxides annealed at 250°C (as shown in Table 5.5) could be a result of surface processes [185] emanating from the fact that these surfaces have higher proportion of hydroxide thereby leading to a higher M-OH coverage. Further, with an increase in hydroxide content in the oxides (Figure 5.4), the number of oxygen vacancies also increased [195, 237]. Considering these two facts, it is more likely that Step (5.2) is *rds* at 250^{o}C, rather than Step (5.1). Further, for the oxides fabricated in the temperature range from 300°C to 500°C, the values of the Tafel slopes indicate that either Step (5.2) or Step (5.4) is the *rds* in the OER. Thus, taking the above two observations into account, it is more likely that the OER on the investigated surfaces proceeds through the Bockris electrochemical oxide reaction pathway, with the moderate surface coverage by OH and Step (5.2) as *rds*. The very high Tafel slope values recorded on the surfaces synthesised at 700°C is due to the fact that these oxides are very poor OER catalysts, as evidenced in Figure 5.5.

The data on the OER electrocatalytic activity of the two oxides produced at different temperatures (presented in Figure 5.5) refers to the materials' extrinsic electrocatalytic activity, which includes the effect of surface area. Thus, the real, intrinsic activity of the OER electrocatalysts was determined next, based on their actual electrochemically-active surface area (EASA) estimated employing the Trasatti method [229, 230]. In essence, a set of cyclic voltammograms were recorded in the double-layer region of the oxides at different scan rates (Figure 5.12(A)) and the corresponding capacitance values were determined. These values correspond both to the capacitance of the electrochemical double-layer (electrostatic charging) and the pseudo-capacitance due to the fast reversible redox transitions in the oxide phase. Then, by extrapolating these values to infinite scan rate (Figure 5.12(B)), only the corresponding double-layer capacitance was determined, and from those values and taking the theoretical double-layer capacitance as $25\mu F/cm^2$ [246, 247], the corresponding EASA values were determined (see Table 5.5). The data in the table show that the EASA is not significantly influenced in the range 250 – 500°C, while the values at 700°C are significantly lower. The results are well-supported by the SEM images depicted in Figures 5.1(A-J), which show rougher morphologies for samples annealed between 250 – 500°C compared to the flatter surfaces at 700°C.

Taking into account the EASA values[8], the polarization curves presented in Figure 5.5 were normalized to evaluate the relative intrinsic (true) activity of the produced electrocatalysts, and the results for both $(Ni_{0.4}Co_{0.6})_{0.90}Ru_{0.10}$-oxide and $(Ni_{0.4}Co_{0.6})_{0.90}Ir_{0.10}$-oxide materials are presented in Figure 5.13. The trend in OER activity with calcination temperature is similar to the one presented in Figure 5.5, showing that the improved OER performance with decreasing fabrication temperature manifested by these oxides is indeed due to their intrinsic properties, not due to the surface area effect.

It is well known that pure Ir- and Ru-oxides are the two best OER electrocatalysts, with the latter one being more active but less stable. Thus, it would be of interest to compare the

---

[8] Note that the EASA values are different from the results obtained by the HexRu(III) redox probe in chapters 3 and 4. See detail explanation in Appendix 5.6.

behaviour of $(Ni_{0.4}Co_{0.6})_{0.90}Ru_{0.10}$-oxide and $(Ni_{0.4}Co_{0.6})_{0.90}Ir_{0.10}$-oxide catalysts presented in this work to the behaviour of the pure Ir- and Ru-oxides, and also the base $Ni_{0.4}Co_{0.6}$-oxide, under the same fabrication and utilisation conditions. For this purpose, the performance of all the oxides produced at two temperatures, 300°C (best-performing oxides in this work) and 500°C in the OER was investigated, and the results are presented in Figure 5.14 (the results for the two oxides discussed in this work are shown in Figure 5.5). First, it is evident from Figures (5.5 and 5.14(A-C)) that each metal oxide exhibited an improvement in its specific OER activity as the calcination temperature decreased from 500°C to 300°C. Next, Figure 5.14(D) evidences that the best OER electrocatalyst is $(Ni_{0.4}Co_{0.6})_{0.90}Ir_{0.10}$-oxide, with the activity at 300 mV of ca. 20 folds higher than that of pure Ir-oxide and the $Ni_{0.4}Co_{0.6}$-oxide base, indicating synergistic interactions between Ir-oxide and $Ni_{0.4}Co_{0.6}$-oxide. Also, the electrocatalytic activity of $(Ni_{0.4}Co_{0.6})_{0.90}Ru_{0.10}$-oxide is ca.10 folds higher than that of $Ni_{0.4}Co_{0.6}$-oxide.

The enhancement in the OER intrinsic behaviour of the trimetal oxides due to the observed synergistic interactions that exist among the constituent oxides can be partly explained by the XPS results (in Figure 5.3) which reveal the favourable modification of the 3d and 4f electronic configurations of $(Ni_{0.4}Co_{0.6})_{0.90}Ru_{0.10}$-oxide and $(Ni_{0.4}Co_{0.6})_{0.90}Ir_{0.10}$-oxide, respectively, with decreasing calcination temperature. Also, the results from the O1s high-resolution spectra and the contact angle measurements indicate that at reduced calcination temperature, there is an increase in both the hydroxide content in the anodes and oxygen vacancies [193]. The increase in oxygen vacancies is substantiated by the XRD result (see Figure 5.9(B)) that depicts a reduction in the crystallinity of the $NiCo_2O_4$ phase with lowering calcination temperature [238]. Consequently, this suggests an improvement in the electronic conductivity due to more available oxygen vacancies [193, 238] and increased electrode/electrolyte contact interfacial area (better wetting of the electrocatalyst) as a result of increased hydrophilicity, thereby augmenting the catalytic activities of the oxides towards OER [239].

Chronopotentiometric measurements were also conducted to study the durability of the best-performing oxides (synthesized at 300°C) at a current density of 10 mA/cm^2 (this is the value typically used in the literature to examine the performance of alkaline water-electrolysis electrodes). The samples were utilized as anodes for a period of 24 hours of electrolysis in 1 M NaOH [231], and the resulting overpotential versus time behaviour is shown in Figure 5.6. Also, the LSV curves recorded on $(Ni_{0.4}Co_{0.6})_{0.90}Ir_{0.10}$-oxide and $Ni_{0.4}Co_{0.6}$-oxide before and after the durability tests showed no statistical difference in the OER activity of the oxides, thus indicating that the anodes did not change, from the OER-activity point of view, during the durability test. Figure 5.6 shows that the overpotential remained stable for all the materials, except for Ir-oxide, evidencing that the OER activity of the anodes remained stable (pure Ir-oxide proved to be unstable in the alkaline medium at the investigated conditions). Considering the durability of the $(Ni_{0.4}Co_{0.6})_{0.9}Ir_{0.1}$-oxide during the investigation span, and the relatively better stability of $(Ni_{0.4}Co_{0.6})_{0.9}Ru_{0.1}$-oxide over Ru-oxide, it can be inferred that under alkaline electrolysis, the $Ni_{0.4}Co_{0.6}$-oxide matrix helped stabilize IrO_2 and RuO_2 in the trimetal oxides. The best-performing material was pure Ru-oxide, which showed the smallest overpotential, followed by $(Ni_{0.4}Co_{0.6})_{0.9}Ir_{0.1}$-oxide and then $(Ni_{0.4}Co_{0.6})_{0.9}Ru_{0.1}$-oxide. However, as shown in Figure 5.14(D), the latter electrode performed very closely to pure Ru-oxide, despite the fact that it only contained 10% of Ru. The results in Figure 5.6 further evidence the synergistic action between the $Ni_{0.4}Co_{0.6}$-oxide matrix and Ir and Ru “dopants”.

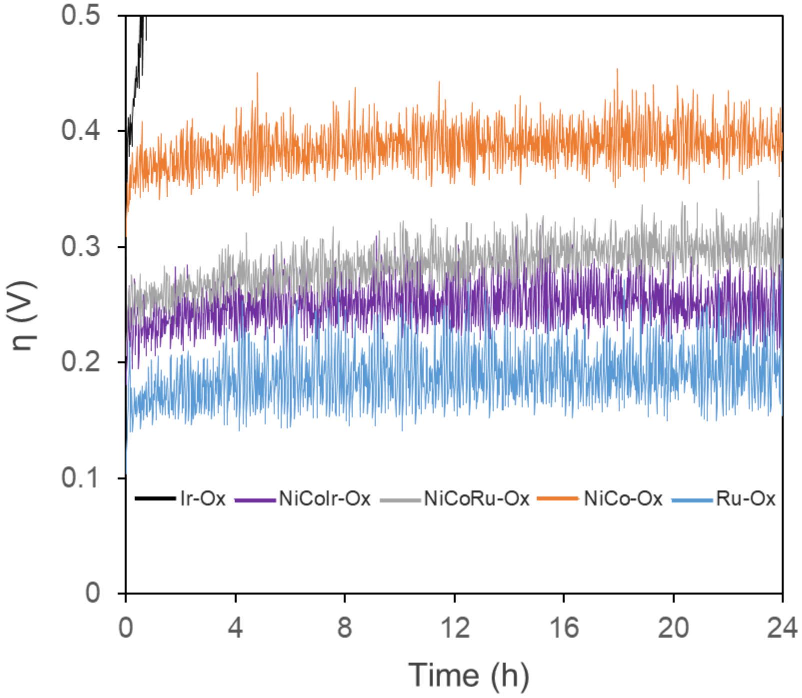

Figure 5.6: Long-term stability test in 1M NaOH measured at 10 mA/cm^2 on $(Ni_{0.4}Co_{0.6})_{1-x}Ru_x$-oxide, $(Ni_{0.4}Co_{0.6})_{1-x}Ir_x$-oxide, $Ni_{0.4}Co_{0.6}$-oxide, Ir-oxide and Ru-oxide anodes thermally prepared at 300°C.

5.5. Conclusion

The OER electrocatalytic performance of $(Ni_{0.4}Co_{0.6})_{0.90}Ru_{0.10}$-oxide and $(Ni_{0.4}Co_{0.6})_{0.90}Ir_{0.10}$-oxide are profoundly affected by the calcination temperature employed during their synthesis. It was found that fabricating the trimetal oxide materials at 300°C, produces stable OER electrocatalysts of high activity, either surpassing that of state-of-the-art pure Ir-oxide, or very close to the best anode OER catalyst, pure Ru-oxide. This makes them interesting as potential commercial anode candidates in the alkaline electrolytic hydrogen production.

The SEM micrographs showed that the granular, porous morphologies of the synthesized coatings were temperature dependent. The porous network of granular particles became more evident with the increasing calcination temperature as a result of increased particle size. The analysis of the EDX and XPS results revealed the actual atomic compositions of the oxide samples and the preferential distribution of Ni/Co in the $Ni_{0.4}Co_{0.6}$-oxide core matrix. The X-ray diffraction studies elucidated changes in the crystallinity of the oxide phases with varying calcination temperature. The contact angle measurements revealed an increase in the oxide surface wettability with reducing calcination temperature, which may be due to an increase in hydroxide content as reported in literature.

The evolution of oxygen on the synthesized electrocatalysts was deduced to follow the Bockris electrochemical oxide reaction pathway, with the proton-coupled electron transfer step being the rate determining step. Furthermore, the XPS results showed that the improvement in the OER kinetics of the anodes might be due to the increased hydroxide content and a higher number of oxygen vacancies. The results indicated the synergistic action of the three metals in the corresponding $(Ni_{0.4}Co_{0.6})_{0.90}Ru_{0.10}$-oxide and $(Ni_{0.4}Co_{0.6})_{0.90}Ir_{0.10}$-oxide. The intrinsic synergistic enhancement of activity may be due to the modification in the Ir-4f and Ru-3d electronic structures in the respective ternary oxides and in part due to the increased oxygen vacancies in the trimetal oxides at the lower fabrication temperature.

Acknowledgement: The authors are highly appreciative of the funds provided in support of this work by the Nigerian Petroleum Technology Development Fund (PTDF), Natural Sciences and Engineering Research Council of Canada (NSERC), and the McGill Engineering Doctoral Award (MEDA). Also, it is important to mention the supervisory role played by Dr. Marwan Azzi in reviewing some part of this report.

5.6. Appendix A. Supplementary material

This section contains the supplemental information to the manuscript.

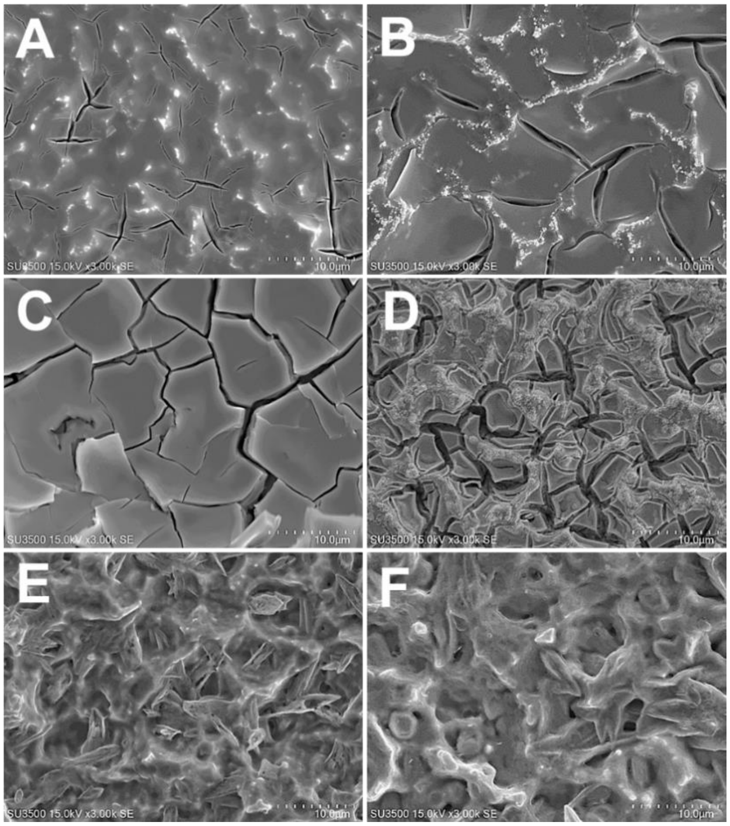

Figure 5.7: SEM images of (A) & (B) Ru-oxide; (C) & (D) Ir-oxide; (E) & (F) ($Ni_{0.4}Co_{0.6}$)-oxide coatings annealed at 300°C and 500°C respectively.

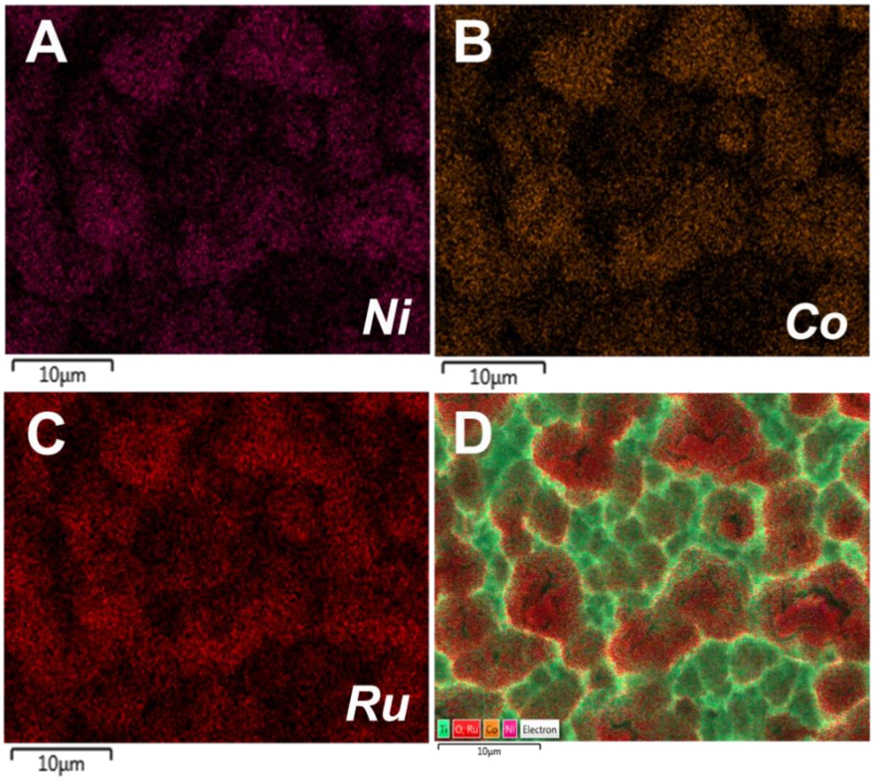

Figure 5.8: Morphological distribution of (A) Ni, (B) Co, (C) Ru, and (D) Ni/Co/Ru/O including the Ti substrate as-synthesized $(Ni_{0.4}Co_{0.6})_{0.90}Ru_{0.10}$-oxide surface calcined at 300°C.

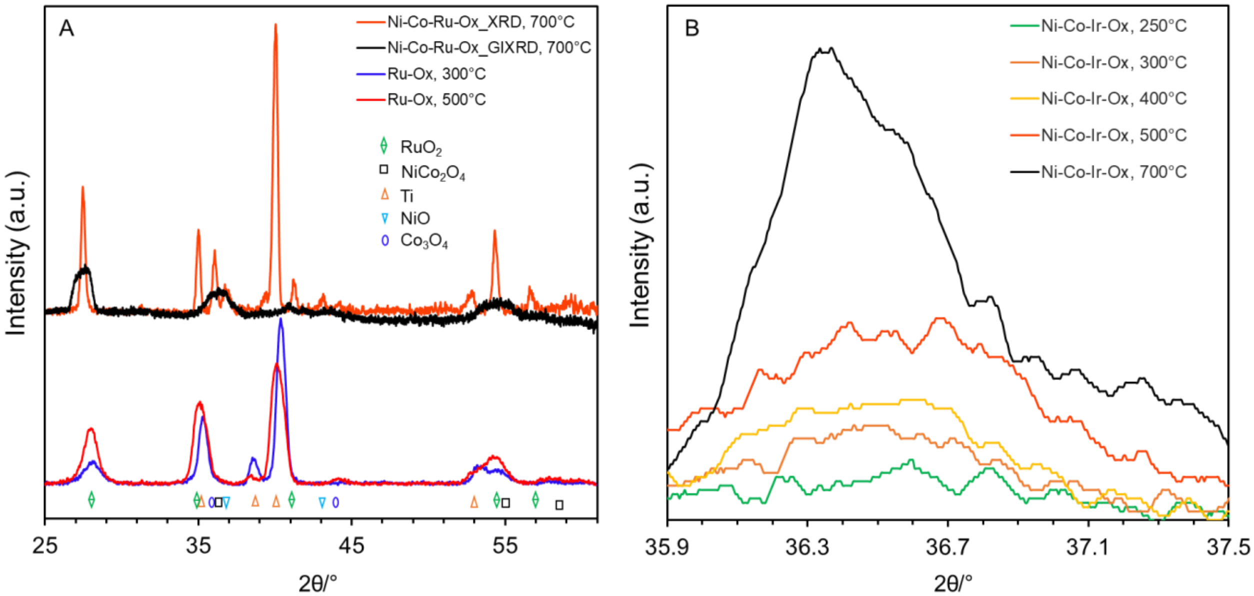

Figure 5.9: Diffraction patterns of: A) $(Ni_{0.4}Co_{0.6})_{0.90}Ru_{0.10}$-oxide synthesised at 700°C and Ru-oxide prepared at 300°C and 500°C temperatures; and B) $(Ni_{0.4}Co_{0.6})_{0.90}Ir_{0.10}$-oxide to magnify the (311) reflection of the spinel $NiCo_2O_4$ oxide phase formed at different calcination temperatures.

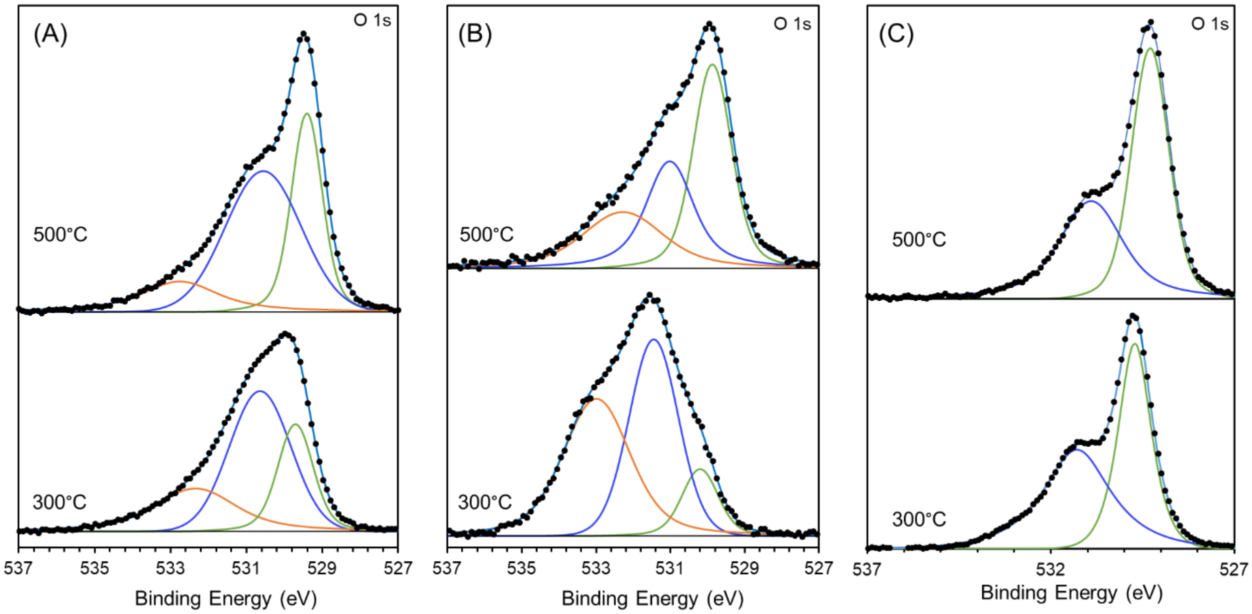

Figure 5.10: High-resolution O1s XPS spectra of (A) Ru-oxide, (B) Ir-oxide and (C) $Ni_{0.4}Co_{0.6}$-oxide samples fabricated at 500°C (top) and 300°C (bottom).

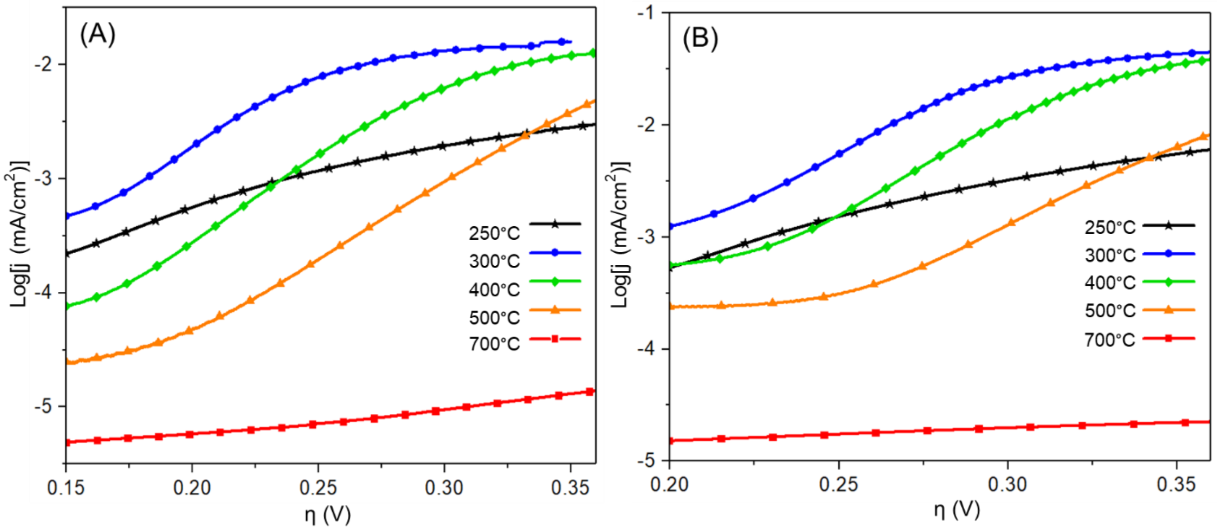

Figure 5.11: Tafel curves recorded on (A) $(Ni_{0.4}Co_{0.6})_{0.90}Ru_{0.10}$-oxide and (B) $(Ni_{0.4}Co_{0.6})_{0.90}Ir_{0.10}$-oxide fabricated at different calcination temperatures. The curves were recorded in 1M NaOH. Sweep rate: 1 mV/s.

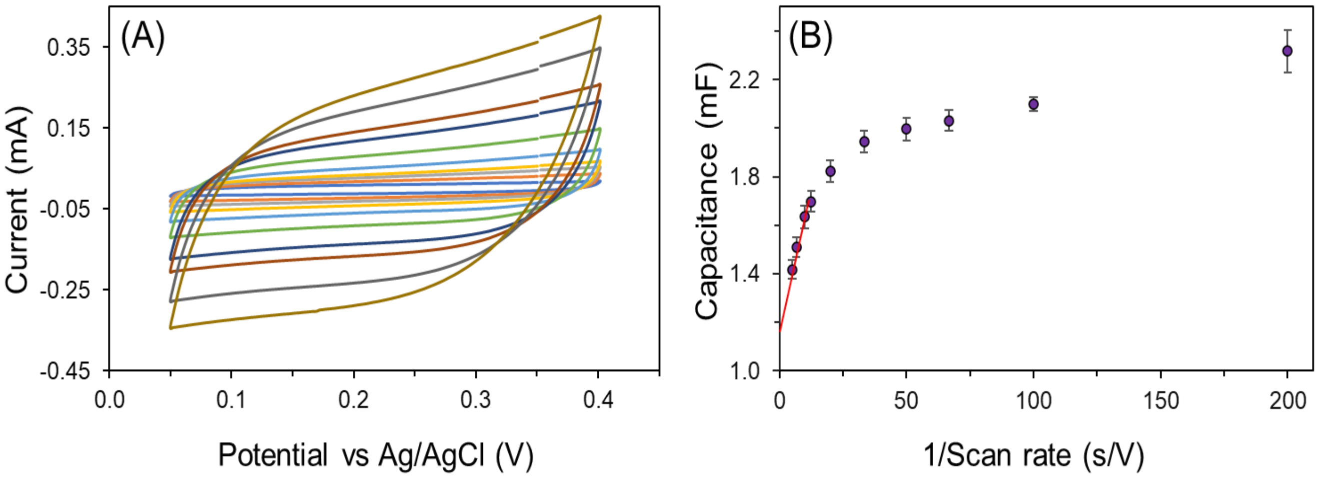

Figure 5.12: (A) CV curves of $(Ni_{0.4}Co_{0.6})_{0.90}Ir_{0.10}$-oxide annealed at 500°C recorded in 0.17M Na_2HPO_4 at scan rates of 5, 10, 15, 20, 30, 50, 80, 100, 150, 200 mV/s (the area under the CV curves increases with scan rate); (B) The variation of capacitance with the inverse of scan rate for $(Ni_{0.4}Co_{0.6})_{0.90}Ir_{0.10}$-oxide electrodes annealed at 500°C. The red line indicates the linear fit of equation: $y = 0.0425x + 1.214$.

Note that the electrochemically active surface area (EASA) of the samples obtained *via* the Trasatti method is about one order of magnitude larger than that presented in chapter 3 and 4 determined *via* the redox probe procedure (see Table 5.6). Therefore, it was necessary to compare the results from both methods by normalizing the absolute EASA values with respect to the EASA of $Ni_{0.4}Co_{0.6}$-oxide (the minimum EASA). Table 5.6 shows that for each sample, the relative EASA obtained from the two area determination methods are statistically similar. This implies that regardless of either technique used, the trend in the intrinsic OER activity of the oxide samples will be the same. Moreover, it is the relative EASA and not the absolute EASA value that is important since the goal was to compare the oxide materials' relative OER performance. Further, the discrepancy in the absolute EASAs from the two procedures may be explained by the fact that the coatings are porous, and the redox probe procedure is more suitable for a 2D diffusion plane.

Table 5.6: The electrochemically active surface area of $(Ni_{0.4}Co_{0.6})_{1-x}Ir_x$-oxide coatings annealed at 500°C obtained via the HexRu(III) redox probe and the Trasatti area determination methods.

Sample	EASA by redox probe		EASA by Trasatti	
	$EASA_{Redox}$ (cm^2)	Normalized EASA	$EASA_{Trasatti}$ (cm^2)	Normalized EASA
Ir-oxide	52.2 ± 1.1	1.202 ± 0.013	0.373 ± 0.005	1.193 ± 0.003
$Ni_{0.4}Co_{0.6}$-oxide	43.4 ± 1.6	1	0.313 ± 0.005	1
$(Ni_{0.4}Co_{0.6})_{0.9}Ir_{0.1}$-oxide	48.6 ± 1.4	1.121 ± 0.002	0.362 ± 0.004	1.157 ± 0.005

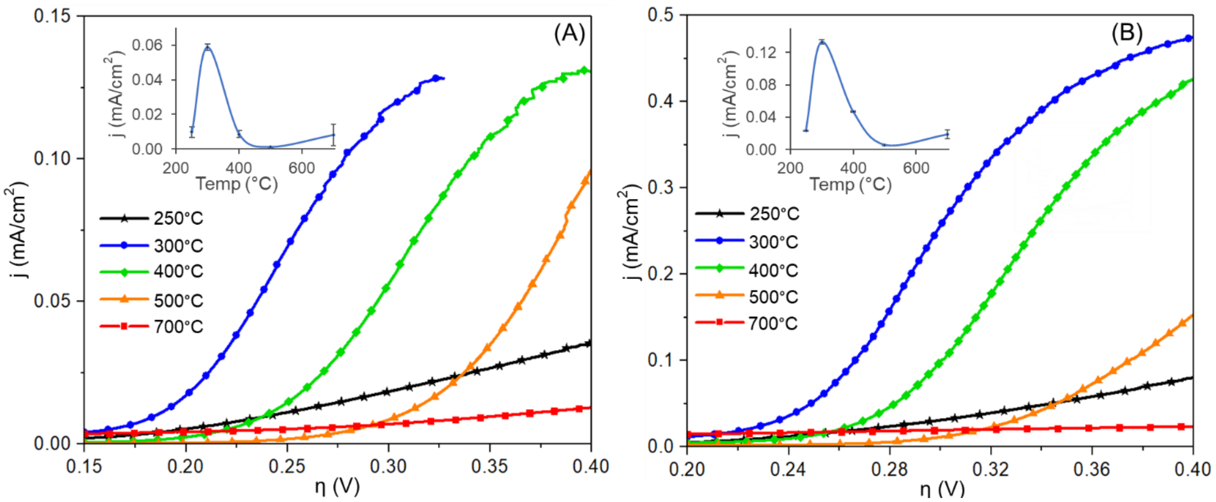

Figure 5.13: Results from Figure 5.5 normalised based on the electrochemically active surface area of (A) $(Ni_{0.4}Co_{0.6})_{0.90}Ir_{0.10}$-oxide and (B) $(Ni_{0.4}Co_{0.6})_{0.90}Ru_{0.10}$-oxide.

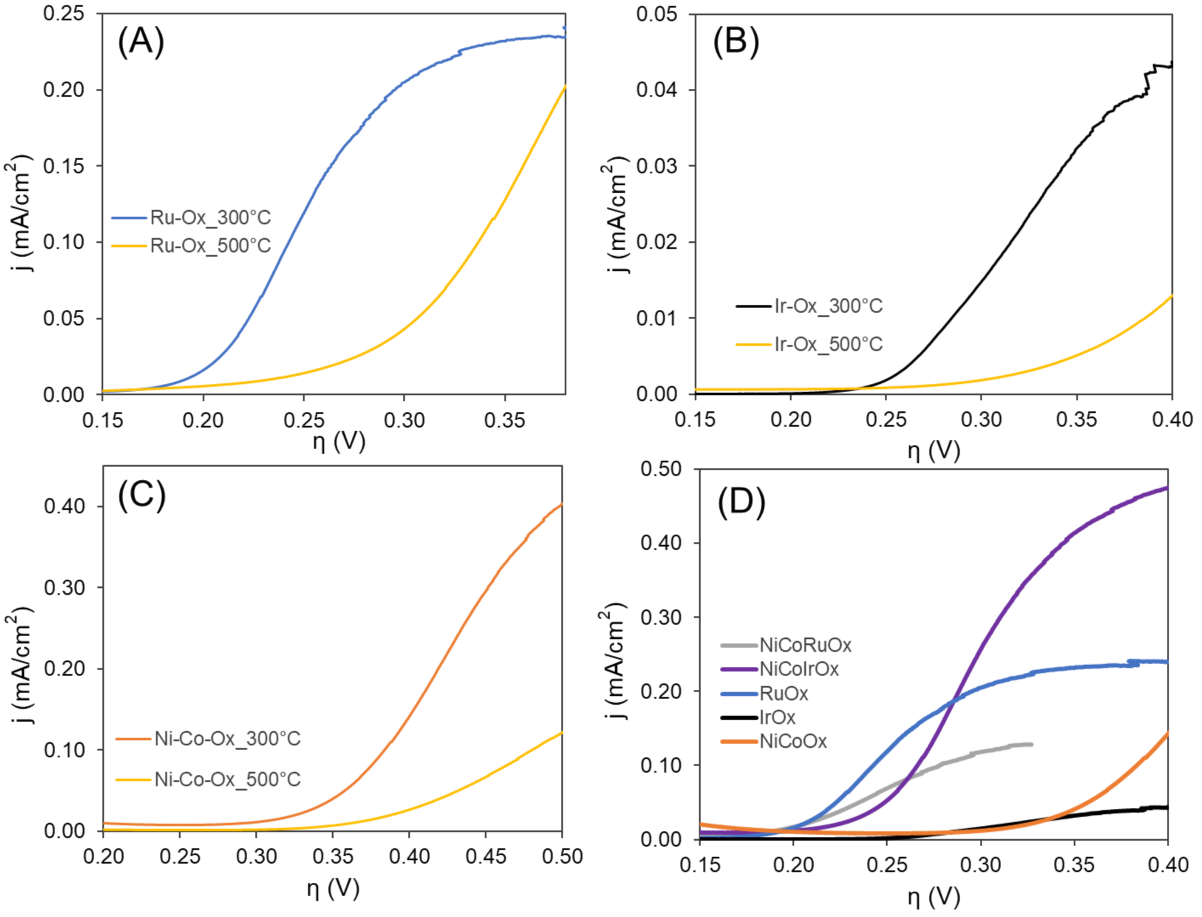

Figure 5.14: The intrinsic electrocatalytic activity of (A) Ru-oxide (B) Ir-oxide (C) $Ni_{0.4}Co_{0.6}$-oxide calcined at 300°C & 500°C. (D) compares the OER activity of $(Ni_{0.4}Co_{0.6})_{0.90}Ir_{0.10}$-oxide, $(Ni_{0.4}Co_{0.6})_{0.90}Ru_{0.10}$-oxide to that of pure Ru-oxide, Ir-oxide and base $Ni_{0.4}Co_{0.6}$-oxide matrix, synthesized at 300°C. The EASA data for the pure oxides are given in Table 5.7.

Table 5.7: The Tafel slope data for the pure oxides fabricated at 300°C & 500°C, and their corresponding electrochemically-active surface area (EASA) obtained from cyclic voltammetry data. Geometric surface area of the electrodes = 0.43 cm^2.

Sample	300 (°C)		500 (°C)	
	Tafel slope (mV/dec)	EASA/cm^2	Tafel slope (mV/dec)	EASA/cm^2
Ru-Ox	51.2 ± 3.9	77.3 ± 4.2	106.5 ± 1.1	43.1 ± 2.8
Ir-Ox	38.9 ± 0.3	96.4 ± 5.0	108.8 ± 4.2	51.2 ± 1.1
$Ni_{0.4}Co_{0.6}$-Ox	83.3 ± 1.7	45.1 ± 0.9	80.8 ± 0.8	43.4 ± 1.6

Chapter 6 - Electrochemical Degradation of Methylene Blue using a Novel Ni-Co-oxide Anode

Emmanuel Onyekachi Nwanebu*,♣, Xiaocheng Liu♣ and Sasha Omanovic♣

Department of Chemical Engineering, McGill University, 3610 University St., Montreal,
Quebec, H3A 0C5, Canada

*corresponding author: emmanuel.nwanebu@mail.mcgill.ca

♣ preliminary list of authors (additional experiments are currently being performed, with additional researchers to be listed as co-authors)

6.1. Preface

The potential of using NiCo-oxide-based coatings as commercial anodes in the oxygen evolution reaction for the electrolytic production of hydrogen was discussed in the preceding chapters. However, during the screening for the best intrinsic NiCo-oxide composition, it was found that the $Ni_{0.6}Co_{0.4}$-oxide composition is the least OER electroactive composition. Hence, it was hypothesized that this oxide could serve as a good electrochemical anode for the degradation of organic pollutants in wastewater owing to its high OER overpotential. The rationale behind this is given by the fact that reports in the literature have shown that electrode materials of slow OER kinetics are potentially good for the anodic oxidation of wastewater contaminants.

The current chapter presents the results on the investigation of $Ni_{0.6}Co_{0.4}$-oxide as an effective electrochemical anode for the destruction of organic pollutants in wastewater. It will be demonstrated that $Ni_{0.6}Co_{0.4}$-oxide is an effective and highly energy-efficient anode in the electrochemical degradation of methylene blue dye, a common (and model) wastewater contaminant. The electrocatalytic performance of the oxide was tremendously accentuated in the presence of small amount of chloride ions in the aqueous solution. The catalytic performance of the oxide was ascribed to the *in-situ* electrogeneration of strong oxidizing hydroxyl intermediates and active chlorine species.

The results presented in this thesis constitute part of the sub-project related to the employment of the $Ni_{0.6}Co_{0.4}$-oxide anode for wastewater treatment. Additional experiments related to the identification of methylene blue degradation products are currently being performed in collaboration with Prof. Yargeau's research group (Chemical Engineering, McGill). After completion of these experiments, the work will be formulated into a publication and it will be submitted to a peer-reviewed journal.

Highlights

- Low-cost $Ni_{0.6}Co_{0.4}$-oxide is an effective electrochemical anode for degradation of aqueous methylene blue dye solution
- $Ni_{0.6}Co_{0.4}$-oxide showed good durability and low-energy consumption in the destruction of methylene blue
- The electrochemical activity of $Ni_{0.6}Co_{0.4}$-oxide is significantly influenced by electrogenerated active chlorine species

Abstract

The potential of using thermally-prepared $Ni_{0.6}Co_{0.4}$-oxide in the facile electrochemical degradation of methylene blue (MB) in an aqueous solution was investigated. The anode demonstrated good electrocatalytic activity towards the destruction of the methylene blue dye solution and the incineration of its intermediates to carbon dioxide. It was found that the electrocatalytic performance of the electrode in the anodic degradation of the organic pollutant was significantly enhanced by the presence of chloride ions in the solution. The improvement in the degradation rate of MB was attributed to the *in-situ* electrogeneration of chlorine active species. The results show that $Ni_{0.6}Co_{0.4}$-oxide anode can be employed as a durable energy-efficient electrocatalyst in the electrochemical purification of wastewater.

Keywords: Electrochemical Anode; Wastewater; Nickel; Cobalt; Metal-oxide; Methylene blue

6.2. Introduction

Safe drinking water may be taken for granted in advanced countries of the World simply because potable water is considered to be always within reach. However, according to the World Health Organization (WHO), close to 800 million people around the globe lack access to clean drinking water, including ca.140 million people that are dependent on surface water [248]. Although, majority of the populace deprived of safe drinking water are from Sub-Saharan Africa, nonetheless, it has been reported that in the developed countries like Canada, access to safely-managed drinking water services still poses a challenge [249]. For example, in 2015, CBC News reported that two-thirds of the First Nation communities in Canada have been under at least one drinking-water advisory for a decade [250]. Therefore, it is clear that access to sustainable, safe, and affordable drinking water is indeed a mondial problem. Globally, a minimum of 2 billion people are exposed to contaminated water service [248]. The sources of contamination for drinking-water supply are primarily due to improperly managed communal, urban, industrial, and agricultural wastewater, leading to the introduction of chemicals such as pharmaceuticals, hormones, organic contaminants, etc. into aquatic bodies [77, 248]. These prevalent compounds in the water supply expose individuals to preventable health risks associated with exposure to wastewater. Thus, it is essential to employ a wastewater treatment system in the water cycle.

Generally, a conventional wastewater treatment scheme consists of the pre-treatment, primary, secondary, and tertiary treatment operations that involve physical, chemical, and biological processes which are determined based on the properties of the targeted-contaminants, for effective decontamination. However, conventional wastewater treatment methods are sometimes ineffective or insufficient for the removal of recalcitrant organic compounds with prevalent aromatic rings or they generate additional problems [119, 126]. In order to address the issues associated with conventional wastewater treatment plants, a lot of recent research has been done on the development of advanced oxidation processes (AOPs) [77, 119, 121, 124-127, 251]. These processes are based on the *in-situ* generation of a sufficient quantity of highly reactive oxidizing agents such as ozone or hydroxyl radicals that are more efficient in breaking down persistent organic contaminants. AOPs can be utilized as an effective pre-treatment step to increase the biodegradability of recalcitrant organic matters that are difficult to breakdown through biological treatment. Further, the advanced treatment procedures can help reduce the total organic concentration to obtain a specific effluent requirement. Among the advanced oxidation technologies such as ozonation [251], photocatalytic degradation [125], and Fenton Process [124] just to name a few, the electrochemical oxidation method has received wide recognition for its effectiveness in the removal of toxic and bio-refractory organic compounds [74, 77, 119, 121].

The electrochemical oxidation of wastewater offers a plethora of advantages, in comparison to other AOPs such as low-cost, simplicity, versatility, amenability of automation, environmental compatibility, small foot-print and modularity, handling safety and minimum waste production [77, 121]. Consequently, there is a greater interest in the utilization of this anodic oxidization technique for efficient treatment of certain organics-contaminated wastewaters. In electrochemical oxidation, the choice of anode material is a critical determining factor as this influences the overall efficiency of the electrocatalytic process and the selectivity of the anodic reaction [120, 122]. Studies have shown that the anodic oxidation (removal) of pollutants can be "direct", whereby the pollutants are electrochemically oxidized directly at the anode surface, or "indirect" by the electro-generated oxidizing agents such as hydroxyl radicals [122, 252, 253]. In direct oxidation, there is a possibility of electrode fouling leading to the passivation of the electrode surface which results in poor chemical decontamination [122, 252, 253].

A number of research works on the use of various electrochemical decontamination of wastewater by indirect anodic oxidation have been reported, including boron-doped diamond (BDD) [254-257], metal oxides such as PbO_2 [258], SnO_2 [259], Sb-doped SnO_2 [260], and Sb-doped $Sn_{0.8}W_{0.2}$-Ox anodes [77]. BDD has shown to be the best anode material for this purpose, but its commercial use is prohibited by its very high cost. The main issues with the remaining anode materials cited above, is their long-term stability and slow kinetics of the degradation reaction, depending on the pollutant. Thus, there is a need to develop better anode materials for wastewater treatment.

One major characteristic of anodes used for the electrochemical wastewater treatment is that they should offer high overpotential towards the oxygen evolution reaction (OER) which is, in this case, an unwanted parallel reaction that decreases the efficiency of the wastewater treatment process [121]. In our research on the influence of Ni-Co-oxide composition on their electrocatalytic activity in the OER electrocatalytic activity, $Ni_{0.6}Co_{0.4}$-oxide was identified to exhibit a large OER overpotential [185]. Therefore, this low-cost, durable, non-toxic binary metal-oxide anode is well-placed as a promising candidate for the electrochemical degradation of wastewater contaminants. Consequently, this original and novel work reports the result on the degradation of methylene blue (MB) dye solution using this $Ni_{0.6}Co_{0.4}$-oxide anode. The results are comparable to those reported in the literature for a more expensive $TiRuO_2$ anode [119].

6.3. Experimental Methodology[9]

6.3.1. Anode Preparation

The synthesis of the $Ni_{0.6}Co_{0.4}$-oxide coating involved several preparation steps that ranged from the pre-treatment of the underlying 50 mm × 50 mm × 2 mm Ti substrate to the formation of the $Ni_{0.6}Co_{0.4}$-oxide film on the Ti substrate [185]. First, the titanium substrate support (99 % pure, McMaster Carr) was pretreated via wet-polishing using a 600-grit SiC sandpaper. Thereafter, the substrate was rinsed in nanopure water of resistivity 18.2 MΩ cm and then sonicated in ethanol for 30 min to remove any leftover polishing residues. The polished sample was next etched in a boiling equivolume mixture of nanopure water and HCl for 30 min and the dried with argon gas (purity 99.998 wt.%, MEGS Specialty Gases Inc., Canada) [231].

The coating precursor solution of 0.5 M concentration was prepared by dissolving the appropriate amounts $NiCl_2 \cdot 6H_2O$ (ReagentPlus, 100%, Sigma Aldrich) and $Co(NO_3)_2 \cdot 6H_2O$ (99% pure, ACROS Organics) in an equivolume mixture of isopropanol (Fisher Scientific) and nanopure water so as to yield a coating of relative Ni/Co atomic ratio of 3:2. The surface characterization of the oxide film by energy-dispersive X-ray spectroscopic (EDX) analysis showed that the oxide is composed of 60.8 ± 0.8 atomic percentage of Ni [185]. The Ni-Co-oxide coating was formed by brush-painting the precursor salt solution onto one side of the pretreated Ti substrate. This was followed by a 5 min drying in an oven at 383 K to vaporize the solvent and then calcination for 15 min in a furnace at 773 K. The coated surface was allowed to cool down to room temperature over a period of 20 min. Subsequently, the coating process was repeated six times to form a seven-layered coating on the Ti surface. Finally, the sample was annealed for 2 h at 773 K to form a uniform thick binary metal oxide coating. X-ray diffraction (XRD) analysis was used to characterize the coatings' crystalline oxide phases, as presented in a previous work [185]. Before

---

[9] All the measurements were done in multiplets and the presented data are the average values with the accompanying errors

using the $Ni_{0.6}Co_{0.4}$-oxide/Ti substrate as the working electrode, the back (uncoated) side of the sample was covered with a waterproof, electrically insulating film (3M Electrical Tape, Ruban isolant, USA).

6.3.2. Electrochemical Degradation of Methylene Blue

The methylene blue degradation studies were conducted in a one-compartment, two-electrode electrochemical cell at atmospheric pressure and ambient temperature (295 ± 2 K). The electrochemical cell comprised of the $Ni_{0.6}Co_{0.4}$-oxide working electrode, described above, and a 50 mm × 53 mm × 2 mm flat stainless steel (316L) counter electrode. The vertically-suspended electrodes were kept ca. 1 cm apart and connected to a power supply that operated in a constant current mode during the degradation investigation. The electrolyte was a 50 mg/L methylene blue (MB) solution in 0.17 M sodium sulfate (≥99% pure, Fisher Scientific) of pH 5.8, prepared from a stock solution of 500 mg/L MB (Certified biological stain, Fisher Chemical). A total of 25 cm^2 geometric area of the working electrode was exposed to the 250-mL electrolyte. The solution was stirred by a magnetic stir bar at 300 rpm agitation speed to ensure that the solution is adequately mixed throughout the experiment and aliquots of 500 μL were taken from the solution at selected time intervals. At each sampling time, the corresponding potential difference across the electrodes were noted and the electrolyte temperature at the start and end of the experiment was reported. The aliquots were then diluted with a solution of 0.17 M sodium sulfate by a requisite factor for analysis.

The observed electrolyte colour removal, i.e. the MB degradation rate, was monitored over time by measuring the reduction in the peak absorbance of MB at 660 nm wavelength employing UV/Vis spectrophotometry (ThermoScientific Evolution 300) – the scanning range was from 380 – 780 nm. Through the use of a linear calibration curve ($R^2 = 0.996$), the measured absorbance was correlated to the concentration of MB. The electrochemical degradation of the methylene blue was studied at different constant current densities of 10, 20, 40, and 60 mA/cm^2.

The effect of chloride ion concentration on the electrochemical degradation performance of $Ni_{0.6}Co_{0.4}$-oxide for the decontamination of MB containing water was investigated at 20 mA/cm^2 and at 0.25, 0.5, 1.0, and 2.0 g/L NaCl concentration in the 50 mg/L MB in 0.17 M Na_2SO_4. Also, chemical oxygen demand (COD) and total organic carbon (TOC) measurements were performed to elicit the mineralization efficiency of the electrochemical MB degradation process. The COD investigation was done using a low range (0 – 150 ppm) COD digestion vials (K-7355, CHEMetrics), COD reactor (HACH, DRB 200) and a HACH spectrophotometer (DR/ 2500). The HACH method is based on the ASTM D 1252-95 standard. The TOC test was performed via a Rosemount DC-80 Total Organic Carbon Analyzer and the EPA Method 415.2. All experiments were at least duplicated, to ensure the reliability of the data.

6.4. Results and Discussion

6.4.1. Electrochemical Degradation of MB in the Absence of Chlorides

The electrocatalytic performance of $Ni_{0.6}Co_{0.4}$-oxide was first evaluated by the electrochemical oxidation of 50 mg/L methylene blue dye in 0.17 M sodium sulfate electrolyte (no chlorides were present). The mechanism of the MB electrochemical oxidation is well established in the literature and is based on the action of anodically electrogenerated active species, which are under these conditions hydroxyl radicals [121, 122]; however, some MB could also be degraded through its direct electrochemical oxidation at the anode surface. The disappearance of the blue colour of MB during the electrolysis was used to monitor the kinetics of the degradation process by utilizing UV-Vis spectrophotometry. The representative MB absorption spectra depicted in Figure 6.1 displays two prominent peaks in the visible region at ca. 610 and 660 nm, that correspond to MB dimer $(MB^+)_2$ and monomer (MB^+), respectively [261-263]. However, the sharper absorption peak at 660 nm was used to correlate MB absorbance with its concentration in the solution over time.

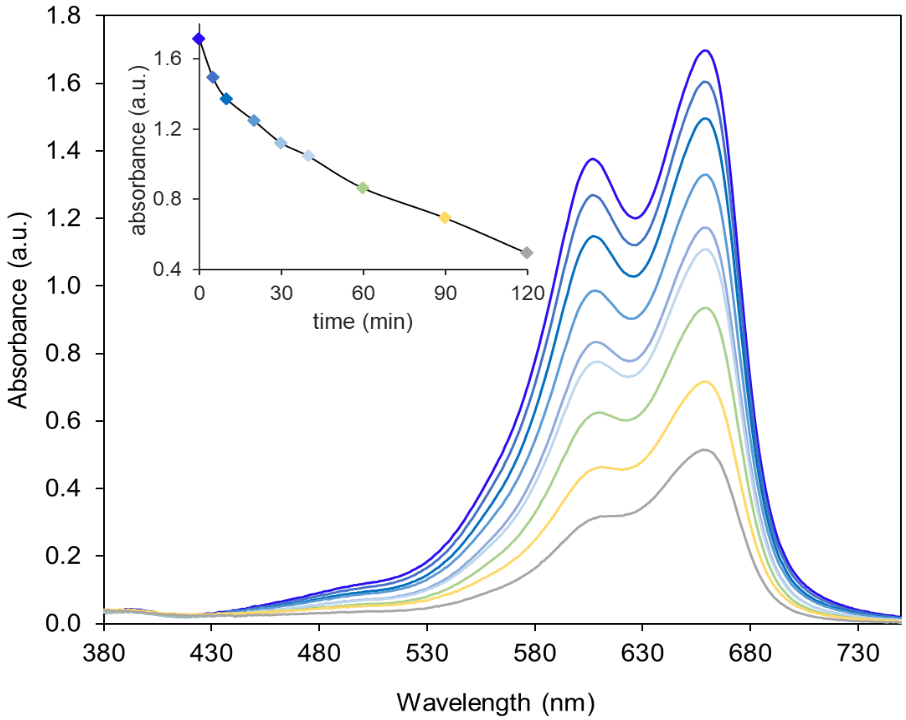

Figure 6.1: The variation of UV spectrum of methylene blue during its electrochemical degradation on $Ni_{0.6}Co_{0.4}$-oxide anode electrode in 0.17 M Na_2SO_4 aqueous solution containing 50 mg/L of MB, at T = 295 ± 2 K; current density = 20 mA/cm^2. The inset shows the change of 660 nm peak intensity with time.

As it can be seen, the MB absorption peaks decrease with time, evidencing the decrease in MB concentration in the electrolyte. It was also visually observed that the intensity of blue colour of electrolyte diminishes with time. The inset to the figure more clearly depicts the gradual decrease in MB peak absorbance with time.

The MB oxidation (degradation) rate depends on the concentration of hydroxyl radicals generated by oxidation of water at the anode surface (indirect oxidation). The kinetics of the hydroxyl radicals generated, in turn, depends on the current passing through the anode surface. Further, if MB is partially degraded by direct oxidation at the anode surface, the rate of this process will also depend on the current passing through the anode surface. Consequently, it was of interest to investigate the influence of applied current density on the kinetics of MB degradation. Therefore, MB degradation experiments in the solution containing 50 mg/L of MB in 0.17M of Na_2SO_4 were performed at different current densities, and Figure 6.2 shows the corresponding MB degradation kinetic curves. It is observed that the methylene blue degradation kinetics increases with an increase in current density, as expected. After two hours, 70% of the initially-present MB was degraded at 10 mA/cm^2, while at 60 mA/cm^2, all of the MB was degraded. In fact, the percentage of initially-present MB degraded is directly proportional to the charge passed through the anode, and Figure 6.2(B) shows that this dependence is linear. This indicates good performance of the anode in MB degradation. Namely, the anodic MB degradation reaction is always paralleled by the oxygen evolution reaction (the same is true in case of electrochemical anodic degradation of any organic compound in an aqueous solution). If the $Ni_{0.6}Co_{0.4}$-oxide anode was a poor MB degradation electrocatalyst, with an increase in current density, the proportion of current that goes to MB degradation would decrease on the account of OER current increase. However, Figure 6.2(B) shows that the kinetics of MB degradation is proportional to the current density (i.e. charge), evidencing that the $Ni_{0.6}Co_{0.4}$-oxide is indeed a good MB-degradation anode. Further, during the electrolysis, the solution pH remained stable, at ca. 5.8 ± 0.1, also indicating that the predominant anodic reaction was MB degradation.

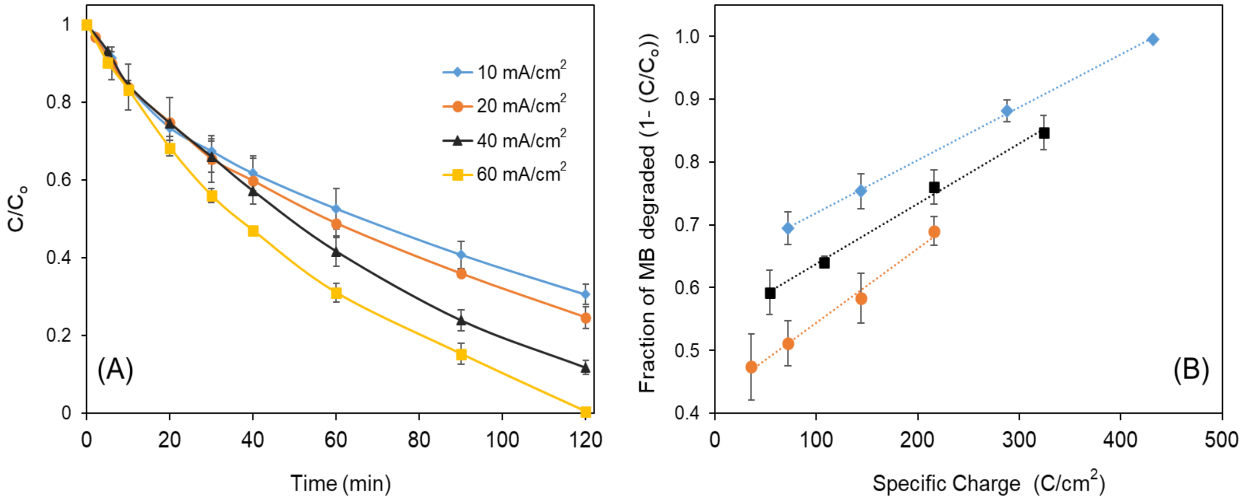

Figure 6.2: (A) Kinetics of electrochemical degradation of methylene blue dye (50 mg/L) at the $Ni_{0.6}Co_{0.4}$-oxide anode recorded at different current densities; (B) Fraction of the initial MB degraded as a function of charge passed through the anode after (●) 60, (■) 90 and (◆) 120 minutes of degradation. Electrolyte: 0.17 M Na_2SO_4 aqueous solution.

6.4.2. Influence of chloride ion concentration on the electrocatalytic degradation rate

It is important to note that in every wastewater system, there could be a certain amount of chloride ion present, which emanates from the ubiquity of common salt, especially in the daily human nutritional habit. The dissolved chloride ion can be, at the anode, converted to strong oxidants of active chlorine (such as Cl_2, HOCl, ClO^-) during the electrochemical treatment of wastewater [121]:

$$2Cl^- \rightarrow Cl_2 + 2e^- \tag{6.1}$$

$$Cl_2 + H_2O \rightarrow HClO + H^+ + Cl^- \tag{6.2}$$

$$HClO \rightarrow H^+ + ClO^- \tag{6.3}$$

Therefore, it was pertinent to investigate the influence of chloride ion concentration on the rate of MB removal employing the $Ni_{0.6}Co_{0.4}$-oxide anode, in addition to its removal by hydroxyl radicals (and potentially by direct oxidation) in the absence of chlorides, as shown in Figure 6.2. A relatively low concentration of chlorides, in the range of 0.25 to 2 g/L, was selected, which is comparatively lower than the concentration of chlorides in a sea water (35 g/L). The investigation was initially done at a current density of 20 mA/cm^2, and the results are presented in Figure 6.3.

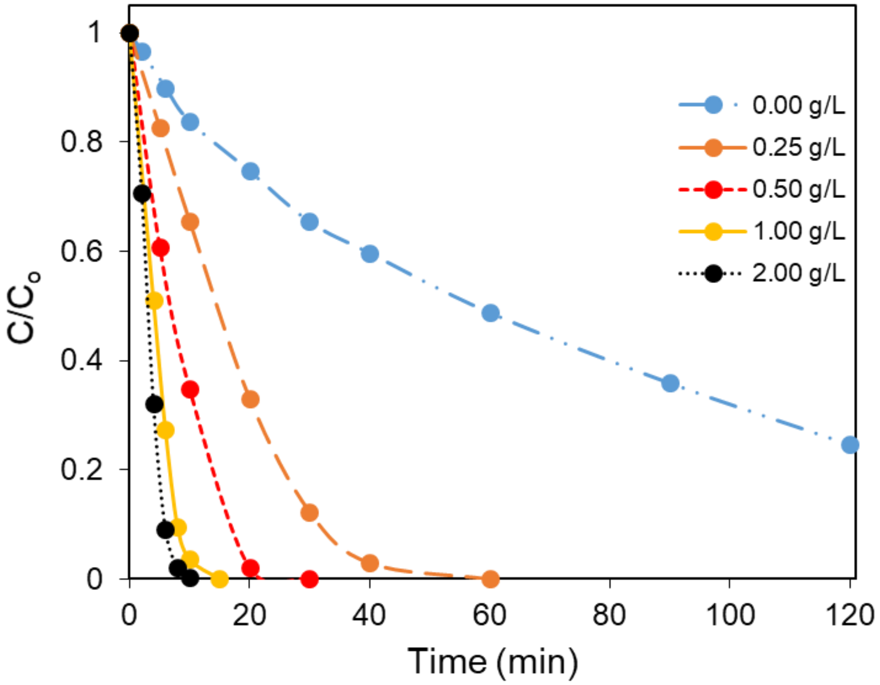

Figure 6.3: Influence of NaCl concentration on the electrochemical degradation of methylene blue dye by $Ni_{0.6}Co_{0.4}$-oxide at 20 mA/cm^2 current density in 0.17 M Na_2SO_4 aqueous solution.

From the result, it is evident that there was a dramatic improvement in the kinetics of MB degradation as the chloride ion concentration increased, which could be attributed to the strong oxidative action of electrogenerated chlorine species oxidants.

6.4.3. Influence of current density on active chlorine assisted degradation

Although the degree of MB degradation at the applied current density of 20 mA/cm^2 increased significantly with increasing concentration of Cl$^-$ ion (Figure 6.3), the time taken to completely destroy the methylene blue dye did not change significantly for [NaCl] ≥ 1 g/L. Consequently, it was of interest to determine the effect of current density on the MB degradation time at a fixed chloride concentration of 2 g/L, and the results are presented in Figure 6.4. From the results presented in the figure, it is evident that the MB oxidation rate increased with increasing current density.

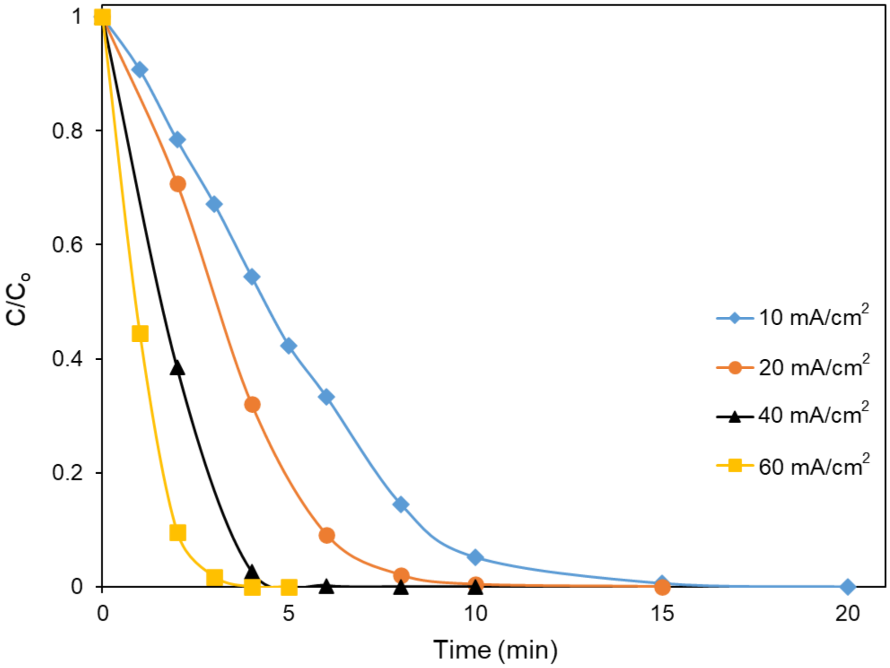

Figure 6.4: Degree of degradation of methylene blue with varying current density in 0.17 M Na_2SO_4 aqueous electrolyte containing 2 g/L NaCl salt.

Thus, it took almost 20 min for the concentration of MB to drop to zero at 10 mA/cm^2, while at 60 mA/cm^2 this occurred within less than 4 min from the start of the process. When the charge invested in degrading MB completely was calculated at different current densities, the average value was 12.5±0.6 C/cm^2; the small standard deviation value (the relative value is 4.6%) indicates that the current that passed through the cell was predominantly invested in MB degradation, rather than in oxygen evolution. Further, given the fact that in the presence of chloride ions, the MB degradation rate is significantly faster (Figure 6.3), owing to the formation of active chlorine species that are strong oxidants. This small relative standard deviation value also indicates that most of the chloride ions oxidized at the anode into chlorine (active species) was used to degrade MB. Otherwise, the charge required to degrade MB to zero concentration would increase with increased current density. Further, the temperature of the chloride ion-containing electrolyte was observed to change only slightly, by ca. 1.8 ± 0.6K, during the electrochemical degradation. Hence, the observed improvement in the oxidation rate is negligibly affected by the electrolyte temperature. Nonetheless, the conductivity of the 0.17 M Na_2SO_4 aqueous solution is expected to improve with an increase in the NaCl concentration. However, there is no consensus as to whether the improved solution conductivity leads to improved oxidation efficiency, but rather it is indicative of lower overpotential at a given current density, due to the lower jR drop [121]. Further, the pH of the solution at the start and at the end of the degradation process was observed to change from 7.6 ± 0.2 to 8.3 ± 0.3, for all NaCl concentrations.

Although it is useful to determine the extent of MB removal by measuring the C/Co ratio via the UV-Vis spectrophotometric measurement, it is also relevant to investigate the chemical oxygen demand (COD) and the total organic carbon (TOC) of the degrading MB analyte in order to elicit its degree of mineralization in the solution. Figure 6.5 presents the evolution of removal efficiency based on the COD and TOC measurements during the electrochemical oxidation of MB at 20 mA/cm^2 in 0.17 M Na_2SO_4 aqueous solution containing 2g/L NaCl (the colour removal, i.e. MB oxidation efficiency is presented for comparison). Note that the initial COD and TOC values were ca. 63 mg/L and 26.5 mg/L, respectively. Figure 6.5 shows that the COD and TOC decreased progressively with time (i.e. the corresponding removal efficiency increased) leading to the complete mineralisation of the blue dye. Notice that it took ca, 10 min to decolorize the MB-containing solution, however, only ca. 76% and ca. 58% of the initial COD and TOC were removed during this time, respectively. The complete abatement of COD and TOC was achieved after 50 and 60 min, respectively. The COD and TOC results are indicative of the formation of intermediate products that are less rapidly converted to carbon dioxide than the disappearance of the methylene blue.

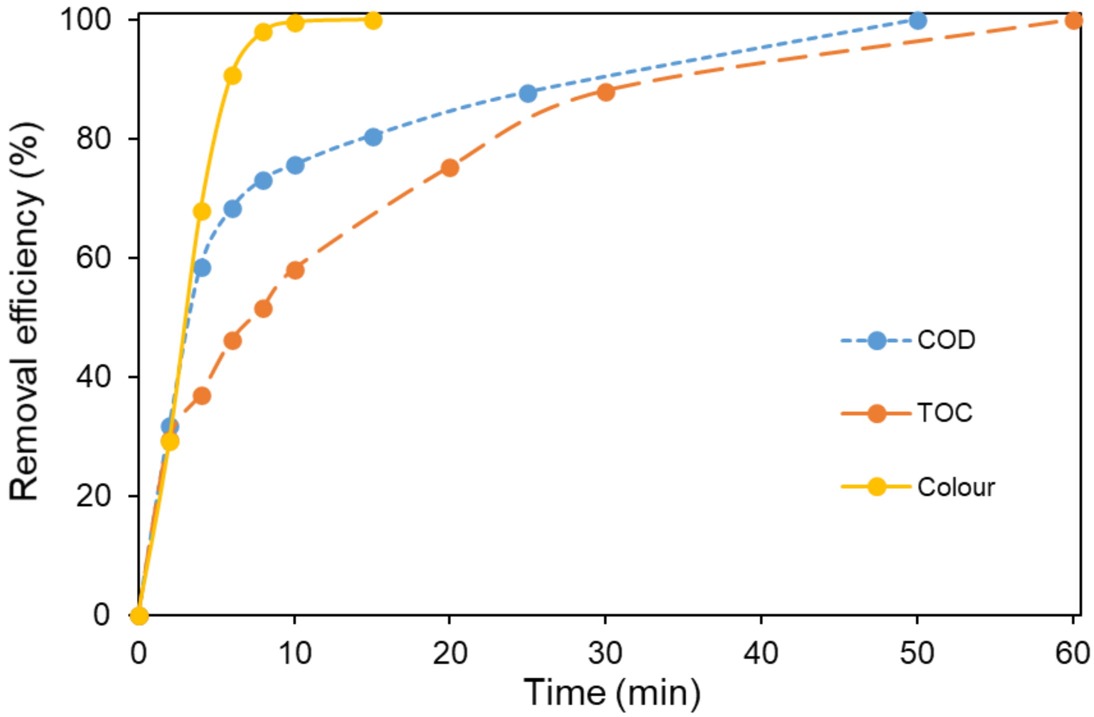

Figure 6.5: The COD, TOC and colour removal efficiency with time of MB on $Ni_{0.6}Co_{0.4}$-oxide at 20 mA/cm^2 current density in 0.17 M Na_2SO_4 aqueous solution containing 2 g/L NaCl salt.

Nevertheless, these results further support that $Ni_{0.6}Co_{0.4}$-oxide is an effective material for the electrochemical degradation of the MB, organic contaminant. Notably, at similar current density and chloride ion concentration, the NiCo-oxide material showed comparable performance to $TiRuO_2$, BDD, PbO_2/Ti which are among some of the best electrochemical anodes for MB degradation reported in the literature [119, 264]. However, in terms of cost, the NiCo-oxide anode is much cheaper than Ti/$TiRuO_2$ anode [119], and significantly more environmentally-friendly than PbO_2/Ti electrode [264].

6.4.4. Stability of the anode material

In as much as electrochemical anodes are supposed to be effective in treating a given volume of wastewater system per unit time, it is also necessary for the electrodes to be electrochemically stable over a longer period of time. One way of estimating the wastewater treatment anode stability is to monitor its potential (or cell voltage) with time at a constant current density. Figure 6.6 shows the cell voltage measured when a constant current density of 20 mA/cm^2

was applied between the $Ni_{0.6}Co_{0.4}$-oxide anode and the stainless steel cathode over a period of 50 hours electrolysis of 1g/L MB in 0.17 M Na_2SO_4 aqueous solution (pH = 4.2). The lifetime test result of Figure 6.6 evidences that the anode material is sufficiently stable over the time interval investigated. Similar stability results were obtained for other sets of conditions already highlighted above. Furthermore, energy-dispersive X-ray spectroscopic (EDX) analysis of the residual solutions dried on a filter paper revealed no appreciable dissolution of the active metals during the electrochemical degradation. Nevertheless, it should be noted that the aim of the research presented here was not to produce a highly stable $Ni_{0.6}Co_{0.4}$-oxide, but rather to investigate its applicability in the MB degradation process. For the former, a range of other $Ni_{0.6}Co_{0.4}$-oxide production methods could be used, which could potentially result in an even more stable oxide layer.

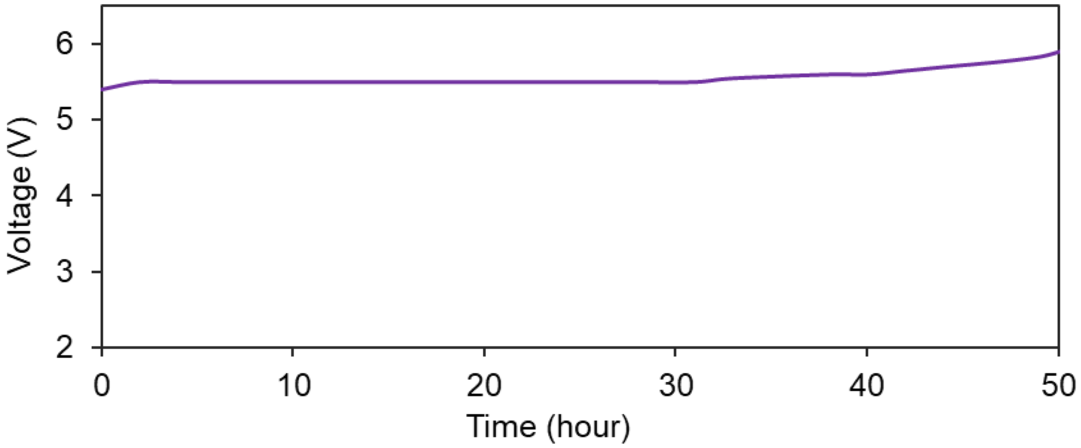

Figure 6.6: Voltage difference between the $Ni_{0.6}Co_{0.4}$-oxide anode and stainless steel cathode during the electrochemical degradation of methylene blue dye of 1g/L in 0.17 M Na_2SO_4 at a current density of 20 mA/cm^2.

6.4.5. Energy consumption determination

Although it may be beneficial to achieve useful oxidation rate at a higher current density, however this may lead to increased energy consumption [120]. Consequently, to appreciate the, cost-effectiveness of the electrochemical oxidation treatment technique, it is important to determine if the process is energy efficient. Typically, the energy consumption of electrochemical decontamination is dependent on key parameters such as reactor configuration, concentration of treated contaminant [125] etc. In this work, the overall energy consumed was primarily estimated as the electrical energy consumption per volume of treated solution (in kWh/m^3) as described in literature [125].

Figure 6.7 showcases the total energy consumption for the complete removal of 50 mg/L methylene blue in 0.17 M Na_2SO_4 containing 2 g/L of NaCl (in blue) and that required for 70% degree of degradation in the absence of chloride ions (in red), here noted as case A and B respectively. In both cases, a linear relationship was found to exist between the total input energy and the applied current density. The result indicates that although the degradation process can be sped up in both cases by operating at higher current densities, this leads to a corresponding increase in operational cost. However, it was previously determined that the charge required to degrade MB either in the absence or presence of chloride ions was constant with current density. Thus, the increase in power consumption comes from the increase in cell potential required to 'push' the required current through the system, which is common in electrochemistry and is predominantly related to the kinetics of electrochemical reactions, but also to the presence of other resistances in the system (see Eq.(2.7)).

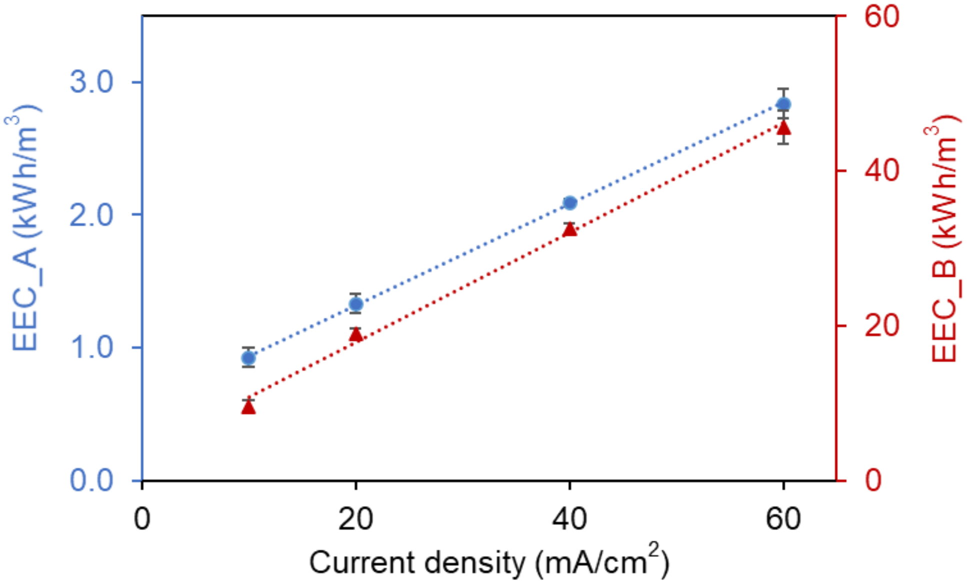

Figure 6.7: Energy consumption required for 100% MB degradation in 0.17 M Na_2SO_4 + 2 g/L NaCl (EEC_A) and for 70% MB degradation in 0.17 M Na_2SO_4 in the absence of Cl^- ions (EEC_B) in a current density range of 10 – 60 mA/cm^2.

The main observation in Figure 6.7 is that the power needed to completely degrade MB is significantly lower when chlorides are present in the electrolyte than even the power required for a non-complete (70%) degradation of MB in the absence of chlorides.

Furthermore, it is useful to determine the specific energy consumption and the corresponding current efficiency based on COD since this outlines the amount of energy necessary for the complete mineralisation of the MB. Hence, the instantaneous current efficiency (ICE) which is the ratio of the charge employed in the anodic oxidation of each MB compound to the total charge passed during the electrolysis was evaluated from COD values [265, 266]. The specific energy consumption, in kWh/kgCOD, which is the energy needed to remove one kg of COD from the wastewater was also calculated from equation 6.5 [119]:

$$ICE\ (\%) = \frac{COD_t - COD_{t+\Delta t}}{8I\Delta t} F\nu \tag{6.4}$$

$$SEC = \frac{VI\Delta t}{\Delta COD \times \nu} \tag{6.5}$$

where COD_t and $COD_{\Delta t}$ are the COD at time t and t + Δt [gO_2 /L], respectively. The number "8" represents the oxygen equivalent mass (g/eq). F is the Faraday constant (96486 C/mol), V is the potential difference across the electrodes (V), I is the applied current (A), Δt is the electrolysis time (in sec for Eq. (6.4) and in hours for Eq. (6.5)). ΔCOD is the COD reduction in g/L during the time Δt and ν is the volume of treated wastewater in L.

The complete electrochemical mineralisation of MB at 20mA/cm^2 in the chloride ion-influenced anodic oxidation (Figure 6.5) yielded a current efficiency of 26.4% which is similar to value reported elsewhere in the literature [119]. The results presented in Figure 6.5 also depict that the SEC needed to completely mineralize MB is 101.6 kWh/kgCOD whereas to achieve ca.70% degradation of 50 mg/L MB, a SEC value of 12.9 kWh/kgCOD which is substantially lower than 82.4 kWh/kgCOD needed to remove less MB in another study [266]. It should also be noted that power requirement can further be decreased by a proper design of the electrochemical treatment reactor; however, this was not within the scope of this PhD project.

6.5. Conclusion

The $Ni_{0.6}Co_{0.4}$-oxide demonstrated to be an effective anode candidate for the electrochemical degradation of methylene blue (MB) dye in an aqueous solution. The kinetics of MB degradation was found to be largely dependant on the current density that passed through the cell, and was found to increase with an increase in current density. It was also found that the increase in current density was invested predominantly in improving the kinetics of the MB degradation reaction, rather than in the competitive oxygen evaluation reaction, making the $Ni_{0.6}Co_{0.4}$-oxide a good candidate for degradation of organic compounds in aqueous solutions. The presence of chloride ions in the electrolyte was found to significantly improve the kinetics of MB degradation, which was attributed to the formation of electrogenerated active chlorine species.

Acknowledgement: The authors are indebted to the Nigerian Petroleum Technology Development Fund (PTDF), Natural Sciences and Engineering Research Council of Canada (NSERC), and the McGill Engineering Doctoral Award (MEDA) for their financial support. Our immense gratitude also goes to Mr. Ranjan Roy and Mr. Andrew Golsztajn for their technical input during the UV/Vis spectrophotometric measurements.

Chapter 7 Conclusions

The current practice of meeting global energy demand with limited, unsustainable hydrocarbon energy sources is inimical to the environment. As a result, significant research efforts have been made to address this challenge. Consequently, the production of sustainable hydrogen as an alternative energy source from a seemingly unlimited earth-abundant resource, water, has been touted as a possible viable solution. However, the production process by water-splitting is commercially-limited by the slow kinetics of its anodic oxidation process, among other factors. In light of this, the primary focus of this Ph.D. project work was to develop effective, low-cost electrochemical anodes for the electrolytic production of hydrogen (water splitting). Taking into account that poorly-performing OER anodes could be used for oxidation of molecules in aqueous solution, the project also investigated the applicability of such an anode material produced in current work as a possible material for the destruction of organics in wastewater treatment, more specifically, for the oxidation (treatment) of dye-containing wastewater.

This section reports the ensuing main conclusions drawn from the different subprojects presented in chapters 3 to 6 of this Ph.D. thesis work by summarizing the key project outcomes:

7.1. Investigation of Ni-Co-oxides as a base OER anode material

The electrocatalytic activity of different binary Ni_xCo_{1-x}-oxide anode compositions prepared by thermal salt decomposition on titanium substrate was investigated in a harsh acidic medium to assess the potential of the electrodes as viable alternative catalysts to the exorbitant state of the art IrO_2 anode in PEM electrolysers. The elicited conclusions are given below:

- The durable Ni-Co-oxide films were composed of crystalline oxide phases that are morphologically characterized by rough microporous surfaces.
- It was observed that the surface roughness of the oxide coatings was dependent on their chemical composition.
- Augmentation of Co content in the mixed metal oxide increased the electrochemically-active surface area of the electrocatalyst.

- The relative electrocatalytic activity of the Ni_xCo_{1-x}-oxide coatings was related predominantly to the intrinsic electrocatalytic properties of the coatings, rather than their extrinsic nature.
- $Ni_{0.4}Co_{0.6}$-oxide was identified as the best binary oxide composition of all the investigated mixed metal oxides both intrinsically and extrinsically.
- Even though the state-of-the-art anode, Ir-oxide, yielded OER activity of one order of magnitude better than $Ni_{0.4}Co_{0.6}$-oxide, the latter anode is of a significantly lower cost. Therefore, the discrepancy in activity can easily be compensated by a larger catalyst loading of $Ni_{0.4}Co_{0.6}$-oxide. Further, this anode composition can serve as a basis for its further improvement, as outlined below.

7.2. Influence of Ir content on the activity of Ni-Co-oxide Anode

The relatively good OER activity of $Ni_{0.4}Co_{0.6}$-oxide, which was found to be purely intrinsic, could be further enhanced by the incorporation of a small amount of a state-of-the-art OER electrocatalyst material in the binary oxide film - iridium. Consequently, the effect of Ir content on the catalytic activity of ternary $(Ni_{0.4}Co_{0.6})_{1-x}Ir_x$-oxide coatings towards OER was studied in acidic and alkaline media. The following specific conclusions were drawn:

- Addition of small amount ($\leq 10\%$) of Ir to $Ni_{0.4}Co_{0.6}$-oxide increases its electrocatalytic activity towards OER.
- The enhancement in OER activity of $Ni_{0.4}Co_{0.6}$-oxide by the addition of Ir is attributed to the synergistic relationship among crystalline oxide phases (IrO_2, Co_3O_4, CoO and NiO) leading to the modification of the Ir f-shell electronic configuration and the reduction in band gap energy relative to $Ni_{0.4}Co_{0.6}$-oxide and Ir-oxide.
- Surface characterization of the coated surfaces showed that the morphology of the crystalline oxides was composition-dependent.
- The ternary oxides demonstrated significantly higher OER activity in the alkaline medium than the current state-of-the-art alkaline Ni anode.
- In the acidic media, the electrocatalytic activity of the $(Ni_{0.4}Co_{0.6})_{1-x}Ir_x$-oxide varied linearly with Ir content at a fixed overpotential (input energy). The $(Ni_{0.4}Co_{0.6})_{0.90}Ir_{0.10}$-

oxide composition was also found to be significantly more active than the state-of-the-art IrO_2 PEM anode.

- A 24-hour long-term stability test performed on $(Ni_{0.4}Co_{0.6})_{0.90}Ir_{0.10}$-oxide showed both good electrochemical and structural durability of the material in acidic and basic media.
- $(Ni_{0.4}Co_{0.6})_{0.90}Ir_{0.10}$-oxide is an excellent anode material that can serve as a potential cost-effective replacement for currently used expensive anodes both in acidic and alkaline electrolysers.

7.3. Calcination Temperature Effect on Ni-Co-Ir/Ru-oxides OER activity

It was considered that varying the fabrication temperature of the trimetal oxides could be a useful way to further improve the OER activity of the oxides. Hence, the influence of calcination temperature on the electrocatalytic properties of $(Ni_{0.4}Co_{0.6})_{0.9}Ir_{0.1}$-oxide and $(Ni_{0.4}Co_{0.6})_{0.9}Ru_{0.1}$-oxide in the oxygen evolution reaction was studied in alkaline solution of 1 M NaOH. The following pertinent conclusions are presented:

- The OER electrocatalytic performance of trimetal oxides of $(Ni_{0.4}Co_{0.6})_{0.9}Ir_{0.1}$-oxide and $(Ni_{0.4}Co_{0.6})_{0.9}Ru_{0.1}$-oxide are significantly influenced by the calcination temperature in the thermal-preparation of the oxides.
- An optimum synthesis temperature of 300°C was observed for the two different oxides, at which the electrocatalysts exhibited excellent OER activity far superior to Ni and IrO_2 state-of-the-art electrodes and close to RuO_2, the best OER anode in the alkaline medium.
- The surface morphologies of the coatings and the crystallinity of the coatings' oxide phases are calcination temperature-dependent.
- The OER kinetics data analysis showed that the oxygen evolution reaction on both trimetal oxides followed the Bockris electrochemical oxide mechanism with the following step: $M\text{–}OH + OH^- \rightarrow M\text{–}O + H_2O + e^-$, being rate-determining.
- XPS results showed that the improvement in OER performance of the ternary oxides can be explained predominantly by the modification of the Ir-4f and Ru-3d electronic structures and in part by increase in the hydroxide content and oxygen vacancies.

- The long-term durability test of Ni-Co-Ir/Ru-oxides in the alkaline medium revealed that the trimetal oxides were more stable than the current state-of-the-art Ir- and Ru-oxides due to the stabilizing effect of $Ni_{0.4}Co_{0.6}$-oxide in the medium.
- $(Ni_{0.4}Co_{0.6})_{0.9}Ir_{0.1}$-oxide and $(Ni_{0.4}Co_{0.6})_{0.9}Ru_{0.1}$-oxide have enormous potential to be used as excellent OER anodes in the commercial production of hydrogen.

7.4. Electrochemical Oxidation of Wastewater by Ni-Co-Oxide

A relatively poor OER anode may be a good candidate for the electrochemical decontamination of wastewater system because of the large anodic overpotential generally required for such applications. However, this material is expected to be conductive to facilitate ease of charge transfer or electron flow through the electrochemical cell. Therefore, $Ni_{0.6}Co_{0.4}$-oxide, which was found to be the least intrinsically active OER during the initial screening of Ni_xCo_{1-x}-oxide compositions, was evaluated for the degradation of a model dye, methylene blue (MB), in aqueous solution. The main conclusions obtained are outlined below:

- The fabricated Ti/$Ni_{0.6}Co_{0.4}$-oxide was found to be an effective electrode in the anodic oxidation of MB in 0.17 M Na_2SO_4 solution.
- The degradation mechanism is considered to proceed predominantly *via* indirect oxidation of MB at the anode surface owing to the electrogeneration of strong oxidant of hydroxyl radicals.
- Addition of chloride ions into the electrolyte dramatically increased the oxidation rate of MB. This is due to the *in situ* electrogeneration of active chlorine species that are strong oxidants.
- The chronopotentiometric data recorded during the degradation process show that the $Ni_{0.6}Co_{0.4}$-oxide anode exhibited durable performance for 10 hours of electrolysis.
- $Ni_{0.6}Co_{0.4}$-oxide is a low-cost, effective and highly energy-efficient anode material for MB degradation. Therefore, it has the potential to be utilized in the industrial treatment of organic pollutants in a wastewater treatment plant.

In conclusion, this Ph.D. thesis presents Ni-Co-oxide-based electrodes as efficient oxygen-evolving anodes in the electrolytic production of hydrogen and as good candidates for wastewater treatment anodes, depending on their chemical composition. The catalytic activity of the best performing $Ni_{0.4}Co_{0.6}$-oxide was substantially enhanced when doped with small amount of Ir and Ru. The activities of $(Ni_{0.4}Co_{0.6})_{0.90}Ir_{0.1}$-oxide and $(Ni_{0.4}Co_{0.6})_{0.9}Ru_{0.1}$-oxide were further augmented when annealed at 300°C, outperforming the state-of-the-art IrO_2 anode. Hence, these materials are potentially excellent OER catalyst for the commercial production of inexpensive hydrogen. Also, $Ni_{0.6}Co_{0.4}$-oxide (the least OER active anode) demonstrated good performance in the electrochemical oxidation of methylene blue (MB). In the presence of low amounts of chloride ions, the kinetics of electrochemical degradation of MB was enormously improved by the *in situ* electrogenerated active chlorine species. Subsequently, the energy consumption for the degradation process was tremendously lowered, making it more energy-efficient than some other advanced oxidation processes. Therefore, the developed electrode material could potentially be considered as a very good anode material in the industrial electrochemical wastewater treatment of organic pollutants.

Chapter 8 Original Contributions and Future Work

8.1. Original contributions to knowledge

This Ph.D. project was successful in developing low-cost, active and highly energy-efficient anode electrocatalysts, which when employed in the anodic oxidation process have immense potential to contribute to sustainable hydrogen energy production and can also be applied in the wastewater treatment technology. The following are the key original contributions to knowledge:

- The developed Ni-Co-oxide-based electrodes are potentially low-cost, effective replacements for expensive noble metal anodes in water electrolysis.
- Particularly, the addition of Ir to Ni-Co-oxide-based anode yielded excellent OER electrocatalyst that can easily replace the state-of-the-art IrO_2 anode thereby making the electrolytic production of hydrogen more commercially viable.
- It was found that the fabrication of Ni-Co-Ir-oxide and Ni-Co-Ru-oxide at the appropriate temperature is a beneficial approach to augmenting their OER performance.
- It was shown that Ni-Co-oxide can be utilized as a low-cost efficient electrochemical anode for the degradation of organic pollutants in wastewater treatment.

8.2. Recommendations for future work

Despite the fact that progress has been made in the development of electrocatalyst materials of useful oxygen evolution kinetics and the application of such active anodes in the oxidation of organic contaminants in wastewater treatment plants, further research work can still be done. The following research project options can be undertaken to extend the accomplishments of this Ph.D. thesis:

- It would be interesting to try other combinations of non-noble transition metal oxides (such as Ni-W, Ni-Mn, Co-Fe) that have shown relatively good electroactivity in order to see if there exists an intrinsically best composition that can serve as a base to develop highly electroactive catalysts for the oxygen evolution reaction.

- Electrode preparation techniques namely, sol-gel, electrochemical vapor deposition, hydrothermal, co-precipitation can be employed to compare the performance of the electrodes through these synthesis procedures.
- Production of nanoparticle-based metal oxides should be explored since OER activity can be increased substantially due to increased available active surface area and improved conductivity of the nanomaterials.
- Oxygen evolution is more aggressive than the hydrogen evolution reaction (HER), therefore these OER metal oxides that have shown to be electroactive can be tested in the HER. In addition, the highly electroactive Ni-Co-Ir-oxide and Ni-Co-Ru-oxide composites can each be used as a dual electrode for the overall water-splitting process.
- Typically, the long-term stability investigations in this research were done over 24-hour water electrolysis. Hence, it would be pertinent to test the durability of the mixed metal oxides over an extended period of time (months) in preparation for large-scale deployment of the anode.
- In the electrochemical degradation of methylene blue (MB), it would be useful to monitor the destruction of MB via other methods such as chemical oxygen demand (COD) and total organic carbon (TOC) content. Moreover, the electrochemical degradation should be evaluated for applicability by determining possible transformation products that might be formed in the course of MB destruction.

References

[1] NASA. (2020). *Global Climate Change: Vital Signs of the Planet (2020).https://climate.nasa.gov/vital-signs/carbon-dioxide/, Accessed 6 July 2020*.

[2] Y. Li, H. Wang, L. Xie, Y. Liang, G. Hong, and H. Dai, "MoS_2 Nanoparticles Grown on Graphene: An Advanced Catalyst for the Hydrogen Evolution Reaction," *Journal of the American Chemical Society,* vol. 133, pp. 7296-7299, 2011/05/18 2011.

[3] A. J. Bard and M. A. Fox, "Artificial photosynthesis: solar splitting of water to hydrogen and oxygen," *Accounts of Chemical Research,* vol. 28, pp. 141-145, 1995.

[4] T. Hijikata, "Research and development of international clean energy network using hydrogen energy (WE-NET)," *International Journal of Hydrogen Energy,* vol. 27, pp. 115-129, 2002.

[5] P. Kruger, "Electric power requirement for large-scale production of hydrogen fuel for the world vehicle fleet," *International Journal of Hydrogen Energy,* vol. 26, pp. 1137-1147, 2001.

[6] C. Mitsugi, A. Harumi, and F. Kenzo, "WE-NET: Japanese hydrogen program," *International Journal of Hydrogen Energy,* vol. 23, pp. 159-165, 1998.

[7] R. LeRoy, "Industrial water electrolysis: present and future," *International journal of hydrogen energy,* vol. 8, pp. 401-417, 1983.

[8] E. Zoulias, E. Varkaraki, N. Lymberopoulos, C. N. Christodoulou, and G. N. Karagiorgis, "A review on water electrolysis," *The Cyprus Journal of Science and Technology,* vol. 4, pp. 41-71, 2004.

[9] B. Ewan and R. Allen, "A figure of merit assessment of the routes to hydrogen," *International Journal of Hydrogen Energy,* vol. 30, pp. 809-819, 2005.

[10] D. Hall, "Ni (OH) 2-Impregnated Anodes for Alkaline Water Electrolysis," *Journal of The Electrochemical Society,* vol. 130, pp. 317-321, 1983.

[11] M. E. Lyons and M. P. Brandon, "A comparative study of the oxygen evolution reaction on oxidised nickel, cobalt and iron electrodes in base," *Journal of Electroanalytical Chemistry,* vol. 641, pp. 119-130, 2010.

[12] M. Lundberg and P. E. Siegbahn, "Minimum energy spin crossings for an O–O bond formation reaction," *Chemical Physics Letters,* vol. 401, pp. 347-351, 2005.

[13] I. Herraiz-Cardona, E. Ortega, L. Vázquez-Gómez, and V. Pérez-Herranz, "Electrochemical characterization of a NiCo/Zn cathode for hydrogen generation," *international journal of hydrogen energy,* vol. 36, pp. 11578-11587, 2011.

[14] G. Lodi, E. Sivieri, A. De Battisti, and S. Trasatti, "Ruthenium dioxide-based film electrodes," *Journal of Applied Electrochemistry,* vol. 8, pp. 135-143, 1978.

[15] S. Trasatti, "Electrocatalysis by oxides—attempt at a unifying approach," *Journal of Electroanalytical Chemistry and Interfacial Electrochemistry,* vol. 111, pp. 125-131, 1980.

[16] C. Angelinetta, S. Trasatti, L. D. Atanasoska, Z. Minevski, and R. Atanasoski, "Effect of preparation on the surface and electrocatalytic properties of RuO 2+ IrO 2 mixed oxide electrodes," *Materials chemistry and physics,* vol. 22, pp. 231-247, 1989.

[17] M. D. Merrill and R. C. Dougherty, "Metal Oxide Catalysts for the Evolution of O2 from H2O," *The Journal of Physical Chemistry C,* vol. 112, pp. 3655-3666, 2008.

[18] H. Ali-Löytty, M. W. Louie, M. R. Singh, L. Li, H. G. Sanchez Casalongue, H. Ogasawara, *et al.*, "Ambient-pressure XPS study of a Ni–Fe electrocatalyst for the oxygen evolution reaction," *The Journal of Physical Chemistry C,* vol. 120, pp. 2247-2253, 2016.

[19] A. H. Imani, R. Ojani, and J.-B. Raoof, "In situ synthesis of a novel organic-inorganic composite as a non-noble metal electrocatalyst for the oxygen evolution reaction," *International Journal of Hydrogen Energy,* vol. 43, pp. 8267-8277, 2018.

[20] E. Veggetti, I. Kodintsev, and S. Trasatti, "Hydrogen evolution on oxide electrodes: Co_3O_4 in alkaline solution," *Journal of Electroanalytical Chemistry,* vol. 339, pp. 255-268, 1992.

[21] F. Cardarelli, P. Taxil, A. Savall, C. Comninellis, G. Manoli, and O. Leclerc, "Preparation of oxygen evolving electrodes with long service life under extreme conditions," *Journal of Applied Electrochemistry,* vol. 28, pp. 245-250, 1998.

[22] S. Trasatti, "Electrocatalysis: understanding the success of DSA®," *Electrochimica Acta,* vol. 45, pp. 2377-2385, 2000.

[23] M.-R. Gao, Y.-F. Xu, J. Jiang, Y.-R. Zheng, and S.-H. Yu, "Water oxidation electrocatalyzed by an efficient $Mn_3O_4/CoSe_2$ nanocomposite," *Journal of the American Chemical Society,* vol. 134, pp. 2930-2933, 2012.

[24] S. Shibli and J. Sebeelamol, "Development of Fe 2 O 3–TiO 2 mixed oxide incorporated Ni–P coating for electrocatalytic hydrogen evolution reaction," *International Journal of Hydrogen Energy,* vol. 38, pp. 2271-2282, 2013.

[25] A. Tavares and S. Trasatti, "Ni+ RuO 2 co-deposited electrodes for hydrogen evolution," *Electrochimica acta,* vol. 45, pp. 4195-4202, 2000.

[26] Y. Gorlin and T. F. Jaramillo, "A bifunctional nonprecious metal catalyst for oxygen reduction and water oxidation," *Journal of the American Chemical Society,* vol. 132, pp. 13612-13614, 2010.

[27] R. Huo, W.-J. Jiang, S. Xu, F. Zhang, and J.-S. Hu, "Co/CoO/CoFe 2 O 4/G nanocomposites derived from layered double hydroxides towards mass production of efficient Pt-free electrocatalysts for oxygen reduction reaction," *Nanoscale,* vol. 6, pp. 203-206, 2014.

[28] R. Kötz and S. Stucki, "Stabilization of RuO 2 by IrO 2 for anodic oxygen evolution in acid media," *Electrochimica acta*, vol. 31, pp. 1311-1316, 1986.

[29] J. Brey, R. Brey, A. Carazo, I. Contreras, A. Hernandez-Diaz, and V. Gallardo, "Designing a gradual transition to a hydrogen economy in Spain," *Journal of power sources,* vol. 159, pp. 1231-1240, 2006.

[30] A. Gemain, W. D'haeseleer, and D. Haeseldonckx, "Hydrogen as an energy carrier," *Royal Belgian Academy Council of Applied Science*, pp. 3-34, 2006.

[31] K. Willquist. (2012). *Hydrogen: the green energy carrier of the future*. Available: http://ieahia.org

[32] M. A. Rosen and S. Koohi-Fayegh, "The prospects for hydrogen as an energy carrier: an overview of hydrogen energy and hydrogen energy systems," *Energy, Ecology and Environment*, vol. 1, pp. 10-29, 2016.

[33] L. F. Brown, "A comparative study of fuels for on-board hydrogen production for fuel-cell-powered automobiles," *International Journal of Hydrogen Energy,* vol. 26, pp. 381-397, 2001.

[34] J. D. Holladay, J. Hu, D. L. King, and Y. Wang, "An overview of hydrogen production technologies," *Catalysis today,* vol. 139, pp. 244-260, 2009.

[35] M. J. Prins, K. J. Ptasinski, and F. J. Janssen, "From coal to biomass gasification: Comparison of thermodynamic efficiency," *Energy,* vol. 32, pp. 1248-1259, 2007.

[36] S. Satyapal, J. Petrovic, C. Read, G. Thomas, and G. Ordaz, "The US Department of Energy's National Hydrogen Storage Project: Progress towards meeting hydrogen-powered vehicle requirements," *Catalysis today,* vol. 120, pp. 246-256, 2007.

[37] ESA. (2016). *Hydrogen Energy Storage*. Available: http://energystorage.org/energy-storage/technologies/hydrogen-energy-storage

[38] US Department of Energy, "DOE Technical Targets for Onboard Hydrogen Storage for Light-Duty Vehicles," ed: Office of Energy Efficiency and Renewable Energy, 2017.

[39] S. M. Lee, K. S. Park, Y. C. Choi, Y. S. Park, J. M. Bok, D. J. Bae, *et al.*, "Hydrogen adsorption and storage in carbon nanotubes," *Synthetic metals*, vol. 113, pp. 209-216, 2000.

[40] K. Jurewicz, E. Frackowiak, and F. Beguin, "Electrochemical storage of hydrogen in activated carbons," *Fuel processing technology,* vol. 77, pp. 415-421, 2002.

[41] Z. Zhao, H. Wu, H. He, X. Xu, and Y. Jin, "A High-Performance Binary Ni–Co Hydroxide-based Water Oxidation Electrode with Three-Dimensional Coaxial Nanotube Array Structure," *Advanced Functional Materials,* vol. 24, pp. 4698-4705, 2014.

[42] K. Chen, L. Ouyang, H. Zhong, J. Liu, H. Wang, H. Shao, *et al.*, "Converting H+ from coordinated water into H− enables super facile synthesis of LiBH 4," *Green Chemistry,* vol. 21, pp. 4380-4387, 2019.

[43] F. Zhao, T. N. Asmus, D. N. Assanis, J. E. Dec, J. A. Eng, and P. M. Najt, "Homogeneous charge compression ignition (HCCI) engines," SAE Technical Paper2003.

[44] X. Li, F. C. Walsh, and D. Pletcher, "Nickel based electrocatalysts for oxygen evolution in high current density, alkaline water electrolysers," *Physical Chemistry Chemical Physics,* vol. 13, pp. 1162-1167, 2011.

[45] V. Vij, S. Sultan, A. M. Harzandi, A. Meena, J. N. Tiwari, W.-G. Lee, *et al.*, "Nickel-based electrocatalysts for energy-related applications: oxygen reduction, oxygen evolution, and hydrogen evolution reactions," *Acs Catalysis,* vol. 7, pp. 7196-7225, 2017.

[46] C. Neagu, H. Jansen, H. Gardeniers, and M. Elwenspoek, "The electrolysis of water: an actuation principle for MEMS with a big opportunity," *Mechatronics,* vol. 10, pp. 571-581, 2000.

[47] R. V. Mom, J. Cheng, M. T. Koper, and M. Sprik, "Modeling the Oxygen Evolution Reaction on Metal Oxides: The Infuence of Unrestricted DFT Calculations," *The Journal of Physical Chemistry C,* vol. 118, pp. 4095-4102, 2014.

[48] Y. Jiao, Y. Zheng, M. Jaroniec, and S. Z. Qiao, "Design of electrocatalysts for oxygen-and hydrogen-involving energy conversion reactions," *Chemical Society Reviews,* vol. 44, pp. 2060-2086, 2015.

[49] P. Liao, J. A. Keith, and E. A. Carter, "Water oxidation on pure and doped hematite (0001) surfaces: Prediction of Co and Ni as effective dopants for electrocatalysis," *Journal of the American Chemical Society,* vol. 134, pp. 13296-13309, 2012.

[50] H. Dau, C. Limberg, T. Reier, M. Risch, S. Roggan, and P. Strasser, "The mechanism of water oxidation: from electrolysis via homogeneous to biological catalysis," *ChemCatChem,* vol. 2, pp. 724-761, 2010.

[51] I. C. Man, H. Y. Su, F. Calle-Vallejo, H. A. Hansen, J. I. Martínez, N. G. Inoglu*, et al.*, "Universality in oxygen evolution electrocatalysis on oxide surfaces," *ChemCatChem,* vol. 3, pp. 1159-1165, 2011.

[52] R. L. Doyle and M. E. G. Lyons, "The Oxygen Evolution Reaction: Mechanistic Concepts and Catalyst Design," in *Photoelectrochemical Solar Fuel Production: From Basic Principles to Advanced Devices*, S. Giménez and J. Bisquert, Eds., ed Cham: Springer International Publishing, 2016, pp. 41-104.

[53] R. L. Doyle and M. E. Lyons, "The oxygen evolution reaction: mechanistic concepts and catalyst design," in *Photoelectrochemical solar fuel production*, ed: Springer, 2016, pp. 41-104.

[54] T. Shinagawa, A. T. Garcia-Esparza, and K. Takanabe, "Insight on Tafel slopes from a microkinetic analysis of aqueous electrocatalysis for energy conversion," *Scientific reports,* vol. 5, p. 13801, 2015.

[55] J. Rossmeisl, Z.-W. Qu, H. Zhu, G.-J. Kroes, and J. K. Nørskov, "Electrolysis of water on oxide surfaces," *Journal of Electroanalytical Chemistry,* vol. 607, pp. 83-89, 2007.

[56] E. Fabbri, A. Habereder, K. Waltar, R. Kötz, and T. Schmidt, "Developments and perspectives of oxide-based catalysts for the oxygen evolution reaction," *Catalysis Science & Technology,* vol. 4, pp. 3800-3821, 2014.

[57] Y. Matsumoto and E. Sato, "Electrocatalytic properties of transition metal oxides for oxygen evolution reaction," *Materials chemistry and physics,* vol. 14, pp. 397-426, 1986.

[58] H. B. Alam, R. Das, M. Shajahan, A. A. Ullah, and A. F. Kibria, "Surface characteristics and electrolysis efficiency of a Palladium-Nickel electrode," *international journal of hydrogen energy,* vol. 43, pp. 1998-2008, 2018.

[59] R. Guidelli, R. G. Compton, J. M. Feliu, E. Gileadi, J. Lipkowski, W. Schmickler*, et al.*, "Defining the transfer coefficient in electrochemistry: An assessment (IUPAC Technical Report)," *Pure and Applied Chemistry,* vol. 86, pp. 245-258, 2014.

[60] R. Parsons, "The kinetics of electrode reactions and the electrode material," *Surface Science,* vol. 2, pp. 418-435, 1964.

[61] N. Suzuki, T. Horie, G. Kitahara, M. Murase, K. Shinozaki, and Y. Morimoto, "Novel Noble-Metal-Free Electrocatalyst for Oxygen Evolution Reaction in Acidic and Alkaline Media," *Electrocatalysis,* vol. 7, pp. 115-120, March 01 2016.

[62] W. Sun, Y. Song, X.-Q. Gong, L.-m. Cao, and J. Yang, "An efficiently tuned d-orbital occupation of IrO 2 by doping with Cu for enhancing the oxygen evolution reaction activity," *Chemical science,* vol. 6, pp. 4993-4999, 2015.

[63] T. Reier, Z. Pawolek, S. Cherevko, M. Bruns, T. Jones, D. Teschner*, et al.*, "Molecular insight in structure and activity of highly efficient, low-Ir Ir–Ni oxide catalysts for electrochemical water splitting (OER)," *Journal of the American Chemical Society,* vol. 137, pp. 13031-13040, 2015.

[64] T. Reier, M. Oezaslan, and P. Strasser, "Electrocatalytic oxygen evolution reaction (OER) on Ru, Ir, and Pt catalysts: a comparative study of nanoparticles and bulk materials," *Acs Catalysis,* vol. 2, pp. 1765-1772, 2012.

[65] E. A. Paoli, F. Masini, R. Frydendal, D. Deiana, C. Schlaup, M. Malizia*, et al.*, "Oxygen evolution on well-characterized mass-selected Ru and RuO 2 nanoparticles," *Chemical science,* vol. 6, pp. 190-196, 2015.

[66] A. Yu, C. Lee, M. H. Kim, and Y. Lee, "Nanotubular Iridium–Cobalt Mixed Oxide Crystalline Architectures Inherited from Cobalt Oxide for Highly Efficient Oxygen Evolution Reaction Catalysis," *ACS applied materials & interfaces,* vol. 9, pp. 35057-35066, 2017.

[67] D. Weber, L. M. Schoop, D. Wurmbrand, S. Laha, F. Podjaski, V. Duppel*, et al.*, "IrOOH nanosheets as acid stable electrocatalysts for the oxygen evolution reaction," *Journal of Materials Chemistry A,* vol. 6, pp. 21558-21566, 2018.

[68] A. T. Marshall and R. G. Haverkamp, "Nanoparticles of IrO 2 or Sb–SnO 2 increase the performance of iridium oxide DSA electrodes," *Journal of Materials Science,* vol. 47, pp. 1135-1141, 2012.

[69] S. Trasatti, "Electrocatalysis in the anodic evolution of oxygen and chlorine," *Electrochimica Acta,* vol. 29, pp. 1503-1512, 1984.

[70] A. R. Zeradjanin, N. Menzel, W. Schuhmann, and P. Strasser, "On the faradaic selectivity and the role of surface inhomogeneity during the chlorine evolution reaction on ternary Ti–Ru–Ir mixed metal oxide electrocatalysts," *Physical Chemistry Chemical Physics,* vol. 16, pp. 13741-13747, 2014.

[71] A. R. Zeradjanin, A. A. Topalov, Q. Van Overmeere, S. Cherevko, X. Chen, E. Ventosa, *et al.*, "Rational design of the electrode morphology for oxygen evolution–enhancing the performance for catalytic water oxidation," *RSC Advances,* vol. 4, pp. 9579-9587, 2014.

[72] A. Damjanovic, A. Dey, and J. M. Bockris, "Electrode kinetics of oxygen evolution and dissolution on Rh, Ir, and Pt-Rh alloy electrodes," *Journal of The Electrochemical Society,* vol. 113, pp. 739-746, 1966.

[73] M. Miles and M. Thomason, "Periodic variations of overvoltages for water electrolysis in acid solutions from cyclic voltammetric studies," *Journal of the Electrochemical Society,* vol. 123, p. 1459, 1976.

[74] W. Zhao, J. Xing, D. Chen, D. Jin, and J. Shen, "Electrochemical degradation of Musk ketone in aqueous solutions using a novel porous Ti/SnO2-Sb2O3/PbO2 electrodes," *Journal of Electroanalytical Chemistry,* vol. 775, pp. 179-188, 2016.

[75] X. Shang, B. Dong, Y.-M. Chai, and C.-G. Liu, "In-situ electrochemical activation designed hybrid electrocatalysts for water electrolysis," *Science Bulletin,* 2018.

[76] D. M. L. M. Blejan, "Corrosion behavior of Zn–Ni–Al2O3 nanocomposite coatings obtained by electrodeposition from alkaline electrolytes," *MACO Materials and Corrosion,* vol. 64, pp. 433-438, 2013.

[77] S. Ghasemian and S. Omanovic, "Fabrication and characterization of photoelectrochemically-active Sb-doped Snx-W(100-x)%-oxide anodes: Towards the removal of organic pollutants from wastewater," *Applied Surface Science,* vol. 416, pp. 318-328, 2017/09/15/ 2017.

[78] N. Danilovic, R. Subbaraman, K.-C. Chang, S. H. Chang, Y. J. Kang, J. Snyder, *et al.*, "Activity–stability trends for the oxygen evolution reaction on monometallic oxides in acidic environments," *The journal of physical chemistry letters,* vol. 5, pp. 2474-2478, 2014.

[79] T. Reier, H. N. Nong, D. Teschner, R. Schlögl, and P. Strasser, "Electrocatalytic oxygen evolution reaction in acidic environments–reaction mechanisms and catalysts," *Advanced Energy Materials*, vol. 7, p. 1601275, 2017.

[80] S. Cherevko, A. R. Zeradjanin, A. A. Topalov, N. Kulyk, I. Katsounaros, and K. J. Mayrhofer, "Dissolution of noble metals during oxygen evolution in acidic media," *ChemCatChem*, vol. 6, pp. 2219-2223, 2014.

[81] R. J. Colton, A. M. Guzman, and J. W. Rabalais, "Electrochromism in some thin-film transition-metal oxides characterized by x-ray electron spectroscopy," *Journal of Applied Physics*, vol. 49, pp. 409-416, 1978.

[82] J. W. D. Ng, M. García-Melchor, M. Bajdich, P. Chakthranont, C. Kirk, A. Vojvodic, *et al.*, "Gold-supported cerium-doped NiO x catalysts for water oxidation," *Nature Energy*, vol. 1, pp. 1-8, 2016.

[83] S. Cherevko, S. Geiger, O. Kasian, A. Mingers, and K. J. Mayrhofer, "Oxygen evolution activity and stability of iridium in acidic media. Part 2.–Electrochemically grown hydrous iridium oxide," *Journal of Electroanalytical Chemistry*, vol. 774, pp. 102-110, 2016.

[84] R. Frydendal, E. A. Paoli, B. P. Knudsen, B. Wickman, P. Malacrida, I. E. Stephens, *et al.*, "Benchmarking the stability of oxygen evolution reaction catalysts: the importance of monitoring mass losses," *ChemElectroChem*, vol. 1, pp. 2075-2081, 2014.

[85] A. Weremfo, X. Lu, P. Carter, D. B. Hibbert, and C. Zhao, "Modelling an electrochemically roughened porous platinum electrode for water oxidation," *Chemical communications*, vol. 52, pp. 4068-4071, 2016.

[86] J. A. Koza, Z. He, A. S. Miller, and J. A. Switzer, "Electrodeposition of Crystalline Co3O4 - A Catalyst for the Oxygen Evolution Reaction," *Chemistry of Materials*, vol. 24, pp. 3567-3573, 2012.

[87] P. Babar, A. Lokhande, M. Gang, B. Pawar, S. Pawar, and J. H. Kim, "Thermally oxidized porous NiO as an efficient oxygen evolution reaction (OER) electrocatalyst for electrochemical water splitting application," *Journal of industrial and engineering chemistry*, vol. 60, pp. 493-497, 2018.

[88] F. Yan, C. Zhu, S. Wang, Y. Zhao, X. Zhang, C. Li, *et al.*, "Electrochemically activated-iron oxide nanosheet arrays on carbon fiber cloth as a three-dimensional self-supported

electrode for efficient water oxidation," *Journal of Materials Chemistry A,* vol. 4, pp. 6048-6055, 2016.

[89] M. Huynh, D. K. Bediako, and D. G. Nocera, "A functionally stable manganese oxide oxygen evolution catalyst in acid," *Journal of the American Chemical Society,* vol. 136, pp. 6002-6010, 2014.

[90] T. Audichon, T. W. Napporn, C. Canaff, C. u. Morais, C. m. Comminges, and K. B. Kokoh, "IrO_2 coated on RuO_2 as efficient and stable electroactive nanocatalysts for electrochemical water splitting," *The Journal of Physical Chemistry C,* vol. 120, pp. 2562-2573, 2016.

[91] Y. Lee, J. Suntivich, K. J. May, E. E. Perry, and Y. Shao-Horn, "Synthesis and activities of rutile IrO_2 and RuO_2 nanoparticles for oxygen evolution in acid and alkaline solutions," *The Journal of Physical Chemistry Letters,* vol. 3, pp. 399-404, 2012.

[92] S. Cherevko, S. Geiger, O. Kasian, N. Kulyk, J.-P. Grote, A. Savan, *et al.*, "Oxygen and hydrogen evolution reactions on Ru, RuO2, Ir, and IrO2 thin film electrodes in acidic and alkaline electrolytes: A comparative study on activity and stability," *Catalysis Today,* vol. 262, pp. 170-180, 2016.

[93] R. Hutchings, K. Müller, R. Kötz, and S. Stucki, "A structural investigation of stabilized oxygen evolution catalysts," *Journal of materials science,* vol. 19, pp. 3987-3994, 1984.

[94] P. Li and H. C. Zeng, "Sandwich-Like Nanocomposite of CoNiOx/Reduced Graphene Oxide for Enhanced Electrocatalytic Water Oxidation," *Advanced Functional Materials,* vol. 27, p. 1606325, 2017.

[95] R. Frydendal, E. A. Paoli, I. Chorkendorff, J. Rossmeisl, and I. E. Stephens, "Toward an Active and Stable Catalyst for Oxygen Evolution in Acidic Media: Ti-Stabilized MnO2," *Advanced Energy Materials,* vol. 5, p. 1500991, 2015.

[96] P. P. Patel, M. K. Datta, O. I. Velikokhatnyi, R. Kuruba, K. Damodaran, P. Jampani, *et al.*, "Noble metal-free bifunctional oxygen evolution and oxygen reduction acidic media electro-catalysts," *Scientific reports,* vol. 6, p. 28367, 2016.

[97] A. Kleiman-Shwarsctein, Y.-S. Hu, G. D. Stucky, and E. W. McFarland, "NiFe-oxide electrocatalysts for the oxygen evolution reaction on Ti doped hematite photoelectrodes," *Electrochemistry communications,* vol. 11, pp. 1150-1153, 2009.

[98] J. Qi, W. Zhang, R. Xiang, K. Liu, H. Y. Wang, M. Chen, *et al.*, "Porous nickel–iron oxide as a highly efficient electrocatalyst for oxygen evolution reaction," *Advanced Science,* vol. 2, p. 1500199, 2015.

[99] N. Furuya and S. Motoo, "The electrochemical behavior of ad-atoms and their effect on hydrogen evolution: Part I. Order-disorder rearrangement of copper ad-atoms on platinum," *Journal of Electroanalytical Chemistry and Interfacial Electrochemistry,* vol. 72, pp. 165-175, 1976.

[100] M. Carmo, D. L. Fritz, J. Mergel, and D. Stolten, "A comprehensive review on PEM water electrolysis," *International journal of hydrogen energy,* vol. 38, pp. 4901-4934, 2013.

[101] F. Andolfatto, R. Durand, A. Michas, P. Millet, and P. Stevens, "Solid polymer electrolyte water electrolysis: electrocatalysis and long-term stability," *International Journal of Hydrogen Energy,* vol. 19, pp. 421-427, 1994.

[102] E. Kötz and S. Stucki, "Ruthenium dioxide as a hydrogen-evolving cathode," *Journal of applied electrochemistry,* vol. 17, pp. 1190-1197, 1987.

[103] S. Jung, C. C. McCrory, I. M. Ferrer, J. C. Peters, and T. F. Jaramillo, "Benchmarking nanoparticulate metal oxide electrocatalysts for the alkaline water oxidation reaction," *Journal of Materials Chemistry A,* vol. 4, pp. 3068-3076, 2016.

[104] K. C. Leonard, M. I. Tejedor-Anderson, and M. A. Anderson, "Nanoporous oxide coatings on stainless steel to enable water splitting and reduce the hydrogen evolution overpotential," *international journal of hydrogen energy,* vol. 37, pp. 18654-18660, 2012.

[105] A. J. Esswein, M. J. McMurdo, P. N. Ross, A. T. Bell, and T. D. Tilley, "Size-dependent activity of Co3O4 nanoparticle anodes for alkaline water electrolysis," *The Journal of Physical Chemistry C,* vol. 113, pp. 15068-15072, 2009.

[106] M. M. Jakšić, "Hypo–hyper-d-electronic interactive nature of synergism in catalysis and electrocatalysis for hydrogen reactions," *Electrochimica Acta,* vol. 45, pp. 4085-4099, 2000.

[107] E. Navarro-Flores, Z. Chong, and S. Omanovic, "Characterization of Ni, NiMo, NiW and NiFe electroactive coatings as electrocatalysts for hydrogen evolution in an acidic medium," *Journal of Molecular Catalysis A: Chemical,* vol. 226, pp. 179-197, 2005.

[108] S. Shibli and V. Dilimon, "Effect of phosphorous content and TiO2-reinforcement on Ni–P electroless plates for hydrogen evolution reaction," *International Journal of Hydrogen Energy,* vol. 32, pp. 1694-1700, 2007.

[109] H. Suffredini, J. Cerne, F. Crnkovic, S. Machado, and L. Avaca, "Recent developments in electrode materials for water electrolysis," *International Journal of Hydrogen Energy,* vol. 25, pp. 415-423, 2000.

[110] S. Trasatti, "Hydrogen evolution on oxide electrodes," in *Modern chlor-alkali technology*, ed: Springer, 1992, pp. 281-294.

[111] M. Janjua and R. Le Roy, "Electrocatalyst performance in industrial water electrolysers," *International Journal of Hydrogen Energy,* vol. 10, pp. 11-19, 1985.

[112] K. Zeng and D. Zhang, "Recent progress in alkaline water electrolysis for hydrogen production and applications," *Progress in Energy and Combustion Science,* vol. 36, pp. 307-326, 2010.

[113] K. Bhuntumkomol, K. Han, and F. Lawson, "The leaching behaviour of nickel oxides in acid and in ammoniacal solutions," *Hydrometallurgy,* vol. 8, pp. 147-160, 1982.

[114] M. M. Jaksic, "Interionic nature of synergism in catalysis and electrocatalysis," *Solid State Ionics,* vol. 136, pp. 733-746, 2000.

[115] R. Forgie, G. Bugosh, K. Neyerlin, Z. Liu, and P. Strasser, "Bimetallic Ru electrocatalysts for the OER and electrolytic water splitting in acidic media," *Electrochemical and Solid-State Letters,* vol. 13, pp. B36-B39, 2010.

[116] N. B. Halck, V. Petrykin, P. Krtil, and J. Rossmeisl, "Beyond the volcano limitations in electrocatalysis–oxygen evolution reaction," *Physical Chemistry Chemical Physics,* vol. 16, pp. 13682-13688, 2014.

[117] N. Cheng, Q. Liu, J. Tian, X. Sun, Y. He, S. Zhai, *et al.*, "Nickel oxide nanosheets array grown on carbon cloth as a high-performance three-dimensional oxygen evolution electrode," *international journal of hydrogen energy,* vol. 40, pp. 9866-9871, 2015.

[118] I. Nikolov, R. Darkaoui, E. Zhecheva, R. Stoyanova, N. Dimitrov, and T. Vitanov, "Electrocatalytic activity of spinel related cobalties MxCo3− xO4 (M= Li, Ni, Cu) in the oxygen evolution reaction," *Journal of Electroanalytical Chemistry,* vol. 429, pp. 157-168, 1997.

[119] M. Panizza, A. Barbucci, R. Ricotti, and G. Cerisola, "Electrochemical degradation of methylene blue," *Separation and purification technology,* vol. 54, pp. 382-387, 2007.

[120] S. Ghasemian, B. Asadishad, S. Omanovic, and N. Tufenkji, "Electrochemical disinfection of bacteria-laden water using antimony-doped tin-tungsten-oxide electrodes," *Water research,* vol. 126, pp. 299-307, 2017.

[121] A. Anglada, A. Urtiaga, and I. Ortiz, "Contributions of electrochemical oxidation to waste-water treatment: fundamentals and review of applications," *Journal of Chemical Technology & Biotechnology,* vol. 84, pp. 1747-1755, 2009.

[122] Y. Feng, L. Yang, J. Liu, and B. E. Logan, "Electrochemical technologies for wastewater treatment and resource reclamation," *Environmental Science: Water Research & Technology,* vol. 2, pp. 800-831, 2016.

[123] A. Polcaro, A. Vacca, S. Palmas, and M. Mascia, "Electrochemical treatment of wastewater containing phenolic compounds: oxidation at boron-doped diamond electrodes," *Journal of Applied Electrochemistry,* vol. 33, pp. 885-892, 2003.

[124] K. Dutta, S. Mukhopadhyay, S. Bhattacharjee, and B. Chaudhuri, "Chemical oxidation of methylene blue using a Fenton-like reaction," *Journal of hazardous materials,* vol. 84, pp. 57-71, 2001.

[125] S. Ghasemian, D. Nasuhoglu, S. Omanovic, and V. Yargeau, "Photoelectrocatalytic degradation of pharmaceutical carbamazepine using Sb-doped Sn80%-W20%-oxide electrodes," *Separation and Purification Technology,* vol. 188, pp. 52-59, 2017.

[126] A. Kraft, "Electrochemical water disinfection: a short review," *Platinum metals review,* vol. 52, pp. 177-185, 2008.

[127] Y. Deng and R. Zhao, "Advanced oxidation processes (AOPs) in wastewater treatment," *Current Pollution Reports,* vol. 1, pp. 167-176, 2015.

[128] C. A. Martínez-Huitle and M. Panizza, "Electrochemical oxidation of organic pollutants for wastewater treatment," *Current Opinion in Electrochemistry,* vol. 11, pp. 62-71, 2018.

[129] C. Comninellis, "Electrocatalysis in the electrochemical conversion/combustion of organic pollutants for waste water treatment," *Electrochimica Acta,* vol. 39, pp. 1857-1862, 1994.

[130] R. Liang, A. Hu, W. Li, and Y. N. Zhou, "Enhanced degradation of persistent pharmaceuticals found in wastewater treatment effluents using TiO 2 nanobelt photocatalysts," *Journal of nanoparticle research,* vol. 15, p. 1990, 2013.

[131] I. Sirés, E. Brillas, G. Cerisola, and M. Panizza, "Comparative depollution of mecoprop aqueous solutions by electrochemical incineration using BDD and PbO2 as high oxidation power anodes," *Journal of Electroanalytical Chemistry,* vol. 613, pp. 151-159, 2008.

[132] M. Tian, S. S. Thind, M. Simko, F. Gao, and A. Chen, "Quantitative Structure–Reactivity Study of Electrochemical Oxidation of Phenolic Compounds at the SnO2–Based Electrode," *The Journal of Physical Chemistry A,* vol. 116, pp. 2927-2934, 2012.

[133] J. Suntivich, K. J. May, H. A. Gasteiger, J. B. Goodenough, and Y. Shao-Horn, "A perovskite oxide optimized for oxygen evolution catalysis from molecular orbital principles," *Science,* vol. 334, pp. 1383-1385, 2011.

[134] H. Shen, E. Gracia-Espino, L. Wang, D. Qin, S. Gao, X. Mamat, *et al.*, "Microwave-assisted synthesis of multimetal oxygen-evolving catalysts," *Electrochemistry Communications,* 2017.

[135] J. Ping, Y. Wang, Q. Lu, B. Chen, J. Chen, Y. Huang, *et al.*, "Self-Assembly of Single-Layer CoAl-Layered Double Hydroxide Nanosheets on 3D Graphene Network Used as Highly Efficient Electrocatalyst for Oxygen Evolution Reaction," *Advanced Materials,* vol. 28, pp. 7640-7645, 2016.

[136] K. Fan, H. Chen, Y. Ji, H. Huang, P. M. Claesson, Q. Daniel, *et al.*, "Nickel–vanadium monolayer double hydroxide for efficient electrochemical water oxidation," *Nature Communications,* vol. 7, p. 11981, 2016.

[137] Y. Pi, Q. Shao, P. Wang, F. Lv, S. Guo, J. Guo, *et al.*, "Trimetallic Oxyhydroxide Coralloids for Efficient Oxygen Evolution Electrocatalysis," *Angewandte Chemie,* vol. 129, pp. 4573-4577, 2017.

[138] N. Krstajić, L. Gajić-Krstajić, U. Lačnjevac, B. Jović, S. Mora, and V. Jović, "Non-noble metal composite cathodes for hydrogen evolution. Part I: the Ni–MoOx coatings electrodeposited from Watt's type bath containing MoO_3 powder particles," *International Journal of Hydrogen Energy,* vol. 36, pp. 6441-6449, 2011.

[139] A. Grimaud, K. J. May, C. E. Carlton, Y.-L. Lee, M. Risch, W. T. Hong, *et al.*, "Double perovskites as a family of highly active catalysts for oxygen evolution in alkaline solution," *Nature Communications,* vol. 4, p. 2439, 2013.

[140] S. Chen, J. Duan, W. Han, and S. Z. Qiao, "A graphene–MnO_2 framework as a new generation of three-dimensional oxygen evolution promoter," *Chemical Communications,* vol. 50, pp. 207-209, 2014.

[141] Y.-R. Liu, G.-Q. Han, X. Li, B. Dong, X. Shang, W.-H. Hu*, et al.*, "A facile synthesis of reduced Co3O4 nanoparticles with enhanced electrocatalytic activity for oxygen evolution," *International Journal of Hydrogen Energy,* vol. 41, pp. 12976-12982, 2016.

[142] K.-L. Yan, J.-Q. Chi, J.-Y. Xie, B. Dong, Z.-Z. Liu, W.-K. Gao*, et al.*, "Mesoporous Ag-doped Co 3 O 4 nanowire arrays supported on FTO as efficient electrocatalysts for oxygen evolution reaction in acidic media," *Renewable Energy,* vol. 119, pp. 54-61, 2018.

[143] J. Stilling, N. Ullah, and S. Omanovic, "Ir-Ni oxide as a promising material for nerve and brain stimulating electrodes," *Journal of Electrochemical Science and Engineering,* vol. 4, pp. 85-96, 2014.

[144] A. G. Vidales and S. Omanovic, "Evaluation of nickel-molybdenum-oxides as cathodes for hydrogen evolution by water electrolysis in acidic, alkaline, and neutral media," *Electrochimica Acta,* 2018.

[145] Y. Wang, J. G. Limon-Petersen, and R. G. Compton, "Measurement of the diffusion coefficients of $[Ru(NH_3)_6]^{3+}$ and $[Ru(NH_3)_6]^{2+}$ in aqueous solution using microelectrode double potential step chronoamperometry," *Journal of Electroanalytical Chemistry,* vol. 652, pp. 13-17, 2011.

[146] J. G. Limon-Petersen, J. T. Han, N. V. Rees, E. J. Dickinson, I. Streeter, and R. G. Compton, "Quantitative voltammetry in weakly supported media. Chronoamperometric studies on diverse one electron redox couples containing various charged species: dissecting diffusional and migrational contributions and assessing the breakdown of electroneutrality," *The Journal of Physical Chemistry C,* vol. 114, pp. 2227-2236, 2010.

[147] X. Q. Yu, Y. He, J. P. Sun, K. Tang, H. Li, L. Q. Chen*, et al.*, "Nanocrystalline MnO thin film anode for lithium ion batteries with low overpotential," *Electrochemistry Communications,* vol. 11, pp. 791-794, 2009/04/01/ 2009.

[148] A. Marakushev and N. Bezmen, "Chemical affinity of metals for oxygen and sulfur," *International Geology Review,* vol. 13, pp. 1781-1794, 1971.

[149] K. Thamaphat, P. Limsuwan, and B. Ngotawornchai, "Phase characterization of TiO_2 powder by XRD and TEM," *Kasetsart Journal (Natural Science),* vol. 42, pp. 357-361, 2008.

[150] J. Jiang, C. Zhang, and L. Ai, "Hierarchical iron nickel oxide architectures derived from metal-organic frameworks as efficient electrocatalysts for oxygen evolution reaction," *Electrochimica Acta,* vol. 208, pp. 17-24, 2016.

[151] L. Trotochaud, J. K. Ranney, K. N. Williams, and S. W. Boettcher, "Solution-cast metal oxide thin film electrocatalysts for oxygen evolution," *Journal of the American Chemical Society,* vol. 134, pp. 17253-17261, 2012.

[152] W.-Y. Li, L.-N. Xu, and J. Chen, "Co_3O_4 nanomaterials in lithium-ion batteries and gas sensors," *Advanced Functional Materials,* vol. 15, pp. 851-857, 2005.

[153] M. Li, Y.-X. Yin, C. Li, F. Zhang, L.-J. Wan, S. Xu, *et al.*, "Well-dispersed bi-component-active $CoO/CoFe_2O_4$ nanocomposites with tunable performances as anode materials for lithium-ion batteries," *Chemical Communications,* vol. 48, pp. 410-412, 2012.

[154] C. Zhu, D. Wen, S. Leubner, M. Oschatz, W. Liu, M. Holzschuh, *et al.*, "Nickel cobalt oxide hollow nanosponges as advanced electrocatalysts for the oxygen evolution reaction," *Chemical Communications,* vol. 51, pp. 7851-7854, 2015.

[155] S.-Y. Tsai, K.-Z. Fung, C.-N. Wei, and H.-Y. Bor, "Thin film deposition of semiconducting Ni-Co oxide spinel with adequate electrical and optical properties for energy application," *Journal of Electronic Materials,* vol. 43, pp. 2584-2587, 2014.

[156] J.-H. Kim, S. H. Kang, K. Zhu, J. Y. Kim, N. R. Neale, and A. J. Frank, "Ni–NiO core–shell inverse opal electrodes for supercapacitors," *Chemical Communications,* vol. 47, pp. 5214-5216, 2011.

[157] J. F. Moulder, W. F. Stickle, P. E. Sobol, and K. D. Bomben, *Handbook of X-ray photoelectron spectroscopy: A Reference book of Standard Spectra for Identification and Interpretation of XPS Data*: Perkin-Elmer Corporation, 1995.

[158] W. Ren, Z. Ai, F. Jia, L. Zhang, X. Fan, and Z. Zou, "Low temperature preparation and visible light photocatalytic activity of mesoporous carbon-doped crystalline TiO_2," *Applied Catalysis B: Environmental,* vol. 69, pp. 138-144, 2007.

[159] M. M. Natile and A. Glisenti, "Surface reactivity of NiO: Interaction with methanol," *Chemistry of Materials,* vol. 14, pp. 4895-4903, 2002.

[160] B. Sasi and K. Gopchandran, "Nanostructured mesoporous nickel oxide thin films," *Nanotechnology,* vol. 18, p. 115613, 2007.

[161] M. C. Biesinger, B. P. Payne, A. P. Grosvenor, L. W. Lau, A. R. Gerson, and R. S. C. Smart, "Resolving surface chemical states in XPS analysis of first row transition metals, oxides and hydroxides: Cr, Mn, Fe, Co and Ni," *Applied Surface Science,* vol. 257, pp. 2717-2730, 2011.

[162] H. A. Hagelin-Weaver, G. B. Hoflund, D. M. Minahan, and G. N. Salaita, "Electron energy loss spectroscopic investigation of Co metal, CoO, and Co_3O_4 before and after Ar^+ bombardment," *Applied Surface Science,* vol. 235, pp. 420-448, 2004.

[163] M. Langell, M. Anderson, G. Carson, L. Peng, and S. Smith, "Valence-band electronic structure of Co_3O_4 epitaxy on CoO (100)," *Physical Review B,* vol. 59, p. 4791, 1999.

[164] H. Yang, J. Ouyang, and A. Tang, "Single step synthesis of high-purity CoO nanocrystals," *The Journal of Physical Chemistry B,* vol. 111, pp. 8006-8013, 2007.

[165] M. Tahir, L. Pan, F. Idrees, X. Zhang, L. Wang, J.-J. Zou, *et al.*, "Electrocatalytic oxygen evolution reaction for energy conversion and storage: a comprehensive review," *Nano Energy,* vol. 37, pp. 136-157, 2017.

[166] L. Burke and T. Twomey, "Influence of the acid/base character of the surface on the electrocatalytic behaviour of both nickel and nickel oxide anodes, with particular reference to oxygen gas evolution," *Journal of electroanalytical chemistry and interfacial electrochemistry,* vol. 167, pp. 285-290, 1984.

[167] M. E. Lyons and S. Floquet, "Mechanism of oxygen reactions at porous oxide electrodes. Part 2—Oxygen evolution at RuO2, IrO2 and IrxRu1− xO2 electrodes in aqueous acid and alkaline solution," *Physical Chemistry Chemical Physics,* vol. 13, pp. 5314-5335, 2011.

[168] J.-M. Hu, J.-Q. Zhang, and C.-N. Cao, "Oxygen evolution reaction on IrO2-based DSA® type electrodes: kinetics analysis of Tafel lines and EIS," *International Journal of Hydrogen Energy,* vol. 29, pp. 791-797, 2004.

[169] C. C. McCrory, S. Jung, J. C. Peters, and T. F. Jaramillo, "Benchmarking heterogeneous electrocatalysts for the oxygen evolution reaction," *Journal of the American Chemical Society,* vol. 135, pp. 16977-16987, 2013.

[170] I. Abidat, N. Bouchenafa-Saib, A. Habrioux, C. Comminges, C. Canaff, J. Rousseau, *et al.*, "Electrochemically induced surface modifications of mesoporous spinels (Co 3 O 4− δ,

MnCo 2 O 4− δ, NiCo 2 O 4− δ) as the origin of the OER activity and stability in alkaline medium," *Journal of Materials Chemistry A*, vol. 3, pp. 17433-17444, 2015.

[171] J. O. Bockris and T. Otagawa, "Mechanism of oxygen evolution on perovskites," *The Journal of Physical Chemistry*, vol. 87, pp. 2960-2971, 1983.

[172] A. Krasilshchikov, "Intermediate Stages of Oxygen Anodic Evolution," *Zhurnal Fizicheskoi Khimii*, vol. 37, pp. 531-537, 1963.

[173] A. Kobussen and G. Broers, "The oxygen evolution on $La_{0.5}Ba_{0.5}CoO_3$: theoretical impedance behaviour for a multi-step mechanism involving two adsorbates," *Journal of Electroanalytical Chemistry and Interfacial Electrochemistry*, vol. 126, pp. 221-240, 1981.

[174] H. Willems, A. Kobussen, J. De Wit, and G. Broers, "The oxygen evolution reaction on cobalt: part I. Reaction order experiments and impedance measurements," *Journal of Electroanalytical Chemistry and Interfacial Electrochemistry*, vol. 170, pp. 227-242, 1984.

[175] J. O. M. Bockris, "Kinetics of activation controlled consecutive electrochemical reactions: anodic evolution of oxygen," *The Journal of Chemical Physics*, vol. 24, pp. 817-827, 1956.

[176] E. Antolini, "Iridium as catalyst and cocatalyst for oxygen evolution/reduction in acidic polymer electrolyte membrane electrolyzers and fuel cells," *ACS Catalysis*, vol. 4, pp. 1426-1440, 2014.

[177] M. McArthur, L. Jorge, S. Coulombe, and S. Omanovic, "Synthesis and characterization of 3D Ni nanoparticle/carbon nanotube cathodes for hydrogen evolution in alkaline electrolyte," *Journal of Power Sources*, vol. 266, pp. 365-373, 2014.

[178] A. Naldoni, M. Allieta, S. Santangelo, M. Marelli, F. Fabbri, S. Cappelli, *et al.*, "Effect of nature and location of defects on bandgap narrowing in black TiO_2 nanoparticles," *Journal of the American Chemical Society*, vol. 134, pp. 7600-7603, 2012.

[179] F. Lei, Y. Sun, K. Liu, S. Gao, L. Liang, B. Pan, *et al.*, "Oxygen vacancies confined in ultrathin indium oxide porous sheets for promoted visible-light water splitting," *Journal of the American Chemical Society*, vol. 136, pp. 6826-6829, 2014.

[180] N. J. Tharayil, R. Raveendran, A. V. Vaidyan, and P. Chithra, "Optical, electrical and structural studies of nickel-cobalt oxide nanoparticles," 2008.

[181] InfoMine. *Vancouver: InvestmentMine metal prices (2020). http://www.infomine.com/investment, Accessed 6 July 2020.*

[182] M. Busch, E. Ahlberg, and I. Panas, "Hydroxide oxidation and peroxide formation at embedded binuclear transition metal sites; TM = Cr, Mn, Fe, Co," *Physical Chemistry Chemical Physics,* vol. 13, pp. 15062-15068, 2011.

[183] M. Busch, E. Ahlberg, and I. Panas, "Water Oxidation on MnOx and IrOx: Why Similar Performance?," *The Journal of Physical Chemistry C,* vol. 117, pp. 288-292, 2012.

[184] M. Busch, E. Ahlberg, and I. Panas, "Validation of binuclear descriptor for mixed transition metal oxide supported electrocatalytic water oxidation," *Catalysis Today,* vol. 202, pp. 114-119, 2013.

[185] E. O. Nwanebu and S. Omanovic, "The influence of NixCo1-x-oxide composition on its electrocatalytic activity in the oxygen evolution reaction," *Materials Chemistry and Physics,* vol. 228, pp. 80-88, 2019.

[186] H. N. Nong, H. S. Oh, T. Reier, E. Willinger, M. G. Willinger, V. Petkov*, et al.*, "Oxide-Supported IrNiOx Core–Shell Particles as Efficient, Cost-Effective, and Stable Catalysts for Electrochemical Water Splitting," *Angewandte Chemie International Edition,* vol. 54, pp. 2975-2979, 2015.

[187] K. Macounová, J. Jirkovský, M. V. Makarova, J. Franc, and P. Krtil, "Oxygen evolution on Ru 1− x Ni x O 2− y nanocrystalline electrodes," *Journal of Solid State Electrochemistry,* vol. 13, pp. 959-965, 2009.

[188] M. V. Makarova, J. Jirkovský, M. Klementová, I. Jirka, K. Macounová, and P. Krtil, "The electrocatalytic behavior of Ru0. 8Co0. 2O2− x—the effect of particle shape and surface composition," *Electrochimica Acta,* vol. 53, pp. 2656-2664, 2008.

[189] L. Da Silva, J. Boodts, and L. DeFaria, "'In situ'and 'ex situ'characterization of the surface properties of the RuO2 (x)+ Co3O4 (1− x) system," *Electrochimica Acta,* vol. 45, pp. 2719-2727, 2000.

[190] V. Petrykin, K. Macounová, M. Okube, S. Mukerjee, and P. Krtil, "Local structure of Co doped RuO2 nanocrystalline electrocatalytic materials for chlorine and oxygen evolution," *Catalysis today,* vol. 202, pp. 63-69, 2013.

[191] K. Macounová, M. Makarova, J. Franc, J. Jirkovský, and P. Krtil, "Influence of Oxygen on Reactivity of Ru1− x Fe x O2− y-Doped Materials," *Electrochemical and Solid-State Letters,* vol. 11, pp. F27-F29, 2008.

[192] E. L. Tae, J. Song, A. R. Lee, C. H. Kim, S. Yoon, I. C. Hwang, *et al.*, "Cobalt oxide electrode doped with iridium oxide as highly efficient water oxidation electrode," *ACS Catalysis,* vol. 5, pp. 5525-5529, 2015.

[193] W. Q. Zaman, W. Sun, M. Tariq, Z. Zhou, U. Farooq, Z. Abbas, *et al.*, "Iridium substitution in nickel cobaltite renders high mass specific OER activity and durability in acidic media," *Applied Catalysis B: Environmental,* vol. 244, pp. 295-302, 2019.

[194] M. S. Burke, L. J. Enman, A. S. Batchellor, S. Zou, and S. W. Boettcher, "Oxygen evolution reaction electrocatalysis on transition metal oxides and (oxy) hydroxides: activity trends and design principles," *Chemistry of Materials,* vol. 27, pp. 7549-7558, 2015.

[195] T. Reier, D. Teschner, T. Lunkenbein, A. Bergmann, S. Selve, R. Kraehnert, *et al.*, "Electrocatalytic oxygen evolution on iridium oxide: uncovering catalyst-substrate interactions and active iridium oxide species," *Journal of The Electrochemical Society,* vol. 161, pp. F876-F882, 2014.

[196] L. Liu, H. Zhang, L. Fang, Y. Mu, and Y. Wang, "Facile preparation of novel dandelion-like Fe-doped NiCo2O4 microspheres@ nanomeshes for excellent capacitive property in asymmetric supercapacitors," *Journal of Power Sources,* vol. 327, pp. 135-144, 2016.

[197] D. Briggs, "Handbook of X-ray Photoelectron Spectroscopy CD Wanger, WM Riggs, LE Davis, JF Moulder and GE Muilenberg Perkin-Elmer Corp., Physical Electronics Division, Eden Prairie, Minnesota, USA, 1979. 190 pp. $195," *Surface and Interface Analysis,* vol. 3, pp. v-v, 1981.

[198] D. F. Abbott, D. Lebedev, K. Waltar, M. Povia, M. Nachtegaal, E. Fabbri, *et al.*, "Iridium oxide for the oxygen evolution reaction: correlation between particle size, morphology, and the surface hydroxo layer from operando XAS," *Chemistry of Materials,* vol. 28, pp. 6591-6604, 2016.

[199] M. Moser, C. Mondelli, A. P. Amrute, A. Tazawa, D. Teschner, M. E. Schuster, *et al.*, "HCl oxidation on IrO2-based catalysts: from fundamentals to scale-up," *ACS Catalysis,* vol. 3, pp. 2813-2822, 2013.

[200] M. C. Biesinger, L. W. Lau, A. R. Gerson, and R. S. C. Smart, "The role of the Auger parameter in XPS studies of nickel metal, halides and oxides," *Physical Chemistry Chemical Physics,* vol. 14, pp. 2434-2442, 2012.

[201] L. De Faria, J. Boodts, and S. Trasatti, "Electrocatalytic properties of ternary oxide mixtures of composition Ru 0.3 Ti (0.7− x) Ce x O 2: oxygen evolution from acidic solution," *Journal of applied electrochemistry,* vol. 26, pp. 1195-1199, 1996.

[202] W. Ma, R. Ma, C. Wang, J. Liang, X. Liu, K. Zhou, *et al.*, "A superlattice of alternately stacked Ni–Fe hydroxide nanosheets and graphene for efficient splitting of water," *ACS nano,* vol. 9, pp. 1977-1984, 2015.

[203] F. Mattos-Costa, P. de Lima-Neto, S. Machado, and L. Avaca, "Characterisation of surfaces modified by sol-gel derived RuxIr1− xO2 coatings for oxygen evolution in acid medium," *Electrochimica Acta,* vol. 44, pp. 1515-1523, 1998.

[204] W. Hu, H. Zhong, W. Liang, and S. Chen, "Ir-Surface Enriched Porous Ir–Co Oxide Hierarchical Architecture for High Performance Water Oxidation in Acidic Media," *ACS applied materials & interfaces,* vol. 6, pp. 12729-12736, 2014.

[205] S. Xu, Y. Liu, J. Tong, W. Hu, and Q. Xia, "Iridium–nickel composite oxide catalysts for oxygen evolution reaction in acidic water electrolysis," *Russian Journal of Electrochemistry,* vol. 52, pp. 1021-1031, 2016.

[206] K. Sardar, S. C. Ball, J. D. Sharman, D. Thompsett, J. M. Fisher, R. A. Smith, *et al.*, "Bismuth iridium oxide oxygen evolution catalyst from hydrothermal synthesis," *Chemistry of Materials,* vol. 24, pp. 4192-4200, 2012.

[207] J. Corona-Guinto, L. Cardeño-García, D. Martínez-Casillas, J. M. Sandoval-Pineda, P. Tamayo-Meza, R. Silva-Casarin, *et al.*, "Performance of a PEM electrolyzer using RuIrCoOx electrocatalysts for the oxygen evolution electrode," *International Journal of Hydrogen Energy,* vol. 38, pp. 12667-12673, 2013.

[208] O. Gencyilmaz, F. Atay, and İ. AKYÜZ, "Production and characterization of iridium oxide films by ultrasonic chemical spray pyrolysis," *Journal of optoelectronics and advanced materials,* vol. 17, pp. 395-402, 2015.

[209] M. S. Ryang, C. J. Kang, H. C. Choe, and N. H. Kim, "Correlation of electron density and bond length to band gap for binary oxides and halides," *International Journal of Quantum Chemistry,* vol. 119, p. e26022, 2019.

[210] G. W. Crabtree, M. S. Dresselhaus, and M. V. Buchanan, "The hydrogen economy," *Physics today,* vol. 57, pp. 39-44, 2004.

[211] M. Momirlan and T. N. Veziroglu, "The properties of hydrogen as fuel tomorrow in sustainable energy system for a cleaner planet," *International journal of hydrogen energy,* vol. 30, pp. 795-802, 2005.

[212] S.-C. Moon, H. Mametsuka, S. Tabata, and E. Suzuki, "Photocatalytic production of hydrogen from water using TiO2 and B/TiO2," *Catalysis Today,* vol. 58, pp. 125-132, 2000.

[213] T. Yoshida and K. Kojima, "Toyota MIRAI fuel cell vehicle and progress toward a future hydrogen society," *Electrochemical Society Interface,* vol. 24, p. 45, 2015.

[214] M. Balat, "Potential importance of hydrogen as a future solution to environmental and transportation problems," *International journal of hydrogen energy,* vol. 33, pp. 4013-4029, 2008.

[215] J. Greeley and N. M. Markovic, "The road from animal electricity to green energy: combining experiment and theory in electrocatalysis," *Energy & Environmental Science,* vol. 5, pp. 9246-9256, 2012.

[216] H. Zhou, F. Yu, Q. Zhu, J. Sun, F. Qin, L. Yu, *et al.*, "Water splitting by electrolysis at high current densities under 1.6 volts," *Energy & Environmental Science,* vol. 11, pp. 2858-2864, 2018.

[217] C. Bocca, A. Barbucci, M. Delucchi, and G. Cerisola, "Nickel–cobalt oxide-coated electrodes: influence of the preparation technique on oxygen evolution reaction (OER) in an alkaline solution," *International journal of hydrogen energy,* vol. 24, pp. 21-26, 1999.

[218] I. Katsounaros, S. Cherevko, A. R. Zeradjanin, and K. J. Mayrhofer, "Oxygen electrochemistry as a cornerstone for sustainable energy conversion," *Angewandte Chemie International Edition,* vol. 53, pp. 102-121, 2014.

[219] R. Kötz, H. Neff, and S. Stucki, "Anodic Iridium Oxide Films: XPS-Studies of Oxidation State Changes and," *Journal of The Electrochemical Society,* vol. 131, p. 72, 1984.

[220] S. Song, H. Zhang, X. Ma, Z. Shao, R. T. Baker, and B. Yi, "Electrochemical investigation of electrocatalysts for the oxygen evolution reaction in PEM water electrolyzers," *international journal of hydrogen energy,* vol. 33, pp. 4955-4961, 2008.

[221] R. Yeo, J. Orehotsky, W. Visscher, and S. Srinivasan, "Ruthenium-Based Mixed Oxides as Electrocatalysts for Oxygen Evolution in Acid Electrolytes," *Journal of the Electrochemical Society,* vol. 128, pp. 1900-1904, 1981.

[222] S. Themsirimongko, N. Promsawan, and S. Saipanya, "Noble metal and Mn3O4 supported carbon nanotubes: enhanced catalysts for ethanol electrooxidation," *Int J Electrochem Sci,* vol. 11, pp. 967-982, 2016.

[223] H. Ma, C. Liu, J. Liao, Y. Su, X. Xue, and W. Xing, "Study of ruthenium oxide catalyst for electrocatalytic performance in oxygen evolution," *Journal of Molecular Catalysis A: Chemical,* vol. 247, pp. 7-13, 2006.

[224] V. Natarajan, S. Basu, and K. Scott, "Effect of treatment temperature on the performance of RuO2 anode electrocatalyst for high temperature proton exchange membrane water electrolysers," *International journal of hydrogen energy,* vol. 38, pp. 16623-16630, 2013.

[225] G. C. da Silva, N. Perini, and E. A. Ticianelli, "Effect of temperature on the activities and stabilities of hydrothermally prepared IrOx nanocatalyst layers for the oxygen evolution reaction," *Applied Catalysis B: Environmental,* vol. 218, pp. 287-297, 2017.

[226] S. L. Candelaria, N. M. Bedford, T. J. Woehl, N. S. Rentz, A. R. Showalter, S. Pylypenko, *et al.*, "Multi-component Fe–Ni hydroxide nanocatalyst for oxygen evolution and methanol oxidation reactions under alkaline conditions," *ACS Catalysis,* vol. 7, pp. 365-379, 2017.

[227] H. Hwang, T. Kwon, H. Y. Kim, J. Park, A. Oh, B. Kim, *et al.*, "Ni@ Ru and NiCo@ Ru Core–Shell Hexagonal Nanosandwiches with a Compositionally Tunable Core and a Regioselectively Grown Shell," *Small,* vol. 14, p. 1702353, 2018.

[228] Y. Yang, H. Fei, G. Ruan, C. Xiang, and J. M. Tour, "Efficient electrocatalytic oxygen evolution on amorphous nickel–cobalt binary oxide nanoporous layers," *ACS nano,* vol. 8, pp. 9518-9523, 2014.

[229] D. Sridhar, H. Yu, J.-L. Meunier, and S. Omanovic, "Carbon nano-fiber forest foundation for ruthenium oxide pseudo-electrochemical capacitors," *Materials Advances,* 2020.

[230] S. Ardizzone, G. Fregonara, and S. Trasatti, "“Inner” and “outer” active surface of RuO2 electrodes," *Electrochimica Acta,* vol. 35, pp. 263-267, 1990.

[231] E. O. Nwanebu, Y. Yao, and S. Omanovic, "The Influence of Ir Content in $(Ni_{0.4}Co_{0.6})_{1-x}Ir_x$-oxide Anodes on their Electrocatalytic Activity in Oxygen Evolution by Acidic and Alkaline Water Electrolysis," *Journal of Electroanalytical Chemistry,* p. 114122, 2020.

[232] I. Barauskienė and E. Valatka, "Layered nickel-cobalt oxide coatings on stainless steel as an electrocatalyst for oxygen evolution reaction," *Electrocatalysis,* vol. 10, pp. 63-71, 2019.

[233] D. Yang, W. Qiu, J. Xu, P. Wang, D. Jin, X. Peng, *et al.*, "Facilely Synthesized NiCo2O4/CNTs Nanocomposites for Surpercapacitors with Enhanced Performance," *International Journal of Electrochemical Science,* vol. 11, pp. 7262-7268, 2016.

[234] C. Felix, B. J. Bladergroen, V. Linkov, B. G. Pollet, and S. Pasupathi, "Ex-situ electrochemical characterization of IrO2 synthesized by a modified Adams fusion method for the oxygen evolution reaction," *Catalysts,* vol. 9, p. 318, 2019.

[235] J. Balcerzak, W. Redzynia, and J. Tyczkowski, "In-situ XPS analysis of oxidized and reduced plasma deposited ruthenium-based thin catalytic films," *Applied Surface Science,* vol. 426, pp. 852-855, 2017.

[236] A. Foelske, O. Barbieri, M. Hahn, and R. Kötz, "An X-ray photoelectron spectroscopy study of hydrous ruthenium oxide powders with various water contents for supercapacitors," *Electrochemical and Solid State Letters,* vol. 9, p. A268, 2006.

[237] W. Sun, L.-m. Cao, and J. Yang, "Conversion of inert cryptomelane-type manganese oxide into a highly efficient oxygen evolution catalyst via limited Ir doping," *Journal of Materials Chemistry A,* vol. 4, pp. 12561-12570, 2016.

[238] D. Yan, W. Wang, X. Luo, C. Chen, Y. Zeng, and Z. Zhu, "NiCo2O4 with oxygen vacancies as better performance electrode material for supercapacitor," *Chemical Engineering Journal,* vol. 334, pp. 864-872, 2018.

[239] P. M. Kulal, D. P. Dubal, C. D. Lokhande, and V. J. Fulari, "Chemical synthesis of Fe2O3 thin films for supercapacitor application," *Journal of Alloys and Compounds,* vol. 509, pp. 2567-2571, 2011.

[240] M. P. Browne, H. Nolan, G. S. Duesberg, P. E. Colavita, and M. E. Lyons, "Low-overpotential high-activity mixed manganese and ruthenium oxide electrocatalysts for oxygen evolution reaction in alkaline media," *ACS Catalysis,* vol. 6, pp. 2408-2415, 2016.

[241] J. E. Park, H. Lee, S.-H. Oh, S. Y. Kang, I. Choi, Y.-H. Cho, *et al.*, "Electrodeposited mesh-type dimensionally stable anode for oxygen evolution reaction in acidic and alkaline media," *Chemical Engineering Science,* vol. 206, pp. 424-431, 2019.

[242] M. Tariq, W. Q. Zaman, W. Sun, Z. Zhou, Y. Wu, L.-m. Cao, *et al.*, "Unraveling the beneficial electrochemistry of IrO2/MoO3 hybrid as a highly stable and efficient oxygen evolution reaction catalyst," *ACS Sustainable Chemistry & Engineering,* vol. 6, pp. 4854-4862, 2018.

[243] Y. Wu, M. Tariq, W. Q. Zaman, W. Sun, Z. Zhou, and J. Yang, "Ni–Co Codoped RuO2 with Outstanding Oxygen Evolution Reaction Performance," *ACS Applied Energy Materials,* vol. 2, pp. 4105-4110, 2019.

[244] J. O. M. Bockris and T. Otagawa, "Mechanism of oxygen evolution on perovskites," *The Journal of Physical Chemistry,* vol. 87, pp. 2960-2971, 2002.

[245] B. JO'M, T. Otagawa, and V. Young, "Solid state surface studies of the electrocatalysis of oxygen evolution on perovskites," *Journal of Electroanalytical Chemistry and Interfacial Electrochemistry,* vol. 150, pp. 633-643, 1983.

[246] Y. Yoon, B. Yan, and Y. Surendranath, "Suppressing ion transfer enables versatile measurements of electrochemical surface area for intrinsic activity comparisons," *Journal of the American Chemical Society,* vol. 140, pp. 2397-2400, 2018.

[247] C. Wei, S. Sun, D. Mandler, X. Wang, S. Z. Qiao, and Z. J. Xu, "Approaches for measuring the surface areas of metal oxide electrocatalysts for determining their intrinsic electrocatalytic activity," *Chemical Society Reviews,* vol. 48, pp. 2518-2534, 2019.

[248] World Health Organization. (2019). *Drinking-water*. Available: https://www.who.int/news-room/fact-sheets/detail/drinking-water

[249] World Health Organization, "Progress on drinking water, sanitation and hygiene: 2017 update and SDG baselines," 2017.

[250] J. Levasseur and J. Marcoux. (2015). *Bad water: 'Third World' conditions on First Nations in Canada (October 15, 2015 ed.)*.

[251] C. Gottschalk, J. A. Libra, and A. Saupe, *Ozonation of water and waste water: A practical guide to understanding ozone and its applications*: John Wiley & Sons, 2009.

[252] M. Gattrell and D. Kirk, "A study of the oxidation of phenol at platinum and preoxidized platinum surfaces," *Journal of The Electrochemical Society,* vol. 140, p. 1534, 1993.

[253] E. Chatzisymeon, A. Dimou, D. Mantzavinos, and A. Katsaounis, "Electrochemical oxidation of model compounds and olive mill wastewater over DSA electrodes: 1. The case of Ti/IrO2 anode," *Journal of Hazardous Materials,* vol. 167, pp. 268-274, 2009.

[254] M. Panizza and G. Cerisola, "Application of diamond electrodes to electrochemical processes," *Electrochimica Acta,* vol. 51, pp. 191-199, 2005.

[255] E. Lacasa, E. Tsolaki, Z. Sbokou, M. A. Rodrigo, D. Mantzavinos, and E. Diamadopoulos, "Electrochemical disinfection of simulated ballast water on conductive diamond electrodes," *Chemical Engineering Journal*, vol. 223, pp. 516-523, 2013.

[256] A. Katsoni, D. Mantzavinos, and E. Diamadopoulos, "Sequential treatment of diluted olive pomace leachate by digestion in a pilot scale UASB reactor and BDD electrochemical oxidation," *Water research,* vol. 57, pp. 76-86, 2014.

[257] A. M. S. Solano, C. K. C. de Araújo, J. V. de Melo, J. M. Peralta-Hernandez, D. R. da Silva, and C. A. Martínez-Huitle, "Decontamination of real textile industrial effluent by strong oxidant species electrogenerated on diamond electrode: viability and disadvantages of this electrochemical technology," *Applied Catalysis B: Environmental,* vol. 130, pp. 112-120, 2013.

[258] M. Zhou, Q. Dai, L. Lei, C. a. Ma, and D. Wang, "Long life modified lead dioxide anode for organic wastewater treatment: electrochemical characteristics and degradation mechanism," *Environmental science & technology,* vol. 39, pp. 363-370, 2005.

[259] A. Polcaro, S. Palmas, F. Renoldi, and M. Mascia, "On the performance of Ti/SnO2 and Ti/PbO2 anodesin electrochemical degradation of 2-chlorophenolfor wastewater treatment," *Journal of Applied Electrochemistry,* vol. 29, pp. 147-151, 1999.

[260] T. Wu, G. Zhao, Y. Lei, and P. Li, "Distinctive tin dioxide anode fabricated by pulse electrodeposition: high oxygen evolution potential and efficient electrochemical degradation of fluorobenzene," *The Journal of Physical Chemistry C,* vol. 115, pp. 3888-3898, 2011.

[261] E. Morgounova, Q. Shao, B. J. Hackel, D. D. Thomas, and S. Ashkenazi, "Photoacoustic lifetime contrast between methylene blue monomers and self-quenched dimers as a model for dual-labeled activatable probes," *Journal of biomedical optics,* vol. 18, p. 056004, 2013.

[262] M. N. Usacheva, M. C. Teichert, and M. A. Biel, "The role of the methylene blue and toluidine blue monomers and dimers in the photoinactivation of bacteria," *Journal of Photochemistry and Photobiology B: Biology,* vol. 71, pp. 87-98, 2003.

[263] W. Spencer and J. R. Sutter, "Kinetic study of the monomer-dimer equilibrium of methylene blue in aqueous solution," *Journal of Physical Chemistry,* vol. 83, pp. 1573-1576, 1979.

[264] N. M. Abu Ghalwa and F. R. Zaggout, "Electrodegradation of methylene blue dye in water and wastewater using lead oxide/titanium modified electrode," *Journal of Environmental Science and Health, Part A,* vol. 41, pp. 2271-2282, 2006.

[265] C. Comninellis and C. Pulgarin, "Electrochemical oxidation of phenol for wastewater treatment using SnO 2, anodes," *Journal of applied electrochemistry,* vol. 23, pp. 108-112, 1993.

[266] M. Indu, A. Gupta, and C. Sahoo, "Electrochemical oxidation of methylene blue using lead acid battery anode," *APCBEE procedia,* vol. 9, pp. 70-74, 2014.